UNIVERSITY OF STRATHCLYDE
GLASGOW
DEPARTMENT OF MECHANICAL ENGINEERING

SUPPORT TOOLS FOR THE PREDICTION OF DISTORTION IN THE DESIGN AND MANUFACTURE OF THIN PLATE WELDED STRUCTURES

DUNCAN CAMILLERI B.Eng(Hons)

2005

Thesis Presented for
The Degree of Doctor of Philosophy

Declaration of Author's Rights

ABSTRACT

This study aims to develop and validate a wide-ranging simulation tool to predict welding distortion in plates and shells, with particular emphasis on out-of-plane deformation. The approach adopted in this thesis, uncouples the thermal, elasto-plastic and structural effects leading to distortion and makes use of simple algorithms, named *'Mismatched Thermal Strain'* and *'Contraction Thermal Strain'*. These algorithms are generic with respect to material and welding process and they enable the application of finite element simulation and analysis on an economical and industrially practicable scale. The final computational based approach has been used to investigate alternative welding sequences in multiply stiffened plates, with respect to the minimization of out-of-plane deformation.

The theoretical models and results generated in this study have been supported at all stages by welding tests of a realistic nature to maintain confidence in the validity and applicability of the treatments. To achieve this aim, a pilot programme was designed to develop thermal and distortion measurement techniques and computational approaches, before up-scaling to a typical industrial size of fabrication. Steel plates were butt and fillet welded in the pilot programme to give 0.5m square finished test plates, while plates of more realistic dimensions at 4m x 1.5m were welded, to act as a comparison and cross-reference for the large scale computational analysis.

From the computational viewpoint, the problem has been reduced to a single load step analysis per weld pass. Comparison between the results of the simulations and the measured out-of-plane deformations was good. The accuracy of the computational analysis was found to depend on knowledge of the initial out-of-plane deformations and other external factors such as self-weight and support positions. In double-sided fillet welding using two-welding heads in parallel, insufficient spacing or staggering of the heads means that the contraction force could exceed the critical buckling load of the structure. In multiply stiffened plates, minimization of the out-of-plane deformation was achieved by welding the central stiffeners first followed by the adjacent outer stiffeners.

ACKNOWLEDGMENTS

I wish to record my sincere gratitude to my principal supervisor Prof. T.G.F Gray and my second supervisor Dr. T. Comlekci for their continuous assistance, advice and encouragement throughout the course of this project.

The project has been supported by the Engineering and Physical Sciences Research Council (EPSRC contract GR/R35407/01) and BAE Systems Marine, which provided the test plates and welding equipment. I gratefully acknowledge the participation in the project of Dr. N. MacPherson of BAE Systems and colleagues at the University of Strathclyde, in particular Mr. A. Galloway for the continuous assistance, patience and support during the welding of the test plates, the technical staff (Mr. S. Black, Mr. C. Cameron, Mr. R. Mackenzie, Mr. N. McCrindle and Mr. J. Doherty) for building the welding test rigs, Dr C. K. Lee for his advice on the thermal aspects of welding and Prof. J.T. Boyle, Head of Mechanical Engineering Department for making the facilities of the department available during the course of this project.

My colleagues at the University of Strathclyde have been very supportive and our discussions on a wide range of issues proved to be very valuable. I thank you for the encouragement you have given me.

I am particularly grateful to my parents Joseph and Maria Lourdes, my fiancée Ms. Alison Vella and friends for their constant encouragement and support throughout the years spent in Glasgow.

Nomenclature

Upper case:

A	Area (m^2)
A_c	Cross sectional area (m^2)
A_t	Proportional thermal load constant
$A_{t(r)(s)}$	Proportional thermal load constant for weld run r and section s
A_w	Cross sectional area of the weld (m^2)
A_{wd}	Cross sectional area of deposited weld material (m^2)
A_{wp}	Penetrated cross-sectional area in the plate (m^2)
A_{ws}	Penetrated cross-sectional area in the stiffener (m^2)
B_c	Coefficient of loss of temperature $B_c = 2\delta / c\rho d$ (s^{-1})
B_f	Free angular distortion (°)
C_1	Planck's first radiation constant 3. 7415 x 10^{-16} (Wm^2)
C_2	Planck's second radiation constant 1. 4388 x 10^{-2} (mK)
E	Elastic modulus (N/m^2)
$E_{b\lambda}(T)$	Monochromatic emissive power of a blackbody at absolute temperature T (W/m^3)
E_b	Total radiant emittance of a blackbody (W/m^2)
E_r	Total radiant energy captured by camera (W/m^2)
F	Contraction force (N)
Gr	Grashoff number
H	Heat dissipation ratio $H = h_f / K_c$ (m^{-1})
H_e	Enthalpy (J/kg)
K_c	Thermal conductivity (J/msK)
K_{cA}	Thermal conductivity of air (J/msK)

K_o	Modified Bessel function of the second kind and zero order
L	Length of plate (m)
L_{max}	Maximum weld length segment (m)
Nu	Nusselt number
Pr	Prandtl number
Ra	Rayleighs number
T	Temperature (K)
T_a	Ambient temperature (K)
T_c	Temperature read from the thermographic camera when emissivity is set to one (°K).
T_s	Surface temperature (K)
T_o	Initial temperature (K)
T_f	Film temperature (K)
$T_l(y)$	Artificial load temperature at position y (K)
T_{li}	Artificial load temperature at a node in the structural model (K)
T_{lir}	Artificial load temperature at a node and run r in the structural model (K)
T_M	Maximum temperature (K)
T_{Mi}	Maximum temperature reached at node i (K)
T_T	Transverse thermal load (K)
T_{Tr}	Transverse thermal load for weld run r (K)
W	Total weight of weld material per unit length (kg/m)
W_o	Weight of weld material deposited in each successive pass per unit length (kg/m)
W_A	Total weight deposited in first pass per unit length (kg/m)

Lower case:

$a = 1/2\lambda$	Thermal diffusivity (m^2/s) where $\lambda = \frac{c\rho}{2K_c}$ and $a = \frac{K_c}{c\rho}$
a_{air}	Thermal diffusivity of air (m^2/s)
a_c	Weld pool half width (m)
b_w	Width of weld pool (m)
b_M	Transverse distance from weld axis at T_{Mi} (m)
c	Specific heat (J/kgK)
d / d_p	Thickness of plate (m)
d_s	Thickness of stiffener (m)
d_{pen}	Penetration depth of fillet weld (m)
d_K	Arbitrary non-dimensional thickness
d_c	Distance from centre of weld pool to top surface of the plate (m)
f_f	Fraction of heat deposited in front of the weld
fr	Fraction of heat deposited at the rear of the weld
g	Acceleration due to gravity (m/s^2)
h_f	Film coefficient (W/m^2K)
h_{fr}	Radiation film coefficient (W/m^2K)
h_{fc}	Convection film coefficient (W/m^2K)
k	Fraction not contributing to transverse thermal strain
k_f	Fraction not contributing to transverse thermal strain in fillet welding (second weld pass)
l_m	Length of weld pool (m)
l_o	Original length of dilatometer test specimen (m)
q	Rate of heat (J/s)
q_{lin}	Rate of heat input per unit length (J/m)
q_{area}	Rate of heat input per unit section (W/m^2)

q_{vol}	Heat generation rate per unit volume (W/m³)
$q_{m.vol}$	Maximum value of power density at centre of ellipsoid (W/m³)
q_s	Heat flux (W/m²)
q_{rad}	Heat loss due to radiation (W/m²)
$r = \sqrt{\chi^2 + y^2}$	Radial distance from moving coordinate (m)
$R = \sqrt{\chi^2 + y^2 + z^2}$	Spherical distance from moving coordinate (m)
r_a	Radial distance of heat source (m)
s	Depth of penetration of a butt-weld (m)
t	Time (s)
$\{u\}$	Nodal displacement vector
v	Welding speed (m/s)
w	Twist due to local contraction of fillet weld (°)
x	Distance from heat source along the longitudinal axis (m)
y	Distance from heat source along the transverse axis (m)
y_1	Maximum yielded zone distance from heat source(m)
y_2	Maximum elastic/plastic zone distance from heat source (m)
$y_{1(r)(s)}$	Maximum yielded zone distance for weld run r and section s from heat source (m)
$y_{2(r)(s)}$	Maximum elastic/plastic zone distance for weld run r and section s, from heat source (m)
z	Distance from heat source along the through thickness of plate (m)
z_w	Centroid of transverse mechanical deformation (m)

Greek letters:

χ	Distance from moving coordinate along the longitudinal axis (m)
ε	Strain
ε_i	Initial strain
ε_l	Longitudinal strain
ε_t	Transverse strain
ε_x^*	Inherent strain in longitudinal direction
ε_y^*	Inherent strain in transverse direction
ε_y	Yield strain
ε_s	Emissivity
ε_c	Emissivity calibration factor
$\varepsilon_{tensile}$	Initial tensile strain
$\varepsilon_{compresion}$	Initial compressive strain
η	Efficiency
η_m	Fraction of heat used to fuse the base material
σ	Stress (N/m^2)
σ_{sb}	Stefan Boltzman constant $5.67x10^{-8}$ (W/m^2K^4)
σ_y	Yield strength (N/m^2)
λ_e	Eigen value
λ_w	Wavelength (m)
ρ	Density (kg/m^3)
δ	Coefficient of heat emission (J/m^2sK)
δ_l	Longitudinal shrinkage (m)
δ_t	Transverse shrinkage (m)
δ_{lT}	Change in length at temperature T (m)
α	Coefficient of expansivity (K^{-1})
α_x	Arbitrary coefficient of expansivity in longitudinal direction

	(K^{-1})
α_y	Arbitrary coefficient of expansivity in transverse direction (K^{-1})
$\alpha_{T_1-T_2}$	Coefficient of expansivity between T_1 and T_2 (K^{-1})
α_z	Arbitrary coefficient of expansivity in z direction(K^{-1})
$\sum \Delta_T$	Thermal deformation (m)
$\sum \Delta_e$	Elastic / mechanical deformation (m)
Δ_o	Transverse mechanical strain (compression – top surface)
Δ_t	Transverse mechanical strain (tensile – bottom surface)
Δ_{av}	Average transverse mechanical deformation (m)
ν_{air}	Viscosity of air (kg/ms)
ν	Poisson ratio
θ	Bending due to local contraction of fillet weld (°)
β	Bouyancy of air (K^{-1})
ζ	Smoothing parameter

CONTENTS

CHAPTER ONE

CHAPTER 1

INTRODUCTION

1.1 Background

Prior to the introduction of welding, structures such as bridges and ships were fabricated by means of riveted joints. These structures were subjected to intricate designs and took a long time to manufacture. With the arrival of welding in the mid 1930's, more rapid progress in fabrication of these structures was achieved. With the use of welding, an appreciable reduction in material and time, while using simple designs, was viable, thereby reducing the total production costs. However, the complexity of welding processes and possible effects on the structures due to welding were not fully understood. The knowledge was so poor that dramatic accidents to such structures were frequent. Many welded structures fractured due to weld cracks, shape distortions and dimensional contractions. However, as the need for welding has been increasingly realised, research has increased substantially, to understand the physical metallurgy and process parameters of welding. A recent comprehensive review of the finite element simulations of welding performed up to 2001, is given by Lindgren [1.1]. The general understanding from the research is that welding involves a complex thermo-mechanical process. Furthermore, the mode and magnitude of distortion in a given case depends on design/manufacturing variables (such as thickness, spacing of components, material, welding process parameters and fabrication sequences).

The phenomena associated with welding are now much better understood but residual stresses and permanent deformations are unavoidable consequences. These arise from the fact that in fusion welding the work piece is not heated uniformly. The

non-uniform expansion and contraction of the weld and surrounding base metal result in a number of mismatched thermal strains. This leads to local residual deformation, which will then cause distortion. Welding deformations not only complicate the fabrication of welded structures, they are also accompanied by a residual stress field. Both phenomena might reduce suitability of the structure by either departing from the calculated stress or by changing the final desired dimensions.

At present, shipbuilding companies face increasing challenges to produce light weight structures, in order to decrease weight and maintain a low overall centre of gravity of the ship. This constraint is being achieved by using thin plates to build the panels, decks and superstructures that constitute the building blocks of ships. As pointed out by Masubuchi [1.2], '*Engineers in the shipbuilding industry will face severe problems with residual stresses and distortion in the years ahead*,' due to increasing use of thin plates, aluminium alloys and other non-ferrous alloys, and the stringent tolerance for distortion. Thin plates are particularly prone to buckling and even more so when the plates are not perfectly flat as a result of induced welding deformations. The load carrying capacity of these plates is greatly reduced. Thus the problems associated with welding thin plate structures are of particular importance and need to be addressed.

Many industries concerned with the fabrication of thin plate structures, consequently experience difficulties and high rectification costs. Out-of-plane distortion, in particular, makes it difficult to align the edges of sub-assemblies and results in a lack of 'fairness' in the completed structure. A recent review of an extensive, collaborative programme, funded by the U.S. Navy Office of Naval Research [1.3] states that *'Severe distortions have emerged as a major obstacle to the cost-effective fabrication of such lightweight structures'*. In the review performed by Lightfoot [1.4] on the ship building company, BAE systems, states that 10% of the steel work hours involve rework. Typical rework recognised by BAE systems include heat straightening, fairing and aligning, but omits other man hours involved in handling the plates, following standards, delays in the programme and any other subsidiary

effects associated with rectification costs. The total amount of rectification costs probably, therefore, accounts for 20% of the total man-hours involved in the completion of structure. To put some monetary value on this, the sub company BAE Systems, Govan, employs 100 steel workers amounting to 150,000 hours of work per annum. Of this, 60,000 hours are in large unit/block assembly. Thus the actual amount of rectification hours might total, 12,000 hours, leading to rectification cost of at least £120,000 p.a.

Means of mitigating welding distortions during the fabrication process exist. However the complexity of ship structures makes the development of such techniques difficult and dependent on individual welding configurations and material. A better means of controlling distortion is to predict the amount of distortion associated with the different welding techniques available. Following such predictions, the best welding configuration and pre-processing techniques can be employed to achieve the final 'acceptable' panel shape.

The general practice in industry is to base predictions of distortion on previous outcomes of particular cutting and welding procedures and assembly sequences, but this is not always successful. This knowledge is usually specific to the different companies due to the different welding practices employed between them and thus a general trend cannot be defined [1.4]. At present, there are few predictive tools to support design and the interpretation of manufacturing variables on economical and industrial scale. Various analytical and computational approaches to the problem are, possible and have become more applicable as computational capability increases. However, such strategies have not so far been widely used in industries concerned with fabrication of this type, due presumably to the in-house expertise needed and the complexity.

1.2 Scope of work

The overall scope of this study aims to improve the applicability of computational distortion prediction by providing simple and adaptable methodologies, which can be

readily validated through experience of application in the industrial context. While being generic with respect to material properties, welding processes and thickness, efforts were made to produce a computationally economic and robust welding distortion simulation. In so doing, design engineers will be able to explore alternative parameters and find out if the outcome will be acceptable, prior to the manufacturing operations typical of large scale welded structures. A key factor that underlies this aim is an *uncoupled* computational strategy, whereby the thermal transient, thermo-elastic-plastic and structural stages of the thermo-mechanical welding process are treated separately. The theoretical models and results generated in the project have been supported at all stages by welding tests of a realistic nature to maintain confidence in the validity and applicability of the analysis. A pilot programme was designed to test out thermal and distortion measurement techniques and computational approaches, before up-scaling to a typical industrial size of fabrication. Typically plates $0.5m^2$ were butt and fillet welded in the pilot programme, while plates of more realistic dimension at 4m x 1.5m were welded to act as a comparison and cross-reference for the large scale computational analysis.

Experimental tests were performed on two specially designed welding rigs specific to the small and large-scale tests. The rigs were equipped with a thermographic camera, thermocouples, linear variable displacement transducers (LVDTs) and a laser scanning system for the data capture of thermal transients and quantification of the distortion.

1.3 Structure of thesis

The formulation and validation of the uncoupled simplified elastic algorithm is presented in this thesis. The study is subdivided into different sections dealing with different aspects of welding distortion, organised in eight chapters.

In chapter two, a general review of the phenomena leading to welding residual stresses, which consequently give rise to possible different modes of deformation, is presented. Present state of the art analytical and finite element thermo-elasto-plastic

analyses related to the prediction of thermal transients and welding induced stresses are outlined. In particular the review concentrates on work done to predict welding distortions using both simplified analyses and the full thermo-elasto-plastic computational analyses.

In chapter three the theoretical models, formulated from the early insights of Okerblom [1.5], are adapted to give a simplified uncoupled thermo-elasto-plastic welding distortion algorithm. Two orthotropic thermal strains are generated to give a transverse and longitudinal thermal strain, named *'Contraction Thermal Strain'* and *'Mismatched Thermal Strain'* respectively. The presence of previously laid welds are also taken into account in the evolution of the longitudinal thermal strain, while different transverse thermal strains are devised depending on the welding configuration (butt or fillet welding). The thermal loads are later assessed, evaluated and applied to the structural finite element analyses presented in the following chapters

The computational models were cross-referenced to realistic experimental results, to validate the simplified uncoupled elastic algorithms. Two welding rigs were built and are described in chapter four. A general description of the experimental set-up and measurement techniques used in the experimental procedures are given. Calibration methods and errors associated with the different data capturing procedures are addressed. Methods of reducing these errors and a means of representing the final deformation are also given.

The first step of the uncoupled analysis is to establish the thermal transients evolved in welding. Chapter five describes the different thermal analyses adopted in this study and applied to different welding configurations. A comparison between the different finite element and analytical thermal solutions is presented. The simplest analysis, with adequate accuracy when compared to the experimental results is found and this is later used as an input to the structural finite element analysis.

Chapter six offers an initial validation of the simple elastic algorithm via small-scale butt and fillet welds, before up-scaling to industrial sized plates. Test and computational results are examined and evaluated to reveal simplified features of the welding phenomena and thus lead to the prediction of welding distortions using computer efficient finite element structural analyses. The most important variables leading to welding distortions are distinguished and are applied using different computational strategies.

Test specimens and computational analyses dealing with different stiffener/ plate assemblies, including butt welding, double-sided fillet welding and multiply stiffened plate, of 4m x 1.5m plates are presented in chapter seven. The thermo-elasto-plastic algorithms were then applied to different welding sequences to minimize the out-of-plane deformation while taking into consideration other factors such as manufacturing times.

Finally, chapter eight gives conclusions and recommendations for further work.

1.4 References

[1.1] Lindgren,L.E., 'Finite Element Modeling and Simulation of Welding Part 1: Increased Complexity', *Journal of Thermal Stresses,* Vol.24, No.4, pp141-192, 2001.

[1.2] Masubuchi,K., 'Recent M.I.T. Research on Residual Stresses and Distortion in Welded Structures,' *Journal of Ship Production,* Vol.9, No.3, pp 137-145, 1993.

[1.3] Haung,T.D., Dong,P., DeCan,L.A, Harwig,D.D., 'Residual Stresses and Distortions in Lightweight Ship Panel Structures, Northrop Grumman,' *Technology Review Journal,* Vol. 11 No.1 pp1-26, 2003.

[1.4] Lightfoot,M., 'Prediction of Distortion Control and Techniques to avoid Rework,' *A Report on the General Causes of Fabricated Steel Plate Distortion, School of Marine Science and Technology, University of Newcastle Upon Tyne,* 2003.

[1.5] Okerblom,N.O., 'The calculation of deformations of welded metal structures,' *Her Majesty's Stationery Office, London, 1958.*

CHAPTER TWO

CHAPTER 2

LITERATURE REVIEW & THEORETICAL BACKGROUND

2.1 Introduction and scope of review

Large rectification costs are required to 'fair' the deformations (reduce the deformations to an exceptable level and / or align different plate structures) resulting from welding, cutting and any other non-uniform processes. The in-plane deformations, which are usually a shrinkage in the overall size of the plates under construction, are of small magnitude and are usually accounted for by initially specifying larger plates. The out-of-plane deformation is more problematic, in that it makes it difficult to align different sub-structures together, often accompanied by lack of fairness in the overall structure. This study is mainly concerned with the out-of-plane deformation emerging after welding. The phenomena leading to the out-of-plane deformation are complex and a great deal of knowledge is required in the following topics:

1. Temperature transients evolved during the heating and cooling cycles of the welding process, which in turn subject different sections to a non-uniform thermal cycle.
2. The formation of the thermal strains from the thermal transients, leading to residual stresses and strains.
3. Though the residual stresses are in equilibrium within the whole structure, the localised stresses within the vicinity of the weld drive the plate into different modes of deformations. A knowledge of the possible types of deformations and the mechanics that triggers them, will eventually make it possible to predict the final deformation, thereby leading to methods to reduce unwanted effects.

A great deal of research on thermo-mechanical aspects has been performed since the introduction of welding. A bibliography of finite element analyses and simulation of welding presented between 1976-1996 [2.1] and 1996-2001 [2.2] are given by Mavkerle. Most of the work is concentrated in predicting or finding the localised residual stresses. Prior to the development of modern computers, welding distortions and residual stresses were calculated via empirical formulas. These formulas were specific to the different welding processes and type of deformation being analysed. Though most of this work was based on experiments, many simplifications concerning the mechanics of welding and a number of empirical factors were embedded in the formulas. With the introduction of computer technology and commercial finite element software, complex welding processes have been simulated with reasonable accuracy and computing time. The literature review presented in this study presents various analytical solutions and finite element methods in the literature to date.

2.1.1 Evolution of welding deformations

Welding is intended to create a continuous joint between components, for example two plates. A number of joining processes are available, ranging from the creation of a liquid bridge, such as in arc welding, to the plastic deformation stir effect achieved by friction stir welding. The joining process considered in this thesis is arc welding, whereby fusion is achieved by heating up the parent material and the filler metal to the liquid state. This section, which eventually liquefies and mixes, is referred to as the fusion zone or weld pool. In low carbon steels liquid / solid state boundary is distinguished by the eutectic temperature, that is 1493°C. Every point in the material will consequently be subject to a thermal cycle a heating and a cooling cycle, and which is different to other points in their vicinity. The high temperatures involved and the non-uniform heating and cooling cycles, will subject points in the vicinity of the weld to thermal strains that exceed the yield strain. A comprehensive review on the evolution of welding residual stresses is given by Masubuchi [2.3], [2.4]. Masubuchi shows that if the material is only subjected to thermal strains of elastic nature during the entire heating and cooling cycle, the welded structure would follow

the curve OAB'C' shown in Figure 2.1 and hence return to the original shape. However the permanent plastic deformation resulting from the non-uniform thermal strains will deform the plate and it will then follow a curve such as OABC in Figure 2.1.

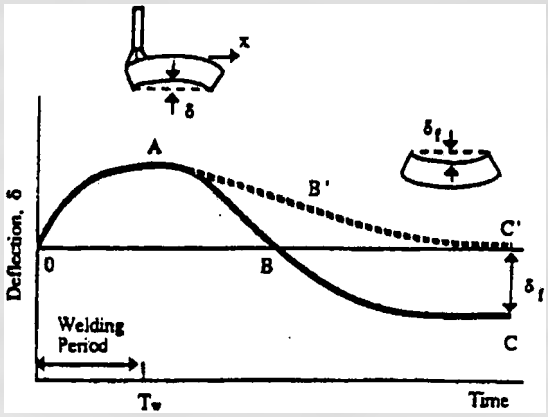

Figure 2.1: Transient deformation of a rectangular plate during and after welding [2.3]

One of the main driver of welding deformation is the longitudinal residual stress. Consider a weld bead deposited along the longitudinal axis of a plate of infinite width, shown in Figure 2.2, where the welding arc, moving at welding speed v, is located at the origin O.

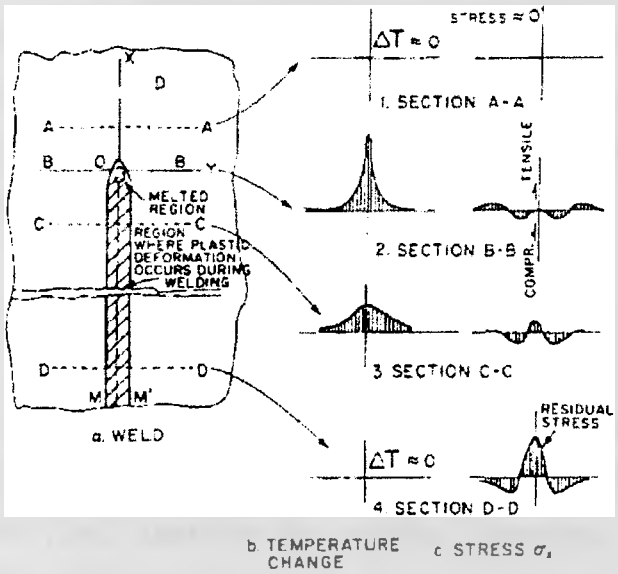

Figure 2.2: Schematic representation of changes in temperature ΔT and stresses during welding [2.4]

Various instances during the welding cycle will be accompanied by different thermal gradients along the transverse direction of the weld. The typical welding speeds associated with common processes are usually fast in relation to the heat conduction and hence the thermal gradients ahead of the arc are usually negligible – section A-A. At the arc a steep thermal gradient evolves, whereby the temperatures in close proximity to the weld are higher – section B-B. Further away from the weld, section C-C, the cooling cycle prevails though points closer to the weld are still at a higher temperature, until no thermal gradient exists, section D-D.

As there are no thermal gradients ahead of the weld, the points residing in these sections are in equilibrium and will not be subjected to any thermal strain. During the heating cycle the heated zone will try to expand but is restrained by the surrounding colder material, further away from the weld, section B-B. It is also important that because the molten material does not support a load, any thermal strains present in the weld pool and at this instance will be relieved. However points further away from the fusion zone will be subjected to large thermal strains, exceeding the yield strain and hence resulting in permanent plastic deformation. During the cooling cycle, the colder material prevents the contraction of the yielded region, causing tensile stresses to develop, section C-C. In short, the expansion and subsequent contraction of the yielded zone, evolved during the heating and cooling cycle of the welding process, will result in a build-up of tensile stresses around the weld combined with simultaneously generated compression stresses in the rest of the plate. The combination of these residual stresses will drive the plate to move away from an initial flat or pre-deformed shape.

2.1.2 Modes of deformations

Depending on the amount of restraint and residual stresses built up in welded structures, the final permanent deformation can follow several different distortion modes. Masubuchi [2.4], classified the welding distortions into seven main distortion modes. These may further be categorized in two main groups, the in-plane

deformations and the out-of-plane deformations. Figure 2.3 shows the different modes of deformations as:

- In-plane deformation
  - Transverse shrinkage resulting from the in-plane transverse contraction - Figure 2.3a.
  - Longitudinal shrinkage an effect of the in-plane longitudinal contraction - Figure 2.3b.
  - Rotational deformation is a change in weld gap due to the subsequent heating and cooling of the material ahead and after the welding arc - Figure 2.3c.
- Out-of-plane deformation
  - Angular distortion due to the non-uniform heating through the thickness resulting in eccentric transverse contraction - Figure 2.3d.
  - Longitudinal deformation (sometimes referred to as bowing distortion) caused by the eccentric longitudinal shrinkage with respect to the neutral axis of the plate - Figure 2.3e.
  - Torsional deformation - Figure 2.3f.
  - Buckling deformation caused by the instability of thin plates due to high residual stresses - Figure 2.3g.

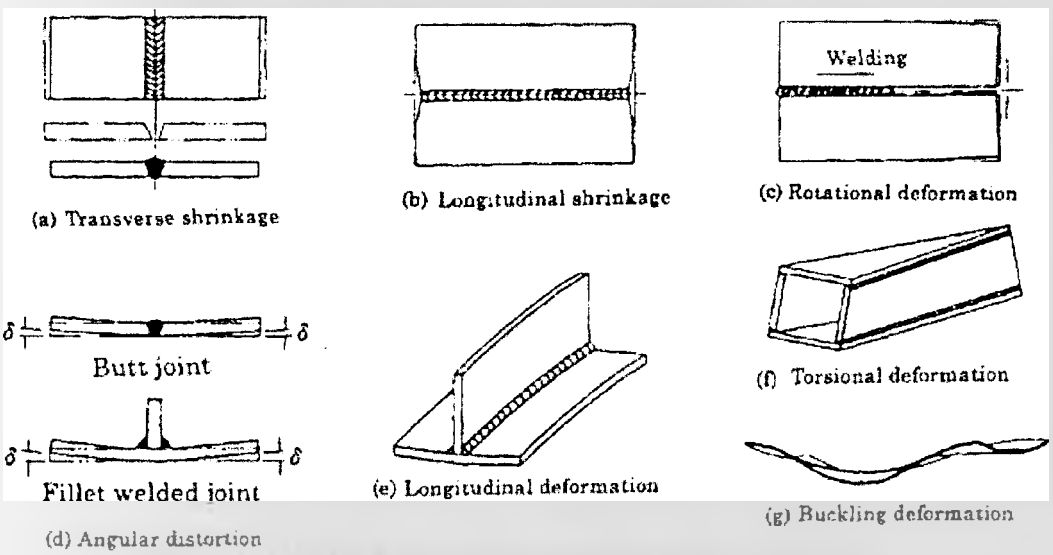

Figure 2.3: Different modes of welding deformations [2.4]

2.1.3 *Phenomena occurring during welding*

The welding process involves many different phenomena, which together generate residual stresses and hence deformations of the welded structure. The coupling that exists between the thermal transients, microstructure evolution and the final structural integrity of the welded structures is very significant. The recent review by Lindgren [2.5],[2.6],[2.7] identifies the coupling in during the welding cycle. The full, coupled thermo-mechanical model is shown in Figure 2.4 and connection points between the heat flow, deformation and microstructure evolution, are identified in Table 2.1.

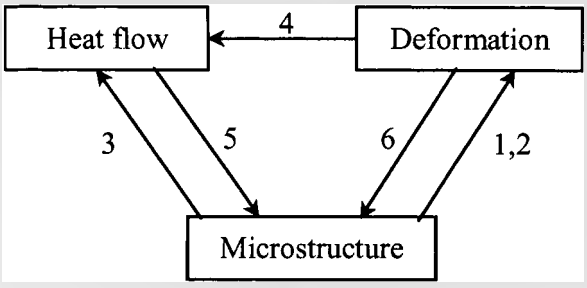

Figure 2.4: Phenomena occurring during welding [2.5],[2.8]

Coupling	Explanation
1a	Thermal expansion depends on microstructure
1b	Volume changes due to phase changes
2a	Plastic material behaviour depend on microstructure of material
2b	Elastic material behaviour depend on microstructure of material
3a	Heat conductivity and heat capacity depend on microstructure of material
3b	Latent heat due to phase changes
4a	Deformation changes thermal boundary conditions
4b	Heat due to plastic dissipation (plastic strain rate)
4c	Heat due to thermal strain rate
4d	Heat due to elastic strain rate
5	Microstructure evolution depends on temperature
6	Microstructure evolution depends on deformation

Table 2.1: Coupling occurring during welding [2.5],[2.8]

Some of the couplings are usually ignored. Typically Lindgren, following Boley and Weiner [2.9], states that the effect of mechanically generated plastic heat is small when compared to the weld heat input. Furthermore it is also often possible to neglect the influence on the changing geometry on the thermal behaviour. In all couplings the thermal dilation, which is the sum of the thermal expansion and the volume changes due to phase transformations, is the main driver of residual welding stresses. The effect on stresses resulting from phase changes is also often ignored and hence with the exception of the thermal dilation the material properties are usually a function of the temperature and not of the temperature history. It is possible to do the full coupling analysis, whereby the thermal and mechanical analyses are solved simultaneously, however this approach is not recommended by Lindgren. If coupling is strong Lindgren recommends to use a staggered approach shown in Figure 2.5.

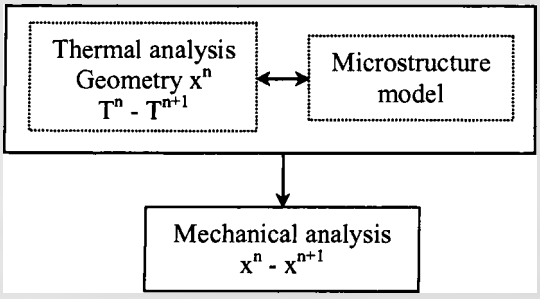

Figure 2.5: A time step in the staggered approach [2.5],[2.8]

Further simplifications can be performed by uncoupling the thermal transients and thermal strains, thereby performing two different analyses i.e. a thermal analysis followed by a structural thermo-mechanical analysis. Figure 2.6 shows a weakly uncoupled analysis, where the coupling numbers have the same meaning given in Table 2.1.

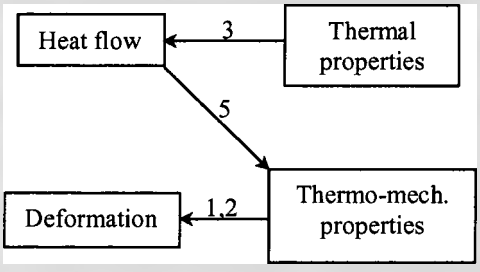

Figure 2.6: A weakly uncoupled analysis [2.5],[2.8]

Depending on the coupling existing between the various phenomena, a simple uncoupled or a staggered approach can give reasonable results when compared to the full coupled analysis.

2.1.4 External factors affecting welding distortions

The couplings presented in section 2.1.3, imply that strong relationships exists between the thermal expansion, specific heat, thermal diffusivity, yield strength and Young's modulus at a given temperature, and therefore influence formation of the final deformations and residual stresses. Verhaeghe [2.10] concluded that any operation influencing the magnitude of any of these factors would alter the ability of the material to resist distortion.

A review of external factors contributing to welding residual stresses and deformations was performed by Lightfoot [2.11] and these may be summarised as follows:

1. *Residual stresses* inherent in the material prior to welding. During the different manufacturing processes such as rolling, forming, shearing and bending, residual stresses will be created. The magnitude of the inherent residual stresses will increase with more change in shape of the components undergoing different manufacturing processes.
2. *Amount and type of restraint.* A means of controlling distortion is by restraining the plate from moving, during the heating and cooling cycle of welding. In so doing more residual stresses will build. A compromise between the residual stresses and the final deformation has to be achieved, in that while more restraint will decrease the final deformation, a higher residual stress will be induced in the material. The amount of restraint is limited by the formation of possible cracks in the welds.
3. *Joint design.* The placing and number of welds needed to produce a structure will have an influence on the final distortion. One good practice is to perform welds parallel to the neutral axis of the structure. Together with this the weld volume

should be as low as possible and hence the weld prep should be limited to accommodate the minimum amount of welding required. This influence is of particular importance in butt-welding. In general, the larger the joint angle groove the more weld metal is deposited, resulting in a different through thickness transverse shrinkage, consequently the out-of-plane angular distortion is increased [2.12].

4. *Manufacturing procedures* before welding. The cutting process and the tack welding procedures impose residual stresses in the plate.
5. *Plate handling and storage.* This is particularly important when handling thin plates. The self-weight of thin plate structures can result in permanent deformations in the plate and are of particular importance when dealing with buckling.
6. *Assembly of structures.* This factor is important when dealing with multiple stiffened plates and multipass welding. The residual stresses imposed during previous welds will contribute to the final residual stresses of later welds. A usual practice adopted in automated welding is to use what is known as egg-crate construction technique [2.13], whereby all the stiffeners are first tack welded onto the plate and then welded on. In the case of most ship building companies the longitudinal stiffeners are tacked and welded first, followed by the tacking and welding of the transverse stiffeners. Methods of finding the best possible welding sequences are essential in this respect.

Tsai *et al* in [2.13] gave an extensive review of literature and patents, regarding the factors affecting distortion and mitigation techniques. In this study Tsai divided the factors affecting distortion in design related variables such as; weld joint details, plate thickness, stiffener spacing, and number of stiffener attachments, and process related variables, including; welding process, heat input and travel speed. A number of mitigation techniques are also presented that include; preheating, mechanical tensioning, prebending fillet joints, presetting butt joints and using appropriate thermal arrangements such as balancing the heat input or balancing about the neutral axis.

Another study concerned with the mitigation of distortion in thin panel structures is given by Conrardy and Dull [2.14]. The authors concluded that in thin panel structures, buckling (due to longitudinal residual stresses) is the predominant form of distortion followed by angular distortion. Clearly, the amount of restraint applied to the structure will significantly reduce the distortion but possibly with the adverse effect of increasing the residual stresses. However the study by Doersksen [2.15] concluded that a high degree of restraint reduces distortion without significantly increasing the residual stress. Of essential importance when dealing with thin plate welded structures is to make sure that the welding induced stresses are lower than the critical buckling stress. Baxter [2.16] presents a rather simple method that relates the maximum heat input that can be applied to specific thin plate structures for the prevention of buckling. This takes into consideration the plate thickness, free span and stiffener spacing.

Research at M.I.T. during the early 1990's, deal with mitigation and rectification techniques for the reduction of welding distortions. These are presented in the study given by Masubuchi in [2.3]. Studies included the preheating of different parts (such as the web in a fillet weld) with different selected initial temperature, analysis to reduce joint mismatch via the appropriate number of tack welds and the application of side heating to high-strength weldments. Further research was performed to control and use automated intelligent systems for line heating with the use of a high power laser source as a rectification procedure.

All the mentioned techniques and procedures to reduce distortion can be employed, but essentially all welded structures will be subjected to residual stress and hence welding distortions. Masubuchi states that *'One must have a proper capability of predicting, by analysis, prior to experiments, how the weldment being studied deforms and how to perform proper controls to change the distortion being considered,'* [2.3]. This implies that ability to predict welding distortions via finite element analysis or analytical solutions is of large importance to the designers of welded structures.

2.2 Welding induced temperature fields

The first step in any computation of welding distortion is to establish the transient thermal distributions caused by a given welding process in the geometry of interest. This may be achieved in a variety of ways, ranging from the early analytical treatments of Rosenthal [2.17], Rykalin [2.18] and Well [2.19], to the finite element based methods, as reviewed by Lindgren [2.5] [2.6].

2.2.1 Heat flow fundamentals

The fundamental behaviour of the heat flow equation is based on the first law of thermodynamics [2.20], [2.21], [2.22], [2.23]. The first law of thermodynamics states that the thermal energy is conserved within a control volume, such that the relationship between the heat generation rate and the volume's temperature is given in equation 2.1.

$$\rho c\left(\frac{\partial T}{\partial t}+\{v\}^T\nabla T\right)+\nabla^T\{q_{hf}\}=\frac{dq_{vol}}{dt} \qquad \textit{Equation (2.1)}$$

where

$T=T(x,y,z,t)$	Temperature (°K)
$\{\nabla\}^T=\left\{\frac{\partial}{\partial x},\frac{\partial}{\partial y},\frac{\partial}{\partial z}\right\}$	Vector operator
$\{v\}^T=\begin{Bmatrix}v_x & v_y & v_z\end{Bmatrix}$	Velocity vector for mass transport of heat
$\{q_{hf}\}$	Heat flux vector (W/m^2)
q_{vol}	Internal heat generation rate per unit volume (J/m^3)

Note that in most welding simulations performed, the velocity vector for mass transportation of heat is usually ignored and drops from equation 2.1. Using Fourier's law, the relationship between the heat flux vector to the thermal gradients, is shown in equation 2.2. When a temperature gradient exists in a solid medium heat will flow from the higher temperature to the lower temperature region, hence the minus sign in equation 2.2.

$$\{q_{hf}\} = -[D]\{\nabla\}T \qquad \textit{Equation (2.2)}$$

where [D] is the conduction matrix:

$$[D] = \begin{bmatrix} K_{xx} & 0 & 0 \\ 0 & K_{yy} & 0 \\ 0 & 0 & K_{zz} \end{bmatrix}$$

K_{xx}, K_{yy}, K_{zz} is the conductivity in the element in the x, y and z directions respectively. Combining equations 2.1 and 2.2 give the general equation 2.3 and in a more familiar form given in equation 2.4.

$$\rho c\left(\frac{\partial T}{\partial t} + \{v\}^T \nabla T\right) = \nabla^T([D]\nabla T) + \frac{dq_{vol}}{dt} \qquad \textit{Equation (2.3)}$$

$$\rho c\left(\frac{\partial T}{\partial t} + v_x\frac{\partial T}{\partial x} + v_y\frac{\partial T}{\partial y} + v_z\frac{\partial T}{\partial z}\right) = \frac{dq_{vol}}{dt} + \frac{\partial}{\partial x}\left(K_{xx}\frac{\partial T}{\partial x}\right) + \frac{\partial}{\partial y}\left(K_{yy}\frac{\partial T}{\partial y}\right) + \frac{\partial}{\partial z}\left(K_{zz}\frac{\partial T}{\partial z}\right)$$

Equation (2.4)

The boundary conditions applied to the thermal analysis can be divided into three, [2.23] (refer to Figure 2.7):

1. Specified temperatures acting on surface S_1, such that $T = T^*$, where T^* is the specified temperatures.

2. Specified heat flows acting over the surface S_2:

$$\{q\}^T\{\eta\} = -q^* \quad or \quad \{\eta\}^T[D]\{\nabla\}T = q^* \qquad \textit{Equation (2.5)}$$

where

$\{\eta\}$ Unit outward normal vector, where positive heat flow is into the boundary, i.e. in the direction opposite to the normal vector

q^* Specified heat flow (W/m²)

3. Specified convection surfaces acting over the surface S_3, following Newton's law of cooling:

$$\{q\}^T\{\eta\} = h_f(T_s - T_a) \quad or \quad \{\eta\}^T[D]\{\nabla\}T = h_f(T_a - T_s) \qquad \textit{Equation (2.6)}$$

Where h_f is the film coefficient evaluated at $(T_a + T_s)/2$. The film coefficient boundary condition can be divided into a radiation h_{fr} and convection h_{fc} film coefficient. Given a body temperature of T_S the amount of heat loss to ambient temperature at T_a due to radiation, will follow the well known Stefan-Boltzmann law, given in equation 2.7.

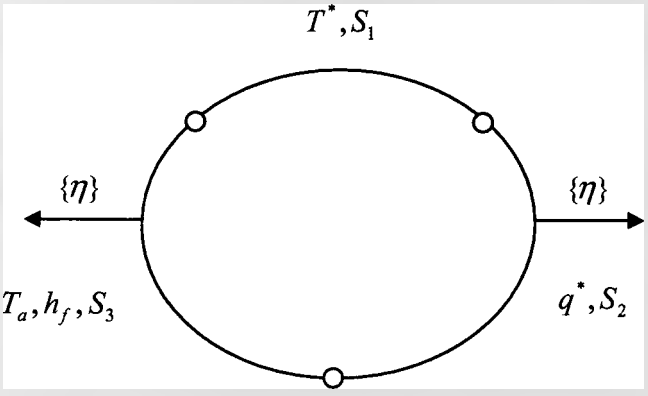

Figure 2.7: Thermal boundary conditions

$$q_{rad} = \sigma_{sb}\varepsilon_s(T_s^4 - T_a^4)$$
$$= h_{fr}(T_s - T_a) \qquad \textit{Equation (2.7)}$$

Hence the film coefficient due to radiation is given by:

$$h_{fr} = \frac{\sigma_{sb}\varepsilon_s(T_s^4 - T_a^4)}{(T_s - T_a)}$$
$$= \sigma_{sb}\varepsilon_s(T_s^2 + T_a^2)(T_s + T_a) \qquad \textit{Equation (2.8)}$$

The convection film coefficient will depend on the fluid (air) flowing over the respective surfaces of the plate. Turbulent and laminar, forced or natural flows will contribute to the convection cooling cycle of the plate. A general relationship that describes the convection film coefficient as a function of the Nusselt number is given in equation 2.9, [2.22].

$$h_{fc} = \frac{K_{cA}.Nu}{L_h} \qquad \textit{Equation (2.9)}$$

where K_{cA} is the thermal conductivity of air calculated at the film temperature $(T_a + T_s)/2$ and L_h is the surface area divided by the perimeter.

The Nusselt number will then take into considerations different aspects of the fluid flowing over the plate. Such include the position of the plate, natural or force cooling and laminar or turbulent fluid flows. For natural cooled plates, the following relationships between Rayleigh's number and Nusselt number exists, [2.22]:

For horizontal plates cooled naturally:

- Heated surface facing up:
  - Laminar range $(10^4 \leq Ra \geq 10^7)$

$$Nu = 0.54Ra^{1/4} \qquad \textit{Equation (2.10)}$$

  - Turbulent range $(10^7 \leq Ra \geq 10^{11})$

$$Nu = 0.15Ra^{1/3} \qquad \textit{Equation (2.11)}$$

- Heated surface facing down:
  - Laminar range $(10^5 \leq Ra \geq 10^{10})$

$$Nu = 0.27Ra^{1/4} \qquad \textit{Equation (2.12)}$$

For vertical plates cooled naturally:

  - Laminar range $(10^4 \leq Ra \geq 10^9)$

$$Nu = 0.6Ra^{1/4} \qquad \textit{Equation (2.13)}$$

  - Turbulent range $(10^9 \leq Ra \geq 10^{12})$

$$Nu = 0.13Ra^{1/3} \qquad \textit{Equation (2.14)}$$

In the above equations the Rayleigh number is given by:

$$Ra = Gr.\Pr = \frac{g\beta(T_s - T_a)L_h^3}{\upsilon_{air} a_{air}} \qquad \textit{Equation (2.15)}$$

where Gr and Pr are Grashof and Prandtl numbers, while β, υ_{air} and a_{air} are the bouyancy, viscosity and thermal diffusivity of air respectively, calculated at the film temperature $T_f = (T_a + T_s)/2$.

2.2.2 Quasi-stationary analytical temperature distributions

The first attempts to define the temperature transients during welding were purely analytical and assumed that the thermal properties of the base material are constant and independent of temperature. The most significant early work was done by Rosenthal [2.17], [2.24], where appropriate solutions for linear, two and three-dimensional heat flows in solids of infinite size are derived. Starting from equation 2.4 and taking into consideration the above assumptions the heat conduction equation reduces to:

$$\frac{\partial^2 T}{\partial x^2} + \frac{\partial^2 T}{\partial y^2} + \frac{\partial^2 T}{\partial z^2} = \frac{1}{a}\frac{\partial T}{\partial t} \qquad \textit{Equation (2.16)}$$

Where a is the thermal diffusivity and is given by $a = K_c / c\rho$. It is convenient to define λ as the reciprocal of twice the thermal diffusivity (i.e. $1/2\lambda = a$ and $2\lambda = \frac{c\rho}{K_c}$), such that equation 2.16 may be represented as equation 2.17

$$\frac{\partial^2 T}{\partial x^2} + \frac{\partial^2 T}{\partial y^2} + \frac{\partial^2 T}{\partial z^2} = 2\lambda\frac{\partial T}{\partial t} \qquad \textit{Equation (2.17)}$$

Further simplification to the problem was done by assuming that the heat sources are moving at a constant steady speed, such that the temperature profile seen at the heat

source is quasi-stationary. In a quasi-stationary state, the temperature distribution around the heat source is constant hence, by modifying equation 2.17 into a moving co-ordinate system, shown in Figure 2.8, the transient temperatures may be treated as a steady-heat flow problem. This is achieved by replacing x co-ordinate along the weld line with a moving co-ordinate χ, where by $\chi = x - vt$ is the distance of the point in consideration from the point source relative to a moving heat source, hence the heat flow equation 2.18 is characterised.

$$\frac{\partial^2 T}{\partial \chi^2} + \frac{\partial^2 T}{\partial y^2} + \frac{\partial^2 T}{\partial z^2} = -2\lambda v \frac{\partial T}{\partial \chi} + 2\lambda \frac{\partial T}{\partial t} \qquad \textit{Equation (2.18)}$$

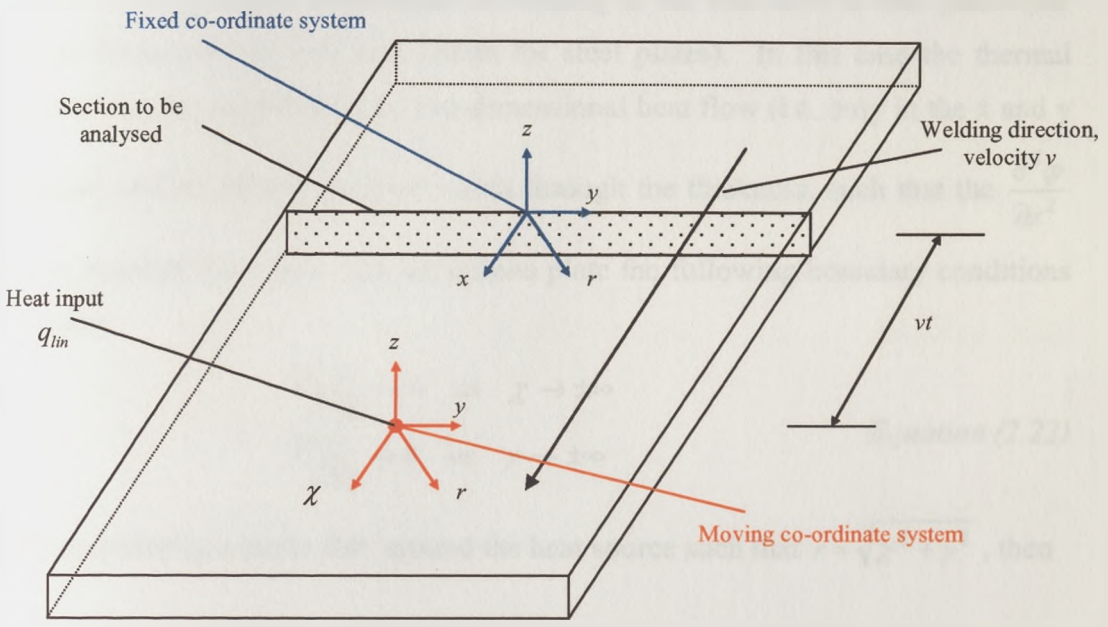

Figure 2.8: Moving heat source model

An important assumption for the quasi-static state to prevail is that the plate must be infinite such that the transient stages at the initiation and ending phase of welding are ignored and assumed not to be present. Following this assumption the $\frac{\partial T}{\partial t}$ term reduces to zero resulting in quasi -stationary heat flow equation 2.19

$$\frac{\partial^2 T}{\partial \chi^2} + \frac{\partial^2 T}{\partial y^2} + \frac{\partial^2 T}{\partial z^2} = -2\lambda v \frac{\partial T}{\partial \chi} \qquad \textit{Equation (2.19)}$$

Equation 2.19 may be simplified to

$$T = T_o + e^{-\lambda v \chi} \varphi(\chi, y, z) \qquad \textit{Equation (2.20)}$$

where T_o is the initial temperature of the solid and $\varphi(\chi, y, z)$ is a function to be determined. After substituting equation 2.20 in 2.19 and reduction of terms the following equation is obtained.

$$\frac{\partial^2 \varphi}{\partial \chi^2} + \frac{\partial^2 \varphi}{\partial y^2} + \frac{\partial^2 \varphi}{\partial z^2} - (\lambda v)^2 \varphi = 0 \quad or \quad \nabla^2 \varphi - (\lambda v)^2 \varphi = 0 \qquad \textit{Equation (2.21)}$$

Rosenthal [2.17], [2.24] develops the above equations for various instance and conditions. Of particular importance to welding is the heat flow in thin plates (for example thicknesses of less than 10mm for steel plates). In this case the thermal transients may be considered as a two-dimensional heat flow (i.e. only in the x and y directions) and no thermal gradient exists through the thickness, such that the $\frac{\partial^2 \varphi}{\partial z^2}$ term, in equation 2.21 falls. For an infinite plate the following boundary conditions are present:

$$\begin{aligned} \partial T / \partial \chi &\to 0 \quad as \quad \chi \to \pm\infty \\ \partial T / \partial y &\to 0 \quad as \quad y \to \pm\infty \end{aligned} \qquad \textit{Equation (2.22)}$$

and by considering a circle $2\pi r$ around the heat source such that $r = \sqrt{\chi^2 + y^2}$, then

$$-\frac{\partial T}{\partial r} 2\pi r K_c \to q_{lin} \quad as \quad r \to 0 \qquad \textit{Equation (2.23)}$$

Equation 2.21 can be further defined in cylindrical co-ordinates, given in equation 2.24.

$$\frac{d^2 \varphi}{dr^2} + \frac{1}{r}\frac{d\varphi}{dr} - (\lambda v)^2 \varphi = 0 \qquad \textit{Equation (2.24)}$$

The solution to equation 2.24 that satisfies the boundary conditions 2.22 and 2.23 is known as the modified Bessel function of the second kind and zero order, given by

$K_o(\lambda vr)$. Hence the solution to the two-dimensional heat flow is given in equation 2.25.

$$T - T_o = \frac{q_{lin}}{2\pi K_c} e^{-\lambda v \chi} K_o(\lambda vr) \text{ or } T - T_o = \frac{q_{lin}}{2\pi K_c} e^{\frac{-v\chi}{2a}} K_o\left(\frac{vr}{2a}\right) \quad \textit{Equation (2.25)}$$

The above solution assumes no heat loss to the environment. The primary drivers to the heat loss are the dissipation due to convection and radiation from the surfaces. For a unit surface area the rate of heat losses due to convection and radiation is given by equation 2.6. For simplification reasons a dissipation ratio will be used such that $H = {}^{h_f}\!/_{K_c}$. By assuming the heat dissipation from the top and bottom surfaces to be H_t and H_b respectively, and if the thickness of the plate d is small enough to neglect the thermal gradients within the thickness (as in thin plates), then equation 2.24 can be made to include the heat loss effect via equation 2.26.

$$\frac{d^2\varphi}{dr^2} + \frac{1}{r}\frac{d\varphi}{dr} - \left[(\lambda v)^2 + \frac{H_t + H_b}{d}\right]\varphi = 0 \quad \textit{Equation (2.26)}$$

Solving equation 2.26 gives the formulation below.

$$T - T_o = \frac{q}{2\pi K_c d} e^{-\lambda v \chi} K_o\left[r\sqrt{(\lambda v)^2 + \frac{H_t + H_b}{d}}\right] \quad \textit{Equation (2.26)}$$

Rosenthal also proposes a temperature distribution for a two dimensional system but with a variable line source. In such case the heat source is not assumed to be constant across the thickness of the plate but varies according to a Fourier series $q_{lin}(z)$ between $z = 0$ and $z = d$, shown in equation 2.27.

$$q_{lin}(z) = q_{lin}(0)\sum_0^n A_n \cos\frac{\pi n z}{d} \quad \textit{Equation (2.27)}$$

The differential equation 2.24 will have to be updated by adding the second derivative with respect to z, to read:

$$\frac{\partial^2\varphi}{\partial z^2}+\frac{\partial^2\varphi}{\partial r^2}+\frac{1}{r}\frac{\partial\varphi}{\partial r}-(\lambda v)^2\varphi=0 \qquad \textit{Equation (2.28)}$$

This equation is satisfied by the function of the form:

$$\cos\frac{\pi nz}{d}K_o\left(r\sqrt{\lambda v^2+\left(\frac{\pi n}{d}\right)^2}\right) \qquad \textit{Equation (2.29)}$$

Thus the thermal distributions are given by:

$$T-T_o=\frac{q_{lin}(0)}{2\pi K_c d}e^{-\lambda v\chi}\sum_0^n A_n\cos\frac{\pi nz}{d}K_o\left(r\sqrt{\lambda v^2+\left(\frac{\pi n}{d}\right)^2}\right) \qquad \textit{Equation (2.30)}$$

In a three-dimensional heat flow where the thermal gradients across the thickness of the plate cannot be neglected (as in thick plates) the following boundary conditions exists:

$$\begin{aligned} \partial T/\partial\chi &\to 0 \quad as \quad \chi\to\pm\infty \\ \partial T/\partial y &\to 0 \quad as \quad y\to\pm\infty \\ \partial T/\partial z &\to 0 \quad as \quad z\to\pm\infty \end{aligned} \qquad \textit{Equation (2.31)}$$

By considering a spherical surface $4\pi R^2$ drawn around the heat source, such that $R=\sqrt{\chi^2+y^2+z^2}$, then

$$-\frac{\partial T}{\partial r}4\pi R^2K_c\to q \quad as \quad R\to 0 \qquad \textit{Equation (2.32)}$$

Using polar co-ordinates equation 2.21 can be rewritten as:

$$\frac{d^2\varphi}{dR^2}+\frac{2}{R}\frac{d\varphi}{dR}-(\lambda v)^2\varphi=0 \quad or \quad \frac{d^2(R\varphi)}{dR^2}-(\lambda v)^2R\varphi=0 \qquad \textit{Equation (2.33)}$$

A solution to equation 2.33 and the boundary conditions in 2.31 and 2.32 is given below

$$R\varphi=Ce^{-\lambda vR} \quad or \quad \varphi=\frac{Ce^{-\lambda vR}}{R} \qquad \textit{Equation (2.34)}$$

Hence the corresponding temperature distribution for a three-dimensional system is:

$$T - T_o = \frac{q}{4\pi K_c} e^{-\lambda v \chi} \frac{e^{-\lambda v R}}{R} \qquad \textit{Equation (2.35)}$$

Figure 2.9 shows the typical temperature contour plot of a 6mm mild steel plate butt welded with a nominal heat input per unit length of 992J/mm. Two observations can be made:

- There is negligible heat flow ahead of the weld resulting in a steeper thermal gradient as opposed to the shallow thermal gradients at the rear of the weld in the longitudinal direction.
- The maximum temperatures at specific point on a cross section transverse to the weld axis are not reached at the same time and a time lag exists.

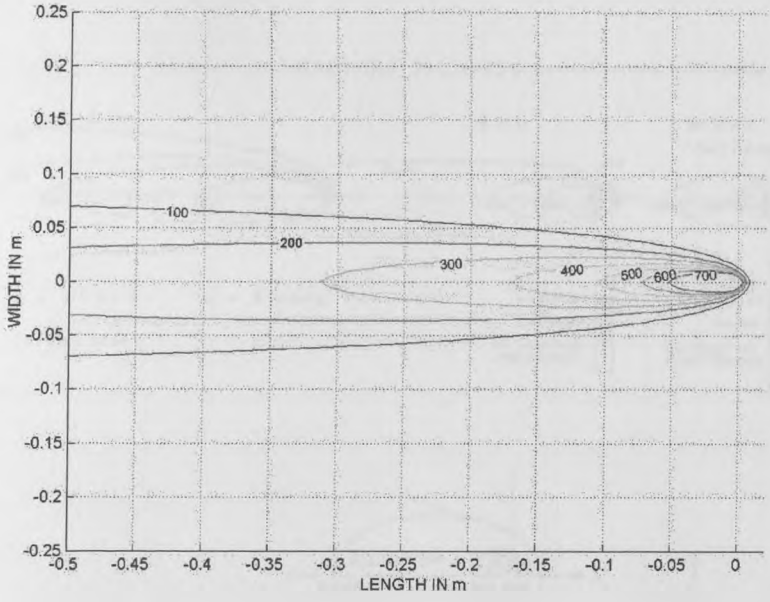

Figure 2.9: Thermal distribution in a butt-welded plate

To a large extent the thermal contours will be influenced by the material properties, welding parameters and thickness of plate under consideration namely, as shown in Figure 2.10:

- An increase in welding speed will produce a greater lag between the isotherms.
- An increase in conductivity and thermal diffusivity will change both the shape and size of the isotherms.

- An increase in thickness will result in more heat being dissipated in the material thus the isotherms are smaller.
- An increase in heat input will increase the range of the isotherms but will not have an effect on the shape of the isotherms.

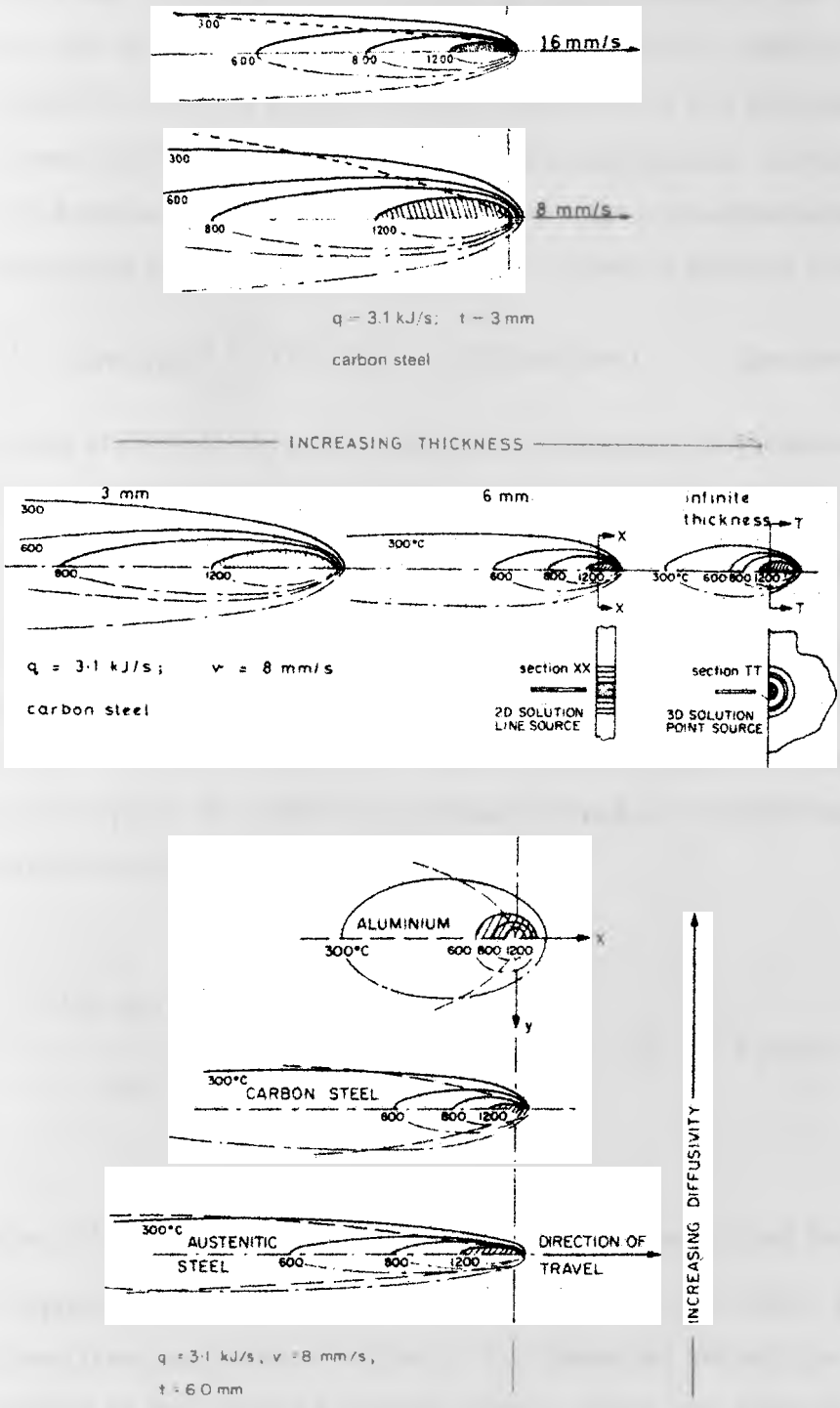

Figure 2.10: Effect of thermal parameters and welding variables [2.25]

2.2.3 *Developments to Rosenthal's quasi-stationary analytical solutions.*

Rosenthal [2.17] has given a number of possible situations. However, the question that always arises is whether the thin plate or thick plate solution is more appropriate to the analyses being performed. By considering the rate of cooling in both the thin plate solutions and the thick plate solutions Birk-Sorenson [2.26], inspired by the works of Rosenthal, derived a non-dimensional thickness d_K, that determines the transition between the thick plate solution and the thin plate solution. Starting from equation 2.25, Rosenthal [2.17] derived the cooling rate for a two-dimensional heat flow by looking at the weld line, i.e. $y = 0$ and $\chi = -vt$, given in equation 2.36.

$$\frac{dT}{dt} = -2\pi K_c c\rho d^2 \left(\frac{v}{q}\right)^2 (T - T_o)^3 \qquad \text{(2D heat flow)} \qquad \textit{Equation (2.36)}$$

By looking again at the weld line and $z = 0$ the rate of cooling in a three-dimensional heat flow is given by:

$$\frac{dT}{dt} = -2\pi K_c \frac{v}{q}(T - T_o)^2 \qquad \text{(3D heat flow)} \qquad \textit{Equation (2.37)}$$

In case of the thick plates, for a given temperature, heat input, material and speed the cooling rate is equal to unity, and is independent of the thickness of the plate. On the other hand in the two-dimensional heat flow equation the cooling rate will depend on the thickness of the plate. By combining equations 2.36 and 2.37 a non-dimensional thickness can be found and is given in equation 2.38.

$$\frac{\left(\frac{dT}{dt}\right)_{2d}}{\left(\frac{dT}{dt}\right)_{3d}} = \frac{-2\pi K_c c\rho d^2 \left(\frac{v}{q}\right)^2 (T - T_o)^3}{-2\pi K_c \frac{v}{q}(T - T_o)^2} = c\rho \frac{v}{q} d^2 (T - T_o)^2 = {d_K}^2 \qquad \textit{Equation (2.38)}$$

Using equation 2.38 if ${d_K}^2$ is less then unity then the two dimensional heat flow solution is appropriate, on the other hand if it is greater than unity, a three dimensional heat flow analysis has to be made. The distinction between one or the other is dependent on the material properties, welding speed, heat input and peak temperature under investigation. Figure 2.11 shows the transition at different peak

temperatures using a nominal heat input of 4760W (252A, 22.9V and efficiency of 0.825), having a welding speed of 4.8mm/s (These parameters are typical welding parameters obtained from the experiments described later). The specific heat and density, typical of the plates under investigation was assumed to be 782.61 J/kgK and 7830 kg/m³.

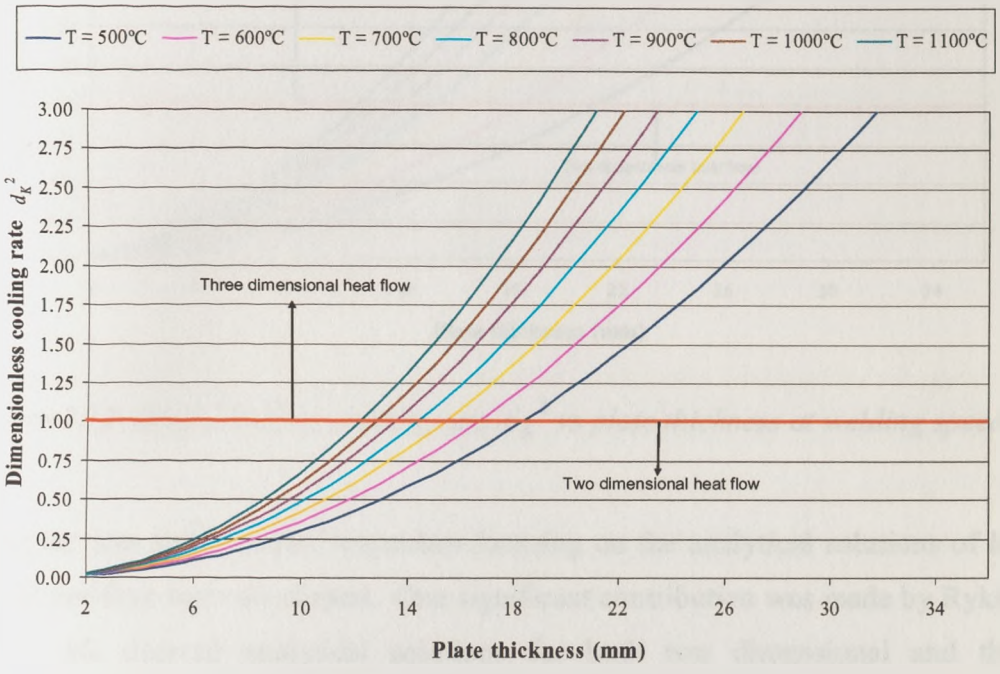

Figure 2.11: Dimensionless cooling rate d_K^2 vs plate thickness at different peak temperatures

It may be concluded that for far field temperatures (below 600°C), plates thinner than 15mm may be considered as a two dimensional heat flow problem, with no thermal gradient existent through the plate thickness. The dependence on variation in welding speed shows that an increase in welding speed, while keeping other variables constant, will result in a three-dimensional heat flow problem. This is shown in Figure 2.12 where the same heat input parameters and material properties mentioned above were used and the peak temperature was taken to be 600°C.

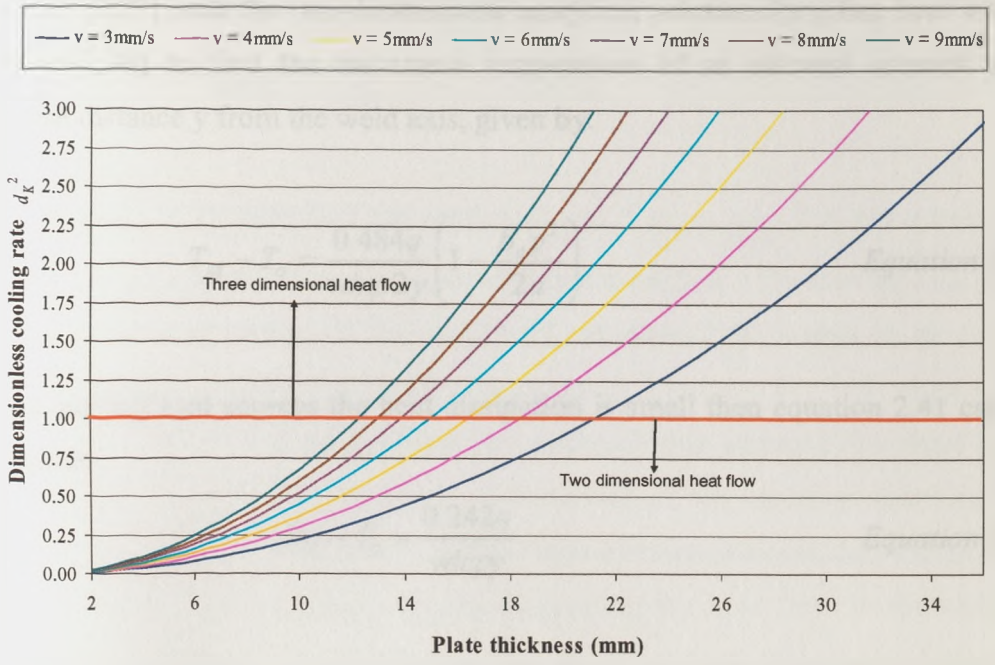

Figure 2.12: Dimensionless cooling rate d_K^2 vs plate thickness at welding speeds

During the late 1940's other researches focusing on the analytical solutions of heat flows in welding were developed. One significant contribution was made by Rykalin [2.18]. He derived analytical solutions for both two dimensional and three dimensional heat flows. The difference lies in an adjustment to the two dimensional analytical solution to compensate for heat dissipation loss and is given by equation 2.39.

$$T - T_o = \frac{q}{2\pi K_c d} e^{\frac{vx}{2a}} \left[K_o\left(\frac{r}{2a} \sqrt{v^2 + 4a\beta_c} \right) \right] \qquad \textit{Equation 2.39}$$

Where β_c is the coefficient of loss of temperature, given by $\beta_c = 2\delta / c\rho d$ and δ is the coefficient of heat emission. For high welding speeds the Bessel function can be expressed $K_o(p) = \sqrt{\frac{\pi}{2p}} e^{-p}$, hence equation 2.39 can be rewritten as:

$$T - T_o = \frac{q\sqrt{a}}{2K_c d\sqrt{\pi v r}} e^{\frac{vx}{2a} - \frac{vr}{2a}} \qquad \textit{Equation 2.40}$$

Okerblom [2.27] used the two dimensional analytical solution for a line heat source (equation 2.39) to find the maximum temperature of an element situated at a transverse distance y from the weld axis, given by:

$$T_M - T_o = \frac{0.484q}{vdc\rho 2y}\left(1 - \frac{\beta_c y^2}{2a}\right) \qquad \textit{Equation 2.41}$$

For fast moving heat sources the heat dissipation is small then equation 2.41 can be rewritten as

$$T_M - T_o = \frac{0.242q}{vdc\rho y} \qquad \textit{Equation 2.42}$$

An important aspect of equation 2.42 is that the maximum temperature, at particular positions transverse to the weld, is inversely proportional to the distance y. A correction due to Wells [2.19] for slower moving heat sources in a material of high diffusivity was applied to provide a relationship between the transverse distance y and T_M as:

$$T_M - T_o = 0.242\frac{q}{vd}\frac{1}{c\rho}\frac{1}{y} - 0.4\frac{a}{v} \qquad \textit{Equation 2.43}$$

One major consequence of the analytical solutions developed during the late 1940's and early 1950's, is that the solutions give an infinite temperature at the arc position and are not able to represent the temperatures developed at the weld pool. Lindgren in [2.28] proposed a dipole expansion of Rosenthal's solution, which models melting and solidifying given by equation 2.44.

$$T(x,y,t) - T_o = \frac{q}{v}\left[F(r_o) + 2\sum_{n=1}^{\infty} F(r_n)\right] \qquad \textit{Equation 2.44}$$

Where

$$r_n = \sqrt{(x - vt)^2 + y^2 + (nd)^2}$$

$$F(r_n) = \frac{1}{4\pi K_c} \frac{e^{\frac{v}{2a}(r_n+(x-vt))}}{r_n} \left[1 - l_m \left\{ \frac{v}{2a} \left(1 + \frac{x-vt}{r_n} \right) + \frac{x-vt}{{r_n}^2} \right\} \right]$$

The value of l_m is the length of the weld pool and if set to zero then equations 2.44 and 2.25 will give approximately the same thermal profiles. By moving heat from the front to the rear surface of the weld pool, equation 2.44 is able to model the melting and freezing of the weld pool. Furthermore, Lindgren in [2.28] gives a one dimensional (transverse direction) heat flow equation that assumes that there is no heat flow in the longitudinal direction. Comparison of the modified solutions and the classic two dimensional solution, to the finite element analysis, has shown very similar results for far field temperatures. Neglecting the heat flow in the welding direction did not affect the temperatures. On the other hand the extended solution gives closer temperatures at the weld pool when compared to the finite element analysis.

Finally Lindgren concludes that the temperature transients could be calculated from analytical solutions, if the residual stresses are of interest. However if the displacements, especially the change in gap width is of interest than finite element methods have to be employed.

2.2.4 Computer aided finite element thermal analyses

With increases in computer efficiency, finite element analysis has been employed for the calculation of thermal transients evolved during welding. As distinct from analytical solutions, finite element analysis offers the advantage of using temperature dependent material properties. Furthermore, any heat generation due to phase transformations and residual strains can be coupled in the thermal analyses. The latter is a very small contribution, however, and is usually omitted from the thermal analyses. Another advantage of finite element analysis is the ability to model a detailed heat source. A number of heat sources can be applied to the model, depending on the region of interest. Radaj [2.29] pointed out that if the far field

temperatures are of interest then a point or a line source is sufficient. However the region next to the weld is best described by spatially distributed heat sources such as a Gaussian distribution.

Research has been conducted in attempt to find the best technique to represent the heat source. In one of the early finite element analyses, Friedman [2.30] modelled the heat source as a surface heat flux having a radially symmetric normal distribution, shown in Figure 2.13.

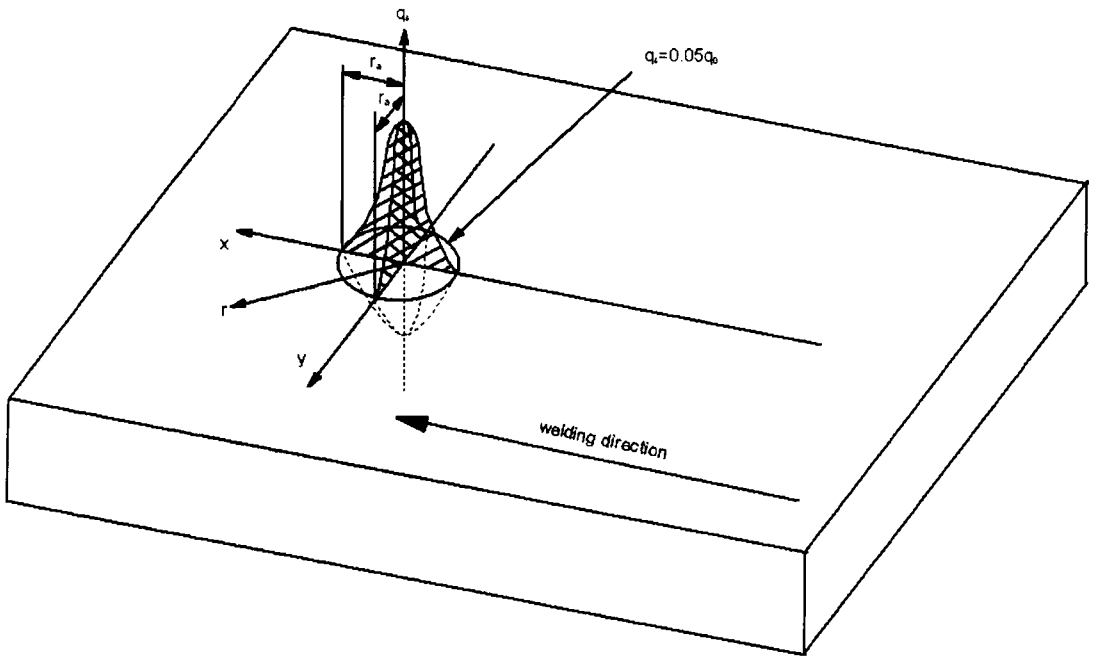

Figure 2.13: Radially symmetric normal distribution heat source model

If r is the distance from the centre of the heat source, then the heat flux q_s is given by:

$$q_s(r) = q_o e^{-Cr^2} \qquad \textit{Equation 2.45}$$

Where q_o and C are constants, determined by the magnitude and distribution of the heat input, hence the parameters q (effective heat input) and r_a (the radial distance in which 95% of the heat flux is deposited) are given by:

$$q = 2\pi \int_0^{\infty} q_s(r).r.dr$$

$$q_s(r_a) = 0.05 q_o$$

Equation 2.46

Solving the above, the heat input may be defined as:

$$q_s(y,x) = \frac{3q}{\pi r_a^{\,2}} e^{-3\left(\frac{r}{r_a}\right)^2}$$

Equation 2.47

The size and shape of the weld pool is determined by the radial parameter r_a. Younan *et al* [2.31] used Friedman's heat source model and have set the value of r_a to 5mm.

A more significant heat source model used by many researchers, typically [2.36],[2.48], [2.52] [2.53], [2.57] is the use of a double ellipsoidal heat distribution proposed by Goldak *et al* [2.32], shown in Figure 2.14.

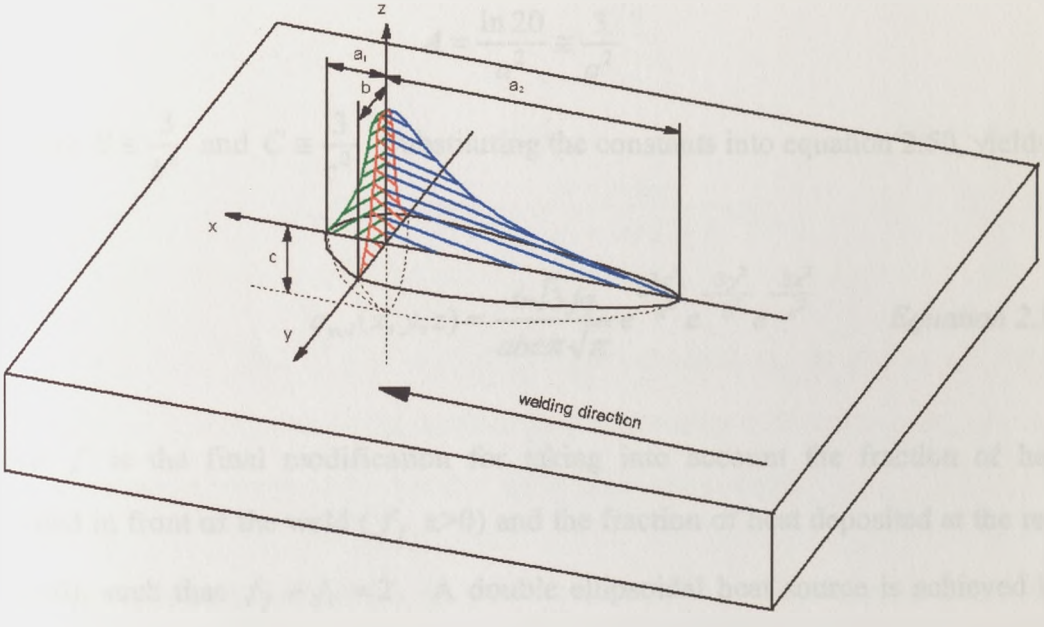

Figure 2.14: Double ellipsoidal heat source model

Starting from an ellipsoid with centre at (0,0,0) and semi-axes, a, b, c parallel to the co-ordinate axes x, y, z , the Guassian distribution of power intensity q_{vol} is given by:

$$q_{vol}(x,y,z) = q_{m.vol}e^{-Ax^2}e^{-By^2}e^{-Cz^2} \qquad \textit{Equation 2.48}$$

Where $q_{m.vol}$ is the maximum value of the power density at the centre of the ellipsoid. From the conversation of energy the heat input is given by:

$$q = 4\int_0^\infty \int_0^\infty \int_0^\infty q_{m.vol}e^{-Ax^2}e^{-By^2}e^{-Cz^2}dx.dy.dz \qquad \textit{Equation 2.49}$$

Evaluating equation 2.49 yields to:

$$q_{m.vol} = \frac{2q\sqrt{A.B.C}}{\pi\sqrt{\pi}} \qquad \textit{Equation 2.50}$$

To evaluate the constants A, B, and C the semi-axes values a, b, and c are defined as the distances where $q_{vol} = 0.05q_{m.vol}$ such that:

$$q_{vol}(a,0,0) = q_{m.vol}e^{-Aa^2} = 0.05q_{m.vol}$$

$$A = \frac{\ln 20}{a^2} \cong \frac{3}{a^2}$$

Similarly $B \cong \frac{3}{b^2}$ and $C \cong \frac{3}{c^2}$. Substituting the constants into equation 2.50, yields:

$$q_{vol}(x,y,z) = \frac{6\sqrt{3}fq}{abc\pi\sqrt{\pi}}e^{\frac{3x^2}{a^2}}e^{\frac{3y^2}{b^2}}e^{\frac{3z^2}{c^2}} \qquad \textit{Equation 2.51}$$

Where f is the final modification for taking into account the fraction of heat deposited in front of the weld (f_f x>0) and the fraction of heat deposited at the rear (f_r x<0), such that $f_f + f_r = 2$. A double ellipsoidal heat source is achieved by specifying two different values for a, i.e. a_1 and a_2 the semi-axis values parallel to the x coordinate at the front and rear to the weld respectively such that a continuous slope is achieved when $a_1 f_f = a_2 f_r$, (refer to Figure 2.14).

The best heat source to adopt also depends on the welding process under investigation. More complex welding processes, such as electron beam welding, with a small concentrated heat inputs, require a more complex heat source description, to represent both the stirring action of the molten metal and the digging action of the key hole. Roberts *et al*, in [2.33] developed two heat source models that best described the penetration associated with tungsten inert gas welding (TIG) and electron beam welding (EBW). For TIG welding Roberts found that a surface disc source is satisfactory to represent the heat source and is given by:

$$q_{area}(x,y) = \frac{\eta q}{a_c^{\,2}} \qquad \textit{Equation 2.52}$$

Where η is the efficiency of the process, a_c is the weld pool half width (in this case assumed to be 4mm) and $x^2 + y^2 \le a_c^{\,2}$. In the case of EBW the heat input consisted of two components, a surface disc and a volumetric conic source such that the total heat input is given by:

$$q_{area}(x,y) = \frac{\eta q}{a_c^{\,2}}$$

and $\qquad \textit{Equation 2.53}$

$$q_{vol}(x,y,z) = \frac{(1-p)\eta q}{s\left(\frac{1}{3}m^2 s^2 + msb_c + b_c^{\,2}\right)}$$

Where $x^2 + y^2 \le a_c^{\,2}$ and $x^2 + y^2 + z^2 \le b_c^{\,2}$. The constants a_c, b_c and m are fitting parameters, p is the partitioning coefficient (determining how much heat goes into the surface disc and conic source) and s is the penetration depth.

For a transient thermal analysis, the most important thermal properties associated with phase transformations are the latent heats. Care has to be taken to model these material properties, due to the sudden increase in latent heat capacity when compared to the solidus specific heat capacity. This may give rise to a stiff equation. Lindgren in [2.6] suggests either to specify the latent heat capacity over a larger temperature

range or to specify the heat capacity using the enthalpy method described in [2.34]. The use of enthalpy will result in a smoother curve and hence easier convergence. The enthalpy and heat capacity are related according to the following relation:

$$H_e(T) = \int_0^T \rho c(\tau) d\tau \qquad \textit{Equation 2.54}$$

Here the heat conduction equation 2.17 is reformulated into enthalpy as shown below:

$$\frac{K_c}{c\rho}\left(\frac{\partial^2 H_e}{\partial \chi^2} + \frac{\partial^2 H_e}{\partial y^2} + \frac{\partial^2 H_e}{\partial z^2}\right) = \frac{\partial H_e}{\partial t} \qquad \textit{Equation 2.55}$$

Another important aspect when modelling the weld pool is the conductivity. At the weld pool the heat is not only transmitted by conduction but also through convection due to fluid flow and other stirring effects. Many analyses [2.34], [2.35], [2.36], imitate this by increasing the thermal conductivity at high temperatures.

2.3 Analytical solutions for the prediction of welding deformations

Prior to the development of finite element analysis, extensive work has been done to derive analytical solutions for the prediction of welding distortions. Typical works include the Russian solutions derived by Okerblom [2.27], the Japanese work by Watanabe and Satoh [2.37] and the more recent studies by White, Leggatt and Dwight [2.38]. The analytical solutions are specific to the different types of deformation and often bulky analytical solutions have to be performed to find longitudinal shrinkage, transverse shrinkage and angular distortion. Most of the analytical solutions, based on experimental results, take crude assumptions to reduce the complexity of the solutions. However this makes the solutions specific to the welding process and material. An extensive review is given by Verhaeghe [2.39], in which he summarizes the analytical solutions to date in four different types of distortions; longitudinal shrinkage, transverse shrinkage, angular distortion and longitudinal deformation. The analytical solutions related to longitudinal

deformation are a direct consequence of the longitudinal shrinkage via simple bending moment theory and will not be discussed in this review.

2.3.1 Longitudinal shrinkage

In the recent review by Verhaeghe [2.39], the author states that in practice longitudinal shortening can be assumed to be 0.8mm and 3mm per 3m of weld for fillet welds and butt welds respectively. Most of the analytical approaches, establish a force acting at the yielded zone, from which the longitudinal strain can be recognized. Starting from the work proposed by Rykalin, Okerblom derived an expression for the prediction of longitudinal shrinkage given by:

$$\varepsilon_l = \frac{\delta_l}{L} = 0.335 \frac{1}{A_c} \frac{q}{v} \frac{\alpha}{c\rho} \qquad \textit{Equation 2.56}$$

Gray and Spence [2.25] inspired by Wells improved Okerblom's model by incorporating any heat dissipation losses originating in slow moving heat sources, resulting in the modified model given in equation 2.57

$$\varepsilon_l = 0.335 \frac{1}{A_c} \frac{q}{v} \frac{\alpha}{c\rho} - 0.8 \frac{a}{v} \frac{d}{A_c} \varepsilon_y \qquad \textit{Equation 2.57}$$

The work done by White et al [2.38] named the force acting over the yielded zone as a tendon force. Based on experiments the contraction force was found to be $F = 0.2\eta \, {}^{q}\!/_{v}$ where the efficiency η is generally assumed to be 80%. This value relates to Okerblom's force value $F = 0.335 \frac{qE\alpha}{vc\rho}$ or $F = 0.165\eta \frac{q}{v}$ when average specific heat, density, elastic modulus and expansivity of carbon steels are used in equation 2.56, although White et al make no reference to Okerblom. White et al seem to agree with Okerblom's findings in that the tendon force is independent of the type of weld and the yield stress. Furthermore both studies conclude that in multipass welding laid in close proximity the final tendon force is the overlapping force of the different weld runs, such that if two welds having the same parameters are laid on

top of each other with intermediate cooling to ambient temperature the final tendon force will be that of one weld.

2.3.2 Transverse shrinkage

The majority of the work assume that the cross-sectional area of the weld A_w, regulates the amount of transverse shrinkage. Depending on the configuration of the weld, transverse shrinkage will also give rise to angular distortion. Okerblom, defined the transverse shrinkage as dependant on two variables, the transverse contraction and the angular distortion. For fast moving heat sources and short welds having a penetration 40% of the thickness Okerblom suggests that that the transverse shrinkage is given by equation 2.58.

$$\delta_t = 0.293 \frac{1}{d} \frac{q}{v} \frac{\alpha}{c\rho} \qquad \textit{Equation 2.58}$$

For very long plates and slow moving heat sources, Okerblom suggests that the transverse shrinkage may be considered as a longitudinal weld of the same length and equation 2.56 applies.

White et al proposed two formulas for the prediction of transverse shrinkage, that include:

for a fully penetrated weld $$\delta_t = 0.0044 \frac{\eta q}{vd} \qquad \textit{Equation 2.59}$$

for a partially penetrated weld $$\delta_t = 0.0044 \left(\frac{\eta q}{vd} - 50 \right) \qquad \textit{Equation 2.59}$$

Another significant work dealing with transverse shrinkage is that of Watanabe and Satoh [2.37]. The transverse shrinkage is directly related to the weight and size of the weld such that in multi-pass welding the transverse shrinkage is given equation 2.60. This means that the transverse shrinkage is again a function of the heat input, since the net heat input and the size of the weld are directly related.

$$\delta_t = C_1 \frac{A_w}{d^2} \ln \frac{W}{W_o} + C_2 \sqrt{\frac{A_w}{d^2}} \qquad \textit{Equation 2.60}$$

Where W is the total weight of material deposited and W_o is the weight of material deposited in each successive pass. C_1 and C_2 are coefficients determined experimentally depending on electrode diameter, current and speed.

Goglio *et al* [2.40] performed a series of experiments on stainless steels, using manual metal arc process with covered electrodes, gas shielded metal arc welding and tungsten inert gas welding. Three plate thicknesses were used – 6, 12 and 18mm, having a V and X groove with an included angle of 60°. The experimental results were compared to the analytical solutions for the prediction of transverse shrinkage and showed that Okerblom's formula for long welds in stainless steels seem to fail. On the other hand the formulas proposed by Watanabe and Satoh are able to follow the experimental results after calibrating the coefficients in the formulas. The experimental results obtained seem to follow a logarithmic curve as proposed by Satoh et al.

2.3.3 Angular distortion

Okerblom developed a number of analytical solutions, which covered different modes of welding processes including butt welding, fillet welding and multipass welding. He concluded that the angular distortion is a consequence of the weld pool shape and size, penetration and the amount restraint originating from the previous welds and parent plate. The simplest of these analytical solutions is the one proposed for the prediction of angular distortion in fast moving heat sources, with a penetration less then 60% of the plate thickness, given in equation 2.61.

$$B_f = C\eta_m \frac{q}{vd^2} \qquad \textit{Equation 2.61}$$

Where C is a constant dependant on the penetration and η_m is the fraction of heat used for fusing the base material typically 0.3.

Gray and Spence [2.25] inspired by the works of Okerblom, follow the same reasoning for the determination of angular distortion in butt welding, but assume a triangular shaped fusion zone and no external restraint. The angular distortion for the first pass or fully penetrated weld is given by:

$$B_f = \tan^{-1}\left(\alpha \Delta T \frac{b_w}{s}\right) \qquad \textit{Equation 2.62}$$

Where b_w is the width of the weld on the top surface and ΔT is assumed to be 1000°C based on the assumptions taken by Okerblom.

The model proposed by Watanabe *et al* follows the same reasoning as for the transverse shrinkage. The effects due to arc characteristics (heat input), joint characteristics (cross-sectional area) and electrode characteristics are incorporated in the analytical solutions. The angular distortion for multi-pass welding proposed by Watanabe et al is given below in equation 2.63

$$B_f = C_1 \frac{A_w}{d^2}\left[2e^{\left(\frac{C_2}{d^{3/2}}\right)\left(\frac{W}{W_A}\right)^{3/4}} - e^{\left(\frac{C_2}{d^{3/2}}\right)}\right] \qquad \textit{Equation 2.63}$$

Where W_A is the total weight of material deposited during the first pass and C_1 and C_2 are co-efficients determined experimentally depending on electrode diameter, current and speed.

From the tendon force concept, White *et al* proposed a relationship for predicting angular distortion. The study concluded that the maximum angular distortion occurs for a heat input corresponding to a penetration equal to half the plate thickness. In such case and for penetration less then half the plate thickness the angular distortion is given by:

$$B_f = 0.22 \frac{q}{v} \frac{1}{d_c^2} \qquad \textit{Equation 2.64}$$

Where d_c is the distance from the centre of the weld to the top surface of the plate.

In the case were the penetration is larger than half the plate thickness, the unfused material will no longer impose a restraint and in this case the angular distortion is given by:

$$B_f = \frac{q}{v}\frac{1}{d_c^2}\frac{6s(d-s)}{d^2} \qquad \textit{Equation 2.65}$$

Suresh *et al* [2.41] investigated the above solutions by performing a series of experiments on butt welds and fillet welds. The study concluded the following statements:

- Okerblom's analytical solutions were found to be mostly matching with the experimental results for most of the fillet and butt welds analysed, however the complexity of Okerblom's multipass welding analytical solutions proved to be cumbersome and the authors proposed a new analytical solution in the case of multipass fillet welds which does not take into consideration the configuration of the welded section, but is more concerned with the percentage re-fused area.
- Satoh's method gave good results for fillet welds made by submerged arc welding processes, but fell short when applied to multipass single V-butt welds
- Leggatt's method was found to give good reasonable results for multipass butt welding except for the initial two welds.
- Gray and Spence method was found to give the results most coincident with the double V groove butt welding, but is not suitable for the prediction of single V-groove welding, even though the proposed analytical solution is based on Okerblom's work.

2.4 Finite element analyses for the prediction of welding deformations

The main limitation in analytical solutions arises from the fact that such formulas are very specific and cannot be applied to all welding geometry and configurations, particularly when complex welding structures are involved. In these cases the interaction of the whole structure plays an important role in the structural integrity of the structure and must be incorporated in the solutions to calculate the final deformation and welding residual stresses. The use of finite element analysis offers

a great advantage in this context, with the further possibility of incorporating any non-linear temperature dependant material properties. The first welding numerical simulations made their appearance in the early 1970's, such as the work of Ueda *et al* [2.42] and Hibbit *et al* [2.43]. With the increase in computer power and further development of finite element software, the complex phenomena of welding have been successfully investigated by many researchers. The investigations reported within the last twenty years have covered two main directions:

1. Models incorporating most of the complex phenomena occurring during welding via a thermo elastoplastic analysis including phase transformation effects, non linear temperature dependant material properties, and hardening effects. These models are oriented to investigate the trends occurring in the heat affected zone, such as an accurate prediction of the residual stresses and the investigation of any crack propagation essential in finding the life cycle of welded structures. The drawbacks associated with these models are the complexities involved, the requirement of a good data on material properties up to melting point and the large volume of work and computational time required.

2. Simplified models, directed to the industrial scale welding, that do not claim to completely simulate the welding process but are confined to give certain type of results, such as out-of-plane deformation.

2.4.1 Thermo-elasto-plastic analyses

The extensive reviews given by Lindgren in [2.5], [2.6], [2.7] and [2.8] deal with number of possible modelling configurations and recommendations for the finite element simulations of welding. Most of the finite element simulations mentioned to date perform a thermo elastoplastic analysis. The welding residual stress and deformations are a direct effect of the residual strains generated during welding, which can be decomposed into six components:

- Elastic strain

- Plastic strain rate due to rate-independent plasticity
- Viscoplastic strain
- Creep strain
- Thermal strain rate consisting of thermal expansion and volume change due to phase transformations
- Transformation plasticity strain

Radaj [2.29] states that the main driving force of welding residual stresses is the thermal stresses imposed by the expansion and contraction of the material. However the phase change (γ-α transformation) present in ferritic steels will also impose a transformation strain and hence, stress in the final welded structure.

Lindgren in [2.6] concludes that for residual stresses to evolve, the welding simulations must at least account for elastic strains, thermal strains and one more inelastic strain component, of which the plastic strain is usually modelled. A typical plasticity model consists of a yield condition, flow rule and hardening rule. The yield condition, often taken to be the Von Mises criterion, defines the boundary between elastic and plastic behaviour. The flow rule gives equations for the plastic strains in terms of stresses and the hardening rule defines the hardening and possibly also the softening behaviour of material. Temperature dependent non-linear stress strain relationships are used, such that the elastic modulus and yield stress decreases with an increase in temperature, simulating the softening of the material at high temperatures. Due to lack of material properties and softness of the material at high temperature, a cut-off temperature is usually used by various welding simulations. The meaning of cut-off varies between various studies, but in simple terms it may be defined to be the temperature above which changes in the mechanical properties are not accounted for, thus serving as an upper limit to the mechanical analysis. Furthermore, any plastic strains accumulated above the cut-off temperature are removed. For example in the study performed by Nasstrom *et al* [2.44] a cut off temperature of 900°C was used. Previous studies performed by the same researchers, have shown that when a cut of temperature of 1200°C is used the

maximum difference in the maximum residual stress was at most 5%, suggesting that the cut of temperature can have various values.

The most important factor when dealing with thermo elastoplastic analysis is the thermal dilatation (thermal strain incorporating any strain generated by volume change due to phase transformation). A study showing the importance of thermal dilatation in the investigation of changes in weld gap width was done by Jonsson *et al* [2.45]. Among all factors, the authors concluded that the thermal dilatation has the largest influence on the change in gap width, with an increase in weld gap when higher thermal expansion coefficients for temperatures below 500°C, including volume changes, were modelled. It was also found out that the yielding at high temperatures does not affect the gap, however the hardening modulus and the yield stress at lower temperatures play an important role. Higher yield and larger hardening modulus make the tack welds stronger with high residual stresses, causing the plates to deflect more. However their major role is in the residual stress.

Various configurations are possible to model welding, depending on the field of interest. The simplistic way to model the welding residual stresses is to consider that longitudinal stresses are the most important and hence, the use of rod elements reduces the problem to a uniaxial stress. For more significant results, a two-dimensional analysis has to be used. This can take the form a two dimensional cross sectional model or two dimensional in-plane model. In the 2D cross sectional model a plane slice transverse to the weld seam and perpendicular to the in-plane axis is modelled. A number of possible plane rules are possible, which can take the form of a plane strain model, plane deformation model or plane stress model. The use of plain strain condition implies that the longitudinal heat flow and displacement are assumed to be zero. It is as if the whole plate was rigidly fixed in the longitudinal direction. The in-plane deformation approach models the strain in the longitudinal direction as a linear function of the coordinates. In plane stress models it is assumed that everything is constant through the thickness and that the stress normal to the plane is zero. The welding simulations performed during the 1970's and early 1980s,

were limited by computer power and were restricted to two dimensional cross sectional analyses, of which the plane strain model was generally used.

Another two dimensional strategy is a two dimensional plane model consisting of shell elements modelling the in-plane state of the welded structure. Shell elements assume that the stress through the thickness is zero and that a straight line in this direction will remain straight during deformation. Though shell elements can be used successfully in calculations of thin walled structures, in the weld and HAZ, shell elements may not be sufficient, due to the high through thickness stress gradient in these regions and hence are not suitable for predicting the angular distortion.

The study performed by Bergulund *et al* [2.46] has thrown light on what different modelling strategies are able to predict. In this study a two dimensional plane strain model and a two dimensional shell element model were compared with a three dimensional solid element model. It is fairly evident that the two dimensional plane strain model failed to predict the longitudinal out-of-plane deformation (bowing – curvature). Furthermore it was found that the longitudinal stresses in the two dimensional plane strain model were offset with a tensile net stress, due to the restraint imposed by assuming a plane strain criterion. The two dimensional shell elements are able to predict the same residual stresses as the three dimensional solid model but fail to predict the out of plane deformation due to through thickness thermal gradients.

The ultimate modelling approach is to assume a three dimensional solid element model. The response of such analysis would take into consideration all types of deformation but at the expense of considerable computational time. As pointed out by Brown and Song in [2.47], a three dimensional model is essential when considering effects of weld fit up and fixturing. The same conclusion was found by Michaleris *et al* [2.48], where the effects of run-off tabs, tack welds and other fixturings was investigated. However in this study it was also suggested that the restraint imposed by the fixturing can be modelled via a two dimensional analysis with the use of dashpot or link elements that restraints the plate from movement

during the heating stage but un-restraints the model during the cooling stage, with the assumption that during heating the unwelded plate and tabs will restrain the plate from moving.

Another consideration in the modelling of welding processes is the fine mesh required close to the weld, which can be coarsened in the remainder of the structure. This follows due to the high thermal gradient existing in the transverse direction. A number of strategies have been adopted by many researchers, the most effective to date being to move a fine mesh together with the heat source. Nasstrom *et al* [2.44] have combined three-dimensional solid elements with shell elements. In this study solid elements were used to represent the region near the weld and shell elements are used elsewhere. The combined model was integrated together via coupling equations that combined the degrees of freedom of the nodes lying in the boundary defining the solid and shell elements. When compared to a full solid model, the combined model was able to predict the residual stresses, with considerable reduction in computational time.

A fundamental requirement when modelling multi-pass welding, is the modelling of the deposition of the weld metal. Two approaches mentioned by Lindgren are possible The first referred to as 'quiet elements' (also referred to element birth and death in the context of this thesis), has all elements and nodes present in the analysis but the elements corresponding to the 'not-laid' welds are given material properties that do not effect the rest of the model via a low stiffness matrix and are given the appropriate material properties when laid. The other method involves the use of inactive elements, whereby the 'not-laid' elements are not included in the equation. The element birth and death technique is more widely used by a number of researchers in context of simulating the deposition of the weld. Younan *et al* [2.31] developed another method, named 'element movement technique' to model the deposition of the weld. In the element movement technique, the elements of the weld pool are separated from those of the base plate prior to the welding and are made in contact with the base plate to simulate the weld deposition. In the thermal analysis the weld pool elements are linked to the base plate via two noded elements,

such that they allow heat to be transmitted between the different components. The conductivity of such link was initially set to zero and gradually increased as the weld pool elements came in contact. In the structural analysis, a coupling equation is activated when the nodes come in contact. The end result will force the deformations of the coincident nodes to be equal, making the weld pool and base plate act as one body. When this technique was compared with the element 'birth and death' method a significant reduction in time, with negligible differences in the final residual stresses, was achieved.

2.4.2 Simplified finite element welding simulations

In the thermo-elastoplastic finite element analyses mentioned in section 2.4.1, the full heat flow, metallurgical and mechanical processes in welding are simulated via an uncoupled analysis. This requires the knowledge and use of nonlinear material properties, plastic flow, volume expansion and phase transformations. However, due to lack of material property information and knowledge of the thermal strain of the cooling weld, such analyses are complex and unusable during the design stages of most structures. Furthermore, when both volume changes and additional plastic deformation during transformation were applied by Josefson [2.49], it was found that it was difficult to obtain good agreement with the experimental results. This was believed to be due to the lack of information.

Efforts have been made to find the most important material properties that have an effect in the welding simulations. In the study performed by Free *et al* [2.50], room temperature conductivity, specific heat and density, constrained by the limitation of the finite element software package PAFEC used by this study, was used in the thermal analysis. Furthermore in the mechanical analysis, the coefficient of expansion and the elastic modulus was assumed to be independent of temperature, and perfectly elastic plastic material properties were assumed. This study was performed on low carbon steels BS4360 grade 50D and Free et al claim such material can be considered to be perfectly plastic to approximately 3% strain and any strain hardening modulus will reduce at elevated temperatures. Also a temperature

dependent yield stress was modelled. A strong agreement with experimental results was achieved and the authors conclude that time dependant plasticity, non-linear thermal properties and non-linear mechanical properties other then yield strength are not essential. A similar study performed by Zhu *et al* [2.51] on aluminium structures conclude that in the thermal analysis a room temperature density and specific heat can be used with good temperature results in the thermal analysis, as long as the latent heat is specified. The thermal conductivity had the most significant effect on the thermal transients and Zhu *et al* recommended to use an averaged conductivity, though a room temperature thermal conductivity is fairly accurate. In the mechanical analysis it was concluded that a room temperature coefficient of expansion and elastic modulus could be used with substantial accuracy. However the yield stress had a significant effect on the final residual stresses and distortions, and a temperature dependent variable yield stress is essential.

Efforts have been made by various researchers to reduce the computational time in the prediction of the out-of-plane deformation evolved during welding. A particular feature of the 'computer efficient' models is that the thermo-mechanical actions leading to distortion are uncoupled in terms of three basic actions, namely a thermal transient stage that describes the thermal patterns, a thermo-elasto-plastic two dimensional transient cross-sectional structural analysis that establishes the welding residual stresses and a structural static three dimensional model describing the geometry of interest. The end effect is a contraction force applied to the weldment of a three dimensional model. At the other end of the spectrum the welding simulations have been condensed to simple static shrinkage contraction forces that are independent of the thermal, welding transients. The latter simplified approach relies on the fact that the residual stresses and distortion is due to the plastic strain accumulated in the heat affected zone and / or in the fusion zone, during the cooling stages of the welding process. Though the heat affected zone undergoes various changes in microsturcture, thermal and mechanical field, it is the final stages of the cooling cycle that will determine the residual stresses and distortions in welded structures. The methods adopted by the above mentioned schemes are often referred to as inherent shrinkage methods or tendon force method.

Michaleris and De Biccari [2.36], [2.52] present a simplified numerical technique for the prediction of the out-of-plane deformation associated large buckled thin plate structures. The numerical analysis combines a three dimensional large deformation, small deformation buckling eigenvalue analysis, with a two dimensional thermo-elastoplastic analysis. First an uncoupled thermo-elastoplastic two-dimensional (cross-section, transverse slice) plane stress analysis is performed. These analyses provided an 'Applied Welding Load (AWL)' expressed in terms of a cooling thermal strain ΔT in the welding direction, corresponding to a force $EA\alpha\Delta T$, established by matching the far field residual stresses to the results of the two-dimensional analysis. This load was then applied to a large-deformation, three-dimensional analysis. Note, however that the authors did not consider transverse or angular shrinkage and the expansivity coefficient used was considered to be orthotropic. To supplement the analysis a small deformation eigenvalue analysis is also performed such that the thermal strain applied is given by $\lambda_e EA\alpha\Delta T_e$, where λ_e is the eigenvalue and ΔT_e is a -1°C thermal strain, later scaled up by the buckling analysis until the bifurication load is reached. This load is referred to the 'Critical Buckling Load' (CBL) and if AWL is higher then CBL then buckling is expected in the welded structure. In this case imperfections have to be applied to the large deformation analysis in order to simulate the expected buckling mode. Multiple eigenvalues and eigenmodes may exist suggesting that the final predicted out-of-plane deformation will depend on the imperfection applied to achieve the plausible buckling mode. The finite element analyses were supplemented by large scale and small scale mock up tests. A strong agreement with the experimental results was achieved provided that the right buckling mode is selected. In fact, in the small scale test, the plates buckled in the first mode where as in the large scale specimens, buckling was of the fourth order.

Vanli and Michaleris [2.53] used the approach described previously to consider panels with T-stiffeners. This study identifies significant differences in outcome related to angular distortion, bowing (ie out-of-plane longitudinal bending with no buckling component) and buckling. The latter two forms of deformation require a three dimensional analysis and buckling will only take place unless the contraction force due to the residual stresses generated during welding exceed the critical

bifurication loads obtained from the buckling analysis. Another important conclusion mentioned in this study is that although the welding stress is not affected by fixturing and self-weight of the structure, the buckling modes may be influenced. The finite element simulations have shown that bowing distortion is highly plausible in the structures studied by Vanli et al, however if the bowing distortion is prevented, by means of ramming down the stiffener, then buckling will take place.

The simplified numerical analysis of Hinrichsen [2.54] is highly relevant to the present study and is also inspired the work of Okerblom. It is suggested in this reference that the effects of angular distortion are small in such thin-walled structures, when compared with the buckling distortion associated with the stiffeners. Conrardy and Dull [2.14] appear to agree with this view. This assumption permits the use of shell elements in the three-dimensional analysis, where longitudinal and transverse in-plane shrinkages are included, but there is no allowance for through-thickness thermal or strain gradients. These are essential for simulation of angular distortion. The finite-element approach adopted by Hinrichsen involves a two-step thermo-elastoplastic analysis. The transverse shrinkage due to a single pass fillet weld is found in the first step through a two-dimensional cross sectional, thermo-elastoplastic analysis. The longitudinal shrinkage is found from a three-dimensional, shell-element model, whereby the whole length of the plate is assumed to be heated simultaneously along the weld seam. The author implies that the plate reaches the same maximum temperature at a particular distance from the weld along parallel lines. The interaction between transverse and longitudinal shrinkage is achieved by modeling the transverse shrinkage from the first step by spring elements, which are incorporated in the second step. Experimental studies were also described, where the thermal input was calibrated via thermocouple measurements (leading to a weld energy input efficiency of 0.82) and strain gauge patterns were used to monitor the development of residual stresses. Effects of the sequential development of residual stress were not taken into account in the theoretical analysis, as the shrinkages were applied in a single load step. Good correlation between the experimental buckling results and the finite-element analysis was shown.

A similar technique, that follows the works of Michelaris *et al* and Hinrichsen, was performed by Tsai *et al* [2.13]. This study sets out to investigate the effect of welding sequences on distortion of aluminium panels (5456-H116 alloy). Inspired by Michelaris *et al*, Tsai *et al* investigate the effect of welding residual stresses have on buckling, by subjecting the panels to a compressive load, to determine the critical buckling load and assigning a thermal load applied along the weld line, to simulate the welding residual stresses. The thermal load analysis is referred to as the inherent shrinkage method and finds out if the residual stresses exceed the critical buckling load, thereby resulting in buckling. The inherent shrinkage method, used in this context, consists of initially prescribing the weld temperature to 649°C, for an Al alloy with melting point of 1000°C, along the whole weld area and then letting to cool down, such that the plastic strains are calculated from the prescribed temperature. In the analysis non-linear temperature dependent conduction, specific heat, thermal expansion and elastic modulus are used. The end effect will result in a shrinkage volume along the weld line. From these numerical analysis Tsai et al concluded that the least distortion occurs by welding first the most rigid joint and then move to the least rigid ones. Based on this pre-assumption, the study demonstrates a method to find the correct welding sequence in multiple stiffeners assemblies for the reduction of welding distortions. This is referred to as the joint rigidity method (JRM) and sets out to find the most rigid joint. Thus in the JRM a unit moment is applied to each stiffener and while observing the angular rotation, the stiffener with the lowest rotation is welded first. Note that, this procedure has to be performed again after each weld sequence as the joint rigidity may change after each weld sequence. The analyses performed by the finite element analysis were supplemented by experimental results. A strong agreement of out-of-plane deformation was achieved albeit that the proper prescribed weld temperature is found.

A recent review of a large collaborative programme, funded by U.S. Navy Office of Naval Research [2.55], investigated buckling distortion via two methods, the 'shrinkage-force-based' buckling analysis after Michaleris *et al* and a 'thermoplasticity-based' buckling analysis. In the shrinkage-force method the

interaction between the thermo elastoplastic analysis and the buckling analysis is simple a load parameter applied over the weld and does not take into account the non-linear effects caused by the interactions between multiple welds. In the thermoplasticity based analysis, the predicted residual stress distributions is used to form the stress-stiffening matrix $[K]_{\lambda\sigma^r}$ in an eigenvalue analysis by taking the form of:

$$([K]_t + \Delta\lambda_{cr}[K]_{\lambda\sigma^r})\{u\} = \{0\} \qquad \textit{Equation (2.66)}$$

which is solved for $\Delta\lambda_{cr}$. Note that $[K]_t$ is the conventional tangential stiffness matrix and $\{u\}$ is the corresponding displacement vector referred to as the buckling mode. Once the buckling mode is established a non-linear analysis is performed to find out the buckling distortion magnitude. The study also demonstrates an analytical approach to determine the buckling mode but it is limited to simple supported plates and assumes an invariant unit force acting along the in-plane axis.

Another simplified approach that uses the inherent shrinkage method is given in the study presented by Luo *et al* [2.56]. The inherent strains resulting from a two dimensional cross sectional thermo-elastoplatic analysis are used to find the inherent angular distortion, transverse shrinkage and longitudinal tendon force using the approximations given below:

Tendon force $F = \int E\varepsilon_t dydz$ *Equation (2.67)*

Inherent transverse shrinkage $\delta_t = \frac{1}{d}\int \varepsilon_t dydz$ *Equation (2.68)*

Inherent angular distortion $\phi = \frac{1}{I}\int \varepsilon_t (z - d/2) dydz$ *Equation (2.69)*

where

$I = \int (z - d/2)^2 dz$

Once the inherent strains are known an equivalent elastic strain can be applied over a region in an elastic three-dimensional analysis. By assuming the width b to the

region where the inherent strains are applied and using multi layer anisotropic shell elements, a system of elastic strains can be applied to the model, to represent the longitudinal tendon force, transverse shrinkage and angular deformation. Starting from the tendon force, a strain is applied longitudinally along the inherent width after equation 2.70

$$\varepsilon_x^* = \frac{F}{Edb} = \alpha_x \Delta T \qquad \textit{Equation (2.70)}$$

As with the transverse and angular distortion a layered strain is applied, such that the top and bottom layers read:

$$\varepsilon_y^{*top} = \frac{(\delta_t - \frac{2}{3} d\phi)}{b} = \alpha_y^{top} \Delta T$$
$$\varepsilon_y^{*bot} = \frac{(\delta_t + \frac{2}{3} d\phi)}{b} = \alpha_y^{bot} \Delta T \qquad \textit{Equation (2.71)}$$

An even more simpler method is the 'shrinkage volume approach', proposed by Bachorski *et al* in [2.57]. The numerical strategy adopted, consists of a linear elastic analysis, where by the driving force for distortion is assumed to be the linear thermal contraction of a nominal shrinkage volume. This volume is assumed to be the weld prep volume for vee preparations of 50° or less included angle and the fusion zone for angle greater then 50°. For carbon steels the authors propose to apply a thermal load of 900°C. Such temperature corresponds to the temperature at which the yield strength of steel drops significantly that any thermal strains produced above this temperature are considered not to contribute to the final distorted shape. The crude assumptions taken by this method are able to predict the angular distortions, but the residual stresses are not realistic, though having the same profile.

The work performed by Khamassi *et al* [2.58] also uses a shrinkage volume approach, but the contraction force is based on the work done by Okerblom. In this case a cooling contraction starting from 600°C is applied to a volume which

experiences between 100% and 75% of the maximum temperature achieved from the thermal analysis. Inspired by Okerblom, the weld path is discretised into a number of individual segments such that the maximum length of each segment is given by:

$$L_{\max} = 0.506v\left(\frac{q_{lin}}{d}\right)^2 \qquad \textit{Equation (2.72)}$$

The finite element procedure, summarised in Figure 2.15, was adopted. For each weld segment the thermal strains applied to the shrinkage volume, having temperature dependant material properties, was solved. The nodal displacements, in the shrinkage volume, generated from each weld segment, was then applied to the model having room temperature material properties. For every segment a new model consisting of the previous or initial deformation was created. At the end of the loop, a set of forces was collected and applied to the model in order to generate the actual residual distortion.

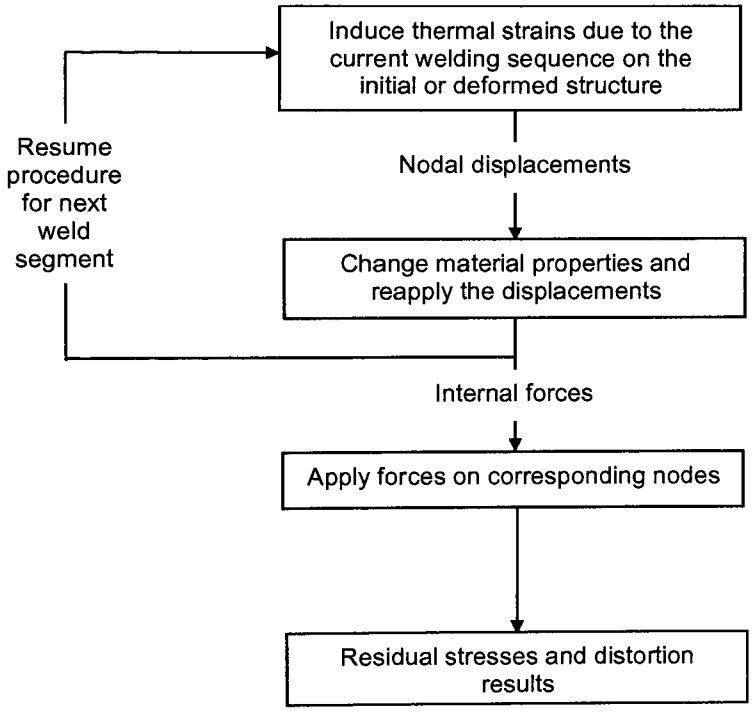

Figure 2.15: Procedure of the welding simulation

2.5 *Discussions*

This chapter sets out to define the phenomena occurring during welding. Present state of the art finite element and analytical approaches directed at the prediction of residual stresses and distortions are presented. While the thermal transients occurring in welding are well established and easily found, the welding residual stresses and hence distortions require a more complex model. This is the most intractable and complex part of the whole procedure, not least because the required high temperature material properties are usually poorly known and the material also changes state Many finite element analysis exists however due to the complexity involved make such analyses unsuitable at the design stages of welded structures. A number of simplified approaches have been proposed ranging from the inherent shrinkage force method to the inherent shrinkage volume approach. Though reducing the computational time certain analyses are still dependant on non-linear temperature material properties. On the other hand the elastic finite element analyses use some crude assumptions, that is the cooling contraction and shrinkage volume is chosen to suit and match the expected level of deformation. Though these assumptions are based on experimental results, the methods are not easily transferable to other materials. The finite element analysis adopted by this study sets out to establish a simplified algorithm that will find the contraction forces to be applied to different welded structures. While being generic with respect to material properties, welding process and material thickness, the simplified approach should be computationally economic, simply to apply, adaptable and robust. The algorithms used in the thermo-elastoplastic stages have benefited from the early insights of Okerblom and are presented in chapter three.

2.6 *References*

[2.1] Mackerle,J., 'Finite Element Analysis and Simulation of Welding: A Bibliography (1976 – 1996),' *Modelling Simul. Mater. Sci. Eng.*, Vol. 4, pp. 501-503, 1996.

[2.2] Mackerle,J., 'Finite Element Analysis and Simulation of Welding – An Addendum: A Bibliography (1996 - 2001). *Modelling Simul. Mater. Sci. Eng.*, Vol. 10, pp. 295-318, 2002.

[2.3] Masubuchi,K., 'Recent M.I.T. Research on Residual Stresses and Distortion in Welded Structures,' *Journal of Ship Production,* Vol.9, No.3, pp.137-145, 1993.

[2.4] Masubuchi,K., 'Analysis of Welded Structures,' *Massachusetts Institute of Technology, Pergamon Press, U.S.A.,* 1980.

[2.5] Lindgren,L.E., 'Finite Element Modeling and Simulation of Welding. Part 1: Increased Complexity,' *Journal of Thermal Stresses,* Vol.24, pp.141-192, 2001.

[2.6] Lindgren,L.E., 'Finite Element Modeling and Simulation of Welding. Part 2: Improved Material Modeling,' *Journal of Thermal Stresses,* Vol.24, pp.195-231, 2001.

[2.7] Lindgren,L.E., 'Finite Element Modeling and Simulation of Welding. Part 3: Efficiency and Integration,' *Journal of Thermal Stresses,* Vol.24, pp.305-334, 2001.

[2.8] Lindgren,L.E. and Josefson,B.L., 'Welding Residual Stresses and Distortions Simulated by the use of Simplified Methods,' *Keynote Lecture at the Symposium 'Recent Advances in Welding Simulation' arranged by The Institution of Mechanical Engineers, London, UK, 1999.*

[2.9] Boley,B.A. and Weiner,J.H., 'Theory of Thermal Stresses,' *J.Wiley, 1960.*

[2.10] Verhaeghe,G., 'Predictive Formulae for Weld Distortion – A Critical Review,' *Abington Publishing, Cambridge, UK,* 1999.

[2.11] Lightfoot,M., 'Prediction of Distortion Control and Techniques to avoid Rework,' *A Report on the General Causes of Fabricated Steel Plate Distortion,*

School of Marine Science and Technology, University of Newcastle Upon Tyne, 2003.

[2.12] Parmar,R.S. and Arya,S.K. 'Studies on Angular Distortion of Butt Welds in Flux Cored Arc Welding,' *Journal of the Institution of Engineers (India), Part PR: Production Eng. Division.,* Vol.69, Pt. 3, pp 65-71, 1989.

[2.13] Tsai,C.L., Park,S.C. and Heng,W.T., 'Welding Distortion of a Thin Plate Panel Structure,' *Welding Journal,* Vol. 78, No.5, pp 156s-165s, 1999.

[2.14] Conrardy,C. and Dull,R., 'Control of Distortion in Thin Ship Panels,' *Journal of Ship Production,* Vol.13, No.2, pp 83-92, 1997.

[2.15] Doersken,R., 'Weld Shrinkage Study,' *National Steel and Shipbuilding Company*, 1992.

[2.16] Baxter,C.F.G, 'Distortion Control in Thin Plate Welded Structures,' *Proceedings of the International Offshore Mechanics and Arctic Engineering Symposium,* Vol.3, Pt. 8, pp 63-68, 1989.

[2.17] Rosenthal,D., 'The Theory of Moving Sources of Heat and its Application to Metal Treatments,' *Transactions of the American Society of Mechanical Engineering,* Vol.68, No.8 pp 849-866, 1946.

[2.18] Rykalin,N.N., 'Thermal Welding Principles.' *I.A.N., SSSR (1947).*

[2.19] Wells,A.A., 'Heat Flow in Welding.', *Welding Journal*, Vol. 31, pp 263s-267s, 1952.

[2.20] Carslaw,H.S and Jaeger,J.C., 'Conduction of Heat in Solids,' *Clarendon Press, Oxford*, 1950.

[2.21] Chapman,A.J., 'Fundamentals of Heat Transfer', *Collier Macmillan, London*, 1987.

[2.22] Burghardt,M.D and Harbach,J.A, 'Engineering Thermodynamics,' *Harper Collins College, New York,* 1993.

[2.23] 'ANSYS 6.1 Documentation,' ANSYS inc Theory Reference, Heat Flow, 2001.

[2.24] Rosenthal,D., 'Mathematical theory of Heat Distribution During Welding and Cutting,' *Welding Journal,* 20(5), pp. 220s-234s, 1941.

[2.25] Gray,T.G.F. and Spence,J., 'Rational Welding Design,' *Buttersworth,* 1982.

[2.26] Birk-Sorensen,M., 'Simulation of Welding Distortions in Ship Section,' *PhD Thesis, Department of Naval Architecture and Offshore Engineering, Technical University of Denmark,* 1999.

[2.27] Okerblom,N.O., 'The calculations of deformations of welded metal structures,' *Her Majesty's Stationery Office, London*, 1958.

[2.28] Lindgren,L.E., 'Temperature Fields in Simulation of Butt-welding of Large Plates,' *Communications in Applied Numerical Methods,* Vol.2, pp 155-164, 1986.

[2.29] Radaj,D., 'Finite-element Analysis of Temperature Field, Residual Stresses and Distortion in Welding,' *Welding Research Abroad,* Vol.35, No. 6/7, pp. 31-38, 1989.

[2.30] Friedman,E., 'Thermomechanical Analysis of the Welding Process Using the Finite Element Method,' *ASME Journal of Pressure Vessel Technology,* Vol. 97, No.3, pp 206-213, 1975.

[2.31] Younan,M.Y.A., Wifi,A.S., and Fanous,I.F.Z, '3D Finite Element Modelling of the Welding Process using Element Birth and Element Movement Techniques,' *ASME Pressure Vessel and Piping Conf., Vancouver, Canada,* Vol.422, pp 165-172, 2002.

[2.32] Goldak,J., Chakravarti,A., and Bibby,M., 'A New Finite Element Model for Welding Heat Sources,' *Metallurgy Transactions B,* Vol.15B, pp. 299-305, 1984.

[2.33] Roberts,S.M., Hunziker,O., Dye,D., Stone,H.J. and Reed,R.C., 'Nickel-base Superalloy Welding – Models for Residual Stress, Distortion and Weldability,' *Keynote Lecture at the Symposium 'Recent Advances in Welding Simulation' arranged by The Institution of Mechanical Engineers, London, UK, 1999.*

[2.34] Jonsson,M., Kaelsson,L., and Lindgren,L.E., 'Deformations and Stresses in Butt-welding of Large Plates,' *Numerical Methods in heat Transfer,* Vol.3, 1985.

[2.35] Papazoglou,V.J. and Masubuchi,K, 'Numerical Analysis of Thermal Stresses During Welding Including Phase Transformation Effects,' *Journal of Pressure Vessel Technology, Transactions of the ASME*, Vol. 104, No. 3, pp. 198-203, 1982.

[2.36] Michaleris,P. and DeBiccarri,A. 'Prediction of Welding Distortion,' *The Welding Journal, Welding Research Supplement,* Vol.76, No.4 pp 172s-181s, 1997.

[2.37] Watanabe,M. and Satoh,K., 'Effect of Welding Conditions on the Shrinkage Distortion in Welded Structures,' *The Welding Journal, Welding Research Supplement,* pp 377s-384s, Aug, 1961.

[2.38] White,J.D, Leggatt,R.H. and Dwight,J.B., 'Weld Shrinkage Prediction,' *Welding and Metal Fabrication,* pp. 587-596, 1980.

[2.39] Verhaeghe,G., 'Predictive Formulae for Weld Distortion - A Critical Review,' *Abington Publishing, Cambridge, England,* 1999.

[2.40] Goglio,L. and Gola,M.M., 'Shrinkage in Butt Welded Joints: Measurement and Prediction,' *Welding International,* Vol.7, Pt 10, pp 776-787, 1993.

[2.41] Suresh,S. and Dattrajan,H. 'An Experimental Study of Angular Distortion in Welded Structures,' *W.R.I. Keywords (Welding Research Inst. Tiruchirapalls, India),* Vol.8, Pt. 1, pp 7-14, 1987.

[2.42] Ueda,Y. and Yamakawa,T., 'Analysis of Thermal Elastic-plastic Stress and Strain During Welding by Finite Element Method,' *JWRI,* Vol. 2, No.2, pp. 90-100, 1971.

[2.43] Hibbitt,H.D. and Marcal,P.V., 'A Numerical Thermo-Mechanical Model for the Welding and Subsequent Loading of a Fabricated Structure,' *Computers and Structures,* Vol. 3, pp. 1145-1174, 1973.

[2.44] Nasstrom,M., Wikander,L., Karlsson,L., Lindgren,L.E. and Goldak,J. 'Combinded 3-D and Shell Element Modelling of Welding,' *IUTAM Symp. on the Mechanical Effects of Welding, Lulea, Sweden,* pp. 10-14, 1991.

[2.45] Jonsson,M., Kaelsson,L., and Lindgrn,L.E., 'Deformations and Stresses in Butt-welding of Large Plates with Special Reference to the Mechanical Material Properties,' *Numerical Methods in Heat Transfer,* Vol. 3, 1985.

[2.46] Berglund,D. and Runnemalm,H., ' Comparison of Deformation Pattern and Residual Stresses in Finite Element Models of TIG-welded Stainless Steel Plate,' *Proc.6th International Conf. On Trends in Welding Research,* Pine Mountain, Georgia, USA, 2002

[2.47] Brown,S. and Song,H., 'Finite Element Simulation of Welding of Large Structure,' *Journal of Engineering for Industry, Transactions of the ASME,* Vol. 114, No. 3, pp 441-451, 1992.

[2.48] Michaleris,P., Feng,Z. and Campbell,G., 'Evaluation of 2D and 3D FEA Models for Predicting Residual Stress and Distortion,' *Approximate Methods in the Design and Analysis of Pressure Vessels and Pipping Components ASME,* Vol. 347, pp 91-102, 1997.

[2.49] Josefson,B.L., 'Prediction of Residual Stresses and Distortions in Welded Structures,' *Trans. of ASME Journal of Offshore Mechanics and Arctic Engineering,* Vol. 115, pp. 52-57, 1993.

[2.50] Free,J.A., and Goff,R.F.D.P., 'Predicting Residual-Stresses in Multi-pass Weldments with the Finite-element Method,' *Computers and Structures,* Vol.32, No.2, pp. 365-378, 1989.

[2.51] Zhu,X.K., Chao,Y.J., 'Effects of Temperature Dependent Material Properties on Welding Simulation,' *Computers and Structures,* Vol.80, pp. 967-976, 2002.

[2.52] Michaleris,P. and DeBicarri,A., 'A Predictive Technique for Buckling Analysis of Thin Section Panels Due to Welding,' *Journal of Ship Production,* Vol.12, No.4, pp. 269-275, 1996.

[2.53] Vanli,O.A. and Michaleris,P., 'Distortion Analysis of Welded Stiffeners,' *Journal of Ship Production,* Vol.17, No.4, pp.226-240, 2001.

[2.54] Hinrichsen,B., 'Prediction of Welding Induced Distortion in Thin-walled Ship Panels,' *Ship Technology Research,* Vol.46, pp. 153-163, 1999.

[2.55] Huang, T.D., Dong, P., DeCan, L.A., Harwig, D.D., 'Residual Stresses and Distortions in Lightweight Ship Panel Structures,' *Technology Review Journal*, pp 1-26, 2003.

[2.56] Luo,Y., Ishiyama,M. and Murakawa,H., 'Welding Deformation of Plates with Longitudinal Curvature,' *Transactions of JWRI,* Vol.28, No.2, 1999.

[2.57] Bachorski,A., Painter,M.J., Smailes,A.J., Wahab,M.A., 'Finite-element Prediction of Distortion During Gas Metal Arc Welding using the Shrinkage Volume Approach,' *Journal of Materials Processing Technology,* Vol. 92-93, pp. 405-409, 1999.

[2.58] Khamassi.A., Armstrong,C.G. and Ou,H., 'A Simplified Approach to Evaluating Weld Induced Distortions,' *Proceedings of the 11th Annual ACME Conference, Glasgow,* pp 21- 24, 2003.

CHAPTER THREE

CHAPTER 3

CONTINUUM ANALYSIS OF WELDING DISTORTION

3.1 Introduction

A combined analytical and finite element approach, that concentrates on the prediction of out-of-plane deformation, is presented in this chapter. The analytical part is based on the work of Okerblom [3.1] and a large reduction in computational time is achieved by applying this approach. The strategy adopted is an uncoupled computational procedure, whereby the thermal transient, thermo-elastic-plastic and structural stages of the thermo-mechanical deformations induced by fusion welding are treated separately.

The first step in any computation of welding distortion is to establish the transient thermal distributions caused by a given welding process in the geometry of interest. This may be achieved in a variety of ways, ranging from the early analytical treatments of Rosenthal [3.2] presented in chapter two, to finite-element based methods, as reviewed recently by Lindgren [3.3]. In Okerblom's work, the heat distribution evolved during welding is based on the work of Rykalin [3.4], and is described in chapter two, section 2.2.3. Depending on the welding conditions and size of the plate, temperatures are determined on the assumption of either a point or extended line heat source. In the context of this thesis, plates of thickness less then 7mm have been modelled and analysed, hence the two dimensional line heat source quasi-static (equation 2.39) is used. For a line heat source, the width of the heat penetration zone at given maximum temperatures is given by equation 3.1. This simplified analytical solution rests on the assumption that the heat source is fast

moving, such that any secondary effects attributed to the coefficient of heat loss are neglected.

$$b_M = 2y = \frac{0.484q}{vdc\rho(T_M - T_o)} \qquad \textit{Equation 3.1}$$

For simplicity the reference temperature T_o is assumed to be 0°C. An important aspect of equation 3.1 is that the distance y is inversely proportional to the maximum temperature reached at that particular point. The relevance of this finding is of particular importance in the evolution of longitudinal residual stresses discussed in section 3.2.1.

In the second computational stage of the uncoupled approach, differential strains induced by the transient thermal gradients are translated into contraction stresses, which produce mechanical distortion. This is the most intractable and complex part of the whole procedure, not least because the required high temperature material properties are usually poorly known and the material also changes state. The algorithms used in the present treatment to solve this stage of the process have benefited from the early insights of Okerblom [3.1]. He noted various typical features of the thermo-mechanical transients generated by fast-moving fusion welding heat sources and made several bold simplifications on the strength of these observations.

The thermal effects on the material during welding result in a non-uniform heating of the material and / or volume changes associated with phase change. The latter effect depends on which type of material being used, which has to be considered when using quench hardened alloy steels. In case of low-carbon steels phase transformations (dissociation of the austenite) takes place at a high temperature where the material is in the plastic state thus Okerblom omits this effect in his solutions. Okerblom approximates the determination of welding deformations and stresses, by considering the heating and cooling thermal cycles during welding, from which areas of plastic deformation in the region about the weld are found in an uncoupled fashion. Any phase transformations are omitted and constant material

properties are considered. The availability of new computational methods means that some of these simplifications are no longer necessary, but others remain very powerful as ways to avoid the problematic aspects described in chapter two.

The analytical solutions developed by Okerblom are investigated and adapted to develop a generic algorithm named *'Mismatched Thermal Strain' (MTS)* and *'Contraction Thermal Strain' (CTS)* algorithms in terms of contraction strains, later applied to the structural finite element model. Of particular importance is the generation of a longitudinal strain (MTS) / force applied in the longitudinal direction, that may give rise to buckling and bowing distortions. Futhermore a localised transverse contraction strain (CTS) applied to the weld is identified, the end effect of which results in both angular distortion and transverse shrinkage. As opposed to purely analytical solutions, the interaction between the analytical solutions and the finite element analyses, provides a means of simulating different welding configurations, while taking into consideration any fixtures and restraint effecting the distortions.

3.2 Determination of residual longitudinal welding deformations via mismatched thermal strain algorithms

The simplified finite element simulation discussed in section 2.42 dealt with establishing contraction forces in the longitudinal direction and transverse direction. Various techniques have been presented in chapter two ranging from the 'inherent shrinkage force' method to the 'inherent shrinkage volume' method. In most of the simplified analyses, a non-linear thermo-elastic-plastic, two-dimensional analysis establishes the contraction force to be applied to the three dimensional analysis. In the presented simplified algorithm the full thermo-elastoplastic analysis is by-passed and the contraction forces depends simply on the thermal cycles undergone by various points within the welded structure. Various assumptions are made, particularly that the material is perfectly elastic and perfectly plastic material, thus omitting any extra strains resulting from strain hardening.

3.2.1 *Simplified evolution of longitudinal residual stresses*

Okerblom firstly recognizes that the major irreversible deformations responsible for distortion are driven by the cooling phase of the process in the region behind the heat source. The thermal gradients transverse to the line of the weld in this region are found typically to be steep, whereas the gradients parallel to the weld are relatively shallow as shown in Figure 3.1. This suggested a simplified treatment for longitudinal contraction, in terms of a transverse plane strain slice, which is passed through the quasi-stationary temperature field. Further simplification is made by assuming a time-independent profile for the maximum temperatures reached at each y position, that is transverse to the weld line and omitting any time lag existing between the maximum temperatures.

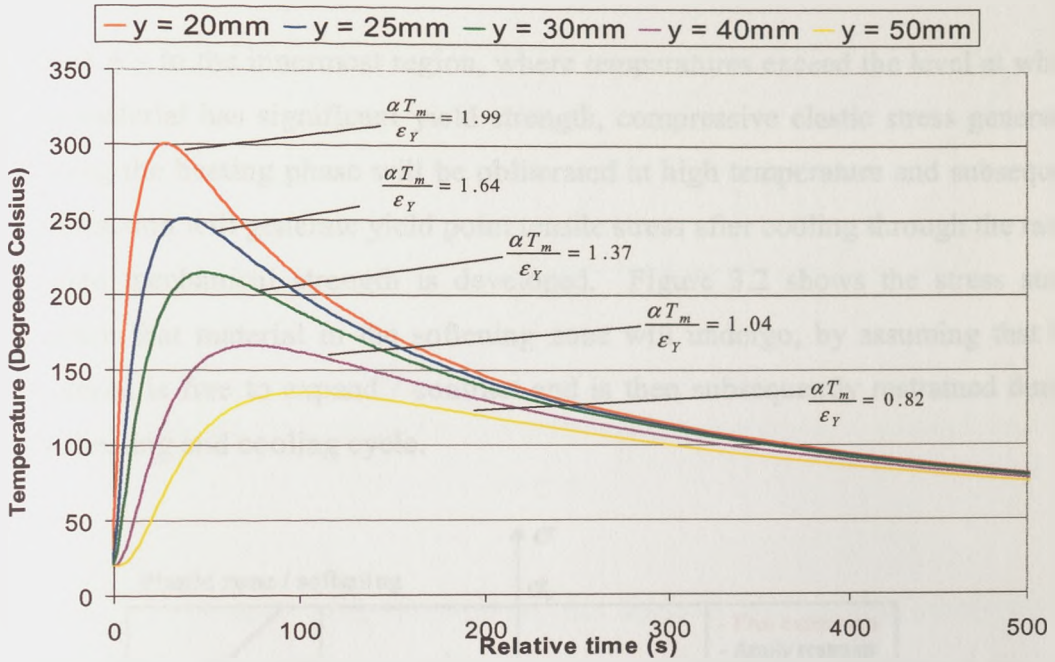

Figure 3.1: Typical thermal history plot at particular distances y from the weld axis

It can be seen from Figure 3.1, that regions nearer the centre of the slice begin to start to cool before adjacent regions further away from the centre and they cool more rapidly, eventually converging to a common rate. The resulting thermal mismatches develop contraction forces, progressively outwards across the slice. As mismatches are always present at each point, it is possible that the full values of contraction stress are developed, corresponding to the maximum thermal strains at each point,

(accepting that the yield strength σ_y cannot be exceeded anywhere). Note that this interpretation differs from that of Okerblom, in that he attributed the overall longitudinal contraction to integration of compressive plastic strains at each point across the width, due to the plane strain suppression of thermal strain. However, the present formulation in terms of contraction forces gives an identical result.

If, for the moment, the final ambient temperature reached by the plate on cooling is taken to be zero ($T_o = T_a = 0$), the elastic longitudinal stress developed during cooling at a given location will depend only on the yield strength and the maximum thermal strain $\varepsilon = \alpha T_M$ experienced at each transverse location. Various regions across the slice in the y direction are identified in Figure 3.6:

- Zone A - In the innermost region, where temperatures exceed the level at which the material has significant yield strength, compressive elastic stress generated during the heating phase will be obliterated at high temperature and subsequent contraction will generate yield point tensile stress after cooling through the range where mechanical strength is developed. Figure 3.2 shows the stress strain pattern that material in the softening zone will undergo, by assuming that the material is free to expand / contract and is then subsequently restrained during the heating and cooling cycle.

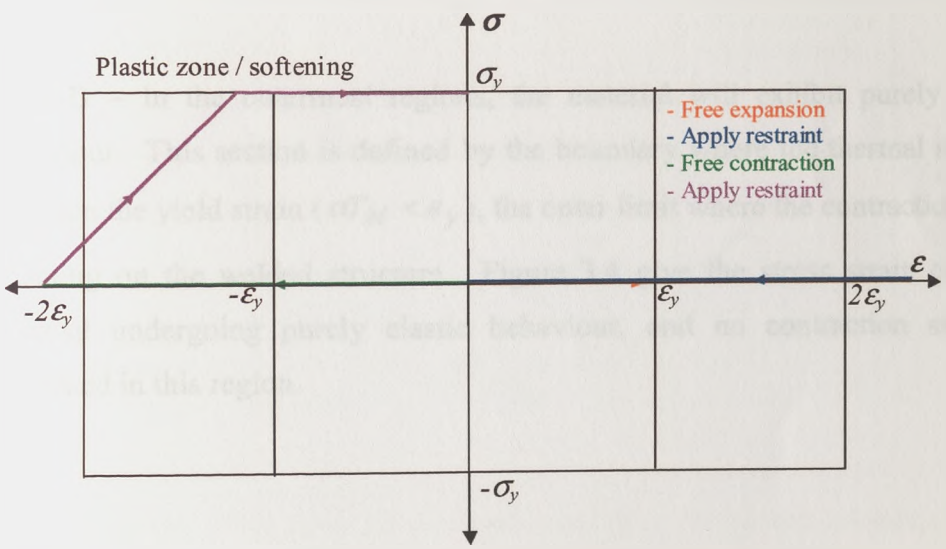

Figure 3.2: Stress-strain cycle for elements residing in the softening zone – zone A

- Zone B - In the adjacent region, working outwards, the tensile stress generated during cooling will also be of yield point magnitude, as long as $\alpha T_M > 2\varepsilon_Y$ - which relation defines the outer y coordinate of the total region exhibiting yield point residual stress. The stress strain cycle is given in Figure 3.3. In this case a compressive residual stress will be generated during the heating cycle, assuming that material residing in this zone has enough strength to oppose the restraint.

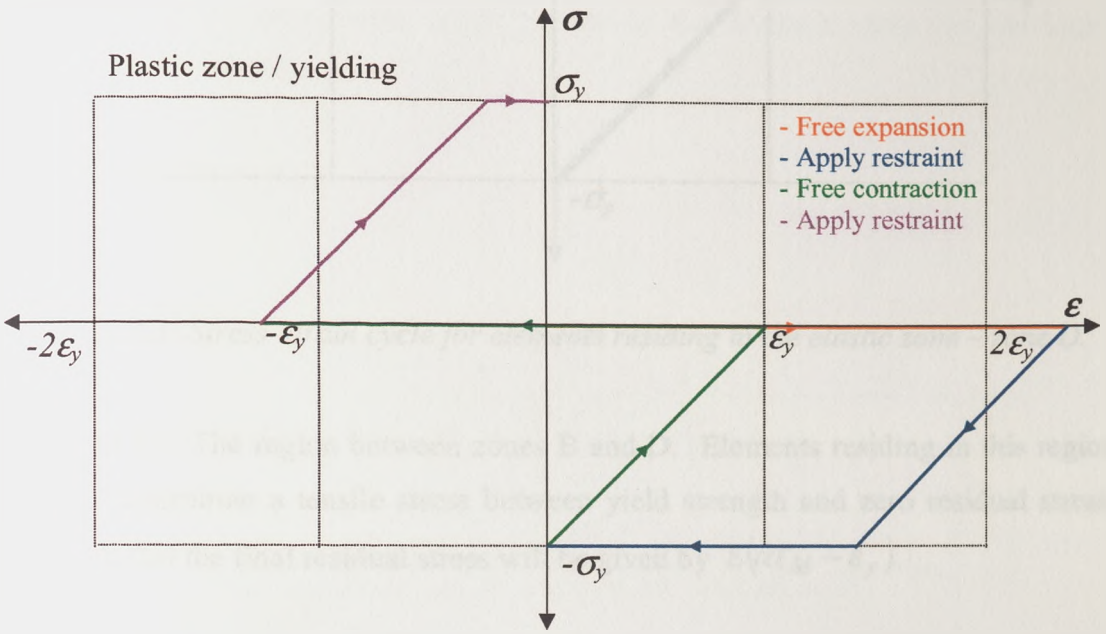

Figure 3.3: Stress-strain cycle for elements residing in the plastic yielded zone – zone B.

- Zone D – In the outermost regions, the material will exhibit purely elastic behaviour. This section is defined by the boundary where the thermal strain is less then the yield strain ($\alpha T_M < \varepsilon_y$), the outer limit where the contraction force is acting on the welded structure. Figure 3.4 give the stress strain cycle of material undergoing purely elastic behaviour, and no contraction stress is generated in this region.

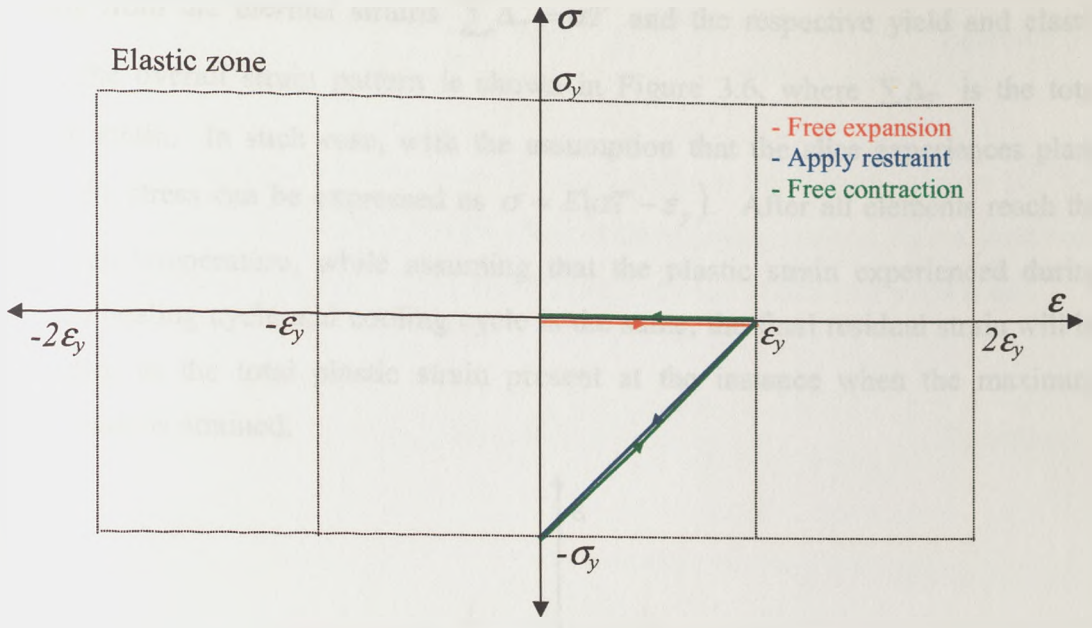

Figure 3.4: Stress-strain cycle for elements residing in the elastic zone – zone D.

- Zone C - The region between zones B and D. Elements residing in this region will contribute a tensile stress between yield strength and zero residual stress, such that the final residual stress will be given by $E(\alpha T_M - \varepsilon_y)$.

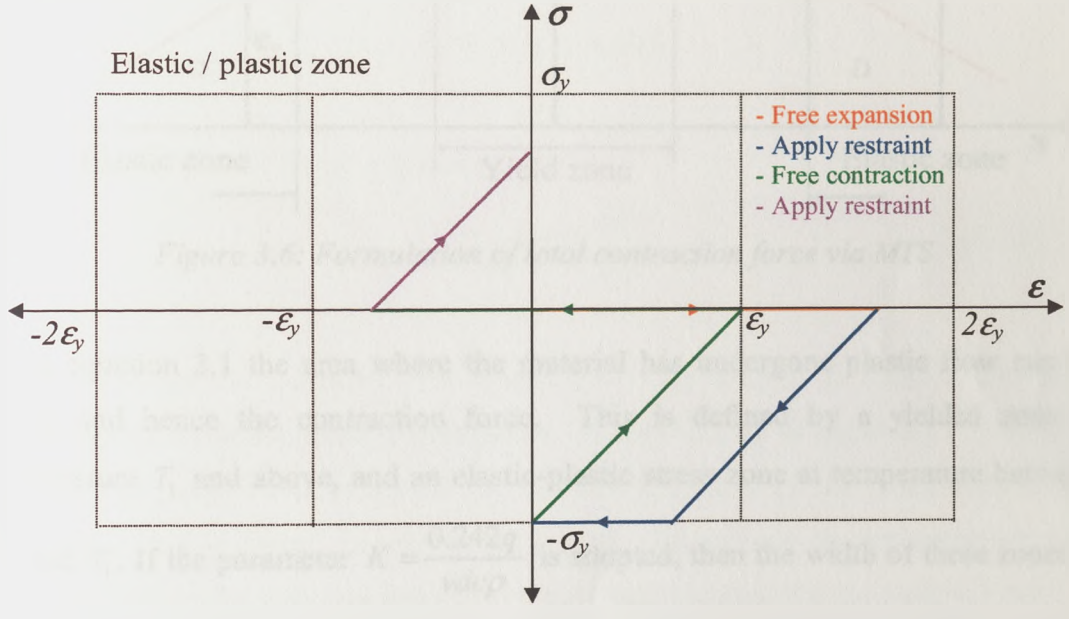

Figure 3.5: Stress-strain cycle for elements residing in the elastic / plastic zone – zone C.

Starting from the thermal strains $\sum \Delta_T = \alpha T$ and the respective yield and elastic zones, the overall strain pattern is shown in Figure 3.6, where $\sum \Delta_T$ is the total thermal strain. In such case, with the assumption that the slice experiences plane strain, the stress can be expressed as $\sigma = E(\alpha T - \varepsilon_y)$. After all elements reach the maximum temperature, while assuming that the plastic strain experienced during both the heating cycle and cooling cycle is the same, the final residual strain will be equivalent to the total plastic strain present at the instance when the maximum temperature is attained.

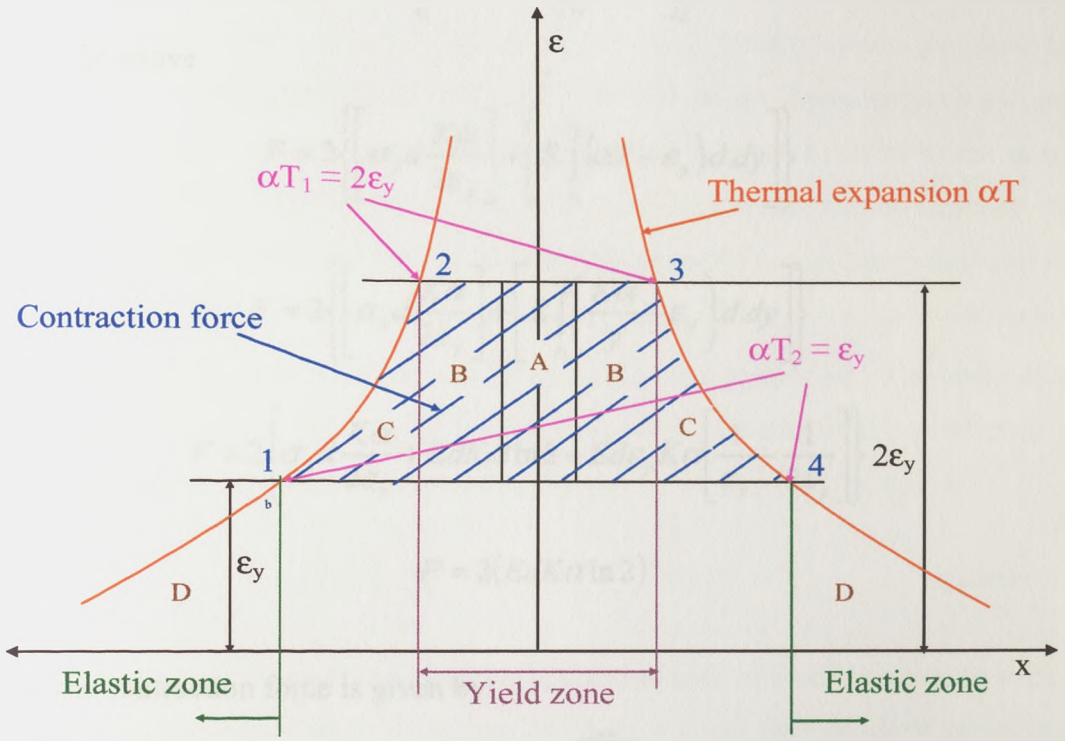

Figure 3.6: Formulation of total contraction force via MTS

From equation 3.1 the area where the material has undergone plastic flow can be found and hence the contraction force. This is defined by a yielded zone at temperature T_1 and above, and an elastic-plastic stress zone at temperature between T_2 and T_1. If the parameter $K = \dfrac{0.242q}{vdc\rho}$ is adopted, then the width of these zones is given by:

$$y_1 = \frac{K}{T_1} = \frac{K\alpha}{2\varepsilon_y} \quad and \quad y_2 = \frac{K}{T_2} = \frac{K\alpha}{\varepsilon_y} \qquad \textit{Equation 3.2}$$

The total force developed by the contracting material is the integral of area 1-2-3-4, given by equation 3.3, whereby the first part of the equation represents the yield zone and the second part represents the zone residing between elastic and yield zone.

$$F = 2\left\{\left[\sigma_y y_1 d\right] + \left[\int_{y_1}^{y_2} \sigma d.dy\right]\right\} \qquad \textit{Equation 3.3}$$

solving the above

$$F = 2\left\{\left[\sigma_y d\frac{K\alpha}{2\varepsilon_y}\right] + \left[E\int_{y_1}^{y_2}\left(\alpha T - \varepsilon_y\right).d.dy\right]\right\}$$

$$F = 2\left\{\left[\sigma_y d\frac{K\alpha}{2\varepsilon_y}\right] + \left[E\int_{y_1}^{y_2}\left(\frac{K\alpha}{y} - \varepsilon_y\right).d.dy\right]\right\}$$

$$F = 2\left\{\sigma_y d\frac{K\alpha}{2\varepsilon_y} + EdK\alpha\ln 2 - Ed\varepsilon_y K\alpha\left[\frac{1}{\varepsilon_y} - \frac{1}{2\varepsilon_y}\right]\right\}$$

$$F = 2\left(EdK\alpha\ln 2\right)$$

Hence the contraction force is given by:

$$F = 0.335\frac{qE\alpha}{vc\rho} \qquad \textit{Equation 3.4}$$

The evolution of the contraction force takes into consideration the material properties of the welded structure under investigation. In the work by White et al [3.5] on steel, a similar approach was proposed for the determination of the contraction force, named the tendon force. In this study, a linear dependency on heat input has also been reported in the determination of the contraction force, but the tendon force was not related to material properties. In such case the tendon force is given by $F = 0.2\eta\, q/v$. White et al did not compare their experimental force equation with

Okerblom's analytical determination, but comparison using standard material data shows that the writers' 'mismatched thermal strain algorithm' underestimates White and Leggatt's experimentally determined force equation by 20%.

3.2.2 Effect of material properties on the contraction force

It is noted in passing that, if a linear inverse relationship exists between T_M and y, as has been shown approximately by applying quasi-stationary solutions (equation 3.1) the yield strength magnitude drops out of the analytical formulation for the elastic longitudinal contraction force. This suggests, somewhat surprisingly, that the dependence on yield strength is weak. This would be an immensely simplifying factor, if the actual transient temperature distribution is indeed similar to the quasi-static solution. When non-linear effects, including heat losses due to radiation and convection together with any non-linear material properties, are incorporated in the thermal simulations, the relationship between T_M and y is not a simple linear inverse relationship and the effects of this will be discussed in chapter five. The contraction force given in equation 3.3 can be further expressed in terms of the coefficient of expansion, thermal strain and the distance y from the weld axis given below.

$$F = 2\left\{\left[E\alpha y_1 d(T_1 - T_2)\right] + \left[\int_{T_2}^{T_1}\int_{y_1}^{y_2} Ed\alpha.dy.dT\right]\right\} \qquad \textit{Equation 3.5}$$

By considering the relationship between the thermal load against the distance y from the weld axis the contraction force can be further simplified in terms of an area undergoing permanent / plastic deformation, defined by the yield strength and co-efficient of expansion and consisting of the thermal load multiplied by the distance y, such that

$$F = 2E\alpha d.Area \qquad \textit{Equation 3.6}$$

Figure 3.7 compares the different areas undergoing permanent deformation when yield strengths of 405 and 360MN/m² were used, together with alternative coefficients of expansion of $14\text{x}10^{-6}$ and $16\text{x}10^{-6}$.

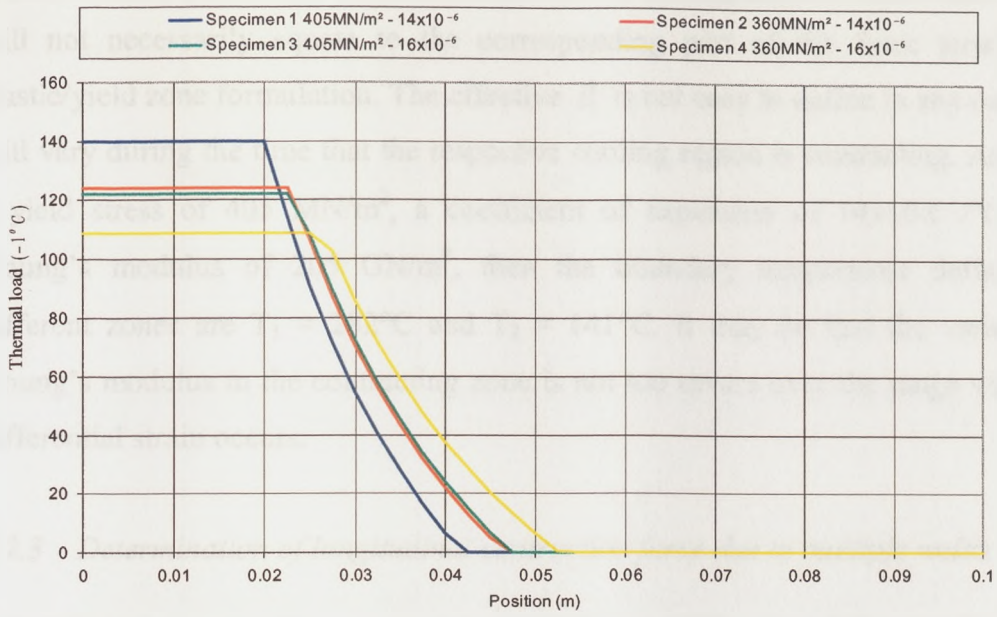

Figure 3.7: Thermal load for different material properties

The comparisons shown in Table 3.1 show that the contraction force is independent of the area undergoing permanent deformation, but depends on the coefficient of expansion, and the Young's modulus of the material. This reinforces to the conclusions derived by Jonsson et al [3.6] that the thermal dilation is the most important factor affecting the residual stress.

Specimen No	Yield strength MN/m²	Co-efficient of expansion	Area under graph (thermal load x distance)	Contraction force kN
1	405	$14x10^{-6}$	4.028	115.6
2	360	$14x10^{-6}$	4.044	116.1
3	405	$16x10^{-6}$	4.046	132.7
4	360	$16x10^{-6}$	4.043	132.6

Table 3.1: Comparison of contraction force for various material properties

The simplified approach considers perfectly elastic/ plastic material properties. However a calibration factor can be inserted in the contraction force formulation to take into account any strain hardening. This has been investigated by the authors in [3.7] who concluded that when strain hardening material properties were incorporated in a particular thermo-elastic-plastic model, an 8% increase in the contraction force was exhibited.

If the Young's modulus is not constant, the force developed in the central yield zone will not necessarily equate to the corresponding part of the force term in the elastic/yield zone formulation. The effective E is not easy to define in any case, as it will vary during the time that the respective cooling region is contracting. Assuming a yield stress of 405 MN/m^2, a coefficient of expansion of 14x10-6 /°C and a Young's modulus of 205 GN/m^2, then the boundary temperature defining the different zones are T_1 = 282°C and T_2 = 141°C. It may be that the variation of Young's modulus in the contracting zone is not too severe over the range where the differential strain occurs.

3.2.3 Determination of longitudinal contraction force due to multiple welds

Most welded structures incorporate more than one weld run and there is therefore a need to establish how best to model a multiply welded structure. It should be useful at least to identify different situations, which might be treated differently. Depending on the distance between the yielded zones of multiple welds, the final contraction force will be influenced by previously laid welds. Two possibilities may be identified; separate single run welds and closely spaced welds

In separate single run welds placed consecutively, the welds may be placed sufficiently far apart so that the local elastic residual stress fields do not overlap. This is very much like the situation created by welding multiple stiffeners consecutively (assuming each stiffener is attached by a single weld). If the second or later weld is placed in a region where there is *no* longitudinal stress field, or it is negligible, then the contraction force developed will be exactly as if the weld had been placed singly.

If the longitudinal residual stress field in the region where the second weld is placed is *tensile*, this will *reduce* the contraction force relative to the contraction force for the first weld (assuming the same heat input rate on both). If the residual stress is *compressive,* this will *increase* the contraction force. Considering the residual stress patterns and starting from an initial tensile stress it can be seen that if the thermal expansion is below $\varepsilon_y + \varepsilon_i$ then on cooling and again restraining the structure, the

final stress state will always result in the initial tensile residual stress, refer to Figure 3.8. Hence the elastic limit is given by $\varepsilon_y + \varepsilon_i$.

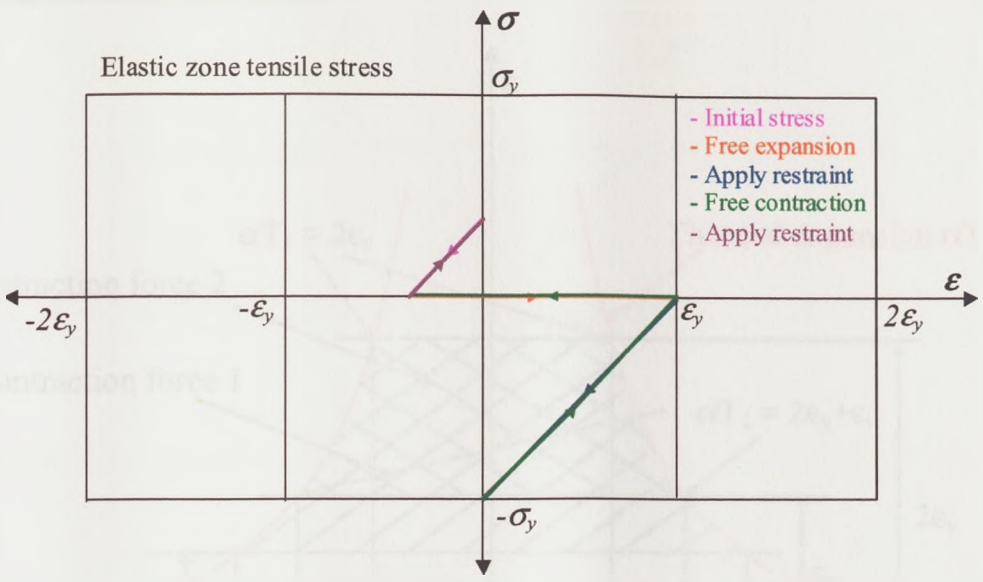

Figure 3.8: Stress-strain cycle with initial tensile stress – elastic limit

Referring to Figure 3.9, a thermal expansion of $2\varepsilon_y$ or above will generate a final residual stress of yield nature.

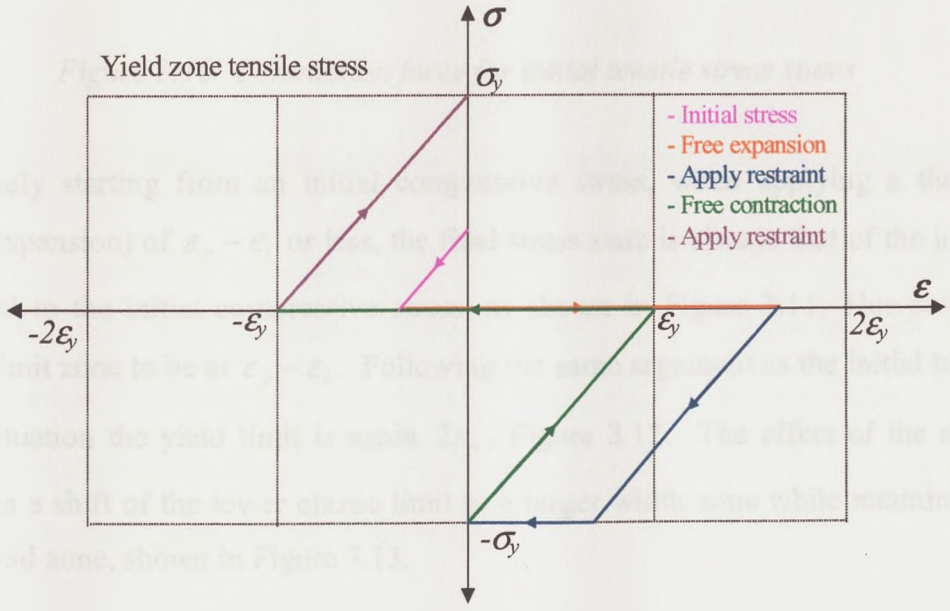

Figure 3.9: Stress-strain cycle with initial tensile stress – yield limit

Considering the above in relation to the contraction force, Figure 3.10 shows that, an initial tensile stress will result in a shift of the lower elastic limit upwards, while retaining the same yield limit.

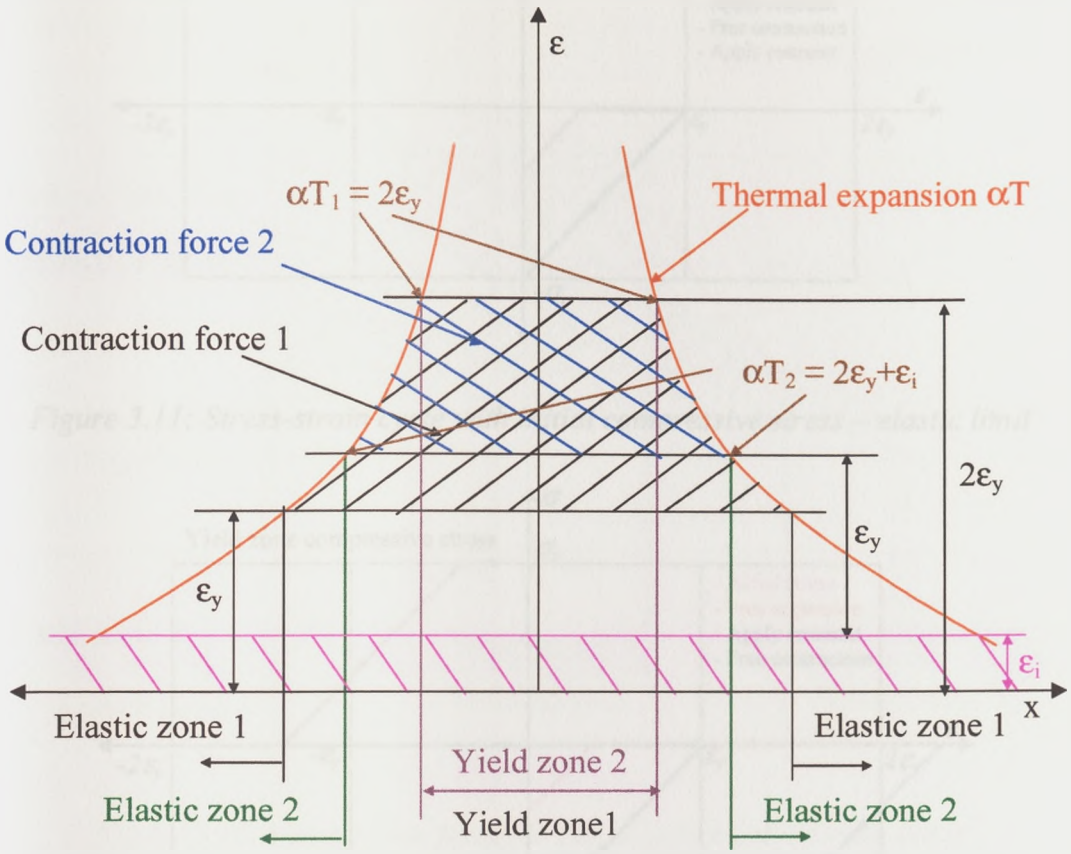

Figure 3.10: Contraction force for initial tensile stress states

Conversely starting from an initial compressive stress, when applying a thermal strain (expansion) of $\varepsilon_y - \varepsilon_i$ or less, the final stress state is always that of the initial, i.e. equal to the initial compressive stress, as shown in Figure 3.11. This puts the elastic limit zone to be at $\varepsilon_y - \varepsilon_i$. Following the same argument as the initial tensile stress situation the yield limit is again $2\varepsilon_y$, Figure 3.12. The effect of the above results in a shift of the lower elastic limit to a larger width zone while retaining the same yield zone, shown in Figure 3.13.

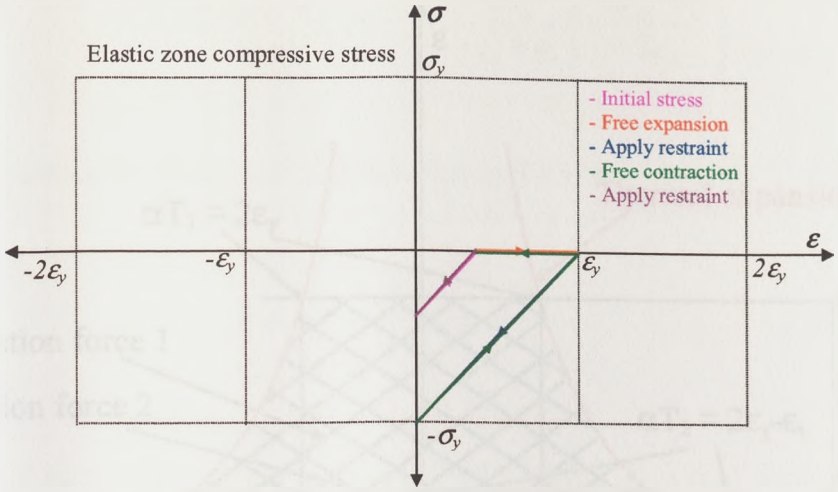

Figure 3.11: Stress-strain cycle with initial compressive stress – elastic limit

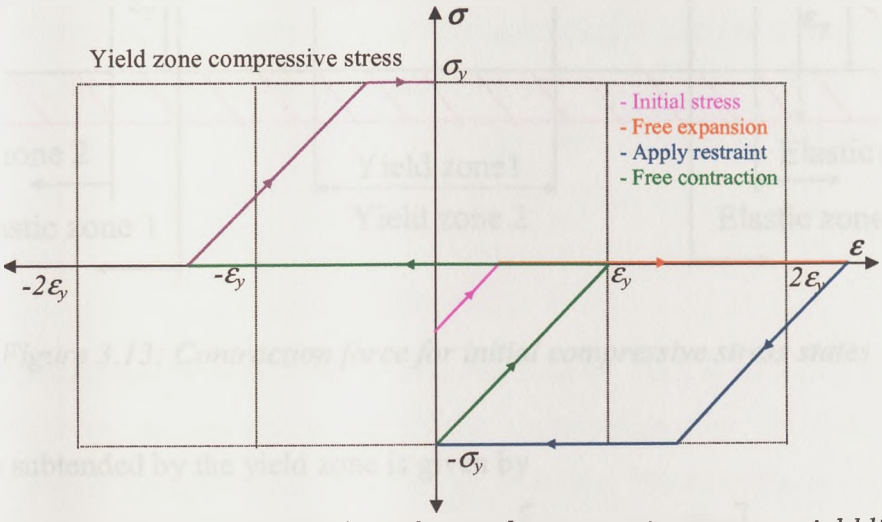

Figure 3.12: Stress-strain cycle with initial compressive stress – yield limit

Integrating over the area will again give the new contraction force to be applied to the structure with an initial stress. If tensile strains $\varepsilon_i = \varepsilon_{tensile}$ are assumed to be positive and an initial compressive strain $\varepsilon_i = \varepsilon_{compression}$ taken to be negative then the developed stress for initially strained plates is given by $\sigma = E\left[\alpha T - \left(\varepsilon_y + \varepsilon_i\right)\right]$ and the corresponding elastic and yield limits to:

$$y_1 = \frac{K}{T_1} = \frac{K\alpha}{2\varepsilon_y} \quad and \quad y_2 = \frac{K}{T_2} = \frac{K\alpha}{\varepsilon_y + \varepsilon_i} \qquad \textit{Equation 3.7}$$

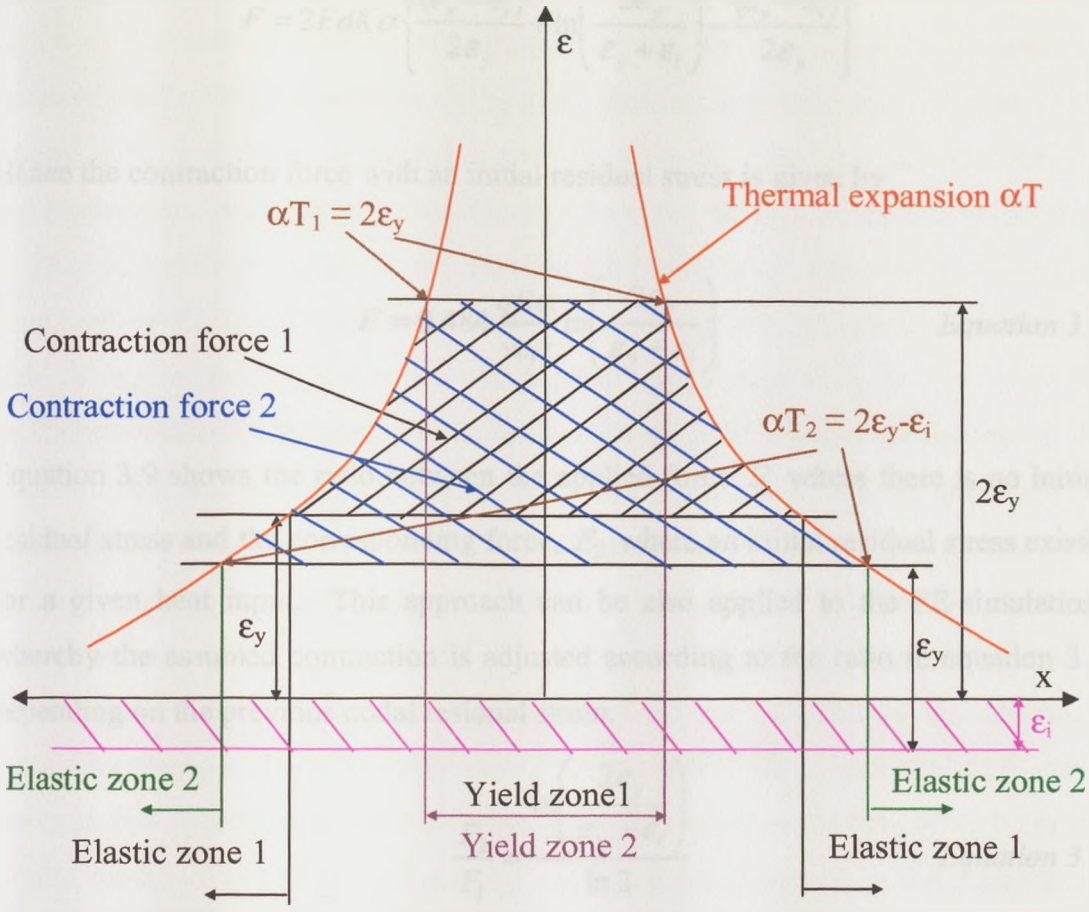

Figure 3.13: Contraction force for initial compressive stress states

The force subtended by the yield zone is given by

$$F_y = 2\left[2\varepsilon_y - (\varepsilon_y + \varepsilon_i)\right]Ey_1 d = 2\left[Ed(\varepsilon_y - \varepsilon_i)\frac{K\alpha}{2\varepsilon_y}\right]$$

The total force is:

$$F = 2\left\{Ed(\varepsilon_y - \varepsilon_i)\frac{K\alpha}{2\varepsilon_y} + \int_{y_1}^{y_2}\left[\alpha T - (\varepsilon_y + \varepsilon_i)\right]Ed.dy\right\}$$

$$F = 2Ed\left\{(\varepsilon_y - \varepsilon_i)\frac{K\alpha}{2\varepsilon_y} + K\alpha \ln\frac{y_2}{y_1} - (\varepsilon_y + \varepsilon_i)(y_2 - y_1)\right\}$$

$$F = 2Ed\left\{(\varepsilon_y - \varepsilon_i)\frac{K\alpha}{2\varepsilon_y} + K\alpha \ln\left(\frac{2\varepsilon_y}{\varepsilon_y + \varepsilon_i}\right) - K\alpha(\varepsilon_y + \varepsilon_i)\left[\frac{1}{\varepsilon_y + \varepsilon_i} - \frac{1}{2\varepsilon_y}\right]\right\}$$

$$F = 2EdK\alpha\left\{\frac{(\varepsilon_y - \varepsilon_i)}{2\varepsilon_y} + \ln\left(\frac{2\varepsilon_y}{\varepsilon_y + \varepsilon_i}\right) - \frac{(\varepsilon_y - \varepsilon_i)}{2\varepsilon_y}\right\}$$

Hence the contraction force with an initial residual stress is given by

$$F = 0.484\frac{qE\alpha}{vc\rho}\ln\left(\frac{2\varepsilon_y}{\varepsilon_y + \varepsilon_i}\right) \qquad \textit{Equation 3.8}$$

Equation 3.9 shows the ratio between the applied force F_1 where there is no initial residual stress and the corresponding force, F_2 where an initial residual stress exists, for a given heat input. This approach can be also applied to the FE-simulation, whereby the assumed contraction is adjusted according to the ratio in equation 3.9 depending on the previous nodal residual strain.

$$\frac{F_2}{F_1} = \frac{\ln\left(\frac{2\varepsilon_y}{\varepsilon_y + \varepsilon_i}\right)}{\ln 2} \qquad \textit{Equation 3.9}$$

Okerblom's argument is rather effective on this subject. Instead of trying to find the contraction force, he considers the plastic deformation that the structure has undergone during the application of a number of welds. His equation to describe the effect is

$$\frac{\varepsilon_{l_2}}{\varepsilon_{l_1}} = \left(\frac{\varepsilon_y - \varepsilon_i}{\varepsilon_y + 0.7\varepsilon_i}\right) \qquad \textit{Equation 3.10}$$

Though the contraction force method is influenced less by the prior welds on the second or later welds, a strong agreement exists between equation 3.9 and 3.10.

In more closely spaced welds, such as the case of multi-pass welding in butt welds and multi pass fillet welds on opposite side of the stiffeners, a simpler algorithm may be used. However, it is important to distinguish the various possible manufacturing strategies adopted in multipass welding. The interpass temperature between one

weld pass and the next and the possible deposition of two staggered or simultaneous welds, in the case of welding of stiffeners are of particular interest. Considering intermediate cooling to ambient temperature between one weld and the next, if the second weld run were to coincide exactly with the first run and the thermal conditions were identical (equivalent to a re-fusion of the first weld, with no addition of filler material) no further distortion should be developed. However if the second fillet weld is displaced transversely relative to the first, the individual thermal strain fields characterised by Figure 3.6 will overlap, rather then coincide. The second weld cannot increase the longitudinal residual stress in the overlap region beyond the yield strength and as postulated initially by Okerblom, the effect will merely be to widen the zone experiencing tensile yield stress by an amount corresponding to the distance between the two fillet weld centrelines. White et al [3.5] follow the same argument on overlapping welds and set out to define the total strain field resulting from the two welds. Thus, completion of the second run will increase the distortion, but not by nearly as much as would have been the case if it had been applied to stress free material. The mentioned thermo-elastoplastic algorithm may therefore be rather simply modified to determine the small additional force caused (if the temperature transient field of the second fillet weld is known).

In one of the studies dealing with multipass welding performed by Ueda et al [3.8], compared a thermo-elastic-plastic analysis of a 20 pass weld, assuming a room temperature interpass temperature, with a simplified version of the analysis involving the simulation of only the finishing bead. Following the same findings as Okerblom, the study has shown that very accurate magnitude and location of the maximum tensile residual stresses appearing near the finishing bead may be found by conducting the theoretical or experimental analysis for the last few welding passes. What is also surprising is that Ueda *et al* believe that simulating the last weld in multipass weld with interpass temperatures higher then ambient temperature, will still give substantial agreement with the full thermo-elasto plastic multipass analysis.

This argument does not of course cover the case where the stiffener is attached by running two welding heads on opposite sides of the same stiffener. If the welding heads are directly adjacent, then the heat input rate is more-or-less doubled and the distortion, likewise, would be expected to double. If the second welding head is positioned to trail the first by some distance, then a fresh thermal simulation is required to determine the maximum temperatures occurring for the weld head spacing used. These ought to be less than in the case where the welding heads are directly adjacent and there is therefore considerable practical interest in investigating the likely effects on the outcome, of relative weld head positioning and thermal input. This has been considered in the theoretical part of the present study and results will be given later in chapter seven. The region undergoing permanent deformation, in multipass welding is given in Figure 3.14. Clearly, in simultaneous or staggered multipass welding this area would be bigger and is not merely an overlap of the individual contraction zone.

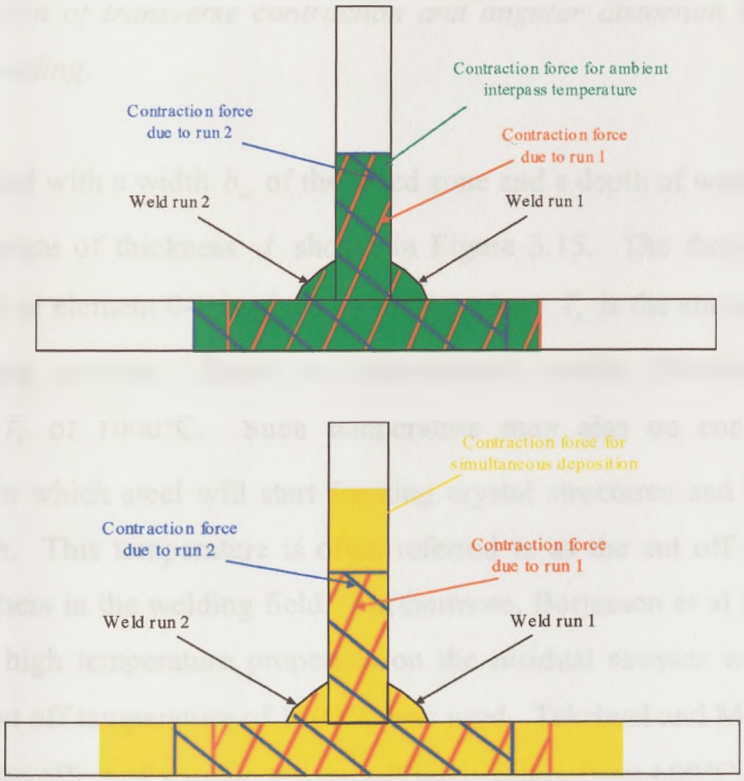

Figure 3.14: Plastised region in multipass welding, a – ambient interpass temperature, b – simultaneous deposition

The angular deformation and transverse contraction can be determined by assuming that it results from the contraction in the fusion zone and that deformations in the surrounding base metal balance each other, resulting in no direct effect on the local angular and transverse deformation. The implications are that the transverse thermal strains in the remainder of the cross section are elastic and offer no restraint on angular deformation, other than that provided by the unwelded area below the fusion zone and any other restraints arising from the structural form in a multiply stiffened structure. In an unrestrained situation such as that of single butt welding and single stiffener fillet welding, the problem may be treated as a two-dimensional one. This assumption also relies on the finding that the thermal gradient is small along the length of the weld. The simplified treatment arising from this assumption will be designated the *'Contraction Thermal Strain'* algorithm (CTS).

3.3.1 Evolution of transverse contraction and angular distortion in unrestrained butt welding.

Consider a weld with a width b_w of the fused zone and a depth of weld penetration s in a welded plate of thickness d shown in Figure 3.15. The thermal contraction from the weld at element 0-1 is given by $\alpha T_t b_w$ where T_t is the starting temperature for the cooling process. Based on experimental results, Okerblom suggests a temperature T_t of 1000°C. Such temperature may also be considered as the temperature in which steel will start forming crystal structures and hence assumes some strength. This temperature is often referred to as the cut off temperature by many researchers in the welding field. Furthermore, Borjesson et al [3.9] claim that the effect of high temperature properties on the residual stresses was found to be small and a cut off temperature of 1100°C was used. Tekriwal and Mazumder [3.10] investigated the effect of varying the cut off temperature from 600°C and above, and concluded that the residual transverse stresses were overestimated by 2 to 15% at the lower value of temperature.

For elements between 2-3 in Figure 3.15, there is no contraction, as the initial expansion will cancel out the contraction during cooling. Due to the resistance imposed by the non-contracting element, the final deformation will follow line 4-5, such that β_f is the free angular distortion, $\Delta_o b_w$ and $\Delta_t b_w$ are the top and bottom transverse deformations respectively. Furthermore, for elements within the fusion zone, the elastic deformation cannot exceed $\varepsilon_y b_w$, that is $\alpha T_t b_w - \Delta_o b_w$ cannot be greater than $\varepsilon_y b_w$. Any region extended above this value may be considered to have undergone plastic deformation. Assuming a perfectly elastic-plastic material, the plastic extension for element 0-1 is given by:

$$\alpha T b_w - \Delta_o b_w - \varepsilon_y b_w = k\alpha T_t b_w \qquad \text{Equation 3.11}$$

Assuming that the total plastic deformation is permanent on cooling, the final residual deformation applied to the molten metal, will be given by:

$$\alpha T_t b_w - k\alpha T_t b_w = (1-k)\alpha T_t b_w \qquad \text{Equation 3.12}$$

Okerblom's reasoning may be adopted in finite element analyses by applying a 'Contraction Thermal Strain', over the area of the fusion zone, equivalent to $(1-k)\alpha T_t$. The determination of k largely depends on the depth of penetration and the amount of restraint developed by the unliquified zone. Okerblom finds a relationship between k and the ratio of the depth of penetration and the thickness by considering the mechanical deformation given in area 0-6-7-2, shown in Figure 3.15.

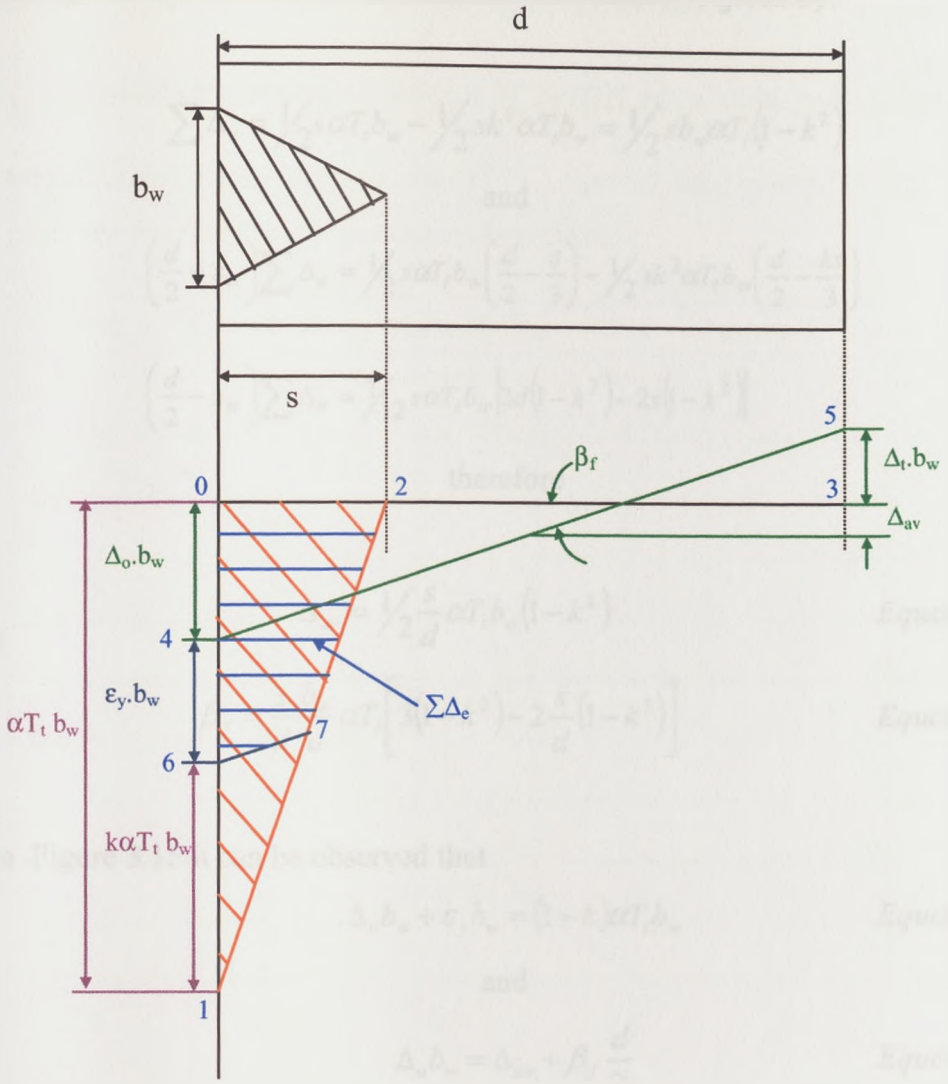

Figure 3.15: Schematic of transverse deformation [3.1]

Taking the transverse deformation to be made up of Δ_{av} (the transverse deformation at midsection) and the angle β_f (the free angle defining the angular distortion), a relationship exits with the mechanical deformation and the final deformed state.

$$\Delta_{av} = \frac{\Delta_o + \Delta_t}{2} b_w = \frac{\sum \Delta_e}{d} \quad \text{and} \quad \beta_f = \frac{12 \sum \Delta_e}{d^3} \left(\frac{d}{2} - z_w \right) \qquad \text{Equation 3.13}$$

where $\sum \Delta_e$ is the sum of the mechanical deformation and $\frac{d}{2} - z_w$ is the distance between the centroid of the plate and the centroid of the mechanical deformations.

Assuming that β_f is small, the mechanical deformation is given by:

$$\sum \Delta_e = \tfrac{1}{2} s \alpha T_t b_w - \tfrac{1}{2} s k^2 \alpha T_t b_w = \tfrac{1}{2} s b_w \alpha T_t \left(1 - k^2\right)$$

and

$$\left(\frac{d}{2} - z_w\right) \sum \Delta_e = \tfrac{1}{2} s \alpha T_t b_w \left(\frac{d}{2} - \frac{s}{3}\right) - \tfrac{1}{2} s k^2 \alpha T_t b_w \left(\frac{d}{2} - \frac{ks}{3}\right)$$

$$\left(\frac{d}{2} - z_w\right) \sum \Delta_e = \tfrac{1}{12} s \alpha T_t b_w \left[3d\left(1 - k^2\right) - 2s\left(1 - k^3\right)\right]$$

therefore

$$\Delta_{av} = \tfrac{1}{2} \frac{s}{d} \alpha T_t b_w \left(1 - k^2\right) \qquad \textit{Equation 3.14}$$

$$\beta_f = \frac{s}{d} \frac{b_w}{d} \alpha T_t \left[3\left(1 - k^2\right) - 2\frac{s}{d}\left(1 - k^3\right)\right] \qquad \textit{Equation 3.15}$$

From Figure 3.15 it can be observed that

$$\Delta_o b_w + \varepsilon_y b_w = (1 - k) \alpha T_t b_w \qquad \textit{Equation 3.16}$$

and

$$\Delta_o b_w = \Delta_{av} + \beta_f \frac{d}{2} \qquad \textit{Equation 3.17}$$

Substituting the equations 3.14 and 3.15 in equation 3.17 yields:

$$\Delta_o b_w = \tfrac{1}{2} \frac{s}{d} b_w \alpha T_t \left(1 - k^2\right) + \frac{s}{d} \frac{b_w}{d} \alpha T_t \left[3\left(1 - k^2\right) - 2\frac{s}{d}\left(1 - k^3\right)\right]$$

After rearranging the above, a relationship between s/d and k is given by equation 3.18

$$\frac{s}{d} = \frac{1 - k^2}{1 - k^3} \pm \sqrt{\left(\frac{1 - k^2}{1 - k^3}\right)^2 - \frac{(1 - k) - \dfrac{\varepsilon_y}{\alpha T_t}}{1 - k^3}} \qquad \textit{Equation 3.18}$$

Figure 3.16 shows the values of k with respect to the ratio s/d for various values of $\varepsilon_y/\alpha T_t$. Assuming a Young's modulus of 207GN/m², a yield stress of 405MN/m² and a coefficient of expansion of 14×10^{-6} /°C, curve 2 may be used to find the value of k when the fused zone is a triangular shaped area.

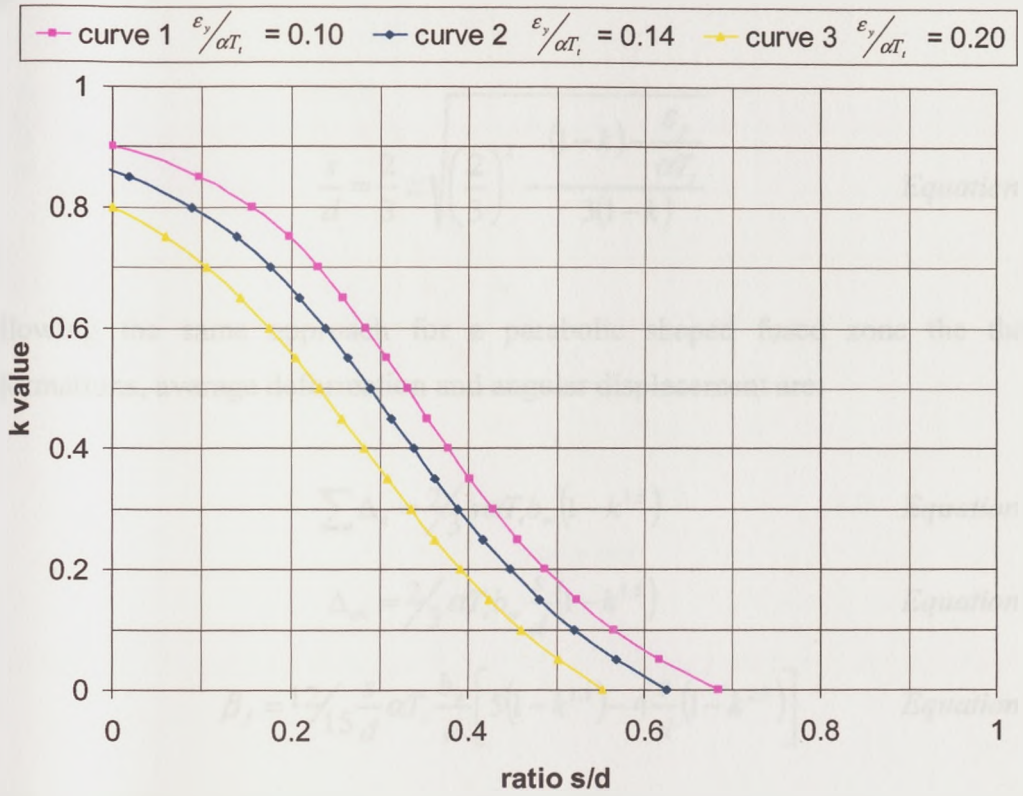

Figure 3.16: Relation between k and s/d for a triangular fused zone

The same method may be applied for a parabolic and a rectangular shaped fused zone. For a rectangular zone the mechanical deformation is given by:

$$\sum \Delta_e = \alpha T_t b_w s(1-k) \qquad \textit{Equation 3.19}$$

The corresponding average deformation and the free angular displacement are given in equations 3.20 and 3.21.

$$\Delta_{av} = \alpha T_t b_w \frac{s}{d}(1-k) \qquad \textit{Equation 3.20}$$

$$\beta_f = 6\alpha T_t \frac{b}{d}\frac{s}{d}\left[(1-k)-\frac{s}{d}(1-k)\right] \qquad \textit{Equation 3.21}$$

After rearranging and substituting in equations 3.16 and 3.17, the relation between s/d and k is given by equation 3.22.

$$\frac{s}{d} = \frac{2}{3} \pm \sqrt{\left(\frac{2}{3}\right)^2 - \frac{(1-k)-\frac{\varepsilon_y}{\alpha T_t}}{3(1-k)}} \qquad \textit{Equation 3.22}$$

Following the same approach for a parabolic shaped fused zone the thermal deformations, average deformation and angular displacement are:

$$\sum \Delta_e = 2/3\, s\alpha T_t b_w \left(1-k^{1.5}\right) \qquad \textit{Equation 3.23}$$

$$\Delta_{av} = 2/3\, \alpha T_t b_w \frac{s}{d}\left(1-k^{1.5}\right) \qquad \textit{Equation 3.24}$$

$$\beta_f = 12/15 \frac{s}{d}\alpha T_t \frac{b_w}{d}\left[5\left(1-k^{1.5}\right)-4\frac{s}{d}\left(1-k^{2.5}\right)\right] \qquad \textit{Equation 3.25}$$

Hence the relation between k and s/d for a parabolic fused zone is shown in equation 3.26.

$$\frac{s}{d} = \frac{5\left(1-k^{1.5}\right)}{6\left(1-k^{2.5}\right)} \pm \sqrt{\left(\frac{5\left(1-k^{1.5}\right)}{6\left(1-k^{2.5}\right)}\right)^2 - \frac{5\left[(1-k)-\varepsilon_y/\alpha T_t\right]}{8\left(1-k^{2.5}\right)}} \qquad \textit{Equation 3.26}$$

Figure 3.17 gives the relation of k with s/d for a triangular, parabolic and rectangle shaped fused zone for a value of $\varepsilon_y/\alpha T_t = 0.14$.

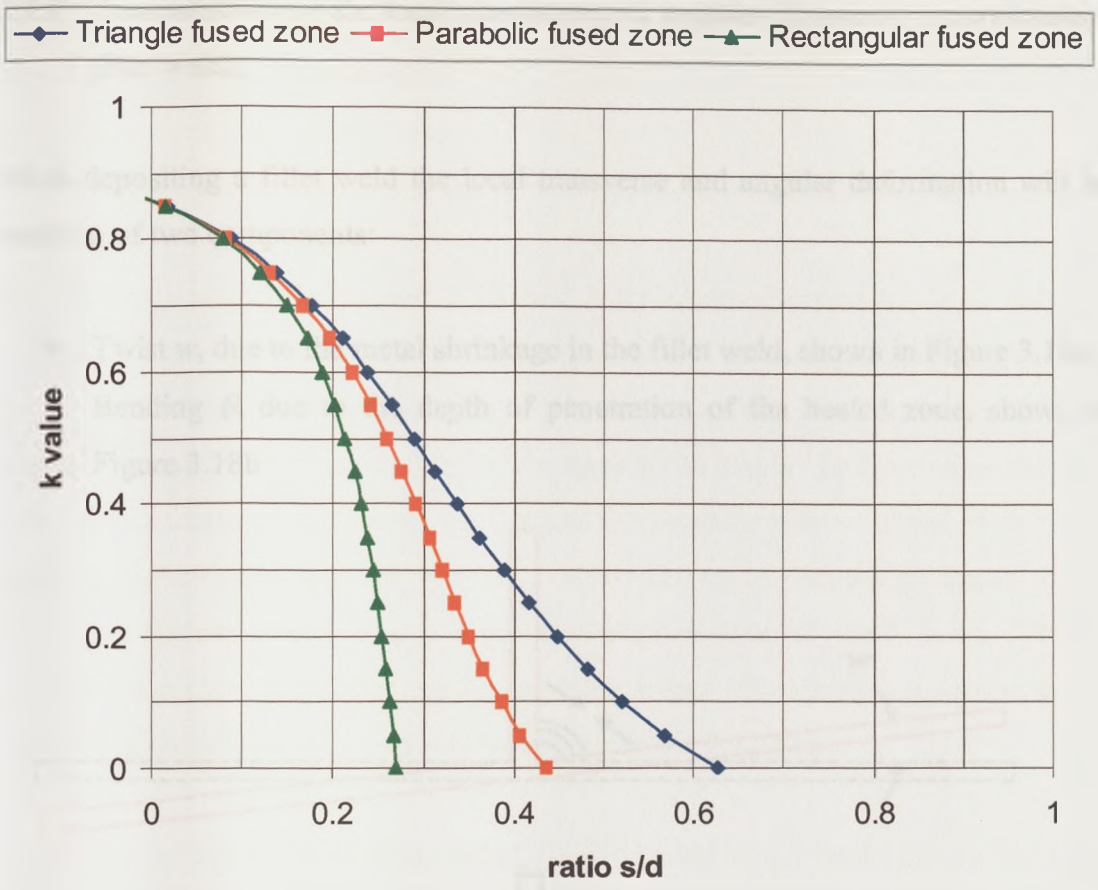

Figure 3.17: Relation between k and s/d for various shapes of the fused zone

From the above, it may be seen that for the same area of fused zone and when k is always zero (s/d greater than 0.62 in case of a triangular fused zone), an increase in depth of penetration will reduce the angular distortion, whilst the transverse contraction will remain constant. In the case where the material underneath the fused zone is restraining the contraction, i.e. $k > 0$, and assuming the same area of fused zone, a decrease in depth of penetration will result in a reduction in both angular distortion and transverse shrinkage. Since the angular distortion triggers the out of plane longitudinal distortion by displacing the longitudinal contraction force away from the neutral axis, one way of mitigating of the out of plane distortion in butt welds is to control the angular distortion. Hence increasing the depth of penetration will reduce the out of plane distortion, (as is known from practical experience).

3.3.2 *Determination of the local transverse and angular distortion in unrestrained fillet welds.*

When depositing a fillet weld the local transverse and angular deformation will be made up of two components:

- Twist w, due to the metal shrinkage in the fillet weld, shown in Figure 3.18a
- Bending θ, due to the depth of penetration of the heated zone, shown in Figure 3.18b

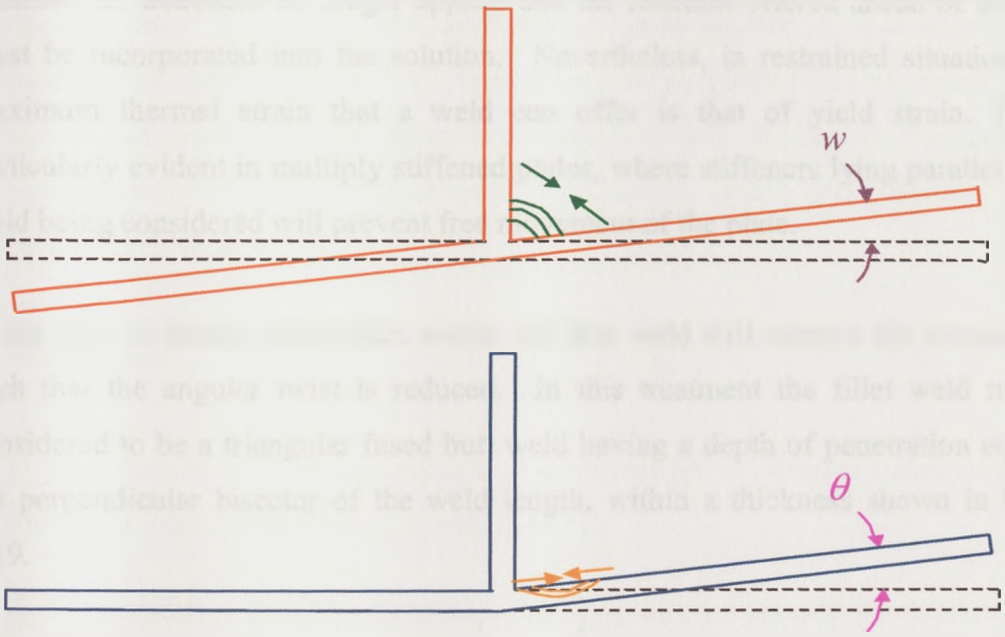

Figure 3.18: Angular distortion in unrestrained fillet weld

Since the deposited weld has reached the melting temperature then the plastic deformation imposed by the weld zone area may be considered to be totally composed of a shrinkage strain. Furthermore since the weld is not restrained by the surrounding base metal, the thermal strain applied to this area is of the form αT_t. Again, a temperature of 1000°C was used by Okerblom.

The bending component may be considered to be the same as for a butt weld, hence, depending on the shape of the refused zone and depth of penetration, a thermal strain

of the form $\alpha T(1-k)$ may be applied. The value of k can be again determined using the previously derived formulas.

3.3.3 Local transverse and angular distortion in restrained butt and fillet welds.

The theory presented in section 3.3.1 and 3.3.2 assumes that there is no restraint applied to the weld other than by the unfused zone. In multipass welding such as double-sided fillet welding and multi stiffened plates, the previous welds and the structural integrity will restrain local movement of the welds. In these cases the two-dimensional treatment no longer applies and the restraint offered ahead of the weld must be incorporated into the solution. Nevertheless, in restrained situations, the maximum thermal strain that a weld can offer is that of yield strain. This is particularly evident in multiply stiffened plates, where stiffeners lying parallel to the weld being considered will prevent free movement of the plate.

In the case of double sided fillet welds, the first weld will restrain the second weld such that the angular twist is reduced. In this treatment the fillet weld may be considered to be a triangular fused butt weld having a depth of penetration equal to the perpendicular bisector of the weld length, within a thickness shown in Figure 3.19.

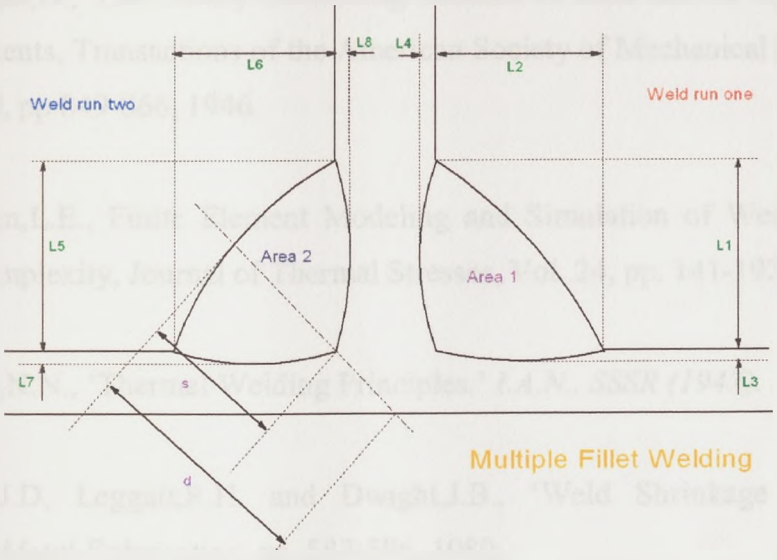

Figure 3.19: Angular distortion in double-sided fillet welds

In the above simplification the final angular distortion will be dependent on the size of the fillet weld and the value k assigned to the weld using equation 3.18.

3.4 Discussions

Simplified thermo-elastic-plastic algorithms are presented in this chapter. The algorithms named *'Mismatched Thermal Strain'* and *'Contraction Thermal Strain'* define the plastic deformations and hence contraction forces applied to a welded structure in the longitudinal and transverse directions. Furthermore, effects arising from previously deposited welds are taken into account by adjusting the respective thermal strains. The proposed algorithms are then applied to a structural finite element model, whereby structural interaction such as gravity and support positions are taken into account. The simplified algorithms are verified in this thesis via experimental results and finite element simulations, which are presented in the subsequent chapters.

3.5 References

[3.1] Okerblom,N.O., The calculations of deformations of welded metal structures, Her Majesty's Stationery Office, London, 1958.

[3.2] Rosenthal,D., The Theory of Moving Sources of Heat and its Application to Metal Treatments, Transactions of the American Society of Mechanical Engineering, Vol. 68, No.8, pp 849-866, 1946.

[3.3] Lindgren,L.E., Finite Element Modeling and Simulation of Welding Part 1: Increased Complexity, Journal of Thermal Stresses, Vol. 24, pp. 141-192, 2001.

[3.4] Rykalin,N.N., 'Thermal Welding Principles.' *I.A.N., SSSR (1947).*

[3.5] White,J.D, Leggatt,R.H. and Dwight,J.B., 'Weld Shrinkage Prediction,' *Welding and Metal Fabrication,* pp. 587-596, 1980.

[3.6] Jonsson,M., Kaelsson,L., and Lindgren,L.E., 'Deformations and Stresses in Butt-welding of Large Plates with Special Reference to the Mechanical Material Properties,' *Numerical Methods in Heat Transfer,* Vol. 3, 1985.

[3.7] Mollicone,P., Camilleri,D. and Gray,T.G.F, 'Simple Thermo-elastic-plastic Models for Welding Distortion Simulation,' *Science Technology of Welding and Joining,* (to be submitted).

[3.8] Ueda,Y. and Nakacho,K., 'Simplifying Methods for Analysis of Transient and Residual Stresses and Deformation due to Multipass Welding,' *Transactions of JWRI, Osaka, Japan,* Vol.11, No.1, pp 95-103, 1982.

[3.9] Borjesson,L. and Lindgren,L.E., 'Simulation of Multipass Welding With Simultaneous Computation of Material Properties,' *Journal of Engineering Materials and Technology,* Vol. 123, Lulea, Sweden, pp. 106-111, 2001.

[3.10] Tekriwal,P. and Mazumder,J., 'Transient and Residual Thermal Strain –Stress Analysis of GMAW,' *ASME Journal of Engineering Material Technology,* Vol. 113, pp. 336-343, 1991.

[3.11] 'ANSYS 6.1 Documentation,' ANSYS inc Theory Reference, Structures, 2001.

CHAPTER FOUR

CHAPTER 4

EXPERIMENTAL PROCEDURES & MEASUREMENT TECHNIQUES

4.1 Introduction

Extensive welding simulation studies have been performed in this project. However, these are of doubtful use without experimental information from actual welding tests. In the first place, the development and verification of the assumptions in the finite element analysis of welding, is dependent on such information. Lindgren [4.1], also concludes that uncertain material properties and the problem of predicting the net heat input make the success of simulations to a large extent dependent on experimental work. Prediction of thermal transients, whether through thermal finite element analysis or empirical formulas, relies on measured transient temperatures and / or information from the resultant weld microstructure. In particular, most of the simulations assume an energy transfer efficiency (ratio between the total electrical power and the heat dissipated in the plate), which is not normally known, unless through comparison with experimental results. This efficiency will adjust the total heat input being induced into the welded plate.

Structural welding analyses, on the other hand, are usually verified via residual strain measurements and / or distortion measurements. While residual stresses and strain measurements, can verify the model in local points, particularly in the case of the fusion zone, overall distortion measurements can give a global characterisation of the structure under investigation.

Lindgren [4.1], [4.2], presents a number of references, together with the experimental procedures adopted by these researchers in order to verify their simulations. Of principal importance to the present study, are experimental measurements performed on large plate welded structures reported by Michaleris and DeBiccari [4.3], Tsai *et al* [4.4] and Huang *et al* [4.5]. In the first two studies, thermocouples were employed to verify the thermal models, while linear variable transducers and a laser displacement sensor where used for the verification of the predicted out-of-plane deformation. Huang et al used the macrographs of the fusion zone to index the thermal analysis and applied a Lidar sensor system to measure the out-of-plane deformation. Other studies exist which provide experimental results only. Typical studies include that of Suresh *et al* [4.6] and Parmar *et al* [4.7], who concentrated their efforts in measuring the out-of-plane angular distortion for different welding configurations and parameters.

4.1.1 Experimental investigations performed – brief overview

The study in this thesis focuses on the global effects of distortion on large ship structures and less emphasis is given to the residual stresses built up in weld zone. A number of experiments have been devised to give better insight and verification of the previously described simplified thermo-elasto-plastic approaches. The experiments maybe divided into two phases. Firstly, a pilot program, consisting of butt welds and fillet welding, was completed. Butt welds were performed on small plates of dimension 0.25m x 0.5m x 6mm. Fillet welds, were also studied, where by a stiffener of dimensions 0.15m x 0.5m x 6mm was welded at the centre of a plate 0.5m x 0.5m x 6mm thick. The above experiments provided a guideline for the large-scale experimental tests. These included butt welding of 0.675m x 4m x 5mm plates, double-sided fillet welding of a central stiffener 0.1m x 4m x 5mm, welded to a plate 1.2m x 4m x 5mm and multiply stiffened plate structures consisting of three stiffeners of dimensions 0.1m x 4m x 5mm, fillet welded at a pitch distance of 0.5m to a plate measuring 1.5m x 4m x 5mm.

The tests were carried out on CMn steel plates conforming to LLOYDS 2000 Grade DH 36 (similar to BS 4360 Grade 50D). Chemical composition tests performed by the ship building company (BAE systems) in collaboration with this project yielded an averaged result shown in Table 4.1. The ship building LLOYDS 2000 grade DH 36 standard, specifies a minimum yield strength of 355N/mm² and a tensile strength ranging from 490 to 620 N/mm². The certified yield strength of the test specimens, according to CORUS inspection certificate [4.8], was 405N/mm². However, tensile testing of the plate specimens, presented in chapter 6, yielded a room temperature yield strength of 360N/mm².

	C	*Si*	*Mn*	*P*	*S*	*Ni*	*Cr*	*Mo*	*Al*
% weight	0.17	0.35	1.22	0.019	0.010	0.04	0.050	<0.002	0.04

Table 4.1: Chemical composition of test specimens obtained from BAE systems

The commitment of obtaining consistent results and simplifications in the boundary conditions assigned in the finite element analyses required the construction of two welding rigs. These include a small-scale welding rig for the pilot programme and a large-scale welding rig to accommodate the welding of 4m long plates.

4.2 Welding rigs design considerations and apparatus used

The welding trials were introduced to reflect industrial practice as far as practical. However, it was considered to be important to device a system whereby transient temperatures and out-of-plane deformations could be captured easily and quickly, while keeping experimental errors to a minimum. The welding rigs at the ship building company impose a large number of restrictions. Particularly, the field of view is obstructed by heavy jigs surrounding the welded plate. Access to the plate for possible transient distortion measurement is also restricted. Furthermore, capturing of the out-of-plane deformation would be difficult without introducing errors due to plate handling during transfer from the welding rig to a reference plane.

Also, since the experiments were principally required to provide verification of the simulations described in the subsequent chapters, the boundary conditions needed to

be definite and easy to obtain. Heat losses imposed by the welding clamps and other machinery in contact with the test plates would be cumbersome to simulate. Therefore a system was adopted whereby the plate would only be subjected to natural cooling, thus easily identifying the thermal boundary conditions. As opposed to real welding situations where the plate can have a number of possible contact points and is usually restrained by welding jigs, the test plates were supported on known points and unrestrained in both the in-plane and out-of-plane axis.

Welds were completed using an automatic GMAW, flux-cored 20% CO_2, 80% Ar gas shielded process. This system involves the use of an electrode, which is fed through the welding gun, by means of a wire feed unit. Shielding from oxides and other harmful gases, is achieved through the shielding gas envelope and flux incorporated in the wire core. Control of the deposition rate is executed through adjustable voltage and current, together with the weld travel speed. The total heat generated by the arc, will never be totally absorbed by the plate but some is lost in heating up the shielding gas, nozzle and the atmosphere. A portable arc monitoring system (P.A.M.S unit) was also used to give a calibrated measure of the voltage and current being used in specific welding configurations, thereby giving an accurate indication of the total energy input used.

4.2.1 Thermal transients data capturing

The thermal transients during the welding and cooling phase of the tests welds were measured via an array of thermocouples and a thermographic camera - ThermaCAM™SC500 manufactured by FLIR systems.

The thermocouple investigation had two purposes: to index the surface emissivity, an essential input for the thermographic data, and to provide accurate comparison of the upper and lower surface temperatures at specific points. Various types of thermocouples exist, the choice depending on the temperature range and sensitivity required. The best known and dominant thermocouple belonging to the chromium-nickel aluminium group is type K. Its temperature range extends from -200°C to

1100°C and, for a class one type K thermocouple the deviation from the actual temperature is ±1.5°C [4.9].

Of vital consideration when dealing with thermocouples is the loop resistance. The resistance of extension and compensating cables varies according to different conducting metals; the limit to cable lengths which can be accommodated by measuring instruments therefore depends on both the thermocouple type and instrument specifications. A general rule for electronics instruments is that up to 100Ω loop cable resistance (i.e. total of both legs) will not result in measurement errors. In the case of 0.315mm type K thermocouple diameter wire, the loop resistance for a type K compensating wire, is 12.8Ω per meter. Hence the length of the cable should not exceed 3.91m. A larger diameter thermocouple can be used to reduce the loop resistance, but since the thermal gradients in welding vary considerable within 0.5mm, it was decided to use a type K, single stranded, 0.315mm thermocouple. Smaller wire diameter thermocouples, would have limited the length of the extension wires, essential in the large scale welding tests.

Thermography makes use of the emitted infrared radiation from an object. The amount of radiation energy emitted from the object under investigation and background radiation are captured by the thermographic camera and interpreted into surface temperature. ThermaCAM™SC500 detects the infrared radiation of spectral range 7.5 - 13μm, via an uncooled focal plane array of 320 x 240 pixels [4.10]. The camera is calibrated for two temperature ranges, that of -40 to 120°C and 10 to 650°C, with an accuracy of ±2°C.

As distinct from the point measurements given by thermocouples, thermography gives an overall thermal picture of the welded plate. The camera also plays an important role in the investigation of thermal transients in indefinite heat absorption systems, where external heat sinks may be relevant. It also determines the thermal patterns towards the ends of the plates, where a non-quasi static pattern exists. Thermography has been used by a number of researchers in the welding field such as Cheng *et al* [4.11]. It offers the possibility to investigate the thermal transients that

trigger welding distortions, without the need for finite element simulations, i.e. the thermal patterns obtained from thermography can act as an input to the decoupled analysis. However, perhaps due to the cumbersome calibration required and understanding of thermography, it has not typically been used in industry for this purpose.

4.2.2 Static and transient out-of-plane deformation data capturing

The transient out-of-plane deformation was investigated via four linear variable displacement transducers (LVDT's), manufactured by R.D.P electronics and having an operating range of ±25mm. They offer a linearity corresponding to 0.1% of the range of operation, that is 0.025mm. The position of LVDT's was such that the transient angular distortion and longitudinal curvature (bowing) could be quantified during the welding and cooling phases of the weld tests.

LVDT's provide only point measurements and hence a system had to be devised to measure the global out-of-plane deformation. Haung *et al* [4.5] used a Lidar system to measure the out-of-plane deformation. This system essentially consists of a laser scan that records the distance between the sensor and the specimen under investigation. The output is a point cloud map of the objects in vision of the laser, which can then be exported to other computer aided design packages for analysis. Masubuchi *et al* [4.12], proposed a non contact measuring system via laser interferometer. The distance between the generated fringes, determines the out-of-plane deformation. Though providing accurate results over a small area, such arrangement cannot be applied to large plate structures due to the complexity involved.

The approach adopted in the present project uses a laser displacement measuring system, based on a M5L/100 Laser sensor, shown in Figure 4.1. The laser displacement sensor consists of a class 2 laser and an electronic module used for the integration and averaging of the distance from the laser diode to the plate. It offers the possibility to measure displacements within a range of 100mm from a stand off

distance of 220mm. The linearity error and resolution is 0.3mm and 30μm respectively [4.13]. The laser sensor configuration will give the initial profile of the plate and the final shape after cooling to ambient temperature, thereby obtaining the out-of-plane deformation.

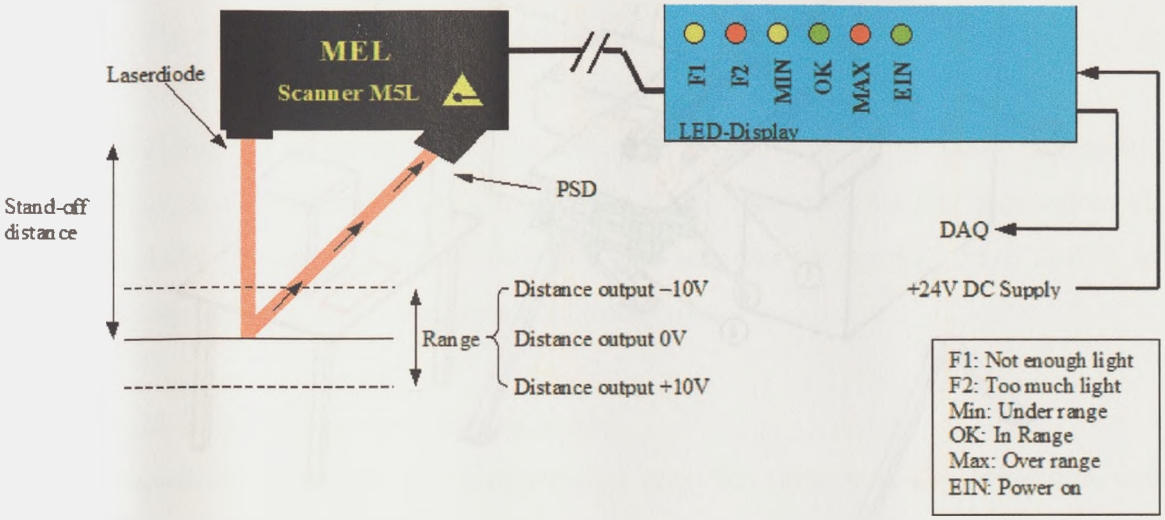

Figure 4.1: Precision optical measurement device –type M5L/100 laser sensor

4.3 Small-scale welding rig

A small welding rig that accommodates plates of maximum dimensions 0.5m x 0.5m, was constructed, as a proof of concept, before up scaling to large scale welding tests. The welded plates were supported on 4 fixed points, so that no restraint was applied on the in-plane or out-of-plane deformation, and natural convection prevailed. In order to reduce errors and disturbed images from the thermographic camera it was decided to keep the welding head and camera fixed, while traversing the plate. The traverse mechanism of the test plates was achieved by means of a three-axis milling machine.

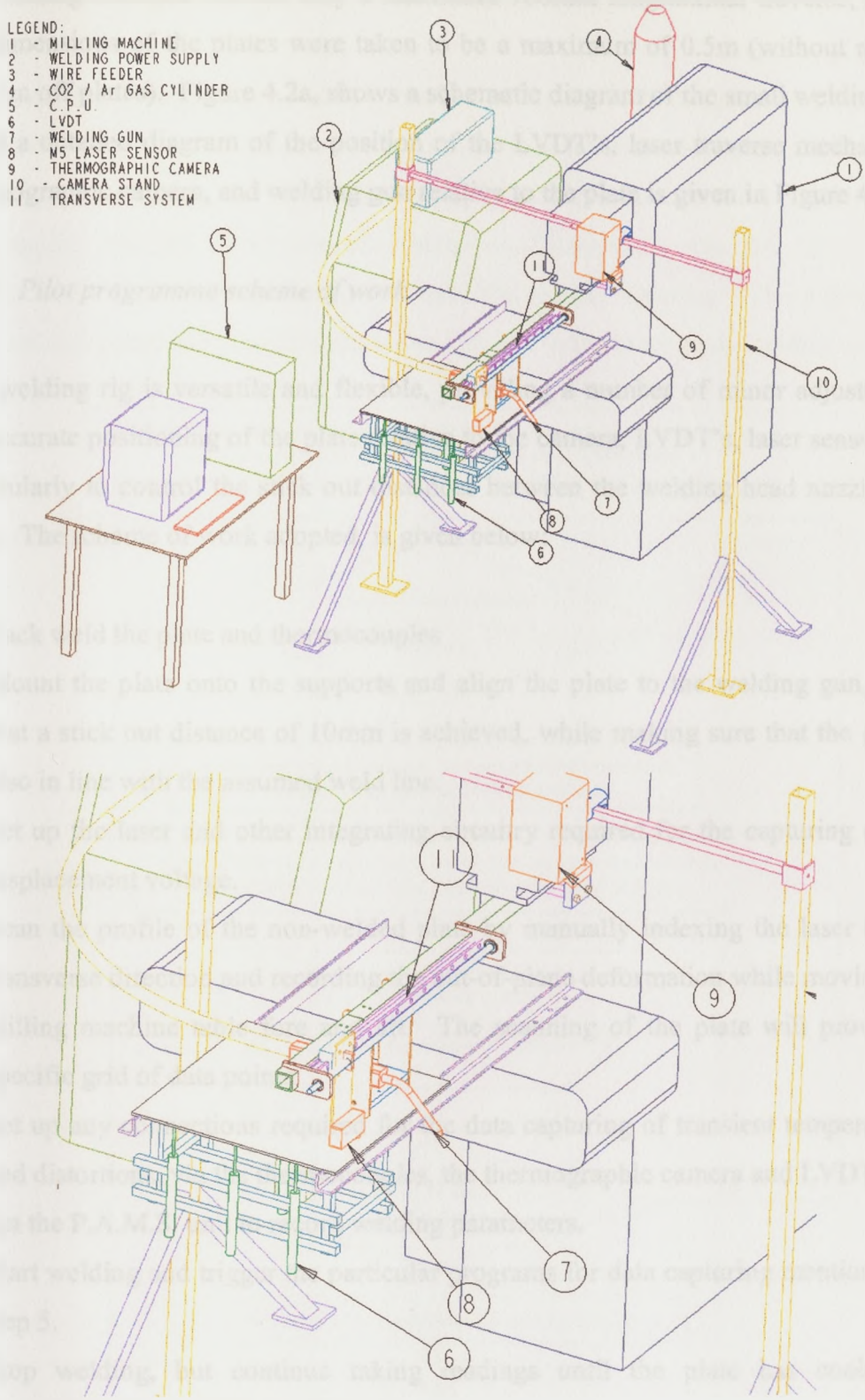

Figure 4.2: Schematic diagram of the small welding rig.

The milling machine offered only a maximum 700mm longitudinal traverse, hence the dimensions of the plates were taken to be a maximum of 0.5m (without run on and run off plates). Figure 4.2a, shows a schematic diagram of the small welding rig, while a detailed diagram of the position of the LVDT's, laser traverse mechanism, thermographic camera, and welding gun relative to the plate is given in Figure 4.2b.

4.3.1 Pilot programme scheme of work

The welding rig is versatile and flexible, providing a number of minor adjustments for accurate positioning of the plate relative to the camera, LVDT's, laser sensor and particularly to control the stick out distances between the welding head nozzle and plate. The scheme of work adopted, is given below:

1. Tack weld the plate and thermocouples
2. Mount the plate onto the supports and align the plate to the welding gun, such that a stick out distance of 10mm is achieved, while making sure that the gun is also in line with the assumed weld line.
3. Set up the laser and other integrating circuitry required for the capturing of the displacement voltage.
4. Scan the profile of the non-welded plate by manually indexing the laser in the transverse direction and recording the out-of-plane deformation while moving the milling machine table fore and aft. The scanning of the plate will provide a specific grid of data points.
5. Set up any connections required for the data capturing of transient temperatures and distortions, via the thermocouples, the thermographic camera and LVDT's.
6. Set the P.A.M.S. unit to record welding parameters.
7. Start welding and trigger the particular programs for data capturing mentioned in step 5.
8. Stop welding, but continue taking readings until the plate has cooled to approximately ambient temperature
9. After complete cooling, re scan the profile of the welded plate as described in step 4.

Data capturing was achieved via a number of LABVIEW programs, specifically designed to measure the temperature transients from the thermocouples, the transient displacement reading of the linear variable transducers and the out-of-plane deformation via the laser sensor system configuration. On the other hand ThermaCAM Researcher software was used for image capturing. These programs were not integrated but provided guidelines for use in the large scale welding tests.

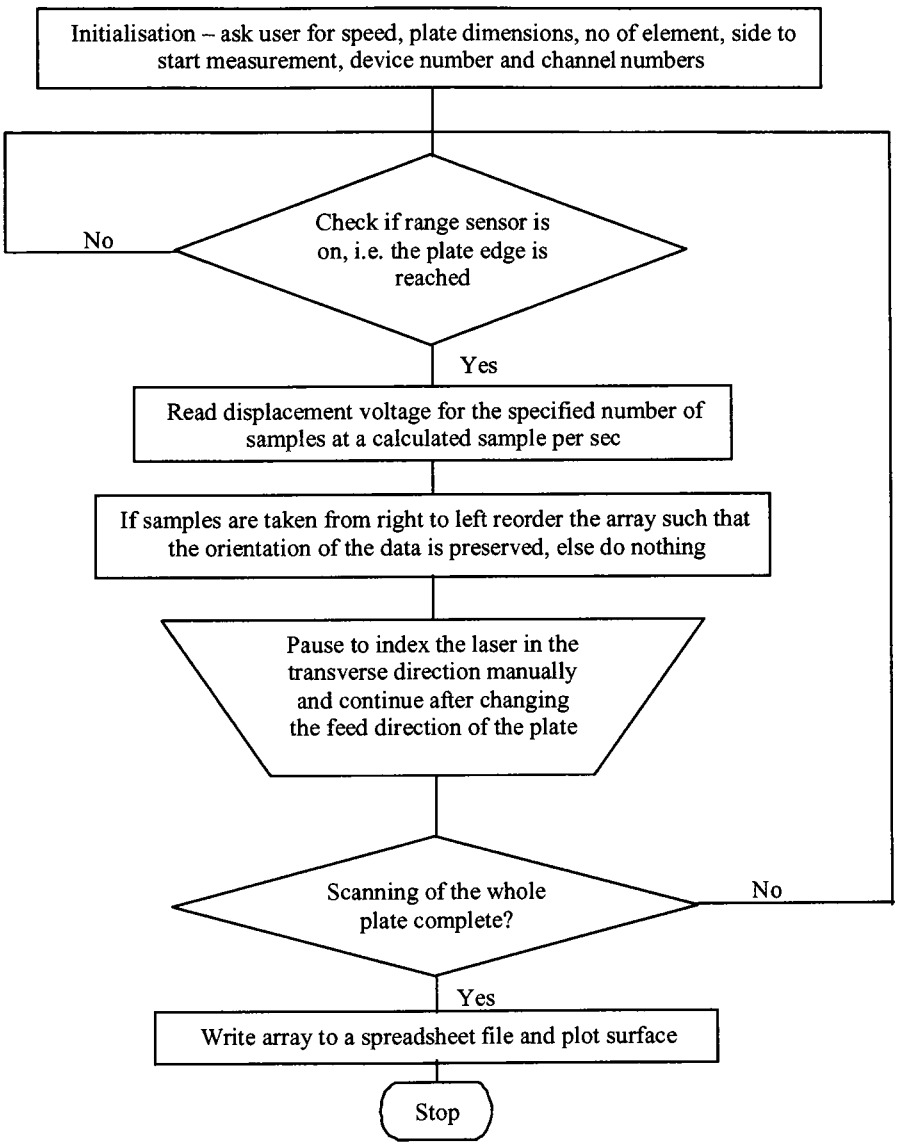

Figure 4.3: Pseudo-code for the pilot programme static out-of-plane distortion measurements

The versatility obtained from the integration of the laser sensor, milling machine, data acquisition card and a real time LABVIEW program, provided options to measure the displacements at accurate specified grid positions. Displacement readings can be recorded while traversing the plate underneath the laser sensor. In the pilot program 816 nodal positions where measured, consisting of an array 16 x 50 with an element size of 32mm x 10mm in the transverse and longitudinal directions respectively. The pseudo-code of the LABVIEW program is given in Figure 4.3.

4.4 Large-scale welding rig

The large-scale tests required a more complex system to accommodate the butt and fillet welding of plates with nominal dimensions of 4m x 1.5m x 6mm. Hence an experimental rig was constructed, consisting of a number of sub-systems to integrate welding and automatic data capturing. A schematic diagram of the large-scale welding rig is given in Figure 4.4.

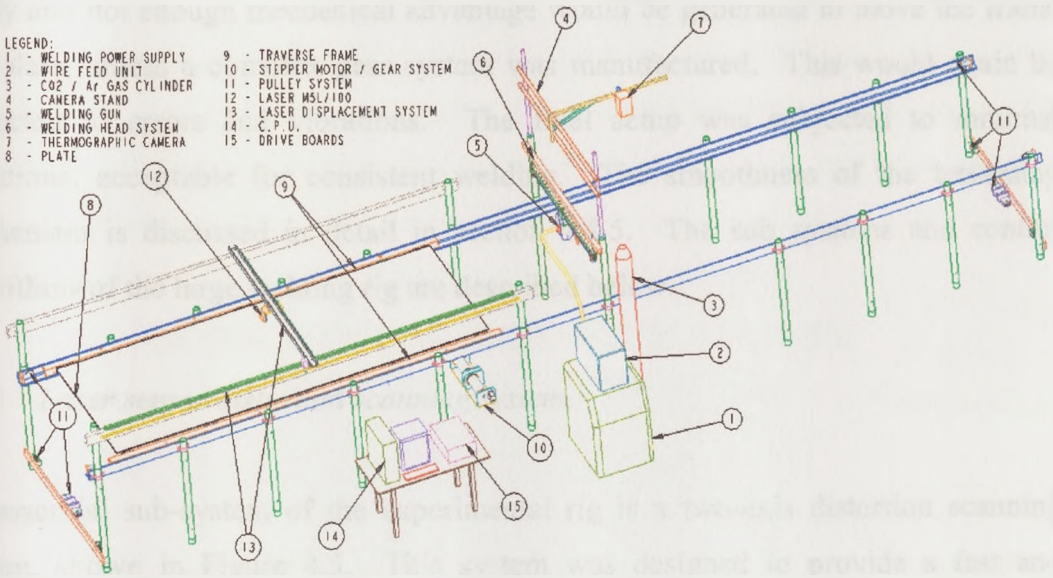

Figure 4.4: Schematic diagram of the large-scale welding rig.

Again for the same reasons mentioned in section 4.3, it was decided to keep the camera and welding head fixed. Longitudinal movement was achieved by means of a traversing frame, rolling on long angle sections, and driven by cables and a remote

drive system, made up of a gear system and bipolar stepper motors. The traversing frame also acted as a reference plane for the out-of-plane distortion measurements, as the plates were supported on ten fixed points. Control to provide steady welding speed was accomplished via the use of remote stepper motors. The 'sticky drawer' effect was eliminated by providing a synchronous movement of opposite ends of the frame through a system of cables and pulleys. Furthermore, a synchronous stepping frequency was supplied to the two stepper motors that wound the separate cables.

The system was initially subject to a number of unwanted vibrations. With the use of two accelerometers attached to the cables the harmonics were quantified, and a strong component at 20Hz was found. This was particularly due to the length of the cables in resonance with the natural frequency generated by the stepper motors. Reduction of harmonics at the typical welding speed was achieved by tensioning the cables, such that less harmonics were evident at normal welding speeds. For total removal of harmonics a different drive system would have to be constructed. Another option would include the use of a rack and pinion setup, but this would be costly and not enough mechanical advantage would be generated to move the frame and plate, unless a complex gear system was manufactured. This would again be subjected to errors and vibrations. The final setup was subjected to minimal vibrations, acceptable for consistent welding. The smoothness of the traversing mechanism is discussed in detail in section 4.4.5. The sub systems and control algorithms of the large welding rig are described below.

4.4.1 Laser sensor distortion scanning system

An essential sub-system of the experimental rig is a two-axis distortion scanning system, shown in Figure 4.5. This system was designed to provide a fast and accurate automated measurement of the out-of-plane profiles of the initial and welded plates. Indexing in the longitudinal and transverse direction is obtained via a rack and pinion, and two bi-polar stepper motors. The use of stepper motors offers the possibility to quantify the position of the laser sensor relative to the plate. This being dependent on the frequency and number of steps categorizing the clock pulse

supplied to the respective drive boards. In so doing the out-of-plane distortion at fixed points can be recorded.

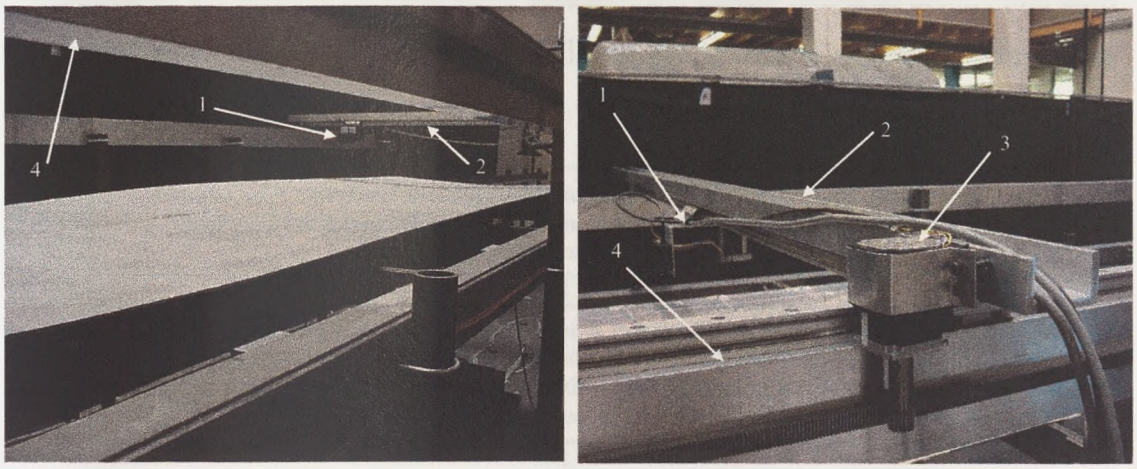

1. Transverse stepper motor & laser unit connected to traverse guide rail
2. Transverse beam with rack attached
3. Longitudinal stepper motor
4. Longitudinal beam with rack attached

Figure 4.5: Laser scanning system

The measurement path taken by the laser sensor is shown in Figure 4.6. It was preferred to take measurements during the longitudinal traverse as, while this measuring path reduces the time of scanning, more nodal points will be recorded in the longitudinal out-plane deformation. The latter being a complex polynomial as opposed to a linear relationship in defining the angular distortion.

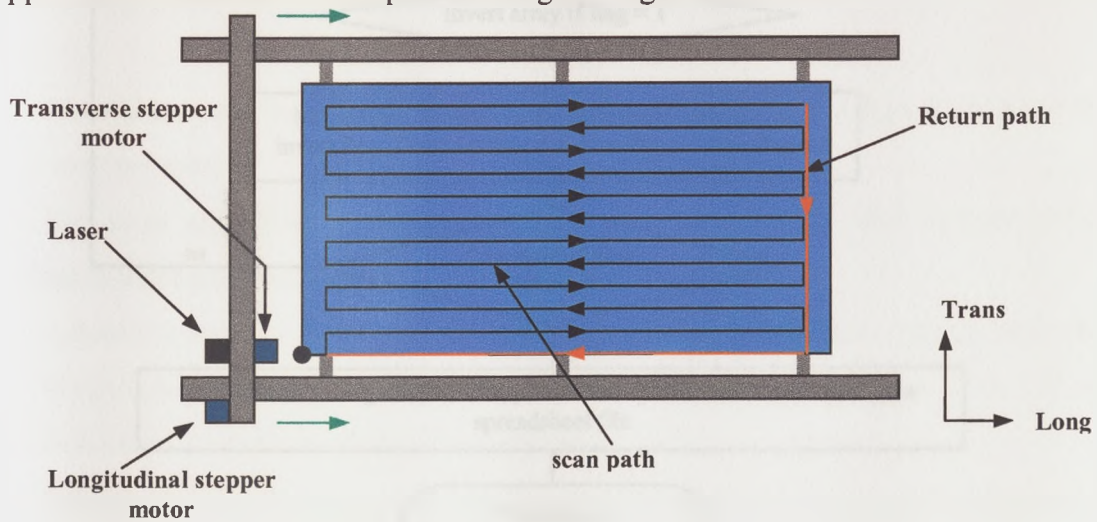

Figure 4.6: Laser measurement path

Integration of the stepper motors, drive boards, laser sensor and data acquisition card was based on a LABVIEW program. Figure 4.7 shows the pseudo-code of the measurement algorithm.

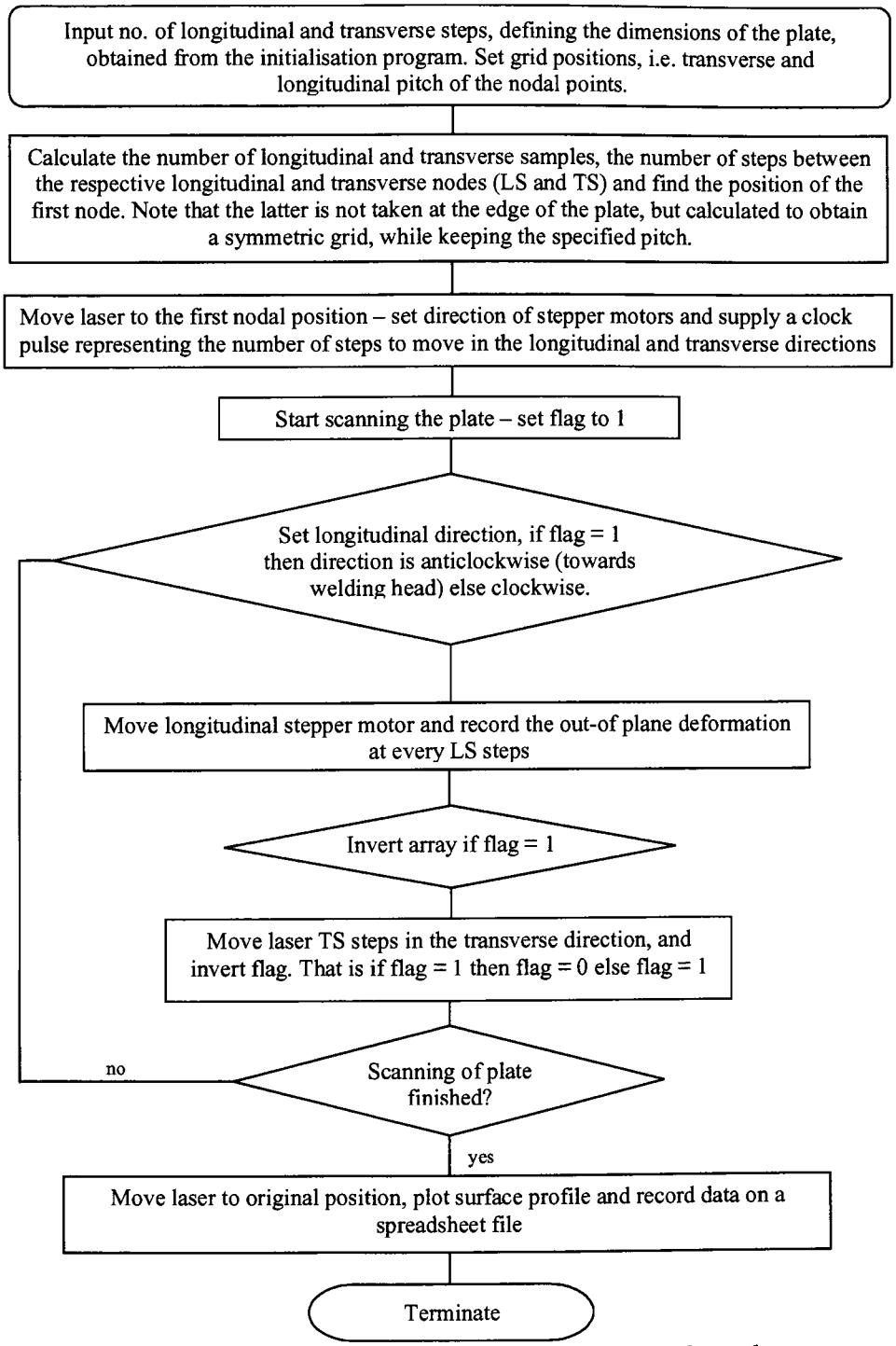

Figure 4.7: Psuedo-code of the measurement algorithm

Two programs are required for the static distortion measurement. The first program provides an initialization process to find the actual dimensions of the plate and attains the relationship between the traverse distance and the number of steps required to move such displacement. The second program, described in figure 4.7, sets out to measure the displacement and consequently out-of-plane deformation.

The control signals required by each of the drive boards include a stepped signal (clock pulse) and a digital high / low output to determine the direction of the stepper motors. The number of steps traversed by the stepper motors is determined by the number of negative edges present in the clock pulse and the period of one step cycle determines the stepping frequency. Hence, rather then outputting a predefined clock pulse from the data acquisition card, a digital output that alternates between high and low at a defined rate, was used to control the frequency and number of steps of the respective stepper motor.

4.4.3 Large-scale experimental scheme of work

Prior to the start of an experiment, the plates undergo a preliminary set-up stage. This involved tack welding the plates or stiffeners, together with the run-on and run-off plates. Note the tack welding in butt welds was performed on the underside of the plate and the configurations adopted are described in chapter 7. Following the plate preparation, the subsequent steps were performed;

1 Place plate onto the frame, supported at ten fixed points and align the plate to the welding head.
2 Fix laser sensor and connect any circuitry required for the stepper motor movement and data capturing of the displacement.
3 Adjust the relative height of the plate with respect to the laser sensor, such that the points at the supports are at the standoff distance of the sensor. This will act as a datum to the out-of-plane deformation.
4 Run the initialization program and the measurement program described in section 4.4.2, to record the initial profile of the plate.

5 Set up the thermographic camera, together with the respective data acquisition circuitry.

6 Set up the P.A.M.'s unit and welding machine, i.e. set the gas flow and welding current / voltage

7 Connect the drive boards to the traverse system stepper motors and set the LVDT's

8 Run the welding program, described in section 4.4.4, thereby welding the plate, while taking thermographic pictures, transient distortions and thermal measurements.

9 After complete cooling to ambient temperature – typically after three hours, retract the frame and plate under the laser scanning system and follow step 4.

4.4.4 Control algorithms of welding rig

The drive system was integrated with a computer, with the use of stepper motors, drive boards and an analogue to digital card, via a LABVIEW program that controlled the starting and finishing of welding, frame movement, thermography, thermocouple measurements and LVDT data capturing. As opposed to the laser scanning system a pulse train directly achieved from the on board clock of the data acquisition card, was used to generate the stepped signal. Limit switches determined the triggering of thermography, thermocouple and LVDT data capturing, together with the start and finishing of welding and the stopping of the frame/plate movement.

The control of the welding rig and data capturing consists of three programs running together in real time. The main program controls the plate movement, welding and triggering of the other two programs. The sub programs include, a LABVIEW program integrated with a data acquisition card and a multiplexer for the thermocouple reading of 30 channels and a ThermaCAM researcher software for the capture of infrared images. The pseudo-code is given in Figure 4.8.

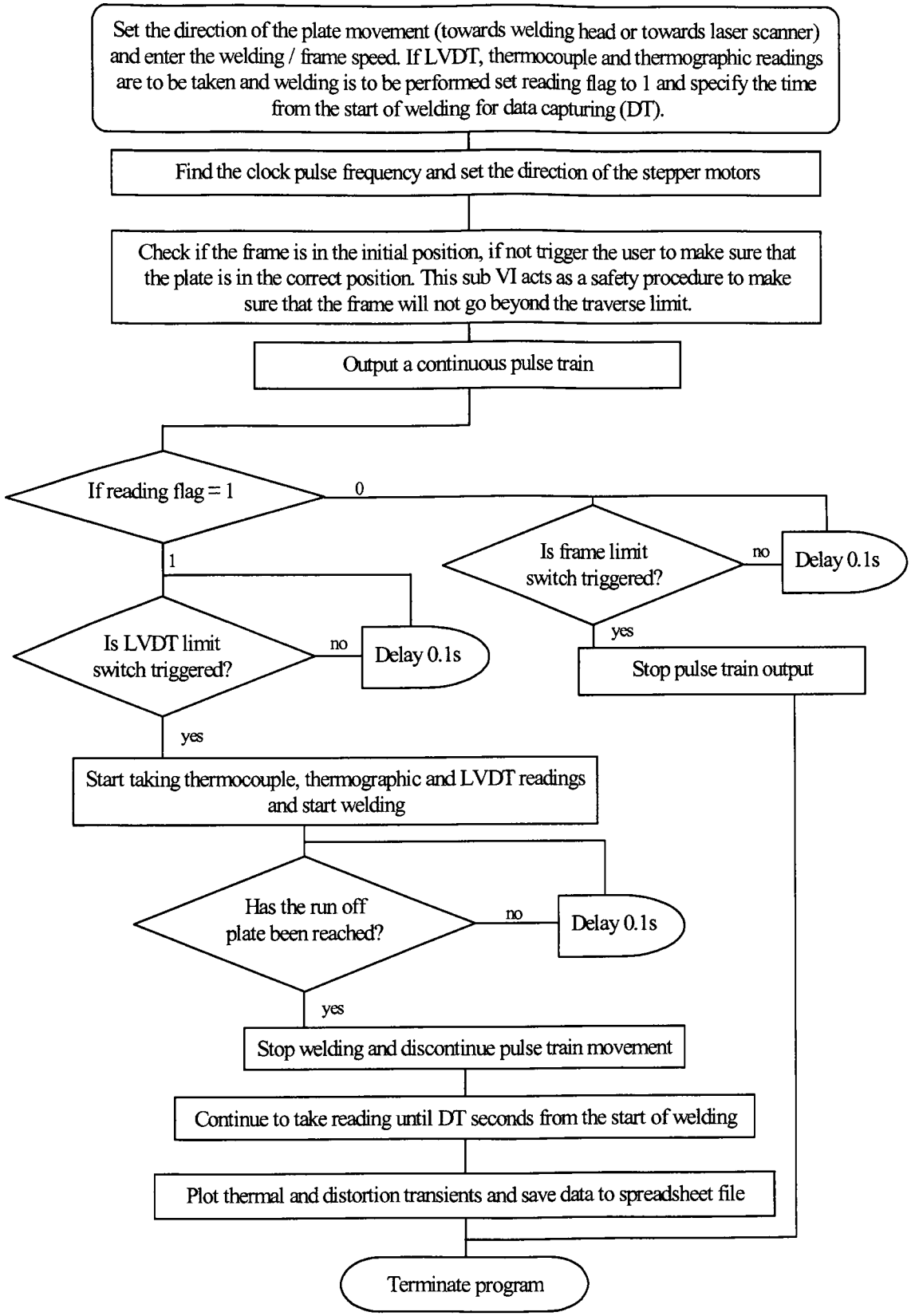

Figure 4.8: Psuedo-code of the main welding rig program

The relationship between the stepping frequency supplied to the stepper motors and the actual traverse/welding speed had to be quantified. This is not a direct relationship, due errors resulting from the backlash of gears and the extension and compression of the cables. The experiment described in this section quantifies the smoothness of the traverse system and finds the calibration factor that relates the stepping frequency to the actual plate movement. The actual displacement of the traversing frame was quantified by means of two draw string potentiometers, attached to both sides of the frame, calibrated such that a linear relationship existed between the output voltage and displacement. This voltage was recorded by means of a real time LABVIEW program at a sample rate of 10 samples per second, i.e. a sample every 0.1 seconds. A linear equation between the displacement and time was fitted to the data and by comparing the actual data with the linear regression relationship the deviation from a smoothed traverse movement was quantified. This experiment was performed at typical welding speeds ranging from 3.5mm/s to 8 mm/s.

Table 4.2 shows the maximum and minimum deviations from the assumed linear relationship together with the standard deviation at the left and right hand side, for different clock frequencies. The staggering quantified in this experiment proved to be acceptable for welding. The relationship between the welding velocity (v – mm/s) and stepping frequency (Hz) is governed by the equation $Hz = 12424v + 2820$.

Frequency (kHz)	*Velocity (mm/s)*	*Maximum deviation (mm)*	*Minimum deviation (mm)*	*Left side standard deviation (mm)*	*Right side standard deviation (mm)*
50	3.784	2.029	-1.655	0.657	0.875
55	4.180	2.517	-1.711	0.865	1.177
60	4.628	2.181	-1.552	0.603	0.731
70	5.403	2.338	-2.361	0.596	0.787
80	6.248	2.507	-1.743	0.782	1.035
90	7.016	2.833	-1.884	0.931	1.173
100	7.799	2.277	-1.630	0.748	0.960

Table 4.2: Deviations from a smoothed traverse movement.

The infrared radiation measured by the thermographic camera not only depends on the temperature of the object under investigation, but is also a function of the surface emissivity. Apart from the radiation emitted from the specimen in consideration, the thermographic camera will also capture any reflected radiation, generated from the surrounding. The infrared radiation, will also be influenced by the absorption of the atmosphere. Thus when measuring temperatures using thermography it is essential to quantify:

- The emissivity of the specimen
- The ambient temperature
- The distance between the specimen and the thermographic camera
- The relative humidity.

While the latter two will determine the absorption of infrared radiation by the atmosphere, the emissivity and ambient temperature will establish the actual temperature of the specimen.

The camera is equipped with two lenses, a 45° lens, for far-field examination and a 24° lens for more close-up imaging, both of which are made up from germanium material. Germanium is transparent to infrared radiation and is difficult to machine. This gives rise to lens aberrations, such that a plane image will not be viewed as a plane rectangular image, but a distorted curved image. In so doing, the relative distance between two specific points, cannot be easily quantified. This section deals with compensation methods for spatial and thermal calibration of thermographic images, through an emissivity calibration factor and a programming methodology that removes effects due to lens aberrations [4.14].

4.5.1 Thermal radiation and emissivity

Thermal radiation is the radiant energy emitted by a medium by virtue of its temperature. The perfect radiator, referred to as a blackbody, is one that emits and

absorbs the maximum amount of radiation at any given wavelength [4.15], [4.17]. According to Planck's law, an ideal radiator at a temperature T emits radiation at a wavelength λ according to the relationship given in equation 4.1.

$$E_{b\lambda}(T) = \frac{C_1}{\lambda_w^{\,5}\left(e^{C_2/\lambda_w T} - 1\right)} \qquad \textit{Equation 4.1}$$

By integrating Planck's formula from $\lambda_w = 0$ and $\lambda_w = \infty$ we obtain the total radiant emittance E_b of a blackbody. This is known as the Stefan-Boltzmann formula and is given in equation 4.2.

$$E_b = \sigma_{sb} T^4 \qquad \textit{Equation 4.2}$$

The above equations apply to blackbody specimens. Real objects never attain blackbody properties, but a fraction, α_a, of the incident radiation may be absorbed, a fraction ρ_r may be reflected and a fraction τ_t may be transmitted, where $\alpha_a + \rho_r + \tau_t = 1$. These materials are referred to as grey bodies. In opaque materials the transmittance τ_t is equal to zero and hence the relationship reduces to $\alpha_a + \rho_r = 1$. From Kirchoff's law the amount of radiant energy absorbed must be equal to the emitted radiation, which is quantified via the emissivity. Hence the emissivity of a material is a measure of how much radiation is emitted from the object, when compared with a perfect blackbody at the same temperature.

The emissivity of a material is highly dependent on the surface conditions of the material. Generally, highly polished surfaces have a low emissivity, while oxdized or painted surfaces exhibit a higher emissivity [4.17]. Also, as a general rule the emissivity of metals is low, while that of non-metals tends to be high [4.17]. Note that emissivity is also a function of temperature, whereby it increases with an increase in temperature for metallic materials and conversely decreases with an increase in temperature for non-metals [4.17]. It should be pointed out that, while grey surfaces radiate a constant fraction of the blackbody radiant energy over the entire spectrum, in real surfaces the emissivity is also a function of the wavelength.

Due to the number of dependent variants, an experiment had to be devised, to quantify the emissivity of the specimens under investigation. This was performed within the spectral range of the thermographic camera and at temperatures ranging from 25°C to 500°C. Higher temperatures were not considered due to the complexity and errors associated with the experiment.

4.5.2 Experimental set-up for the measurement of emissivity

The surface conditions of the plates affects the emittance of the specimen substantially. Hence, for consistent emissivity, all the plates were shot blasted and spray painted with a zinc silicate primer, prior to welding. Shot blasting was performed using a steel grit of particle size 0.6 – 1.0 mm, while the coating was made up of a grey Interplate 937 Nippe Cermao – zinc silicate shop primer, being made up of two parts i.e. ZnO in a silicate binder. The primer is typically used in ship building companies and does not interfere with welding and cutting operations. It is also resistant to damage caused by splatter and, most of all, prevents the formation of oxides. Typical emissivities of ZnO in silicate binders range from 0.7 to 0.96. It is unknown what the silicate binder, chemical composition is, but for a ZnO in K_2SiO_3 binder the emissivity within the whole spectral range according to [4.16], is given in Table 4.3.

Temperature in °C	*Emissivity*
22	0.929
205	0.926
373	0.889
537	0.826

Table 4.3: Emissivity of ZnO in K_2SiO_3 binder at various temperatures [4.16]

The emissivity was measured via a thermocouple array attached at various positions on a heated, shot blasted, primed fin. Figure 4.9 shows the experimental set-up while Figure 4.10 shows the positions of the thermocouples and spot points where thermographic readings were recorded. The fin was heated by means of an oxy-acetylene torch, until a steady state condition prevailed. Synchronous temperature

readings, from the thermocouples and the thermal camera, were taken at various instances during the steady and cooling phase. By assuming symmetry in the temperature profiles, the temperature readings from the thermographic camera at positions shown in Figure 4.10 would relate to the thermocouple readings. These readings, thermocouple readings and ambient temperature were used to determine the emissivity calibration factor at different temperatures. The procedure to achieve this is described below.

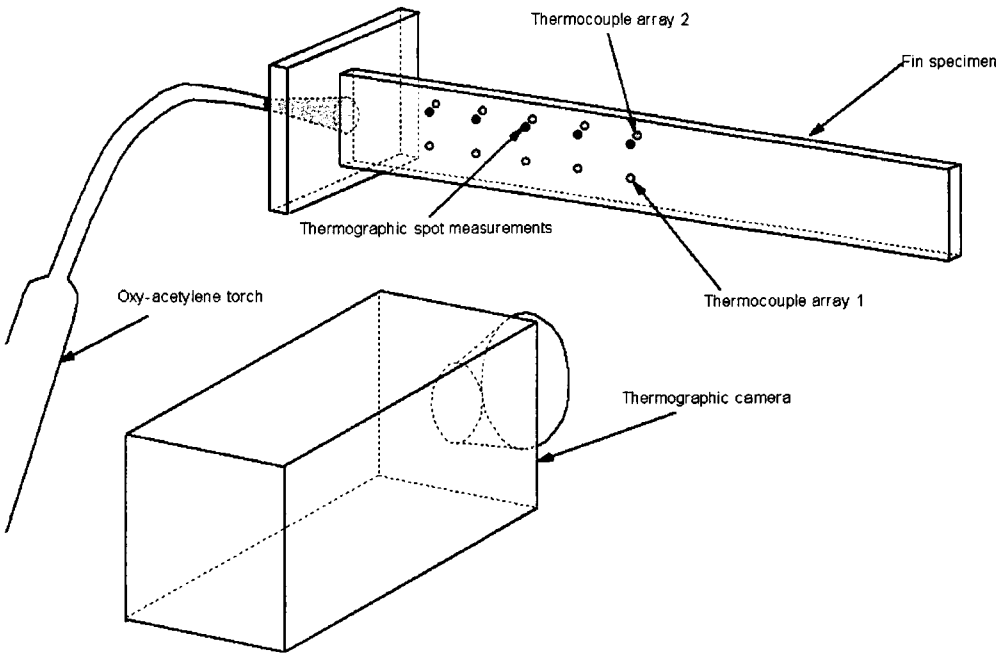

Figure 4.9: Experimental set-up for the determination of emissivity[4.14]

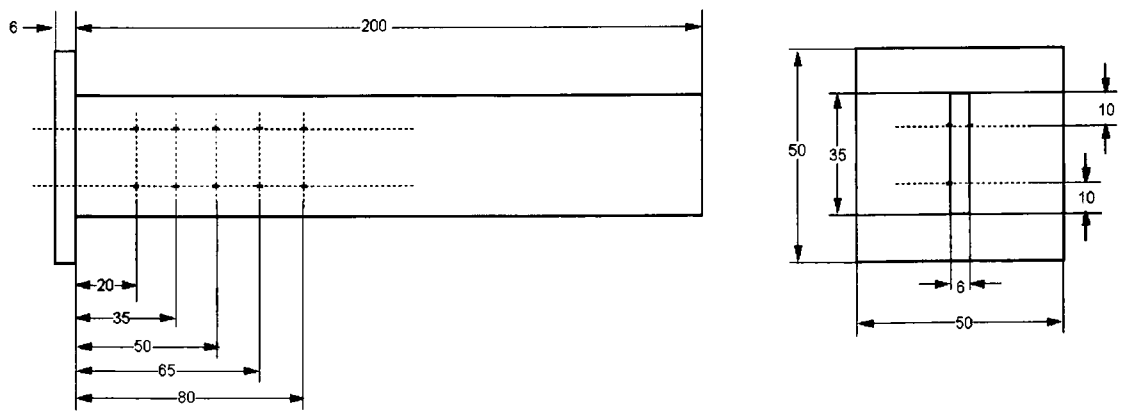

Figure 4.10: Geometry of fin specimen and temperature reading points[4.14]

The thermographic camera measures the radiant energy hence a relationship between the radiant energy and the actual specimen temperature exists, equation 4.3. The following simplifications and assumptions were made:

- The primer was assumed to be opaque to infra red radiation and the absorptivity is equal to the emissivity
- Any background radiation reflected by the specimen was assumed to develop from a blackbody.

$$E_r = \varepsilon_c \sigma_{sb} T_s^{\,4} + (1-\varepsilon_c)\sigma_{sb} T_a^{\,4} \qquad \textit{Equation 4.3}$$

By setting the camera reading to an emissivity of 1 and performing an energy balance between the radiant energy captured by the camera and the actual radiant energy, equation 4.4 prevails.

$$\sigma_{sb} T_c^{\,4} = \varepsilon_c \sigma_{sb} T_s^{\,4} + (1-\varepsilon_c)\sigma_{sb} T_a^{\,4} \qquad \textit{Equation 4.4}$$

Rearranging a relationship between the emissivity and the thermographic, specimen and ambient temperature results in equation 4.5.

$$\varepsilon_c = \frac{T_c^4 - T_a^4}{T_s^4 - T_a^4} \qquad \textit{Equation 4.5}$$

Note that the above relationship will yield the emissivity of the specimen over the whole spectral range, provided the camera measures the radiation emitted by the test specimen through the whole electromagnetic spectrum. The thermographic camera used in this study will measure radiation at wavelengths ranging from 7.5 and 13 μm and hence a radiant energy balance following equation 4.6 will establish the actual emmisivity of the test specimen in the spectral range of the camera, while equation 4.5 gives an emissivity calibration factor.

$$\varepsilon_s\left(\int_{7.5x10^{-6}}^{13x10^{-6}} E_{b\lambda}(T_s)d\lambda_w\right) + (1-\varepsilon_s)\left(\int_{7.5x10^{-6}}^{13x10^{-6}} E_{b\lambda}(T_a)d\lambda_w\right) = E_r = \left(\int_{7.5x10^{-6}}^{13x10^{-6}} E_{b\lambda}(T_c)d\lambda_w\right)$$

Equation 4.6

4.5.3 Emissivity results

Emissivity readings were conducted for the temperature range of 25 - 500°C. The thermal gradients above 500°C were found to be steep and hence even a slight

displacement of 0.5mm in thermocouple or thermographic spot position would result in measurement errors. The symmetry of the experiment was verified via the reading obtained from the two thermocouple arrays. A divergence in symmetrically opposite readings would imply a non-symmetric heat flow. It was found that thermocouple readings at 10mm, from the origin, showed a divergence of 20°C. On the other hand temperature readings at 20mm or further away, showed a maximum divergence of ± 3°C. Figure 4.11, shows the divergence of the thermocouple readings at various temperatures when measured at 10mm and 20mm. The susceptibility of the thermocouple position and thermographic spot readings required a number of experiments to be performed. The experiment was performed 7 times and thermocouple / thermographic reading were taken every second for approximately 5 minutes.

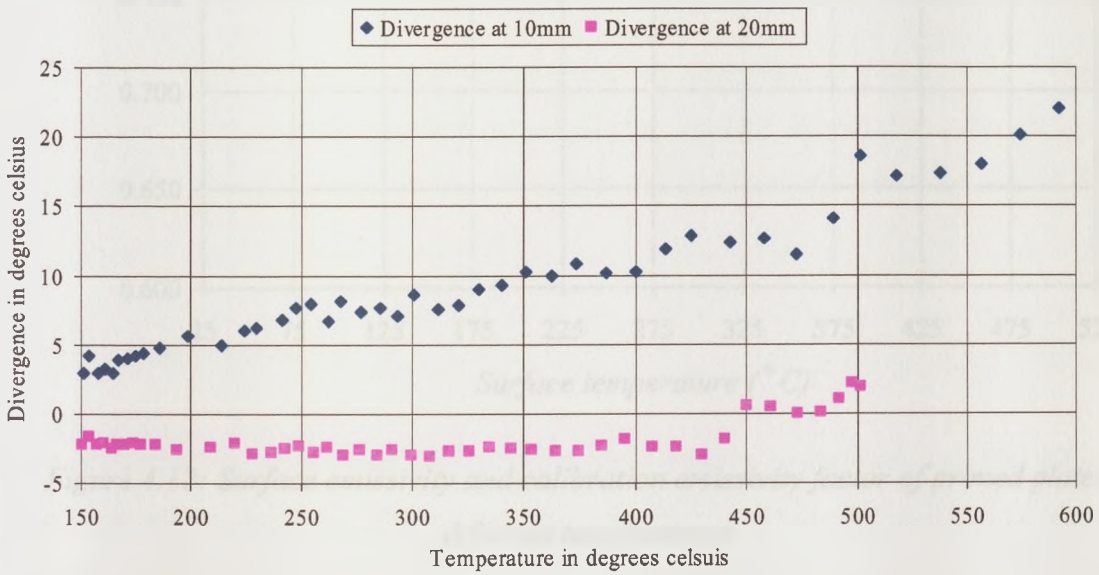

Figure 4.11: Divergence from symmetrically opposite thermocouples

Readings obtained from the 7 experiments were then averaged to obtain specific emissivities at different temperature ranges. Figure 4.12, shows the emissivity of the primer for the camera spectral range and the emissivity calibration factor when using equations 4.6 and 4.5 respectively. The difference between equations 4.5 and 4.6 is small for the temperature range under investigation and for this zinc silicate shop primer. Furthermore any spurious effects such as spectral range will cancel out once one interpolates back to the actual temperature. Hence it is recommended for the

purpose of this study and for simplicity to use an emissivity calibration factor to relate the thermographic temperature to the actual test specimen surface temperature.

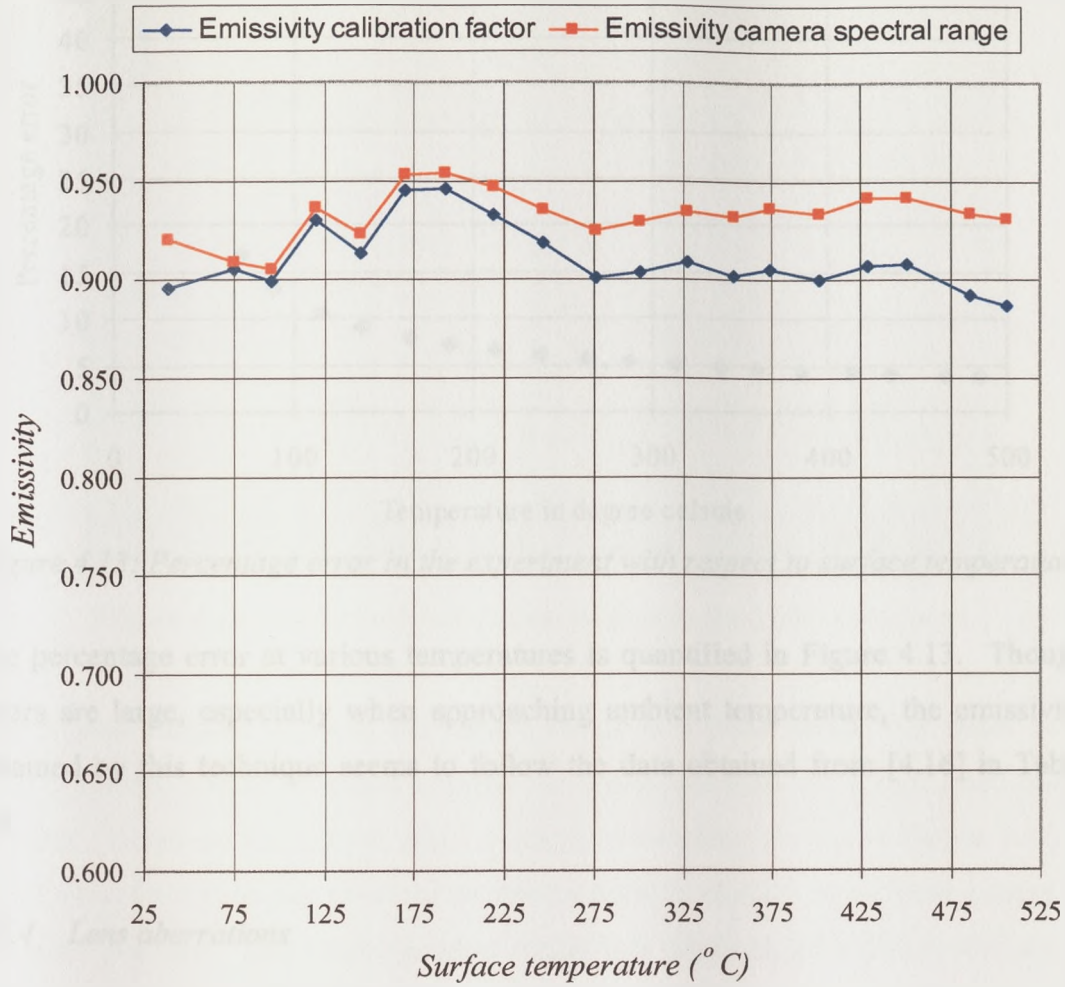

Figure 4.12: Surface emissivity and calibration emissivity factor of primed plate at different temperatures

Apart from the errors resulting in the thermocouple and thermographic position readings, the experiment was also subjected to errors due to the accuracy of both the thermocouples and the camera. The later being, ±1.5°C and ±2°C, respectively. When applying the maximum possible error to equation 4.5, while keeping the ambient temperature constant at 20°C, the experimental error increases exponentially with a decrease in temperature.

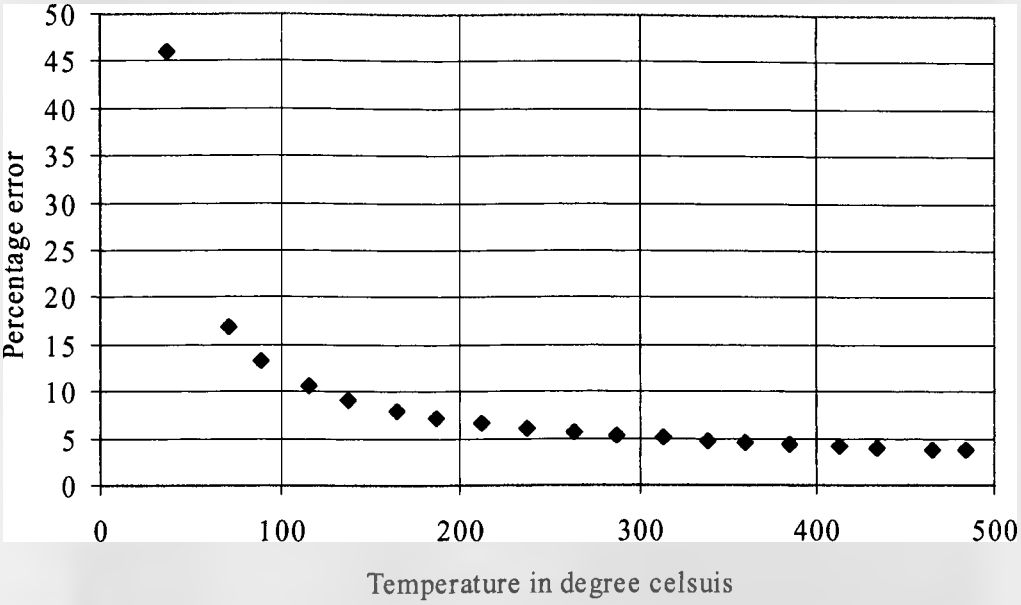

Figure 4.13: Percentage error in the experiment with respect to surface temperature

The percentage error at various temperatures is quantified in Figure 4.13. Though errors are large, especially when approaching ambient temperature, the emissivity obtained by this technique seems to follow the data obtained from [4.16] in Table 4.3.

4.5.4 Lens aberrations

Lens aberrations arise from the different focal lengths associated with the different sections within the lens. This was particularly more evident in the 45° lens whereby a plane rectangular object resulted in a distorted curved image. Figure 4.14, shows the distortion incurred in a rectangular wire mesh when viewed using the 45° lens at a distance of approximately 1m. The image represents a grid of dimensions 550mm x 750mm, the size of each element being 50mm x 50mm. The contrast between the background temperature and the grid was achieved by means of heated nickel chrome wire, equally spaced at fixed distances. The wires were heated by passing a current through them. In so doing the wire would also expand. Hence to make sure that an accurate grid spacing was attained, the wire mesh was kept taut via a series of elastic bands.

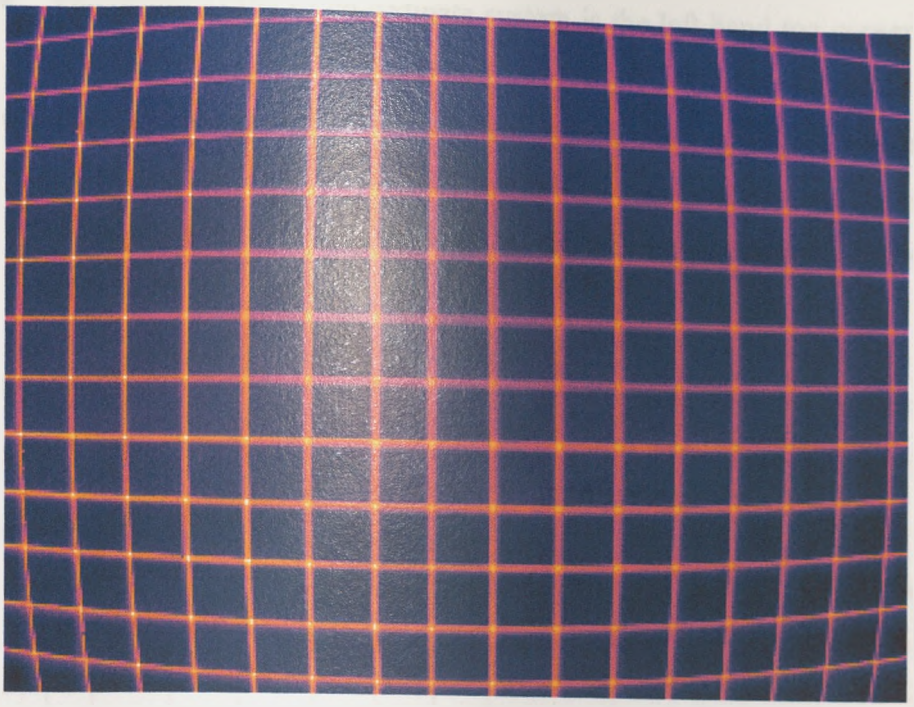

Figure 4.14: Distorted image incurred by a rectangular wire mesh

The method adopted to relate the camera image to a plane image was based on a transformation matrix, obtained through the shape functions of a four node linear element. Based on the known grid / element dimensions, shown in Figure 4.14, a transformation matrix was obtained to relate a point in another co-ordinate system to the pixel position. The thermographic image was made up of a 240 x 320 array, giving a resolution of 0.0026f and 0.0013f for the 45° and 24° lens respectively, with f being the object distance. Hence the temperature at certain points from a specified local co-ordinate, taken to be the origin of the plate under investigation, could be found. This conversion was conducted via a MATLAB program whereby the following conventions, related to Figure 4.15, were taken:

- The i and x co-ordinate axes are parallel to the vertical axis of the image and grid vertical lines respectively.
- The j and y co-ordinate axes are parallel to the horizontal axis of the image and grid horizontal lines respectively.
- The origin of the x - y co-ordinate system is the first grid node at the top left hand corner.

- The origin of the i-j co-ordinate system is the left hand top corner of the pixel array constituting the image.
- The final image is related to another co-ordinate system u-v, whereby the v axis is parallel to the longitudinal axis of the plate, the u axis is parallel to the transverse axis of the plate and the origin is taken to be the position of the welding head.

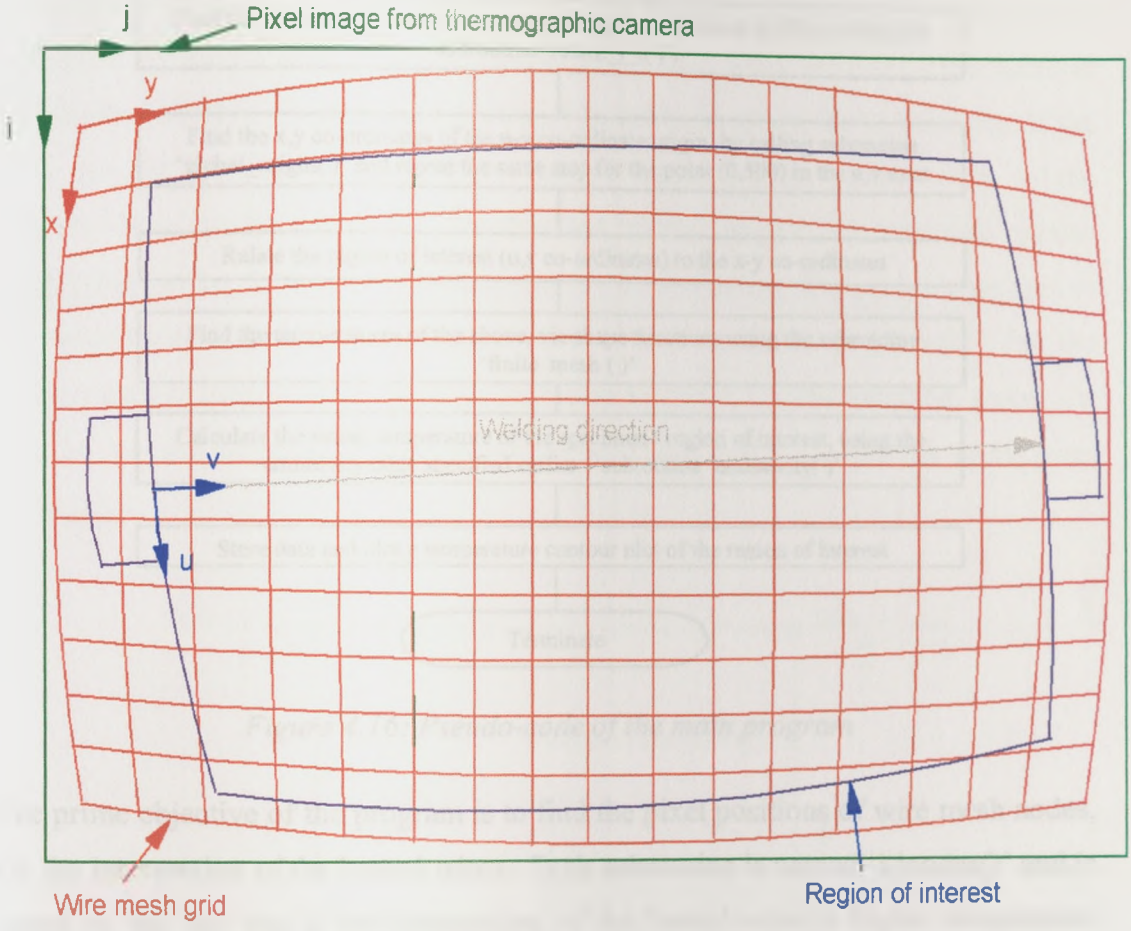

Figure 4.15: Co-ordinates assumed in the program

The program performing the transformation from the u-v to the x-y co-ordiante system and finally to the i-j pixel position is described below in section 4.5.5.

4.5.5 Programming methodology of the camera image transformation

The program consists of a number of subroutines, integrated together in the main program shown in Figure 4.16.

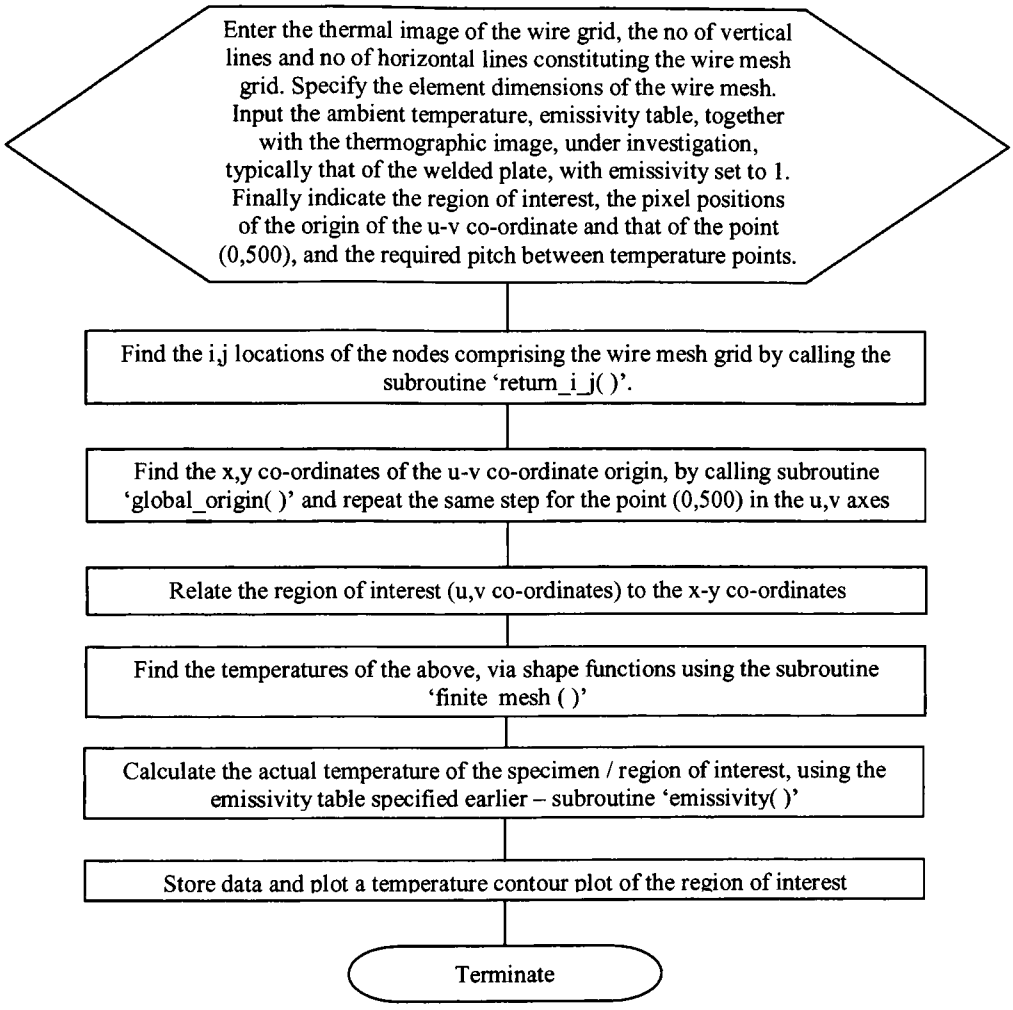

Figure 4.16: Pseudo-code of the main program

The prime objective of the program is to find the pixel positions of wire mesh nodes, i.e. the intersection of the heated wires. Such subroutine is named 'i-jnodes()' and is based on the fact that at the intersection of the heated wires a higher temperature prevails. Each nodal position in the wire mesh grid is assigned five values that include the i, j, x and y location relative to their respective co-ordinates and the temperature ϕ obtained from the thermographic image of the welded plate. The subsequent sub-program, transforms the i-j values of the origin and angular orientation of the u-v co-ordinate system, to the x-y co-ordinate system. The user needs to identify the area of the region of interest and the pitch required between one temperature point and another, in both longitudinal and transverse direction. Both these inputs should be relative to the u-v co-ordinate system. Using this information, the subsequent subroutine 'finite_mesh()' returns a flat undistorted array of the

thermal pattern defining the region of interest. Finally the program goes into another subroutine that finds the actual temperature of the specimen by taking into account the emissivity calibration factor quantified in section 4.5.2.

The following deals with the various subroutines of interest in the transformation program. Starting with the function 'i_jnodes( )', the program divides the thermal image into a number of sub arrays, i.e. the number of horizontal lines (HL) multiplied by the number of vertical lines (VL). Each array assumes dimensions of 240 divided by HL, x 320 divided by VL. For each sub array, the i,j locations of the node having the maximum temperature is found. This would relate to the intersection of the heated wires. The function 'global_origin( )' involves an inverse transformation i.e. from the i-j plane to the x-y co-ordinates. The preliminary part of the subroutine, finds the element associated with the position of interest. For the inverse transformation the convention shown in Figure 4.17, was assumed, where $2a$ and $2b$ are the element dimensions of the wire grid and i_k, j_k are the nodal pixel positions.

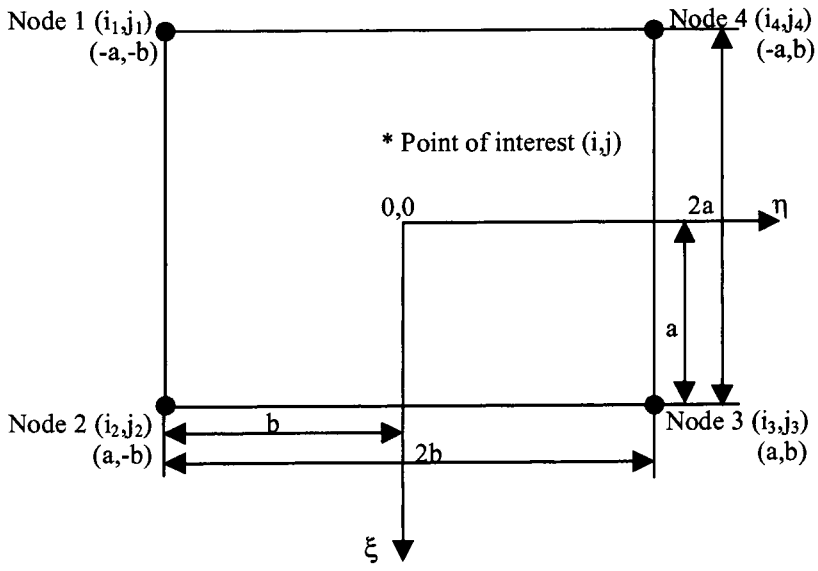

Figure 4.17: Four node linear Lagrangian type element

The shape functions for a four node linear Lagrangian element are given below.

$$N_1 = \frac{(a-\xi)(b-\eta)}{4ab} \qquad N_4 = \frac{(a-\xi)(b+\eta)}{4ab}$$

$$N_2 = \frac{(a+\xi)(b-\eta)}{4ab} \qquad N_3 = \frac{(a+\xi)(b+\eta)}{4ab}$$

Equation 4.7

$$\phi = \sum_{k=1}^{4} N_k \phi_k \qquad \phi = f(i,j)$$

Equation 4.8

Knowing the nodal and point of interest i, j locations and the dimension a, b, equations 4.7 and 4.8 can be used to solve for ξ, η. Considering the i values and substituting equation 4.7 in 4.8 the following relationship exists.

$$4abi = (ab - b\xi - a\eta + \xi\eta)i_1 + (ab + b\xi - a\eta - \xi\eta)i_2$$
$$+ (ab + b\xi + a\eta + \xi\eta)i_3 + (ab - b\xi + a\eta - \xi\eta)i_4$$

Equation 4.9

Rearranging and considering the following constants yields to equation 4.10

$$I_1 = ab(4i - i_1 - i_2 - i_3 - i_4)$$

$$I_2 = b(i_2 + i_3 - i_1 - i_4)$$

$$I_3 = a(i_3 + i_4 - i_1 - i_2)$$

$$I_4 = (i_1 + i_3 - i_2 - i_4)$$

$$I_1 = \xi I_2 + \eta I_3 + \xi\eta I_4$$

Equation 4.10

Similarly considering the j nodes and the following constants yields equation 4.11

$$J_1 = ab(4j - j_1 - j_2 - j_3 - j_4)$$

$$J_2 = b(j_2 + j_3 - j_1 - j_4)$$

$$J_3 = a(j_3 + j_4 - j_1 - j_2)$$

$$J_4 = (j_1 + j_3 - j_2 - j_4)$$

$$J_1 = \xi J_2 + \eta J_3 + \xi\eta J_4$$

Equation 4.11

Combining equations 4.10 and 4.11:

$$\eta = \frac{I_1 - \xi I_2}{I_3 + \xi I_4}$$

Equation 4.12

$$(I_2 J_4 - I_4 J_2)\xi^2 + (I_2 J_3 - I_3 J_2 - I_1 J_4 + I_4 J_1)\xi + (I_3 J_1 - I_1 J_3) = 0$$

Equation 4.13

Solving the quadratic equation 4.13 and equation 4.12 yields ξ,η. The latter stages of this subroutine, converts the isoparametric co-ordinates to the x-y co-ordinate system.

The transformation from the u-v co-ordinate axis to the x-y co-ordinate axis is simply an orientation conversion. It is assumed that both co-ordinates lie in the same plane. On the other hand the transformation from the x-y to the i-j co-ordinates makes use of the linear langragian four node shape functions listed in equation 4.6. The program finds the pixel i-j values of the points of interest, specified within the region of consideration. The subroutine 'finite_mesh( )' makes use of another two functions named 'return_i_j( )' and 'shape_function( )'. The function 'return_i_j( )' finds the i and j values of the nodal position 1 to 4, of the element in question. It then calls the function 'shape_function ( )' which, first converts the x, y co-ordinates of the point of interest into the ξ,η co-ordinates and then makes use of the shape function to calculate its pixel i, j locations. These subroutines are performed for each of the points in consideration, and returns their thermographic reading using the pixel locations, calculated earlier. The actual temperature of the specimen was then calculated via the function 'emissivity( )' via the relationship shown in equation 4.14. Note that the emissivity is a function of temperature and uses a linear interpolation to relate the emissivity calibration factor.

$$T_s = \left(\frac{1}{\varepsilon_c(T_c)} \left[T_c^4 - T_a^4 \right] - T_a^4 \right)^{1/4} \qquad \textit{Equation 4.14}$$

4.6 Use of thermocouples in welding

Welding involves a fairly destructive process, due to the large temperatures generated by the arc. Hot metal splatters are normally dispersed during the process. In this section the effect of splatters on the thermocouples is investigated, and measures to reduce any inherent temperature effects or damage to the thermocouples is investigated.

4.6.1 *Effect of splatters on thermocouples*

The thermocouples used for the measurement of the surface temperatures of the specimens where tack welded onto the surface of the plate at close proximity to the weld line. In so doing the thermocouples were subjected to extra heat derived from the radiation of the arc, together with possible total damage due to splatters. A means of covering the thermocouples from these external influences, was needed. Elimination of external influences due to the arc radiation and splatters could be achieved by tack welding the thermocouple on the opposite side of the arc, that is in butt welding temperature measurements are taken on the bottom surface of the plate. However an essential investigation, required by this research was to quantify any thermal gradients existing within the thickness of the plate. Such investigation required the measuring of the top and bottom surface temperatures at particular positions. The top array was subjected to splatters and a number of possible insulators were investigated to protect the thermocouples from damage caused by splatters. In so doing it was also important that the protective measures would not influence the thermal history recorded by the thermocouples.

Three insulator arrangements were examined, that include a ceramic tube of internal diameter 0.7mm, glass fibre tube of internal diameter 0.7mm and a glass fibre tube of internal diameter 0.4mm. The thermal histories of bare thermocouples and 'protected' thermocouples, tack welded on symmetrically opposite sides of the fin shown in Figure 4.10, were recorded during the heating and cooling cycle. Comparison of the thermal histories will quantify any extra influence due to the insulators. Figure 4.18 shows the thermocouple/ fin configuration.

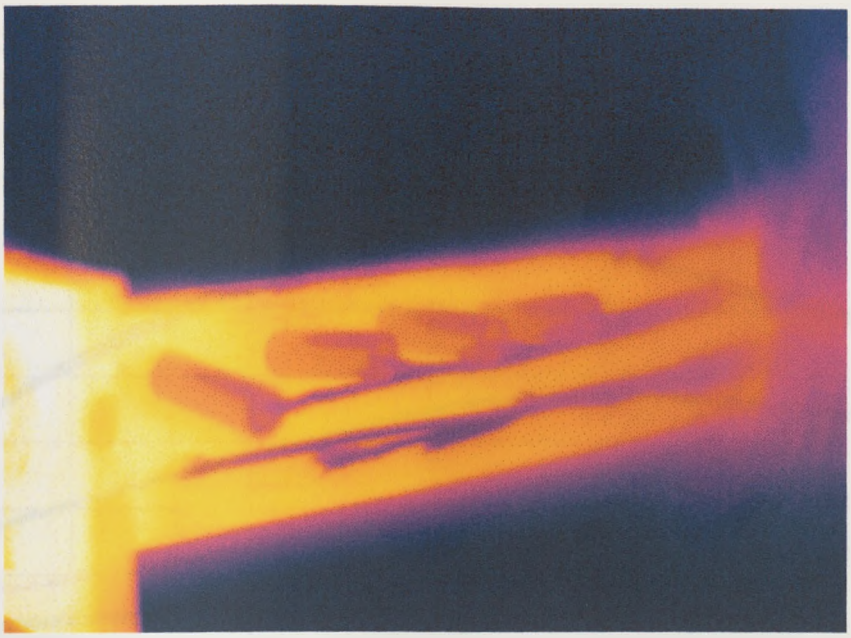

Figure 4.18: Thermographic image of the 'ceramic protected' vs bare thermocouple experimental configuration

Analysis of the results has shown that the use of a ceramic tube had an adverse effect. A maximum difference of 10°C was registered in the maximum temperature reached by both thermocouples, with the bare thermocouple exhibiting a higher temperature. It was also noticed that the thermal patterns of opposite thermocouples did not match, suggesting that at some point the ceramic insulator was absorbing or retaining heat during the heating and cooling cycles respectively. A better protective would be one that follows the same thermal history of the steel plates. The use of glass fibre reduces the possibility of air trapped in the tube, and insulation is diminished due to the reduction of material thickness as compared to the ceramic tubes. Though in this case the maximum difference between the maximum temperatures was also in the region of 10°C, the thermal histories followed the same paths. By reducing the internal diameter of the tube, and hence reducing the air trapped, the maximum deviation was reduced to 6°C, while keeping the same thermal profiles, shown in Figure 4.19.

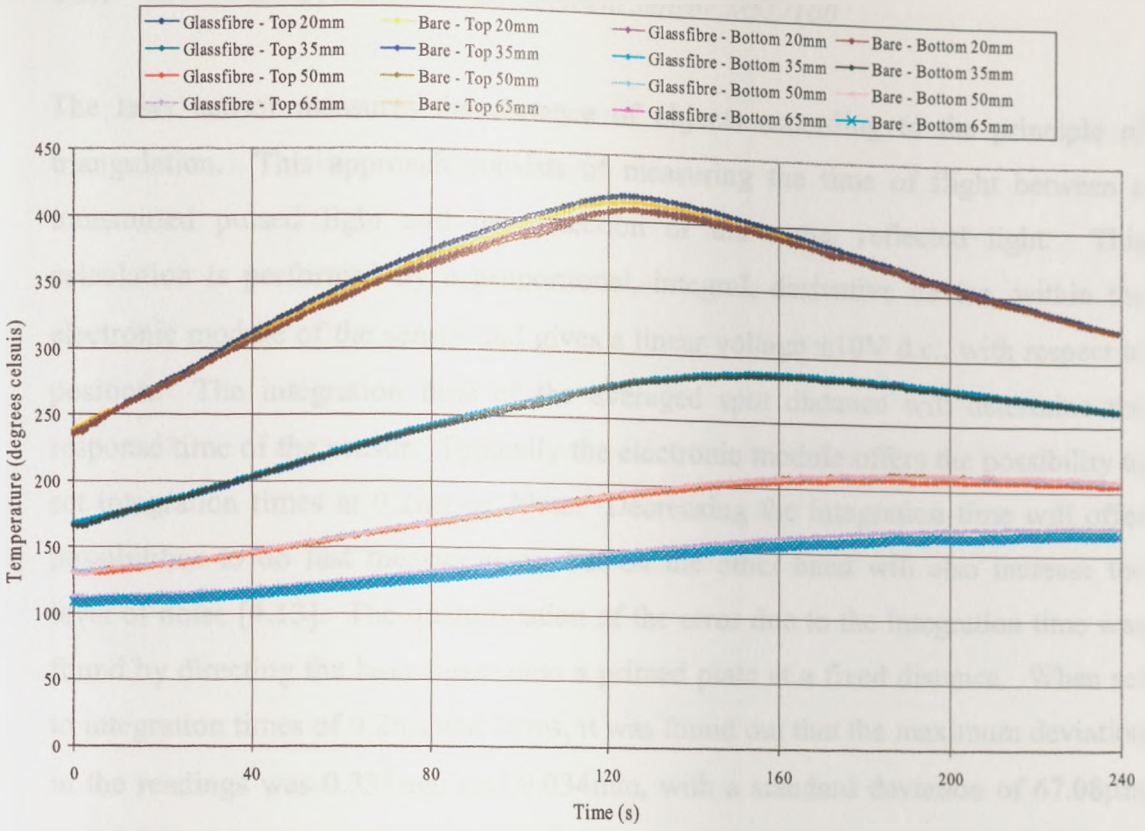

Figure 4.19: Temperature history plots of glass-fibre vs bare thermocouples

4.7 Quantification and reduction of errors of the laser scanning systems

One of the key parameters of the project was the quantification of the out-of-plane deformation. This was measured by means of two laser scanning systems, specifically designed for the investigation of the small and large-scale tests. Both systems where subjected to errors, including:

- Linearity errors
- Noise due to vibration (generated by stepper motors or milling machine)
- Repeatability error
- Electrical noise
- Positional error

This section quantifies the errors involved in both small and large-scale systems and describes methods of reducing them.

4.7.1 Errors due to the laser displacement sensor M5L/100

The laser sensor measures the distance of objects according to the principle of triangulation. This approach consists of measuring the time of flight between a transmitted pulsed light and the detection of the same, reflected light. This calculation is performed by a proportional, integral, derivative device, within the electronic module of the sensor and gives a linear voltage ±10V d.c., with respect to position. The integration time of the averaged spot distance will determine the response time of the sensor. Typically the electronic module offers the possibility to set integration times at 0.2ms or 20ms. Decreasing the integration time will offer possibilities to do fast measurements but on the other hand will also increase the level of noise [4.13]. The quantification of the error due to the integration time was found by directing the laser beam onto a primed plate at a fixed distance. When set to integration times of 0.2ms and 20ms, it was found out that the maximum deviation in the readings was 0.333mm and 0.034mm, with a standard deviation of 67.08μm and 7.10μm, respectively. The strong influence on the reduction of noise with an increase of integration time suggest the use of 20ms integration time, but limits the number of samples recorded per second to 50 samples per second.

Stray light reflected by the specimen under investigation will also be gathered by the position sensor device and will contribute to the final linearization of the displacement/voltage relationship. The laser sensor is adequate for most non-reflective materials. The effect of surface conditions, was investigated by taking measurements in a typical artificial light environment, where the experiments were expected to be performed. The laser diode was directed to a primed non-welded plate and to a welded plate subjected to paint burning due to splatters. While using an integration time of 20ms, the results yielded a maximum deviation of 0.032mm and 0.058mm, with a standard deviation of 5.43μm and 11.34μm for the non-welded and welded plate respectively.

Of particular concern, when dealing with the measurement of the out-of-plane deformation, is the repeatability of the experiment, particularly since the out-of-plane deformation was derived from the subtraction of the initial shape from the final profile of the plate. The repeatability of the experiment was found by scanning a plate of dimensions 500mm x 500mm twice. The difference between the two arrays quantifies the global errors generated during the scanning of the plates. This error also includes any vibration noise generated by the milling machine. The scanning profile of this experiment is shown in Figure 4.20, whereby displacement readings were taken every 10mm in the longitudinal direction and every 70mm in the transverse direction.

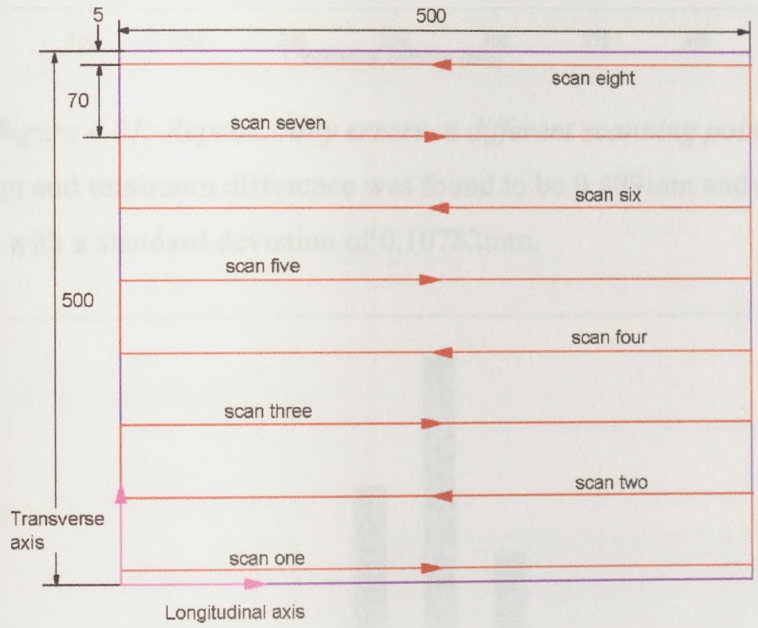

Figure 4.20: Scanning profile used to quantify the repeatability.

The data points obtained at the edge of the plate had a high divergence from the respective results. Such data points were omitted in both the error calculations represented below and in the scanning profile obtained from the test plates. Figure 4.21 shows the representation of the repeatability errors at different scanning points, while a global picture of the error is given in Figure 4.22.

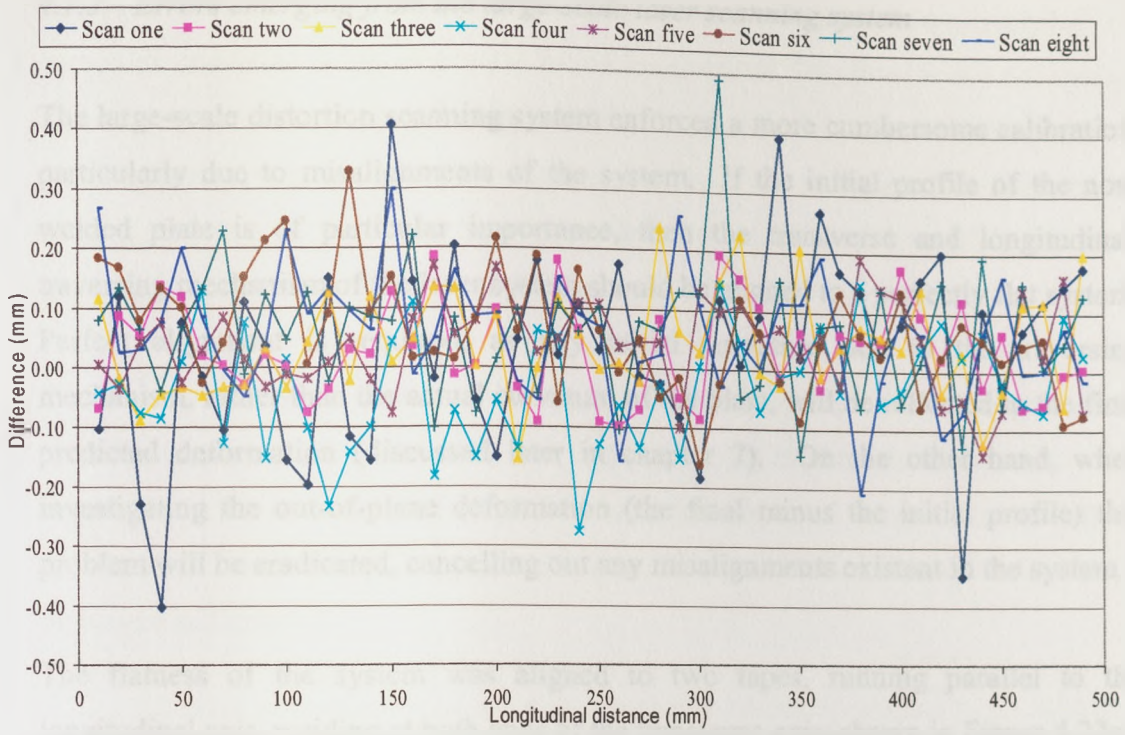

Figure 4.21: Repeatability errors at different scanning points

The maximum and minimum difference was found to be 0.489mm and –0.403mm respectively, with a standard deviation of 0.10782mm.

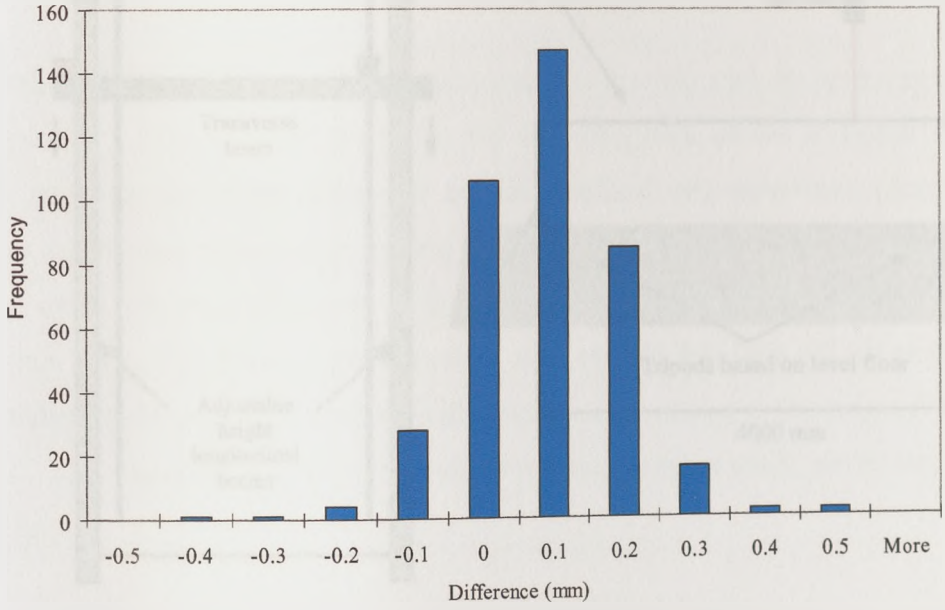

Figure 4.22: Global representation of the repeatability errors

4.7.3 *Errors emerging from the large-scale laser scanning system*

The large-scale distortion scanning system enforced a more cumbersome calibration, particularly due to misalignments of the system. If the initial profile of the non-welded plate is of particular importance, then the transverse and longitudinal, traversing mechanism of the laser system should be aligned to a perfectly flat system. Perfect alignment is required, as any initial curvature due to the traversing mechanism, rather than the actual curvature of the plate, will be reflected in the final predicted deformation (discussed later in chapter 7). On the other hand, when investigating the out-of-plane deformation (the final minus the initial profile) this problem will be eradicated, cancelling out any misalignments existent in the system.

The flatness of the system was aligned to two tapes, running parallel to the longitudinal axis, residing at both ends of the transverse axis, shown in Figure 4.23a.

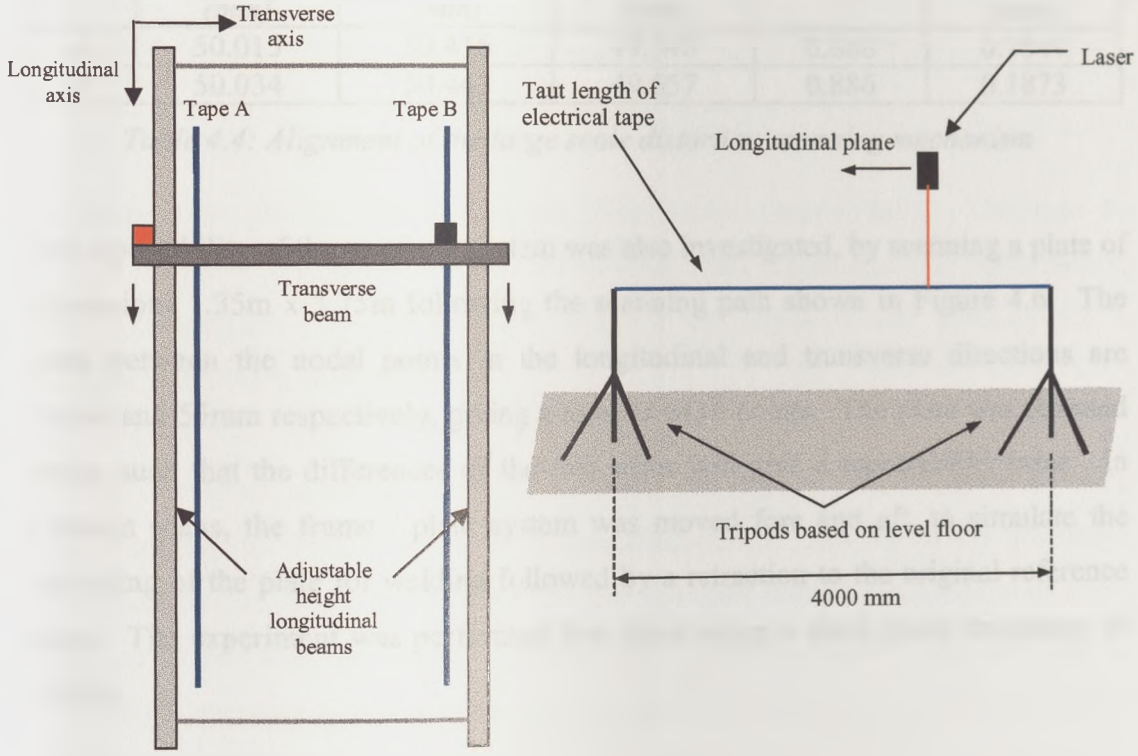

Figure 4.23: Distortion scanning system alignment set-up

The tapes were levelled via a spirit level, and kept taut to prevent any sagging. Of particular relevance is the alignment in the longitudinal direction, hence the system offered a means of adjusting the height of the longitudinal beams. It was assumed that the transverse beam offers no sagging, thus transverse alignment is achieved by making sure that the opposite tapes gave the same readings, while using the same tape/tripod set-up, shown in Figure 4.23b.

The amount of flatness was recorded by looking at the offset voltage/ displacement from the stand off distance of the laser sensor, along the length of the tape. The experiment was run several times until an acceptable level of flatness is achieved, by adjusting the height of the longitudinal beams. The final smoothness of the system is presented in Table 4.4.

Tape	*Average distance (mm)*	*Maximum displacement (mm)*	*Minimum displacement (mm)*	*Range (mm)*	*Standard deviation (mm)*
A	50.015	50.416	49.548	0.868	0.1641
B	50.034	50.443	49.557	0.886	0.1873

Table 4.4: Alignment of the large scale distortion scanning mechanism

The repeatability of the scanning system was also investigated, by scanning a plate of dimensions 1.35m x 3.75m following the scanning path shown in Figure 4.6. The pitch between the nodal points in the longitudinal and transverse directions are 20mm and 55mm respectively, giving a total of 4416 points. The plate was scanned twice, such that the differences of the two scans will give a repeatability error. In between scans, the frame / plate system was moved fore and aft, to simulate the traversing of the plate for welding followed by a retraction to the original reference point. The experiment was performed five times using a clock pulse frequency of 500Hz.

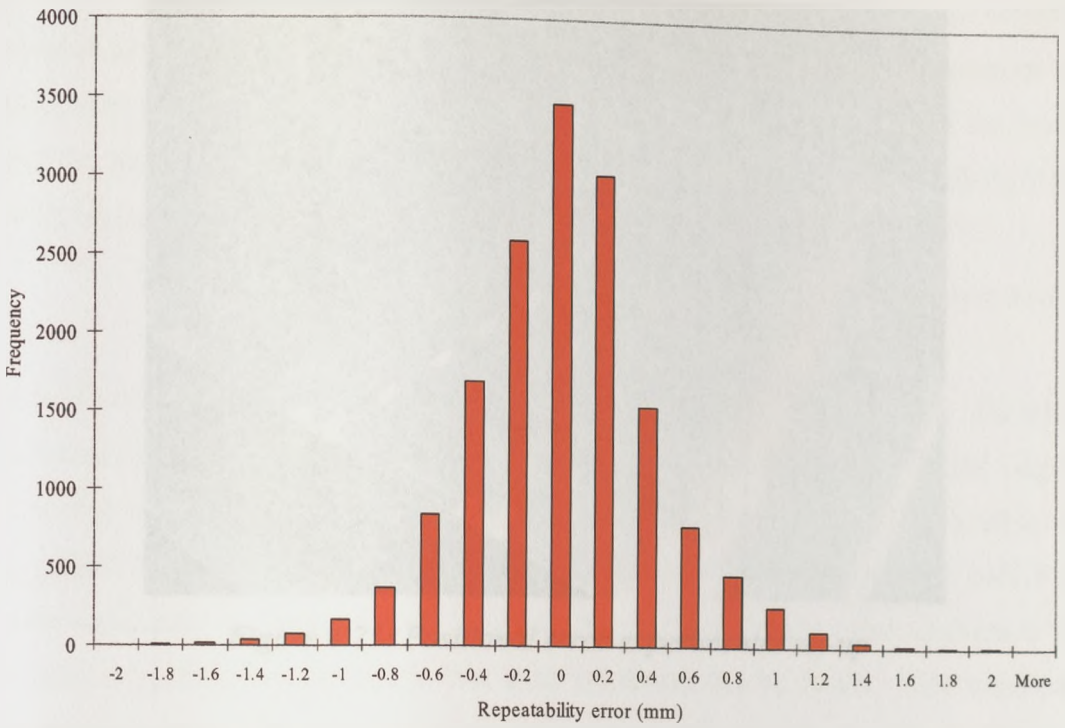

Figure 4.24: Representation of the repeatability error of the large scale distortion scanning configuration

Statistics have shown that the repeatability errors ranged from –1.965mm to 2.348mm, with a standard deviation of 0.424mm. The experiment was performed at slower frequencies. A similar trend was noticed, hence it was decided that a frequency of 500Hz will be used.

Another important aspect in the static distortion measurements is whether the laser was recording the displacements at the specified points. Testing of the positional error was done by means of 58 cubes 7.5mm² and 6mm thick, placed on top of a test plate and in line with the scanning path taken by the laser system. The position of these cubes was known and coincided to a number of nodal positions composing the scanning array. Due to the large difference in displacement these points will emerge from the scanning profile obtained from this test. Figure 4.25 shows the experimental set-up and typical positions of the cubes.

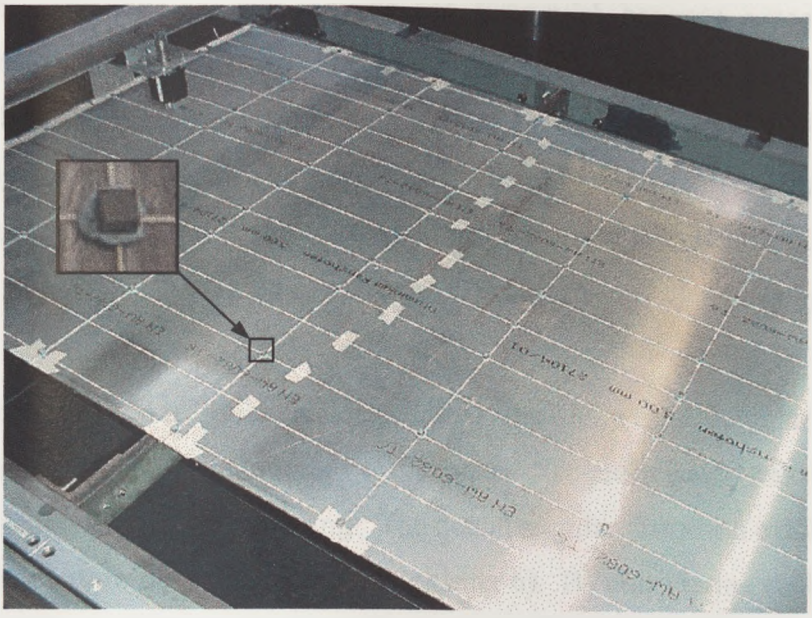

Figure 4.25: Positional error experimental set-up

The results of this test showed that out of the 58 cubes placed on the test plate, 53 were detected, giving an accuracy rate of 91%. The same accuracy was recorded regardless of the frequency. The undetected cubes were at positions relating to the discontinuous slider and rack. These points were subjected to judders in the traversing mechanism.

4.7.4 Representation of the out-of-plane deformation

The versatility of both scanning distortion rigs offers the possibility to obtain a multiple of data points. Averaging these data points provides a means of reducing the errors identified in sections 4.7.2 and 4.7.3, while giving a specific number for representing the out-of-plane deformation. The representation of the out-of-plane deformation has been quantified by various methods. Typically the ship building companies use an I value which quantifies the flatness of the plates. The I value involves a finite difference method that compares the slanted profile of the plate with an assumed flat plate. Two numbers are identified – one representing the longitudinal flatness and the other the transverse flatness, dependent on the frequency of the number of data points defining the plate surface. Other researchers

quantify the out-of-plane deformation via a standard deviation [4.18]. The drawbacks of both representations are that they do not distinguish between a negative and a positive out-of-plane deformation. In this thesis, the out-of-plane deformation was quantified by two numbers, i.e. the longitudinal curvature or flatness of the profile and the angular distortion. The saddle shape predominant in the small-scale test could be easily represented in the form of a function, given in equation 4.14.

$$z = Ax^2 + Bx + Cy^2 + Dy + Exy + F \qquad \textit{Equation 4.14}$$

This function will not yield a longitudinal curvature and angular distortion, independent of the local positions of the plate. Together with this the angular distortion is represented in a gullwing. The actual angular distortion exhibited by the test plates had a definite V shape (refer to chapter 6). By considering each half of the plate separately a function that allocates an average longitudinal curvature and angular distortion, independent of the local positions, can be found. This function is of the form shown in equation 4.15.

$$z = Ax^2 + Bx + Cy + D \qquad \textit{Equation 4.15}$$

The equations given above were fitted to the results using a direct-search algorithm [4.19], to generate a detailed, smooth , out-of-plane deformation profiles. Note that the quadratic function in equation 4.15 defines the longitudinal curvature and the linear function defines the V-shaped angular distortion. Hence by differentiating equation 4.15, twice with respect to x ($\frac{\partial^2 z}{\partial x^2}$) and once with respect to y ($\frac{\partial z}{\partial y}$), two averaged constants defining the longitudinal curvature and angular distortion can be achieved.

The representation of the out-of-plane deformation in the large welding structure, cannot be directly related to a simple function, particularly due to the buckling shapes associated with the different welding configurations. A means of smoothing the errors, while obtaining a differential of the discrete sampled surface deformation, was required. A review of the different conventional and finite element based smoothing methods is given by Comlekci [4.20]. Typical conventional smoothing algorithms make use of Fourier transforms and frequency band passes or averaging

techniques. Finite element based algorithms employ least-square, regression or spline-type analyses and unlike the conventional methods, they offer the possibilities to investigate into more detail specific regions, with a direct relationship to the differentials.

The technique adopted in this thesis, inspired by Feng *et al* [4.21] and adapted by Comlekci *et al* [4.22], involves the minimisation of the Euclidean norm composed of data residuals representing the misfit and second derivatives representing the roughness of the function, to smoothen the experimental data. The finite nodes will also contribute the differential output of the experimental data, whereby differentials with respect to x and y will yield the longitudinal curvature and angular distortion respectively. As opposed to Feng *et al*, Comlekci *et al* [4.20], [4.22], [4.23], used an isoparametric nine node Lagrangian type finite elements, due to the completeness of the cubic polynomial function representing the discretization of the region of interest. The center node not present in the eight-node element, would increase the accuracy of the representation of the data.

The formulation of the minimization of the Euclidean norm, involves an approximate scalar function which behaves more smoothly, but does not agree precisely with the measured values of z. A quadratic positive definite functional $\phi(z)$ is introduced and $\phi(z)$ is minimised using a best approximating function. This relationship is given by:

$$\phi = \phi(z) = \frac{1}{2}\sum_{i=1}^{T} \omega_i [z(x_i.y_i) - z_i]^2 + \frac{\zeta}{2}\int_R \left[\left(\frac{\partial^2 z}{\partial x^2}\right)^2 + 2\left(\frac{\partial^2 z}{\partial x \partial y}\right)^2 + \left(\frac{\partial^2 z}{\partial y^2}\right)^2 \right] dR$$

Equation 4.16

Where

ϕ = quadratic positive definite functional

z = predicted twice-differentiable piecewise function defined in the region of interest R

z_i = measured input value at the i^{th} data point at location x_i, y_i

T = Total number of data points in R

ω_i = weighting parameter of data point

ζ = smoothing parameter

The smoothing parameter will influence the interpolation conditions on the function. As it approaches zero, the predicted smoothing function z will approach the measured values of z_i, giving a pure least square fit of the experimental data. On the other hand the weighting parameter will determine the influence of each data point. This is particularly important when dealing with edge errors. Comlekci *et al* in [4.20] and [4.22], used a weighting parameter in order to reduce the effect of edge errors present in the thermoelastic stress analysis obtained from thermography by applying a low weighting parameter to the data at the edge of each themrographic scan. In the case of the out-of-plane deformation every point had the same contribution to the discretization.

Starting from the scalar and shape functions, equation 4.17, of the nine-node element shown in Figure 4.26, their first order and second order derivatives are required.

$$N(\xi,\eta) = a_1 + a_2\xi + a_3\eta + a_4\xi^2 + a_5\xi\eta + a_6\eta^2 + a_7\xi\eta^2 + a_8\xi^2\eta + a_9\xi^2\eta^2$$

$$N_1 = \frac{(\xi^2\eta^2 - \xi^2\eta - \xi\eta^2 + \xi\eta)}{4} \qquad N_2 = \frac{(\xi^2\eta^2 - \xi^2\eta + \xi\eta^2 - \xi\eta)}{4}$$

$$N_3 = \frac{(\xi^2\eta^2 - \xi^2\eta + \xi\eta^2 - \xi\eta)}{4} \qquad N_4 = \frac{(\xi^2\eta^2 + \xi^2\eta - \xi\eta^2 - \xi\eta)}{4}$$

$$N_5 = \frac{(-\xi^2\eta^2 + \xi^2\eta + \eta^2 - \eta)}{2} \qquad N_6 = \frac{(-\xi^2\eta^2 - \xi^2\eta + \xi^2 + \xi)}{2}$$

$$N_7 = \frac{(-\xi^2\eta^2 - \xi^2\eta + \eta^2 + \eta)}{2} \qquad N_8 = \frac{(-\xi^2\eta^2 + \xi^2\eta + \xi^2 - \xi)}{2}$$

$$N_9 = \xi^2\eta^2 - \xi^2 - \eta^2 + 1$$

Equation 4.17

If $[N]=[N_1 \quad N_2 \quad \ldots \quad N_9]$ then the global co-ordinates within the element are defined as:

$$x=[N]\{C_x\} \text{ and } y=[N]\{C_y\} \qquad \textit{Equation 4.18}$$

where the nodal co-ordinate vectors of the elements are:

$$\{C_x\}=[x_1 \quad x_2 \quad \ldots \quad x_9]^T \text{ and } \{C_y\}=[y_1 \quad y_2 \quad \ldots \quad y_9]^T \qquad \textit{Equation 4.19}$$

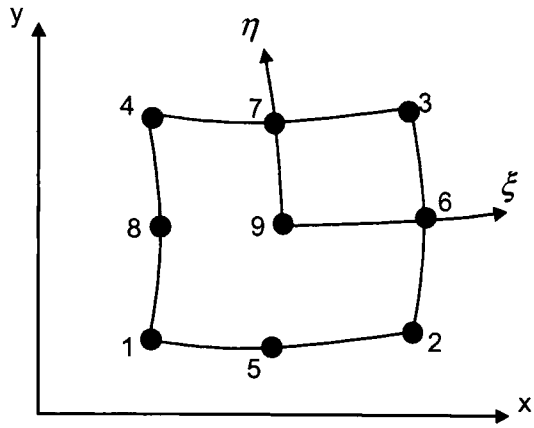

Figure 4.26: Nine-node Langrangian type element

The scalar function within the element is defined as $z=[N]\{z_e\}$ where $\{z_e\}=[z_1 \quad z_2 \quad \ldots \quad z_9]^T$ represents the vector for unknown nodal values. By minimising the quadratic function (equation 4.16) with respect to the unknown nodal values, equation 4.20 prevails.

$$\left\{\frac{\partial\phi(z)}{\partial z}\right\}=0 \qquad \textit{Equation 4.20}$$

Expanding equation 4.20 and using the global co-ordinates, results in the relationship shown below.

$$\sum_{j=1}^{M}\left[\begin{array}{c}\sum_{i=1}^{J}\left[\omega_i\left\{[N(\xi_i,\eta_i)]_j^T[N(\xi_i,\eta_i)]_j\{z_e\}_j-[N(\xi_i,\eta_i)]_j^T z_i\right\}\right] \\ + \\ \zeta\int_{R_j}\left\{\left[\frac{\partial^2 N}{\partial x^2}\right]_j^T\left[\frac{\partial^2 N}{\partial x^2}\right]_j+2\left[\frac{\partial^2 N}{\partial x\partial y}\right]_j^T\left[\frac{\partial^2 N}{\partial x\partial y}\right]_j+\left[\frac{\partial^2 N}{\partial y^2}\right]_j^T\left[\frac{\partial^2 N}{\partial y^2}\right]_j\right\}dR\{z_e\}_j\end{array}\right]=0$$

Equation 4.21

where

M = number of finite elements in region R

J = number of input data points in element j

ξ_i, η_i = local isoparametric co-ordinates of input data point i

Equation 4.21 can be simplified in the form of

$$\sum_{j=1}^{M}[k]_j\{z_e\}_j = \sum_{j=1}^{M}\{p\}_j \qquad \textit{Equation 4.22}$$

where,

$$[k]_j = \sum_{i=1}^{J}\left[\omega_i[N(\xi_i,\eta_i)]_j^T[N(\xi_i,\eta_i)]_j\right] + \zeta\int_{R_j}\left\{\left[\frac{\partial^2 N}{\partial x^2}\right]_j^T\left[\frac{\partial^2 N}{\partial x^2}\right]_j + 2\left[\frac{\partial^2 N}{\partial x\partial y}\right]_j^T\left[\frac{\partial^2 N}{\partial x\partial y}\right]_j + \left[\frac{\partial^2 N}{\partial y^2}\right]_j^T\left[\frac{\partial^2 N}{\partial y^2}\right]_j\right\}dR$$

and

$$\{p\}_j = \sum_{i=1}^{J}\omega_i[N(\xi_i,\eta_i)]_j^T z_i \,.$$

The assembly of the contributions of each element gives the equation 4.23, where $[K]$ is a pseudo-stiffness matrix and $[P]$ is the pseudo-load.

$$[K]\{\sigma\} = [P] \qquad \textit{Equation 4.23}$$

Equation 4.23 was solved via a finite element solver and yielded the nodal unknowns. The derivatives of the scalar function are then evaluated and averaged at the nodes, such that $\frac{\partial^2 z}{\partial x^2}$ will give the longitudinal curvatures and $\tan^{-1}\frac{\partial z}{\partial y}$ will give the angular distortion. The relationship between the cartesian co-ordinate system with the isoparametric co-ordinates is obtained via two jacobian matrices, both making use of a number of chain rule derivatives.

It should be pointed out that the smoothing program, developed by Comlekci in [4.20] was used in the representation of the out-of-plane deformation. Further development of the program was beyond the scope of this project, but the program was essential for a good comparison between the experimental and computational results, when dealing with the large-scale welded structures.

The effectiveness of this smoothing algorithm depends on the number of elements, smoothing parameter and amount of data points used. Thus before using the algorithm the performance, needs to be quantified. Comlecki in [4.20] investigated the smoothness obtained by applying a random noise to a known thermoelastic stress analysis. The performance of the finite element smoothing method, when applied to the out-of-plane deformation was investigated by Comlekci *et al* in [4.23]. In this case a numerical test, consisting of a typical out-of-plane deformation (that of a saddle shape), with added computer generated random noise was analyzed using different smoothing parameters and different number of sample points per finite element. The random noise followed a normal distribution with a standard deviation of 0.1mm. Table 4.5 compares the out-of-plane distortion, angular distortion and longitudinal curvature, of a particular point using different configurations. It was concluded that the number of samples per finite element has a large significance in the final values. A small smoothing parameter and a large number of data points, gives better results for the derivatives. A compromise between the number of data points captured by the distortion scanning rig and the accuracy of the finite element based smoothing algorithm will have to be established.

Number (size mm) of elements	Average samples per element	Out-of-plane deformation z (mm)	Angular distortion $\tan^{-1}\frac{\partial z}{\partial y}$ (°)	Longitudinal curvature $\frac{\partial^2 z}{\partial x^2}$ (mm^{-1})
2x2 (250x250)	200	4.392	2.159	-1.561×10^{-4}
4x4 (125x125)	50	4.410	2.213	-1.743×10^{-4}
6x6 (83.3x83.3)	22	4.353	2.000	-3.352×10^{-4}
Exact value of distortion:		4.488	2.250	-1.424×10^{-4}

Table 4.5: Numerical test results for finite element smoothing of distortion ($\zeta = 0$)

4.8 Discussions

This chapter dealt with the experimental rigs constructed for the data capturing of thermal transients and static / transient out-of-plane deformations. An overview of the equipment used, including the accuracy obtained by each apparatus, is presented. The integration of each of them provided a means of automatic data capturing. The latter sections in this chapter lays emphasis on the methods adopted to reduce and counteract any possible errors. Typically a program that adjusts lens aberration is described. Together with this, a smoothing algorithm, that not only reduces errors associated with the distortion scanning systems but also provides a means of representing the out-of-plane deformations, was described. The combination of these systems and programs were later on used in both the pilot programme and the large scale welding tests, presented in the following chapters.

4.9 *References*

[4.1] Lindgren,L.E., 'Finite Element Modeling and Simulation of Welding Part 3: Efficiency and Integration', *Journal of Thermal Stresses,* Vol.24, No.4, pp269-275, 2001.

[4.2] Lindgren,L.E., 'Finite Element Modeling and Simulation of Welding Part 1: Increased Complexity', *Journal of Thermal Stresses,* Vol.24, No.4, pp141-192, 2001.

[4.3] Michaleris,P. and DeBiccarri,A., 'A Predictive Technique for Buckling Analysis of Thin Section Panels Due to Welding', *Journal of Ship Production,* Vol. 12, No.4, pp269-275, 1996.

[4.4] Tsai,C.L., Park,S.C. and Cheng,W.T., 'Welding Distortion of a Thin-Plate Panel Structure,' *Welding Journal,* Vol. 78, No.5, pp156s-165s, 1999.

[4.5] Haung,T.D., Dong,P., DeCan,L.A, Harwig,D.D., 'Residual Stresses and Distortions in Lightweight Ship Panel Structures, Northrop Grumman,' *Technology Review Journal,* Vol. 11, No.1, pp1-26, 2003.

[4.6] Suresh,S. and Dattrajan,H., 'An Experimental Study of Angular Distortions In Welded Structures,' *WRI keywords (Welding Research Inst. Tiruchirapalls, India),* Vol.8, Pt.1, pp7-14, 1987.

[4.7] Parmar,R.S. and Arya,S.K., 'Studies on Angular Distortion of Butt Welds in Flux Cored Arc Welding,' *Journal of the Institution of Engineers (India), Part Pr: Production Eng. Division,* Vol. 69, Pt 3, pp65-71, 1989.

[4.8] Corus UK limited, 'Inspection Certificate'.

[4.9] 'Labfacility Temperature Hanbook,' Apollo Press, Worthing ,U.K., 1996.

[4.10] FLIR systems, 'ThermaCAM™SC500 Operator's Manual,' FLIR Systems AB, Publ. No. 1 557 491 – Rev.B. 2001.

[4.11] Cheng,W., Dydo,J.R., Feng,Z., Chen,Y. and Cromptom,J.S., 'Finite Element Modeling of Angular Distortion in Stiffened Thin-Section Panels,' Proceedings of the Ninth International Conference on Computer Technology in Welding, No.949, pp120-129, 2000.

[4.12] Masubuchi,K., DeBiccari,A. and Cook,W.J.C, 'Non-Contact Measurement of Out-of-Plane Distortion as a Means For Controlling Distortion in Welded Structures,' *Advances in Welding Science and Technology - TWR '86: Proceedings of an International Conference on Trends in Welding Research,* pp529-532, 1986.

[4.13] MEL Mikroelektronik, 'Precise Optical Measurement –Measuring Sytems M5,' Operating Manual, 2001.

[4.14] Camilleri,D., Comlekci, T. and Gray, T.G.F., 'Use of thermography to calibrate fusion welding procedures in virtual fabrication applications,' *Proccedings of Inframation 2004 Conference,* Vol. 5, pp. 121-131, 2004.

[4.15] Chapman,A.J., 'Fundamentals of Heat Transfer', *Collier Macmillan, London,* 1987.

[4.16] Touloukian,Y.S.M., 'Thermophysical Properties of Matter,' *Plenum Press,* Vol. 7-9, 1970.

[4.17] Holman,J.P., 'Heat Transfer,' *McGraw-Hill inc. 8th Edition,* 1997.

[4.18] Lightfoot,M., 'Prediction of Distortion Control and Techniques to avoid Rework,' *A Report on the General Causes of Fabricated Steel Plate Distortion, School of Marine Science and Technology, University of Newcastle Upon Tyne,* 2003.

[4.19] Hooke,R. and Jeeves,T.A., 'Direct Search Solution of Numerical and Statistical Problems,' *Journal of the ACM,* Vol.8, pp 212-229, 1961.

[4.20] Comlekci,T., 'Development of Hybrid Experimental-Numerical Methods for Thermoelastic Stress Analysis,' *PhD Thesis, Mechanical Engineering Department, University of Strathclyde,* 1996.

[4.21] Feng,Z. and Rowlands, R.E., 'Continuous Full-Field Reperesentation and Differentiation of Three Dimensional Experimental Vector Data,' *Computers and Structures,* Vol.26, No.6, pp. 979-990, 1987.

[4.22] Comlekci,T. and Boyle,J.T., 'Finite Element Smoothing of Experimental Thermographc Data on Arbitrary Two-Dimensional Regions,' *Proc. Computational Mechanics in UK, Manchester,*1994.

[4.23] Comlekci,T., Camilleri,D. and Gray, T.G.F., 'Finite Element Representation of Experimental Surface Deformation Data from Fusion Welded Plates,' Proceedings of the 11th Annual Conference of the Association for Computational Mechanics in Engineering, UK, Glasgow, pp. 33-36, 2003.

CHAPTER FIVE

CHAPTER 5

INVESTIGATION OF WELDING INDUCED THERMAL TRANSIENTS

5.1 Introduction

The first critical step in the uncoupled strategy adopted in this thesis, is to establish accurate knowledge of the transient temperature distributions caused by a given weld process and procedure in the geometry of interest. The effectiveness of the final thermo-elasto-plastic analyses and other simplified methods depends critically on the thermal input stage, where the complex effects of variable arc energy transfer, non-linear material properties and work-piece/fixture heat-sink variables are present in a practical case. Hence, this chapter investigates various models for the thermal stage of welding in an uncoupled computational strategy and sets out to find computationally economic and robust thermal finite element or analytical solutions providing sufficient data for the 'Mismatched Thermal Strain' algorithm. Of particular importance in this aspect, are the far field maximum temperatures, defining the yielded and elastic boundaries mentioned in chapter three.

The application of infrared thermography and thermocouple data to the measurement of transient temperature fields generated by fusion welding is significant in this aspect. Particularly, the net heat input is not known and for every geometry and weld prep condition, different process efficiencies are applied for the correlation of the finite element results with the realistic experimental results. Thus the finite element analyses are cross-referenced to pilot tests and large-scale complementary experimental results dealing with butt welding, fillet welding and multiple-stiffener welding, using thermocouple arrays and a thermographic camera to capture data.

5.1.1 *Thermophysical properties of mild steel*

The predominant heat transfer mode in welded steel plates is conduction. Hence it is essential to have a good literature describing the material properties of steel under investigation. The most important parameters in this aspect are the specific heat or enthalpy and the conductivity (thermal diffusivity). Non-linear conduction properties were introduced through standard conductivity and specific heat values obtained from Corus [5.1] and applied to analytical and finite element solutions for temperatures ranging from ambient temperature to 2000°C. These are given in Figure 5.1.

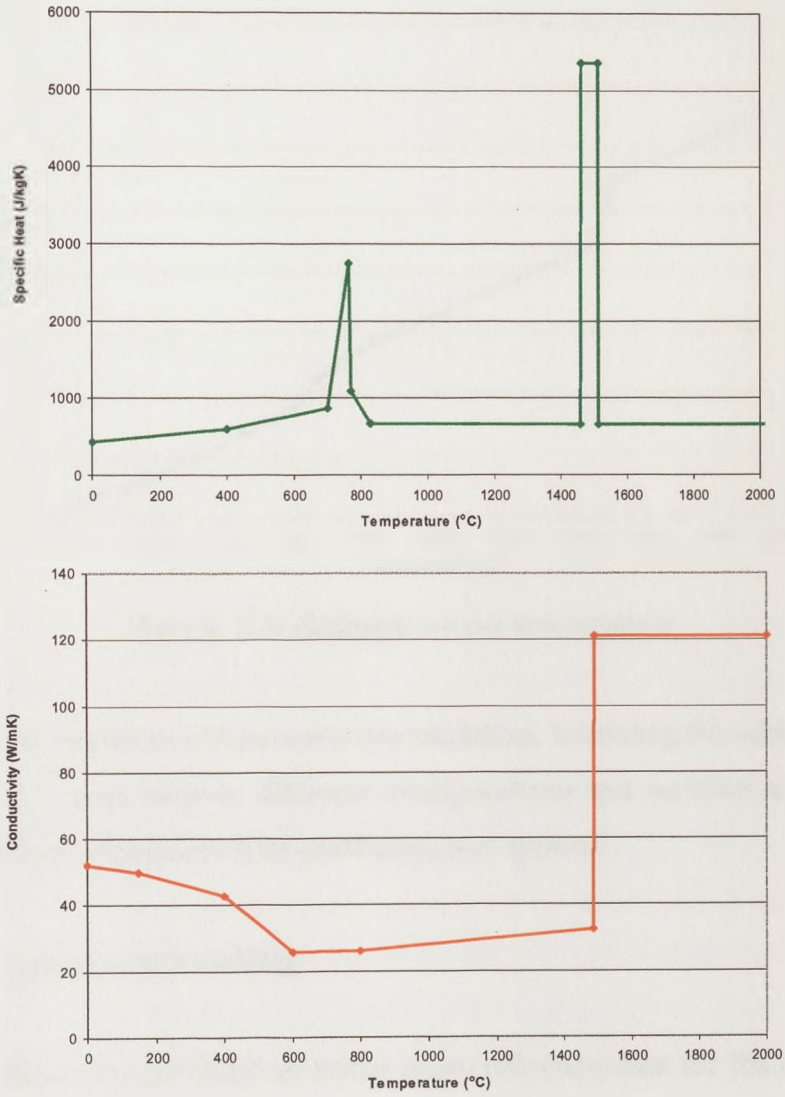

Figure 5.1: a – Specific heat versus temperature, b – Conductivity versus temperature

The step changes in specific heat, associated with phase transformation, give rise to stiff finite element equations, thereby leading to convergence problems. In such cases, Lindgren [5.2] suggests that the heat capacity is specified in terms of enthalpy, following the relationship given in equation 5.1.

$$H_e(T) = \int_0^T \rho c(\tau) d\tau \qquad \textit{Equation 5.1}$$

By assuming that the enthalpy and specific heat are zero at absolute temperature, the conversion from specific heat to enthalpy yields a smoother curve, as shown in Figure 5.2.

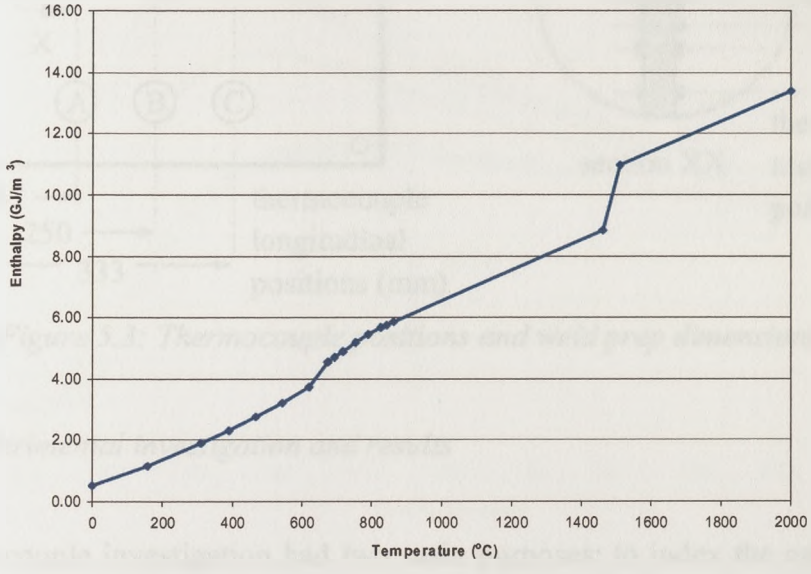

Figure 5.2: Enthalpy versus temperature

Convection and radiation effects were also modelled, following the scheme described in section 2.2.1, such that for different configurations and surfaces a specific non-linear temperature dependant film coefficient was applied.

5.2 Pilot programme butt-welding

The pilot programme provided an initial cross-reference data for the computational and analytical approaches to thermal analysis. Furthermore it provided case material to investigate three-dimensional computational analyses and assess any simplified

methods useful for the computational analysis of the large-scale tests. Test butt welds were carried out on 500mm square x 6mm thick CMn steel plates. The nominal heat input rate was 1.14-1.24 kJ/mm, corresponding to 23V, 250A and 4.8mm/s travel speed. The test details are shown in Figure 5.3.

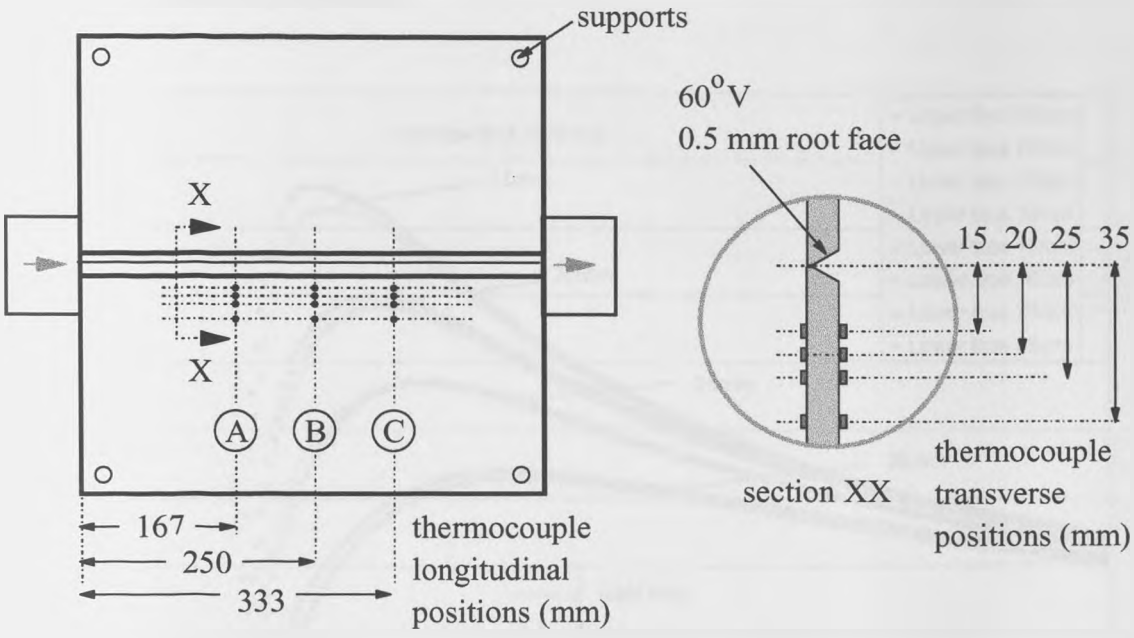

Figure 5.3: Thermocouple positions and weld prep dimensions

5.2.1 Experimental investigation and results

The thermocouple investigation had two main purposes: to index the emissivity for the thermographic camera and to provide accurate comparison of upper and lower surface temperatures at identical positions. The latter was considered to be possibly important with respect to angular distortion. Differences in the upper and lower surface temperatures at the far field positions, particularly at points not exhibiting yielding would result in a through thickness thermal strain, thereby resulting in angular distortion. The work performed by Birk-Sorensen [5.3], inspired by Rosenthal [5.4], [5.5], derived formulas to identify validity boundaries between two-dimensional and three-dimensional treatments. Equation 2.38, indicates the stage where a through thickness thermal gradient is present in the three-dimensional model. Assigning the aforementioned welding parameters and averaged material properties within equation 2.38, it is expected that a through thickness thermal

gradient is non-existent for temperatures below the eutectic temperature (1496°C) and for plate thickness of 10mm and below. This result is rather surprising considering that the weld pool shape is a spherical distribution and is probably due to line heat source model assumed, while neglecting arc stirring effects and temperature dependant material properties.

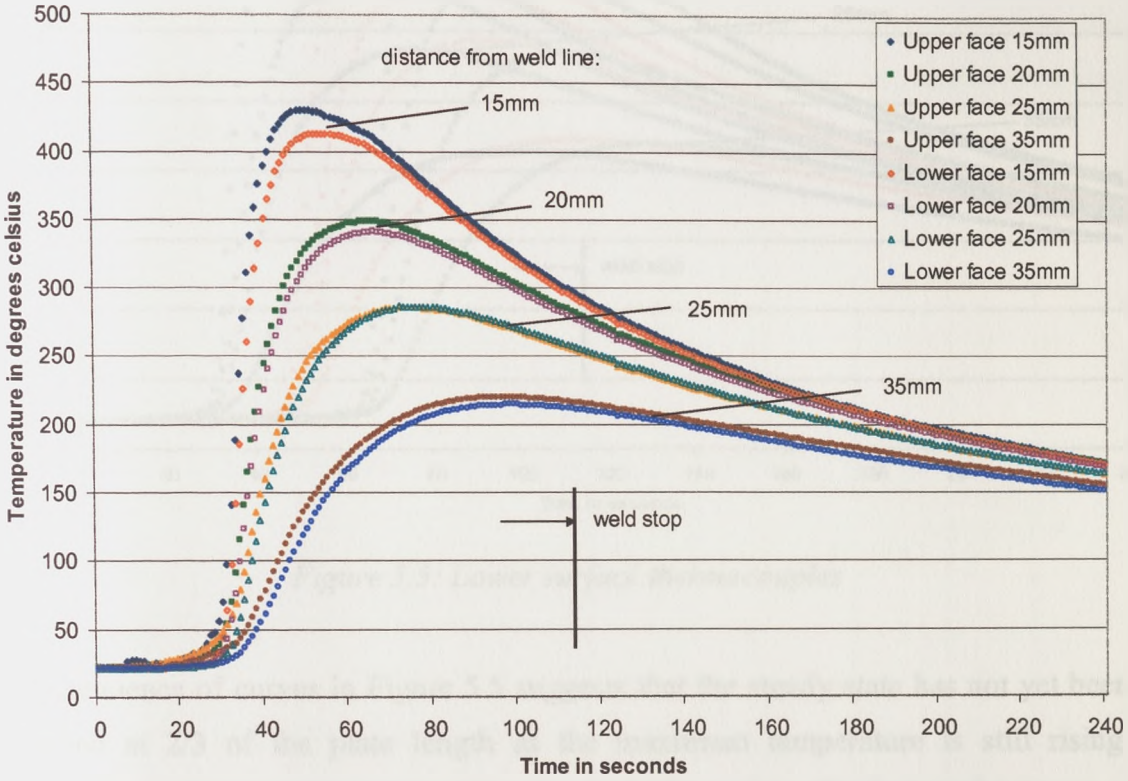

Figure 5.4: Row A thermocouple results

Figure 5.4 shows typical thermocouple results for the upper and lower surfaces at particular distances from the weld line. The upper thermocouples at the first row (A) show a slightly higher temperature than the lower, at least for the two stations nearest the weld, but this is probably due to extra radiation energy impinging on the thermocouples closest to the arc. The difference in metal temperature is probably not more than 8°C. In terms of thermal strain this would only give rise to 6% of the yield strain, suggesting that the angular distortion is a localized effect related to the fusion zone shape and is not a function of the far-field temperatures.

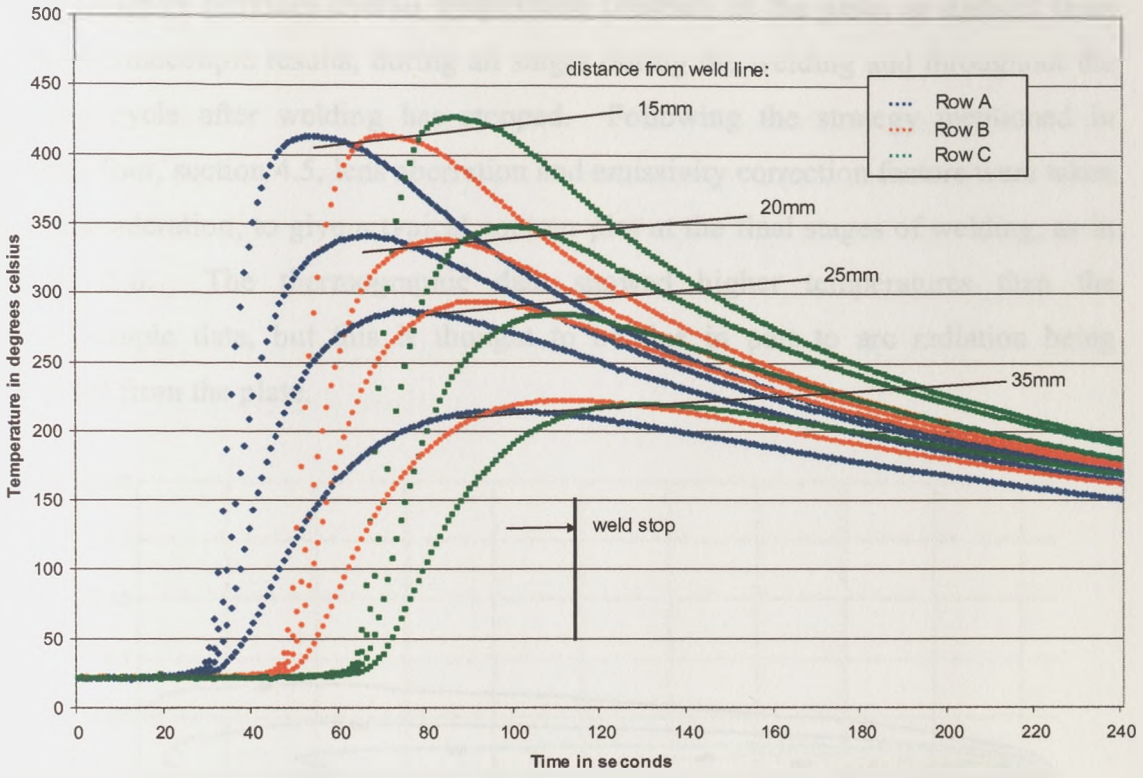

Figure 5.5: Lower surface thermocouples

The sequence of curves in Figure 5.5 suggests that the steady state has not yet been reached at 2/3 of the plate length as the maximum temperature is still rising. However this conclusion is questionable as it depends critically on the accurate positioning of the thermocouples relative to the arc trajectory. The large thermal gradient present across the transverse axis of the weld means that a slight offset of 0.5mm in thermocouple position will contribute a significant difference in the recorded temperature transients. Care has been taken to accurately index the various thermocouples, but it is thought that the positions are only within ± 0.25mm of quoted distances, due to human errors and the size of the thermocouple bead. Finally it was observed that the falling temperatures tend to a common level at long times, corresponding to three times the weld run duration and converging to a temperature less than 150°C. This observation is of particular importance in the evolution of the welding distortions and is discussed in later chapters.

The thermocouple data were supplemented by thermographic camera results. Thermography provides overall temperature contours of the plate, as distinct from point thermocouple results, during all stages during the welding and throughout the cooling cycle after welding has stopped. Following the strategy mentioned in chapter four, section 4.5, lens aberration and emissivity correction factors were taken into consideration, to give a typical contour plot at the final stages of welding, as in Figure 5.6. The thermographic data showed higher temperatures than the thermocouple data, but this is thought to be due in part to arc radiation being reflected from the plate.

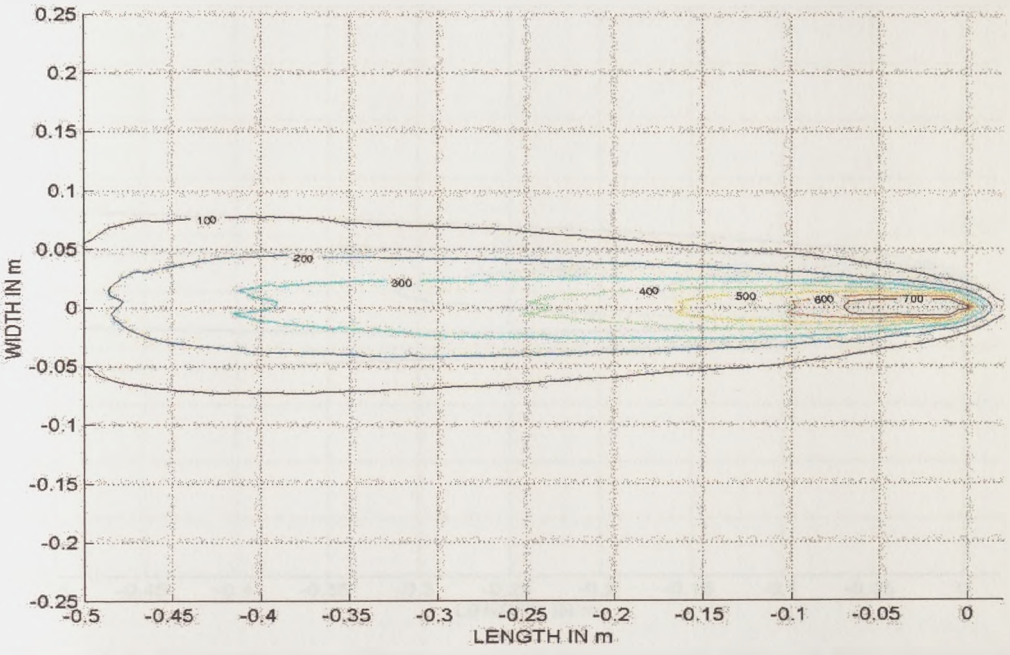

Figure 5.6: Temperature contour plot near end of weld run

5.2.2 Theoretical investigation – analytical model

The well-known two-dimensional heat conduction equation solutions of Rosenthal [5.4] and Rykalin [5.6], equation 5.2, are applicable to the case under consideration. This solution represents a line heat source model, with no thermal gradient through the thickness of the plate and assumes that a steady state has been reached relative to the moving heat source.

$$T - T_o = \frac{q}{2\pi K_c d} e^{\frac{v\chi}{2a}} K_o\left(\frac{vr}{2a}\right) \qquad \textit{Equation 5.2}$$

Figure 5.7 shows a temperature contour plot derived from Rosenthal's two dimensional thermal model, using a nominal energy input rate of 5750W and averaged material properties, corresponding to conductivity of 69.6 J/ms°C, specific heat of 782 J/kg°C and density of 7830 kg/m³. Note, that a process efficiency of 0.825 was applied to obtain direct comparison with the experimental maximum temperature thermocouple results.

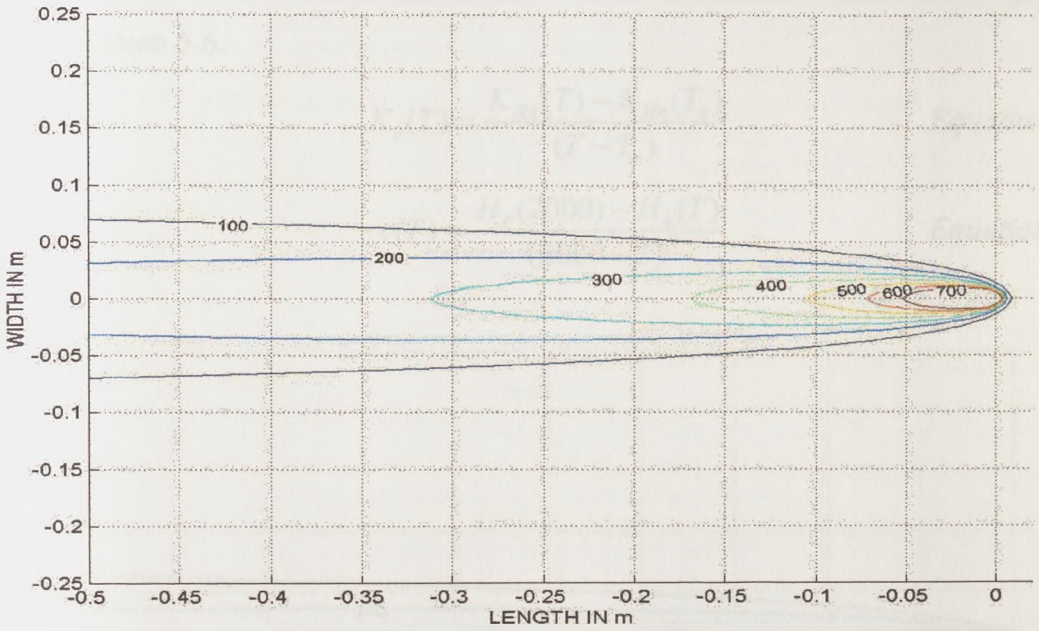

Figure 5.7: Rosenthal two-dimensional theory contour plot – 0.825 efficiency

Most of the analytical models in the literature use constant material properties. Variable material properties may be incorporated within the analytical solution presented in equation 5.2 via linear interpolations of the specific heat and conductivity. An iterative solution is applied to reach a convergence criterion. The presence of phase transformations, particularly during the solid to liquid transformation, makes this interpolation cumbersome and non-convergent. Hence, the interpolation was performed using the enthalpy and an integral of the conductivity (named 'heat absorption'). These relationships are given in equations 5.3 and 5.4, respectively.

$$H_e(T) = \int_0^T c(\tau)d\tau \qquad \textit{Equation 5.3}$$

$$K_{HA}(T) = \int_0^T K_c(\tau)d\tau \qquad \textit{Equation 5.4}$$

The final specific heat and conductivity was obtained by back-differentiating from the interpolated results. Hence the conductivity value obtained will reflect the amount of heat to be absorbed from the temperature obtained using Rosenthal's theory to ambient temperature, via equation 5.5. On the other hand, the specific heat will reflect the heat retained from 2000°C to the temperature under investigation, using equation 5.6.

$$K_c(T) = \frac{K_{HA}(T) - K_{HA}(T_a)}{(T - T_a)} \qquad \textit{Equation 5.5}$$

$$c(T) = \frac{H_e(2000) - H_e(T)}{(2000 - T)} \qquad \textit{Equation 5.6}$$

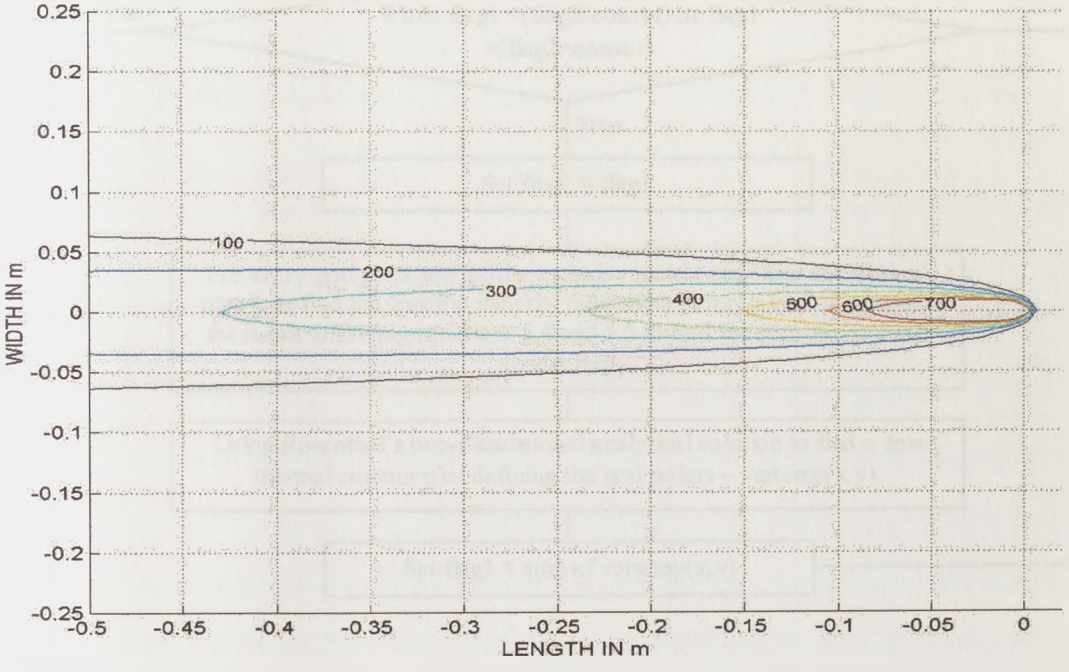

Figure 5.8: Rosenthal's two-dimensional theory contour plot – variable material properties

Figure 5.8 shows a typical contour plot when Rosenthal's two-dimensional theory and variable material properties are used. Note again that for comparison reasons a process efficiency of 0.825 is also used. The pseudo-code of this interpolation and iterative convergence criterion program is given in Figure 5.9.

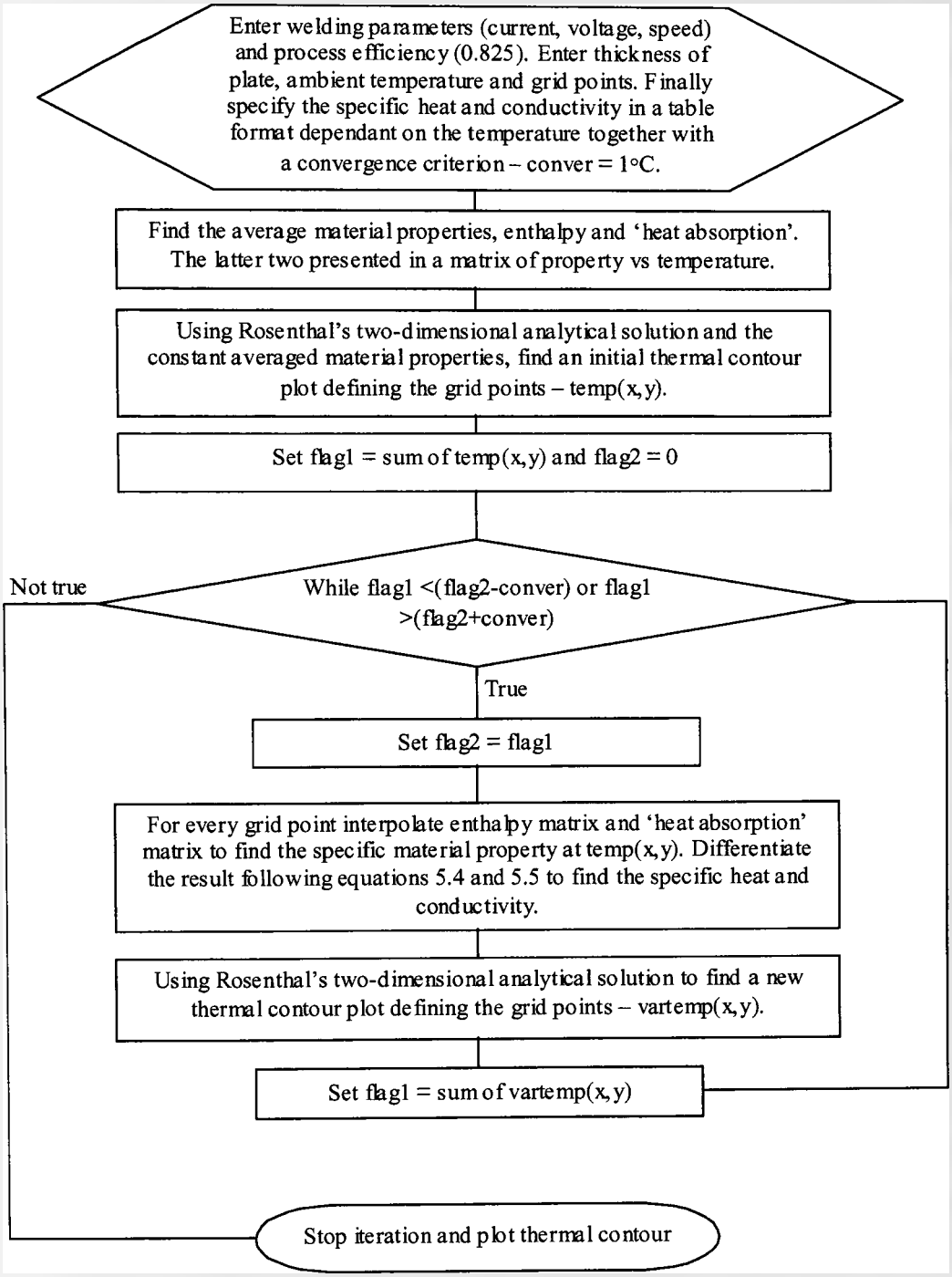

Figure 5.9: Program listing of iterative, convergence criterion, variable material properties Rosenthal's theory.

Comparing the temperature contours in Figures 5.6, 5.7 and 5.8, it is evident that the 'trailing' end of the test plate has not reached the steady state condition, as indicated by the wider and the non-continuous 100°C and 200°C contours in the thermographic case. Towards the end of the plate more heat is being retained, as the heat flow is essentially one-dimensional in the transverse direction to the weld line. Furthermore the isotherms are better represented using variable material properties. The high latent heat of fusion at the weld pool will retain more heat, which is eventually dissipated within the material at a later stage, as opposed to the constant material property solution. Table 5.1 gives a comparison of the maximum temperatures reached at particular distances from the weld line, together with their relative times with respect to the arc. The same argument prevails and the time lag between the different maximum temperatures, are more realistic when using non-linear temperature dependant material properties. However, it should be pointed out that in the simplified approach adopted in this thesis, the temperature history is not a significant parameter, as distinct from the maximum temperatures reached at given distances from the weld line.

Position from weld line (mm)	Thermocouple results		Rosenthal constant material properties		Rosenthal variable material properties	
	Maximum temperature (°C)	Time relative to arc (s)	Maximum temperature (°C)	Time relative to arc (s)	Maximum temperature (°C)	Time relative to arc (s)
15	429.75	15.65	446.93	10.42	431.44	15.63
20	347.07	30.15	343.26	17.71	331.93	27.68
25	290.92	38.32	279.83	28.13	271.56	40.03
35	219.92	60.82	206.37	54.17	201.39	78.13

Table 5.1: Comparison of maximum temperatures between thermocouple results and Rosenthal's theory

Although the analytical solution converges to an unrealistic infinite temperature at the weld pool centre, it provides satisfactory information at the far field, provided that the correct energy efficiency and thermal properties are used. The strong relationship between the thermocouple results and the analytical solution shows that conduction heat flow is predominant. The analytical solutions developed by Rosenthal are economically efficient and simple to adopt for the representation of

thermal transients of simple geometries, but tend to become inapplicable with increase in complexity of the geometry under investigation.

5.2.3 Three-dimensional transient finite element model

The use of finite element analysis, makes it possible to investigate intricate geometry, while taking into account any non-linear temperature dependent material properties and boundary conditions. Though lacking computational economy, a three-dimensional transient model provides the most realistic analysis. Three-dimensional analyses provide the possibility to model any thermal breaks related to geometry, size, tabs and other heat sinks, while offering an investigation of possible thermal gradients present through the thickness of the plate.

In this analysis, the simulated heat source is moved at constant velocity along the weld line in a series of fine load steps. For simplicity and reduction in computational time, half of the plate was modelled. Eight–noded, linear elements (SOLID 70) were used, as the eventual distortion analysis is intended to be uncoupled and therefore, the more advanced elements required for the thermomechanical stages are not required. However, for the direct thermal nodal loading in the distortion analysis, the same mesh design was used for the thermal and structural analyses. The mesh density adopted reflects the high thermal gradient and stress present next to the weld, such that a fine mesh was used at this region and was coarsened for distances departing away from the weld axis, involving transition volumes using tetrahedral elements, shown in Figure 5.10.

Various ways of simulating the weld deposition and energy input were explored (presented in [5.7]). Firstly, the weld was assumed to be present from the beginning (i.e. no weld preparation) and the process energy was generated in selected elements corresponding to the fusion zone shape by the use of a volumetric heat input ('heat generation' method).

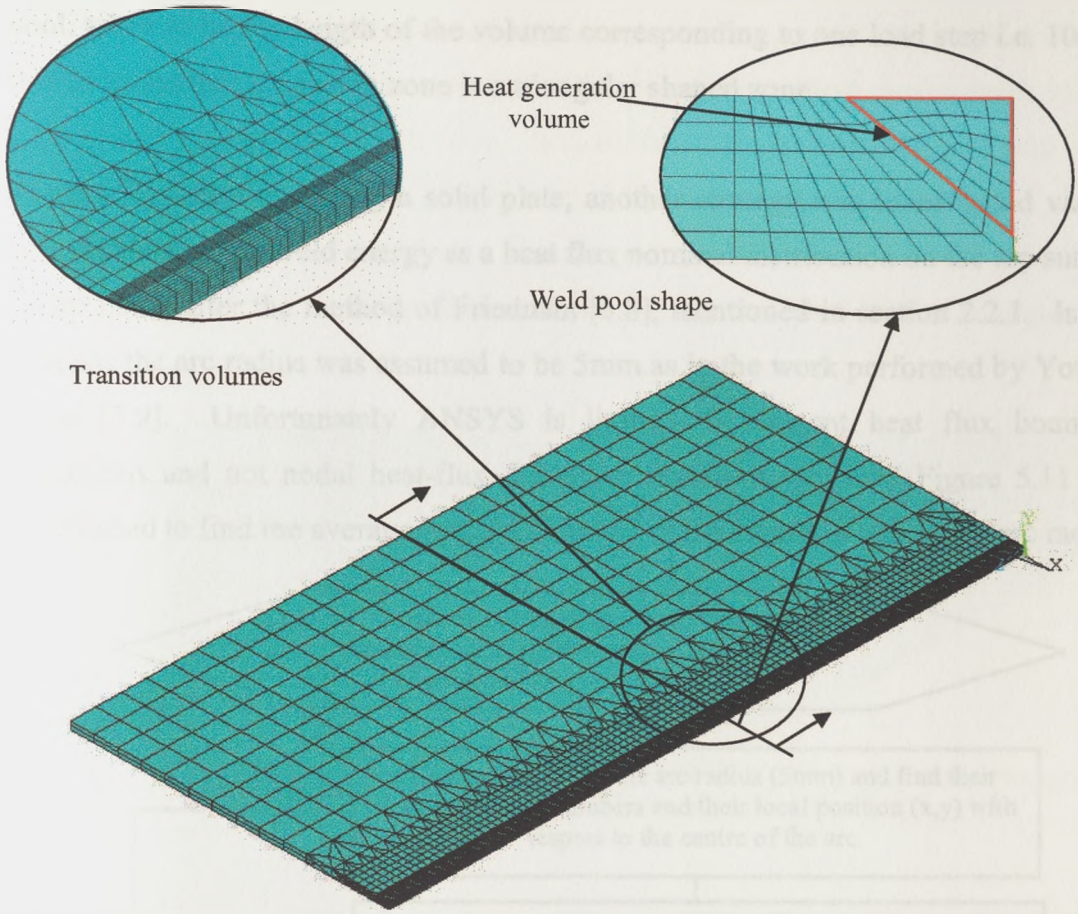

Figure 5.10: Mesh design for pilot programme – butt welds

Secondly, the transition in thermal capacity between the empty groove and filled weld was simulated by using so-called 'birth-and-death' elements, which are in place from the beginning and thus form part of the element matrix, but are only contributing a small effect due to the low stiffness specified, until the arrival of the heat source. Again the heat generation method was applied to these elements. Various weld shapes were considered based on the weld preparation geometry or the molten weld pool shape, such that the volumetric heat input is given by equation 5.7.

$$q_{vol} = \frac{2\eta IV}{b_w s \dot{l}_m} \qquad \textit{Equation 5.7}$$

Where b_w is the weld pool or weld prep width, taken to be 12mm and 6.35mm respectively, s is the depth of penetration (5.5mm) and l_m is the length of the weld

pool, taken to be the length of the volume corresponding to one load step i.e. 10mm. It is assumed that the fusion zone is a triangular shaped zone.

Thirdly, by again assuming a solid plate, another strategy was investigated via the specification of the weld energy as a heat flux nominal distribution on the top surface of the plate, after the method of Friedman [5.8], mentioned in section 2.2.1. In this analysis the arc radius was assumed to be 5mm as in the work performed by Younan *et al* [5.9]. Unfortunately ANSYS is limited to element heat flux boundary conditions and not nodal heat-flux, hence an algorithm given in Figure 5.11 was established to find the average heat flux applied to the elements within the arc radius.

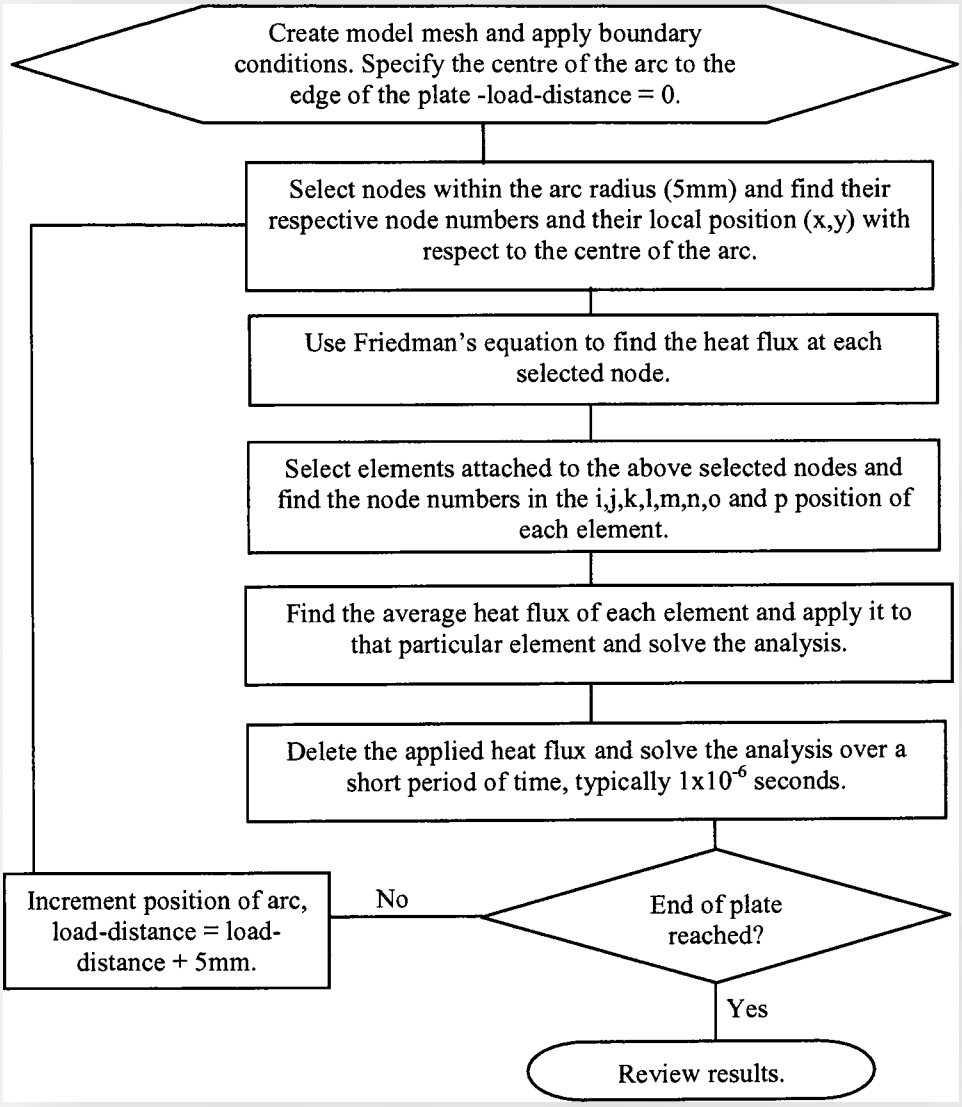

Figure 5.11: Transient load step analysis algorithm

The definition of the heat input largely depends on the size of the mesh at the arc radius. Figure 5.12 shows the definition of the heat input when using a mesh 2.5mm x 1mm and a mesh 1.25mm x 1mm. It is evident that the finer the mesh the more defined is the heat source, but this is limited by the computational time. Typically, when a mesh 2.5mm x 1mm design was adopted for the elements close to the weld, the analysis took 24 hours to compute using a Pentium 4 1.8GHz processor and 512Mb RAM.

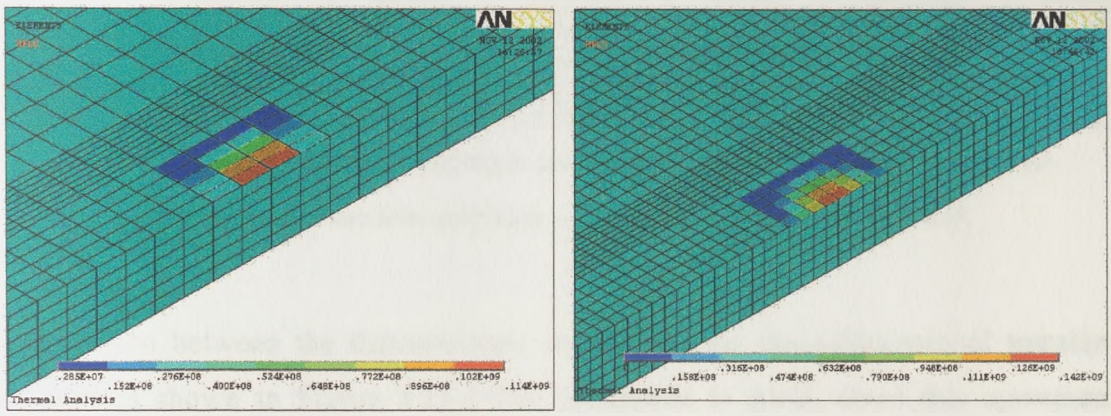

Figure 5.12: Heat source definition- a) mesh design 2.5mm x 1mm, b) mesh design 1.25mm x 1mm.

The resulting differences between these approaches were not major. The different shapes of the weld heat input profile had little or no effect on the temperatures in the region of interest. Hence, one may assume that the region of heat input coincides largely with the weld preparation. The 'birth-and-death' element approach resulted in the highest temperatures, when the same efficiency was used and this is attributed to the fact that less material is available to absorb the given thermal energy.

Table 5.2 gives a comparison between the outcomes of the various strategies adopted in the three-dimensional transient analyses. None of the heat input models show a difference between the top and bottom temperatures at a distance of 15mm from the weld line, as there appears to be present in the test results. This may be because of spurious factors in the thermocouple results, as suggested earlier.

Position from weld line (mm)	Heat generation rate – fusion zone		Heat generation rate and 'birth and death' – fusion zone		Heat flux method	
	Maximum temperature (°C)	Time relative to arc (s)	Maximum temperature (°C)	Time relative to arc (s)	Maximum temperature (°C)	Time relative to arc (s)
Top 15	427.00	19.09	442.60	20.08	421.40	23.96
Bottom 15	427.20	19.09	442.70	20.08	421.40	23.96
Top 20	343.60	31.25	356.60	33.34	346.00	34.38
Bottom 20	343.70	31.25	356.70	33.34	346.00	34.38
Top 25	285.80	41.67	297.90	41.67	291.50	46.88
Bottom 25	285.90	41.67	298.00	41.67	291.50	46.88
Top 35	212.70	64.02	220.90	64.02	214.20	66.25
Bottom 35	212.00	64.02	221.00	64.02	213.20	66.25

Table 5.2: Comparison of maximum temperatures between the various three-dimensional transient analyses using a weld efficiency of 0.825.

Comparison between the thermocouple results and the three-dimensional transient analysis is shown in Figure 5.13. The agreement is good, albeit this agreement depends on the matched weld energy efficiency (taken as 0.825). The present level of agreement is probably more than adequate and tends at least to support the values used for the thermal properties and other parameters assumed in the model.

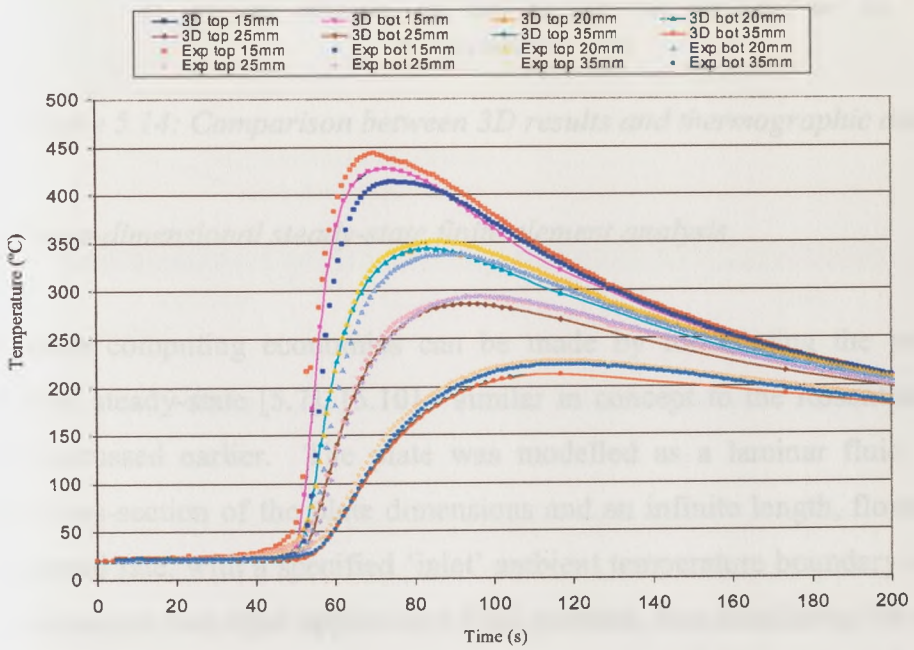

Figure 5.13: Comparison at mid-length between 3-D transient and thermocouple results

Comparison between the three-dimensional thermal analysis and the analytical steady state also showed good agreement apart from slight differences due to different boundary conditions of heat loss from the edges and the ends of the plate. The differences are more apparent when compared with the thermographic results in Figure 5.14. The thermographic data show an offset in temperature, due to the radiation effect from the arc, but also, more heat is being lost from the plate edge after welding. This effect is due to the fact that the run-off plates were not modelled in the computational analysis.

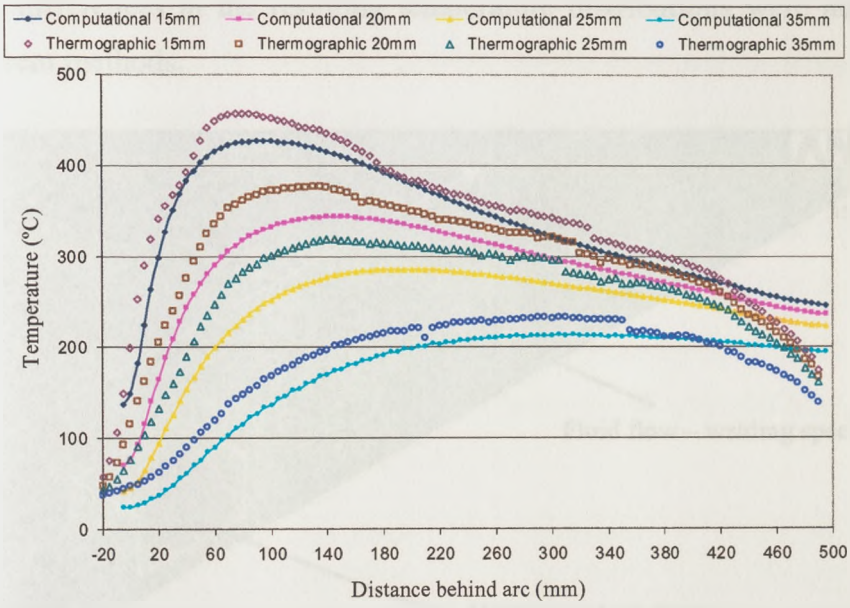

Figure 5.14: Comparison between 3D results and thermographic data

5.2.4 Three-dimensional steady-state finite element analysis

Considerable computing economies can be made by formulating the problem in terms of the steady-state [5.7], [5.10] - similar in concept to the Rosenthal/Rykalin solution discussed earlier. The plate was modelled as a laminar fluid having a constant cross-section of the plate dimensions and an infinite length, flowing at the welding speed rate, with a specified 'inlet' ambient temperature boundary condition, over a continuous heat input applied at a fixed position, thus simulating the weld heat input. The element used in this instance consisted of FLUID142 solid elements, whereby the fluid assumed thermal material properties of steel and flows laminarly

by specifying a viscosity of $1x10^6$. This approach can reflect finite cross-sectional dimensions and surface convection properties, but the particular software (Flotran) used did not have a capability for temperature-dependent film coefficient and enthalpy properties. Hence a constant averaged convection film coefficient was specified for the different surfaces of the plate and the radiation heat loss was incorporated in the heat balance equation through the specification of emissivity. Furthermore the specific heat was used, following Figure 5.1a. Alternative heat input models were investigated - namely, volumetric heat generation and surface heat flux. The differences in the resulting temperature distributions were not large for these different methods.

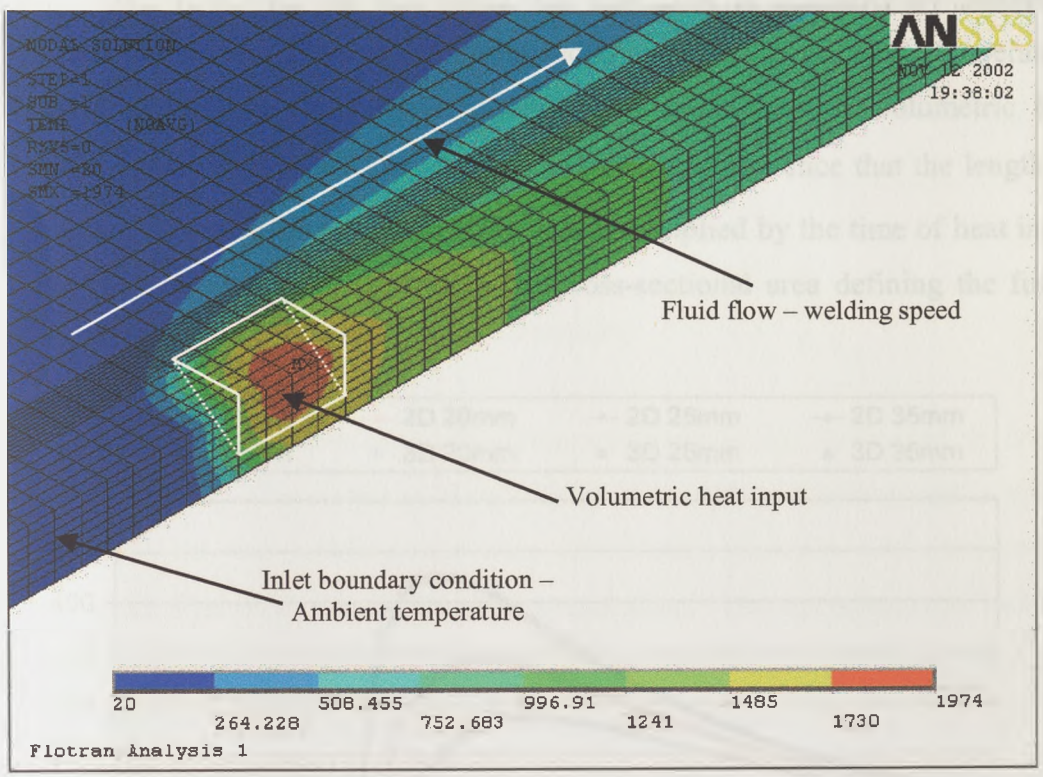

Figure 5.15: Steady-state finite element model – thermal contour plot

Comparison of results with the analytical steady state case (Rosenthal) showed that for the same efficiency of 0.825 the computational steady state analysis gave slightly higher temperature results. This may simply be because the finite size of the computational case did not allow the steady state temperatures to be reached.

5.2.5 *Two-dimensional cross-section transient finite element model*

The heat flow in the case of fast moving sources is predominantly transverse to the weld line. The movement of the heat source overtakes the heat flow in the forward direction and the lack of a temperature gradient inhibits flow backwards. It is therefore reasonable to consider a model consisting of a transverse cross-sectional strip of arbitrary length, with uniform temperatures across the length of the plate and no heat flow normal to the plane of the strip in either direction [5.7], [5.11]. A fixed packet of heat energy is applied appropriately to the strip at the specified rate, for a period corresponding to the distance traveled by the heat source within the strip length. After removing the heat input, the heat flow is primarily by transverse conduction within the plate width, followed by cooling to ambient temperature, corresponding to heat loss by convection and radiation. A volumetric heat generation approach was used for this model, with the difference that the length l_m in equation 5.7 was given by the welding speed multiplied by the time of heat input. The heat source was again applied to the cross-sectional area defining the fusion zone.

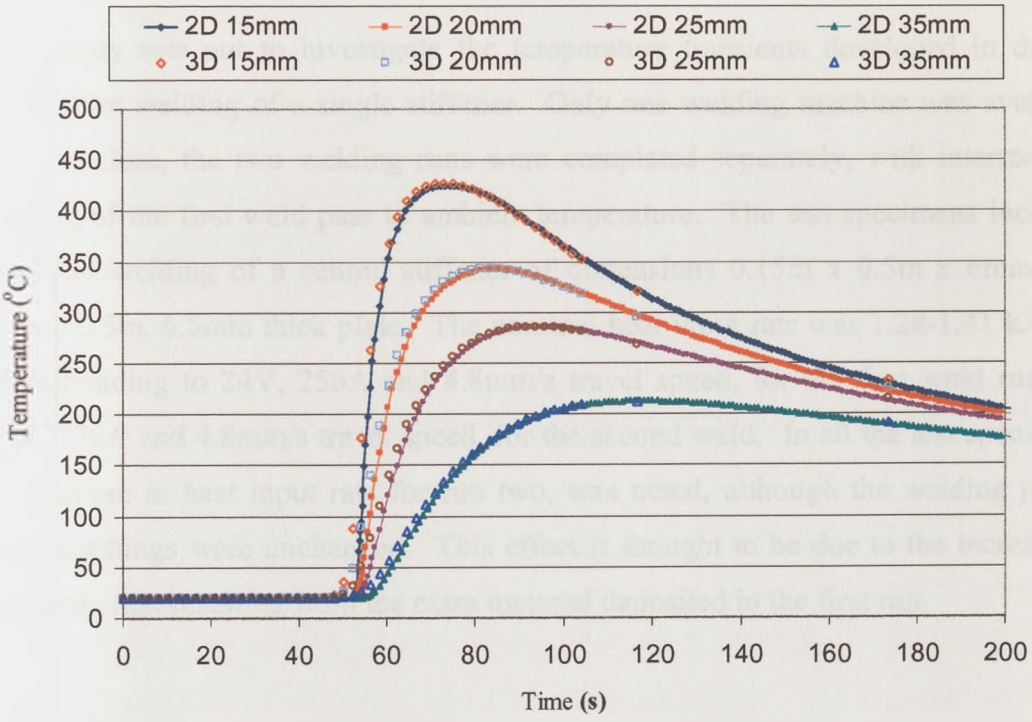

Figure 5.16: Comparison between 3D and 2D transient analyses

It is evident, by comparison with the 3D transient model in Figure 5.16, that the 2D cross-sectional model gives remarkably good results, except in the region of the weld pool where temperatures are unrealistic. The degree of accuracy of the weld pool temperature results depends on how the heat is defined over a specified time. E.Olden and R.Leggatt [5.11] used an amplitude curve to define the addition of heat specified over a finite time. Since the region of interest in the present case lies in the far field, the heat input was modelled as a ramp input, specified over a time period related to the arc diameter.

Comparing the strategies discussed, the two-dimensional cross-section model is very economic and gives good results, which are adequate as input to the structural phase of the uncoupled distortion simulation. Though the analytical solutions require the least computational time, these solutions may become impractical when dealing with more complex geometry.

5.3 Pilot programme – double-sided fillet welding

This study sets out to investigate the temperature transients developed in double sided fillet welding of a single stiffener. Only one welding machine was available and therefore, the two welding runs were completed separately, with intermediate cooling of the first weld pass to ambient temperature. The test specimens included the fillet welding of a central stiffener of dimensions 0.15m x 0.5m x 6mm to a square 0.5m, 6.5mm thick plate. The nominal heat input rate was 1.28-1.41 kJ/mm, corresponding to 24V, 256A and 4.8mm/s travel speed, for the first weld run and 25V, 270A and 4.8mm/s travel speed, for the second weld. In all the test specimens an increase in heat input rate for run two, was noted, although the welding power source settings were unchanged. This effect is thought to be due to the increase of magnetic flux resulting from the extra material deposited in the first run.

5.3.1 *Experimental temperature transients*

The heat flow in fillet welding is more complex, particularly due to the thermal break existing between the stiffener and the plate. Hence an array of thermocouples was placed on the stiffener and on adjacent sides of the plate as shown in Figure 5.17. From the analyses and experimental results obtained in the butt welding pilot programme, it was assumed that the temperatures on opposite sides of the plate and stiffener were similar. Thus the thermocouple arrays were placed on the faces that were least exposed to arc radiation and splatter.

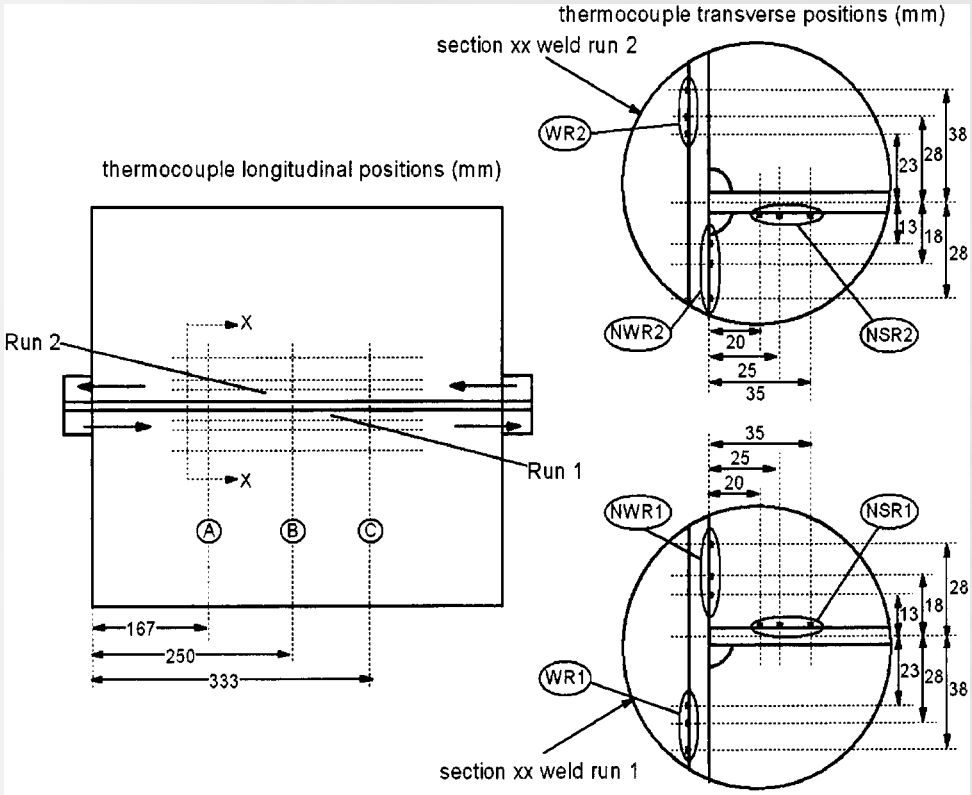

Figure 5.17: Thermocouple positions for different weld runs

The positions of the thermocouples were placed in a manner such that for evenly distributed heat flow in the plate and in the stiffener, thermocouples residing in close proximity to the weld (WR1 23mm, NSR1 20mm, NWR1 13mm) would experience the same temperature histories. Figure 5.18 suggests that this was not the case, which has the further implication the thermal break and the position of the arc are

important factors when dealing with fillet welding, and must be modelled in the finite element analysis.

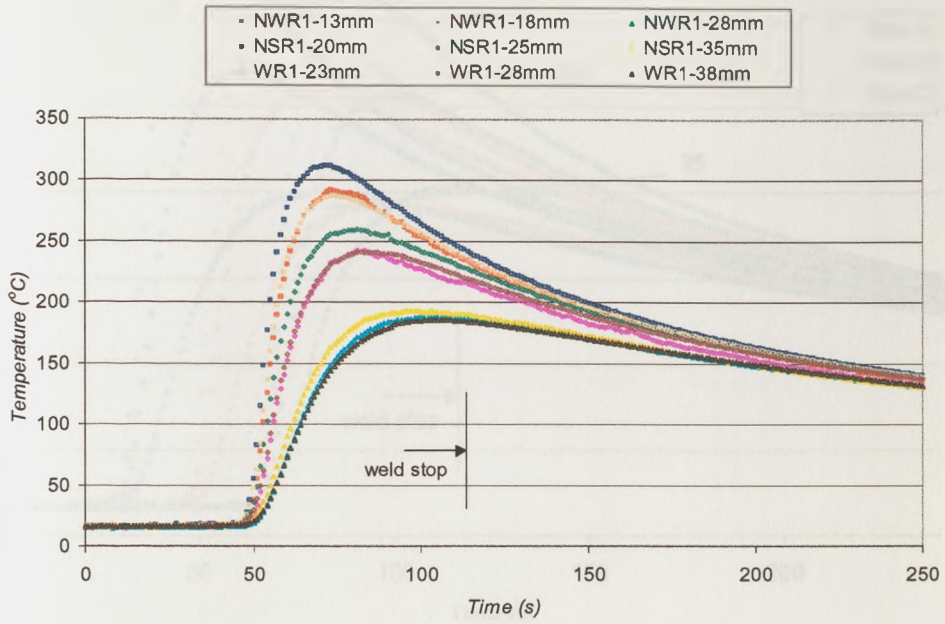

Figure 5.18: Row B thermocouple results-run one

Figure 5.19 shows the thermal histories of the thermocouples residing on the stiffeners at different longitudinal positions. The variations suggest that the amount of heat flowing into the plate and stiffener is not constant and possibly fluctuates according to the position of the arc and thermal gap between stiffener and plate. Although such variations are not large they are sufficient to displace the centroid of the contraction force. For simplification, the average maximum temperatures from row A, B and C were used for comparison with the finite element analysis, and are given in Table 5.3.

Position of Thermocouple	Maximum temperature (°C)	Time relative to arc (s)
WR1-23mm	289.22	23.92
WR1-28mm	243.73	32.92
WR1-38mm	185.27	56.25
NWR1-13mm	287.00	23.59
NWR1-18mm	237.05	35.59
NWR1-28mm	182.34	55.25
NSR1-20mm	324.97	21.92
NSR1-25mm	262.26	30.92
NSR1-35mm	198.80	47.92

Table 5.3: Maximum temperatures at various positions –run one

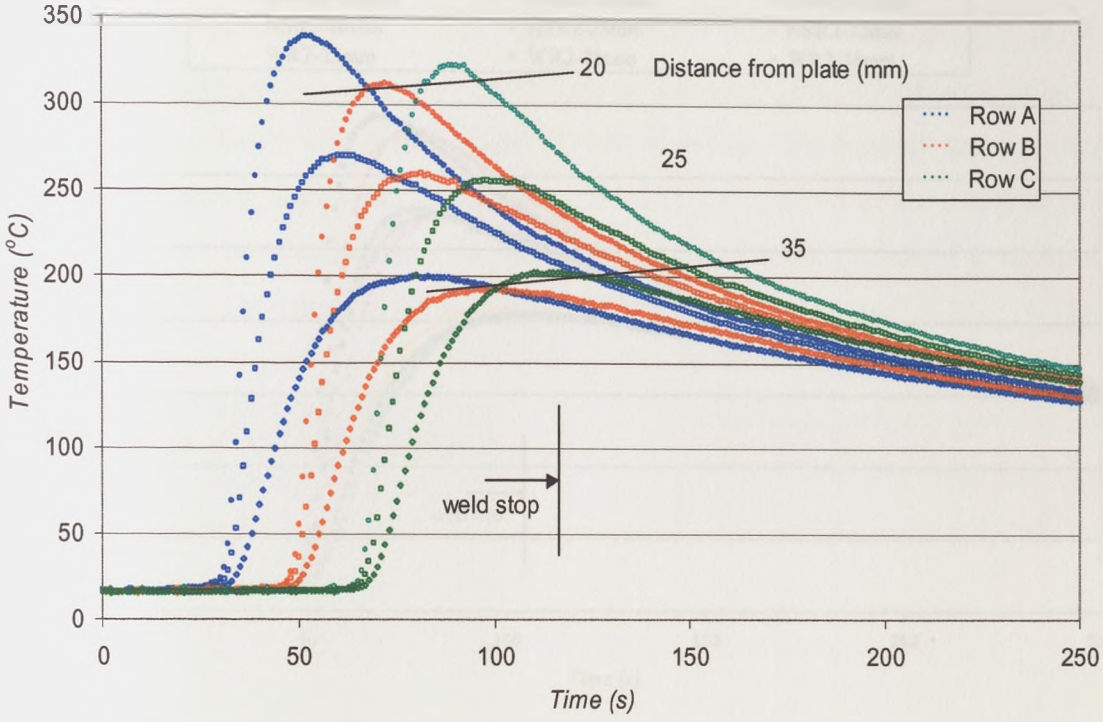

Figure 5.19: Thermocouple results on the stiffener

Relative to the first weld run, the thermocouples on the non-welded side of the plate (NWR2) show an offset timing in the temperature history in the second weld pass. The time when the maximum temperature is attained lags other positions (refer to Table 5.4 and Figure 5.20). This suggests that the boundary conditions in the second weld run were different. This effect is thought to be due to the extra weld material deposited in weld run one, thereby modifying the heat flow patterns.

Position of Thermocouple	Maximum temperature (°C)	Time relative to arc (s)
WR1-23mm	321.70	24.92
WR1-28mm	269.35	30.92
WR1-38mm	201.09	58.25
NWR1-13mm	331.13	26.92
NWR1-18mm	276.01	38.25
NWR1-28mm	205.32	54.92
NSR1-20mm	341.30	18.58
NSR1-25mm	280.46	27.25
NSR1-35mm	207.96	49.58

Table 5.4: Maximum temperatures at various positions-run two

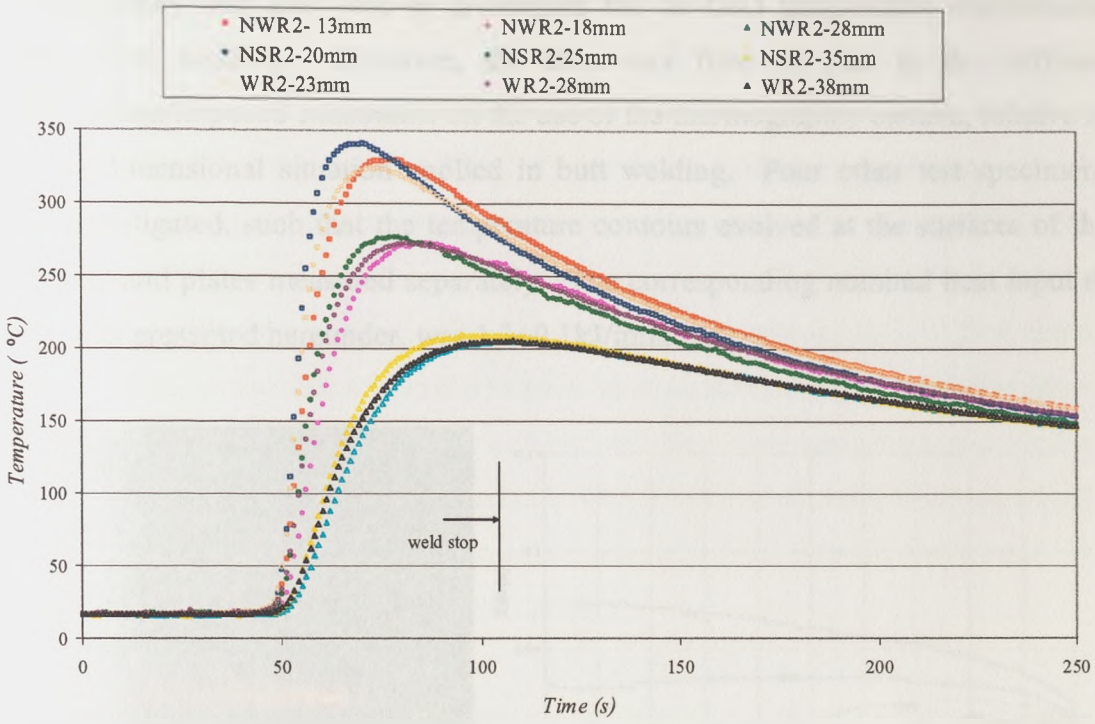

Figure 5.20: Row B thermocouple results-run two

In all test specimens, the temperatures arising in the second weld were higher and this is attributed to the increase in nominal heat input referred to earlier. Furthermore, it is evident that the heat flowing to the stiffener is higher than to the plate. This may be an effect of the position of the arc, and an initial indication of this is the unsymmetric weld pool shapes, shown in Figure 5.21.

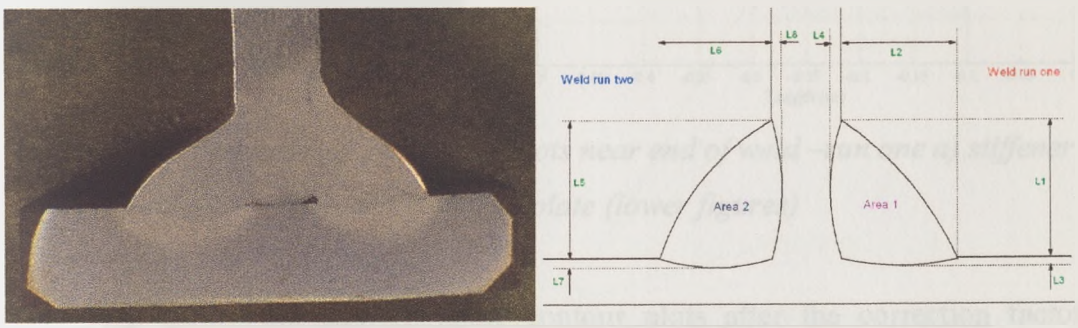

Weld run no.	Run one	Run two
Area (mm²)	43.92	38.23
L1 / L5 (mm)	9.38	6.92
L2 / L6 (mm)	7.06	7.81
L3 / L7 (mm)	0.66	0.93
L4 / L8 (mm)	1.34	0.93

Figure 5.21: Weld pool shapes and dimensions

Thermography was also used to investigate the far-field temperature distributions during fillet welding. However, the three-way flow of heat in the stiffener configuration imposed constraints on the use of the thermographic camera, relative to the two-dimensional situation applied in butt welding. Four other test specimens were investigated, such that the temperature contours evolved at the surfaces of the stiffeners and plates measured separately. The corresponding nominal heat input of the results presented hereunder, was 1.3±0.1kJ/mm.

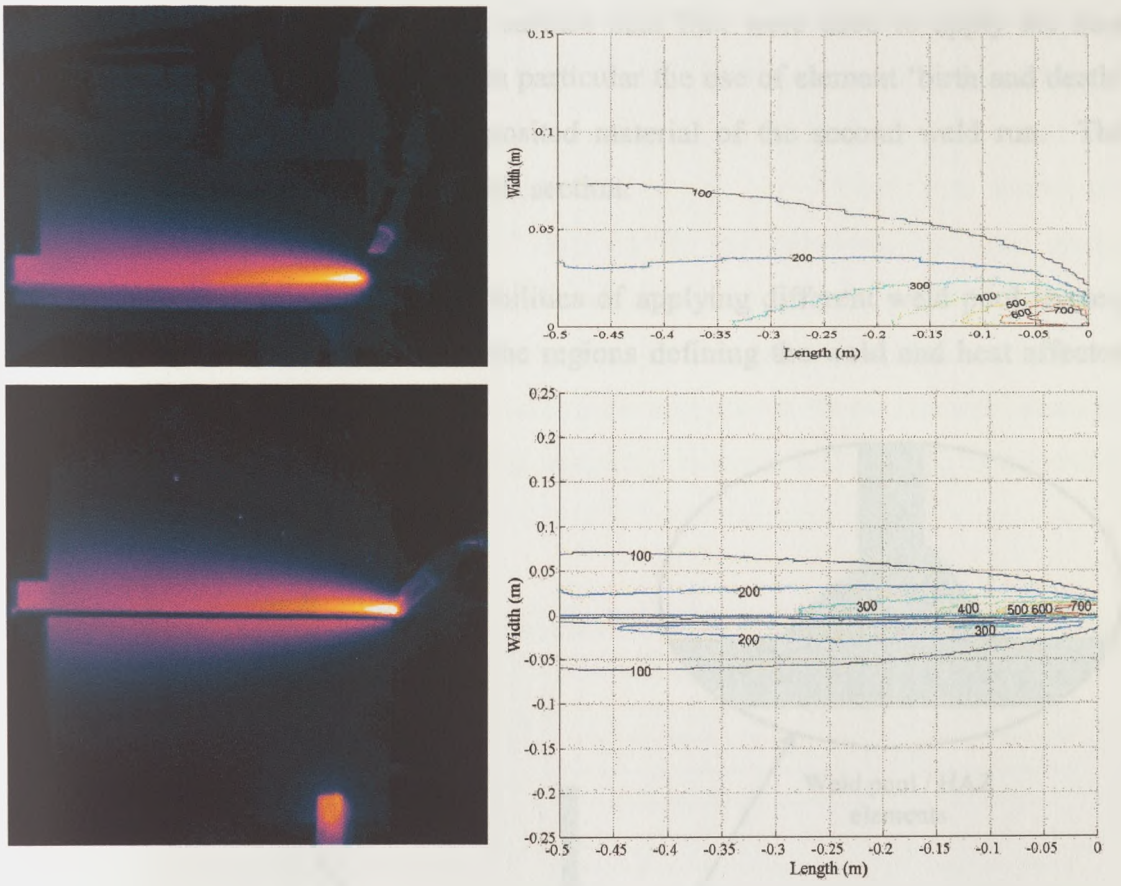

Figure 5.22: Thermographic contour plots near end of weld –run one a) stiffener (upper figures) b) plate (lower figures)

Figure 5.22 shows the thermographic contour plots after the correction factors, including emissivity and lens aberration, were applied to the raw thermal image. The temperature histories at various positions on the plate and stiffener reflect the thermocouple results.

5.3.2 *Two-dimensional finite element analyses*

The strategies adopted in the butt welding thermal analyses have shown that for an economically efficient computational time, the temperature transients can be investigated via a two dimensional cross-sectional analysis, with reasonable results. From the experimental results it is evident that the weld material, gap between stiffener and plate, and position of the arc, play a major role in the heat flow during fillet welding. A number of strategies have been adopted, to investigate the above, whereby volumetric heat input and surface heat flux were used to apply the heat input to the finite element model. In particular the use of element 'birth and death' was essential to simulate the undeposited material of the second weld run. The different strategies are described in this section.

The mesh design reflected the possibilities of applying different weld pool shapes, while a fine mesh was adopted for the regions defining the weld and heat affected zones as shown in Figure 5.23.

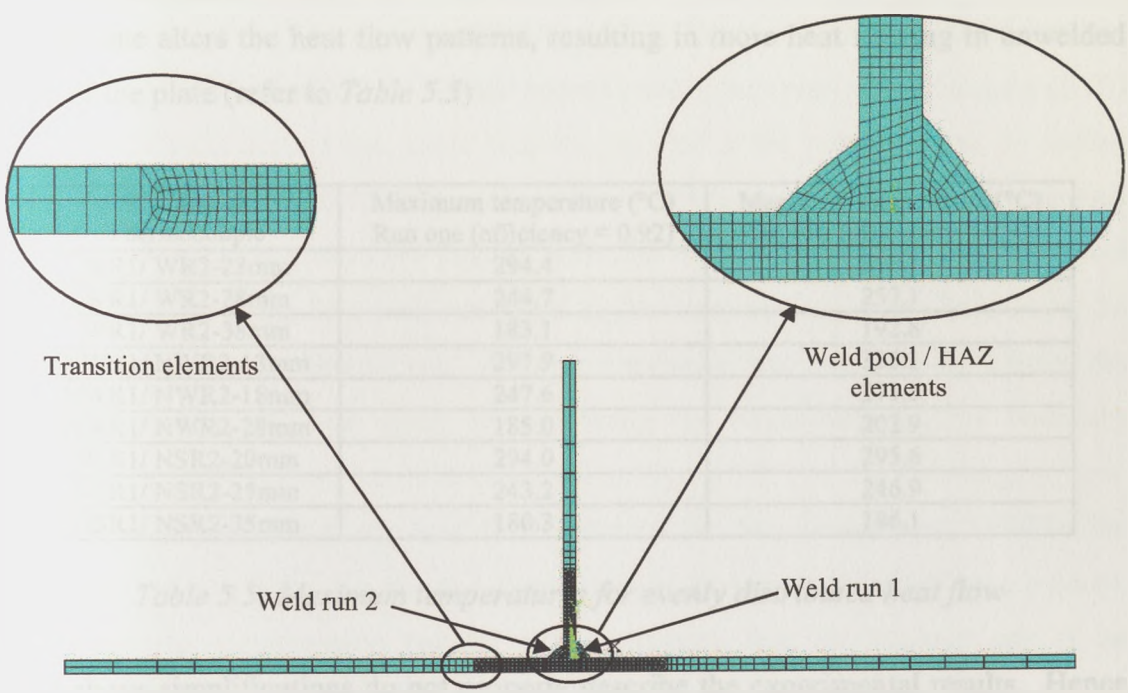

Figure 5.23: Mesh design for two dimensional fillet weld thermal analysis

Heat loss effects due to radiation and convection were modelled in the computational analyses, by defining film coefficients within the boundary conditions of the plate and stiffener. Both coefficients are non-linearly dependant on temperature, and different convection film coefficients were applied to the upper and lower faces of the plate and the faces of the stiffener.

The most simplistic assumption is to assume a symmetric weld pool, having a mean weld leg of 8mm x 8mm, such that an evenly distributed heat flow prevails. Furthermore no air gap is simulated such that stiffener and plate are bonded together via the command 'NUMMRG,ALL', thus allowing full heat flow between the pair. The heat input was applied to the weld pool by means of heat generation rate and elements representing the weld pool region of run two were 'deactivated' during the analysis of run one and 'reactivated' later on for the following run. This model reflects an idealistic approach to double sided fillet welding and the results show that during the first run the heat flows evenly through the plate and stiffener, relative to the weld position. This was not the case in the second run where the weld material of run one alters the heat flow patterns, resulting in more heat flowing in unwelded side of the plate (refer to *Table 5.5*)

Position of Thermocouple	Maximum temperature (°C) Run one (efficiency = 0.92)	Maximum temperature (°C) Run two (efficiency = 0.93)
WR1/ WR2-23mm	294.4	310.1
WR1/ WR2-28mm	244.7	257.1
WR1/ WR2-38mm	183.1	192.8
NWR1/ NWR2-13mm	297.9	325.1
NWR1/ NWR2-18mm	247.6	271.5
NWR1/ NWR2-28mm	185.0	202.9
NSR1/ NSR2-20mm	294.0	295.6
NSR1/ NSR2-25mm	243.2	246.9
NSR1/ NSR2-35mm	180.3	186.1

Table 5.5: Maximum temperatures for evenly distributed heat flow

The above simplifications do not properly describe the experimental results. Hence in the first instance the positioning of the heat input was investigated, via the application of two volumetric heat inputs at the weld pool region as shown in Figure 5.24, defined by the weld shapes given in Figure 5.21. The percentage efficiency

applied to the two volumetric sectors will define the amount of heat being applied at different positions, thereby simulating the fluctuations / position of the arc.

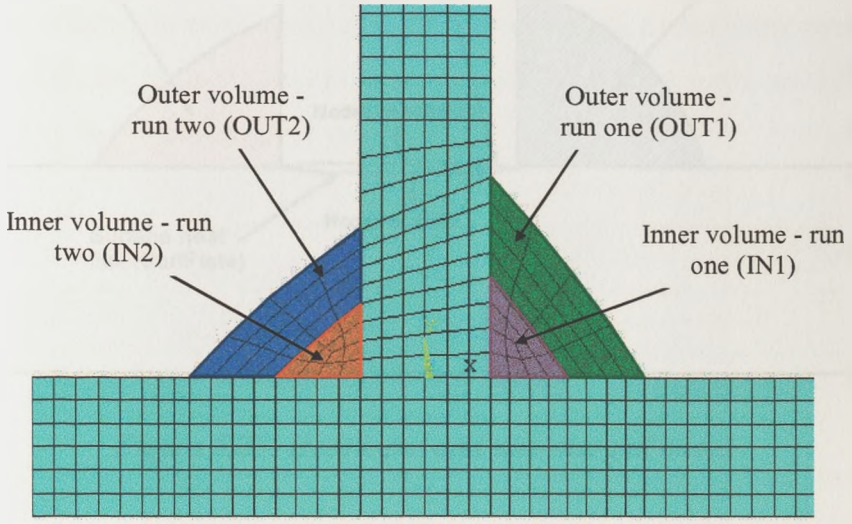

Figure 5.24: Volumetric heat input

For a good matching with the thermocouple results, the total efficiency for the first weld run was set to 0.92, and the efficiency in the inner and outer volumes were set to 0.60 and 0.32 respectively. Though approximately the same total efficiency (0.93) was used for the second run, more heat was applied at the outer volume, by setting the efficiency equivalent to 0.58, with an inner efficiency of 0.35. The distribution of heat influenced the heat flow pattern, such that higher temperatures were recorded on the stiffener in the first weld run while higher temperatures were obtained on the unwelded side for the second run. A better correlation was attained, while using the same efficiency and heat input, by separating the nodes defining the boundary between the stiffener and the plate as shown in Figure 5.25, i.e. by not merging these nodes hence preventing any heat flow between the two boundaries. Unlike the 'merged' case, a time lag for the thermocouple positions 'NWR2' was evident, mirroring the experimental results. This suggests that the thermal gap is an important factor and must be incorporated in the analyses.

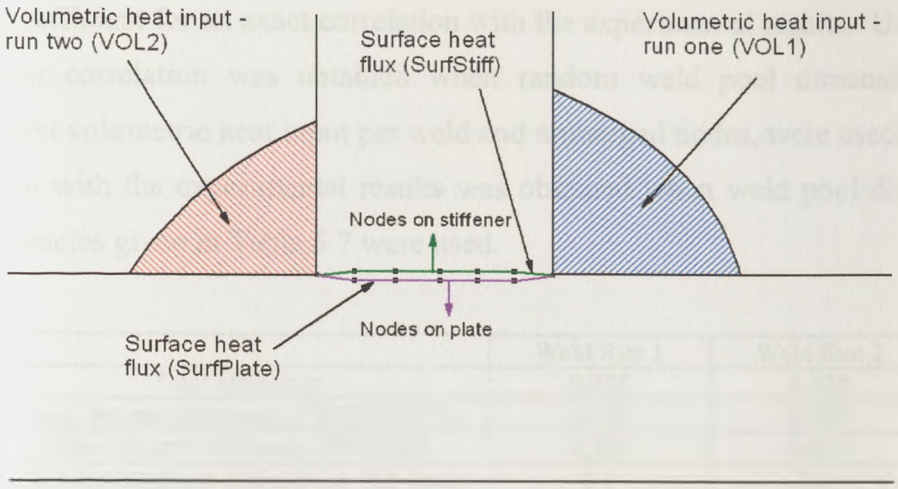

Figure 5.25: Heat input and non-merged nodes

A study on the heat flow between the stiffener and the plate was also performed, via the application of a surface heat flux on the boundaries defining this region as shown in Figure 5.25. In this instance the majority of the heat is delivered as a volumetric heat input characterized by the weld pool shape, while the remainder is supplied to the lines defining the boundaries following equation 5.8.

$$q_{area} = \frac{\eta IV}{l_m (v.heating\_time)(unit\_length)} \qquad \textit{Equation 5.8}$$

Where l_m is the length of the line, in this instance being the stiffener thickness, the heating time is the transient time when the heat input is applied, taken to be 3 seconds and the unit length being equivalent to 1m. The efficiency used determines the heat flow, such that a negative efficiency implies heat withdrawn from the material and a positive efficiency represents a heat input. For close correlation with the experimental results the final efficiencies given in Table 5.6, were used.

	Weld run one	Weld run two
Total Efficiency	0.900	0.925
Volumetric Efficiency	0.725	0.750
SurfPlate Efficiency	0.000	-0.150
SurfStiff Efficiency	0.175	0.325

Table 5.6: Efficiencies used for multiple fillet welding

seconds. This was not the case for weld run two where the maximum temperatures were not attained, despite using an artificially high weld efficiency. Furthermore the computational thermal histories show a slower temperature decay and converge to a higher temperature after 300 seconds. The comparison between the thermocouple results and the finite element simulation model for weld run two is given in Figure 5.27.

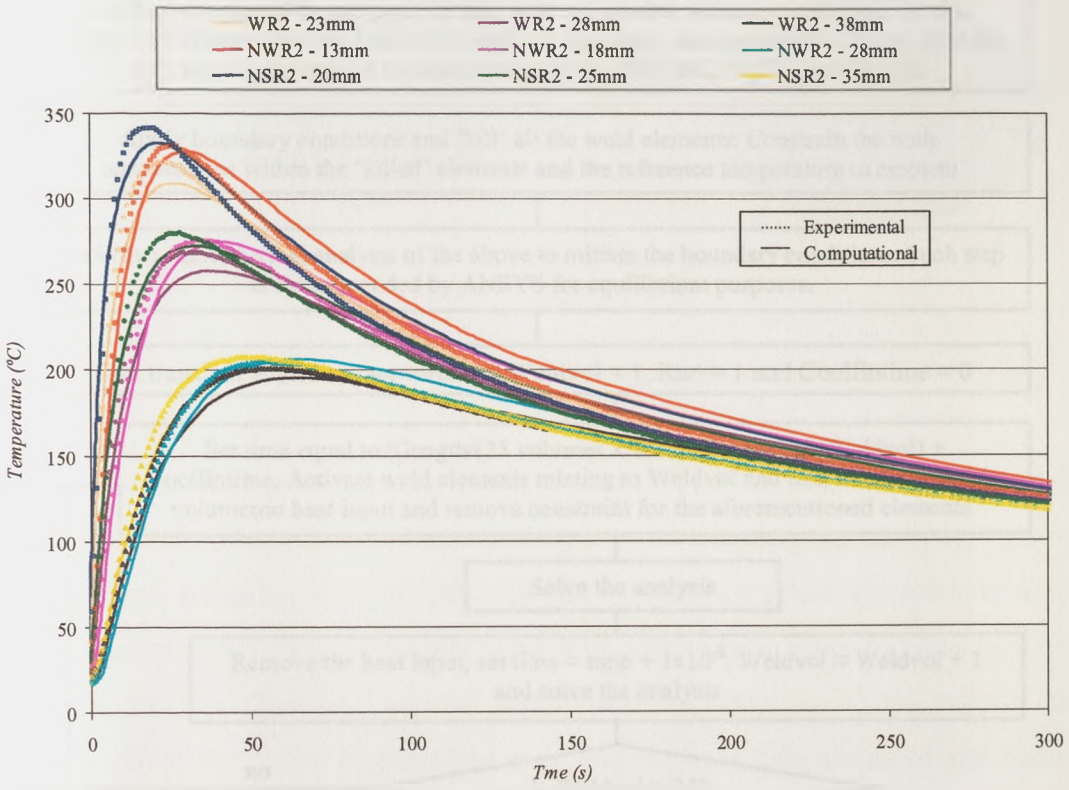

Figure 5.27: Comparison between average thermocouple results and simulation – run two

5.3.3 Three-dimensional finite element model

In the cross-sectional two-dimensional models, unrealistically high weld efficiencies were used, in order to match the experimental results. This was particular the case for the second weld run, where the thermal histories did not follow the experimental results. Three-dimensional analysis can be used to investigate the assumptions adopted in the two-dimensional analyses, and in particular, examines the assumption that no heat flows in the longitudinal direction. Together with the above, the study

performed on the three-dimensional transient thermal analysis, inspects the effect of the undeposited weld, ahead of the arc, via the use of the element 'birth and death' technique through the algorithm given in Figure 5.28.

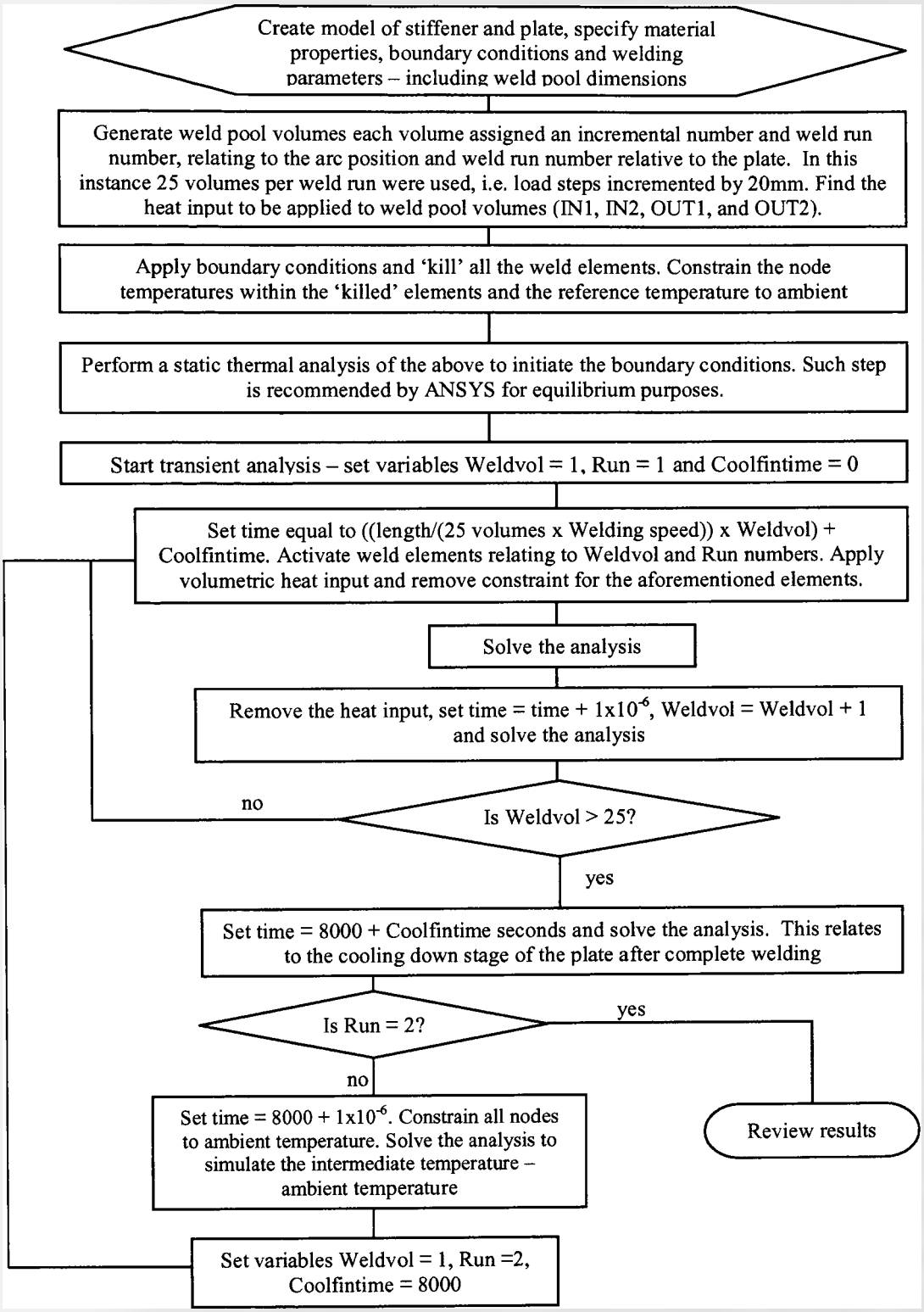

Figure 5.28: Algorithm for transient multiple fillet thermal analysis

Figure 5.29 shows the finite element model together with the activated elements at arc position 260mm from the edge of the plate.

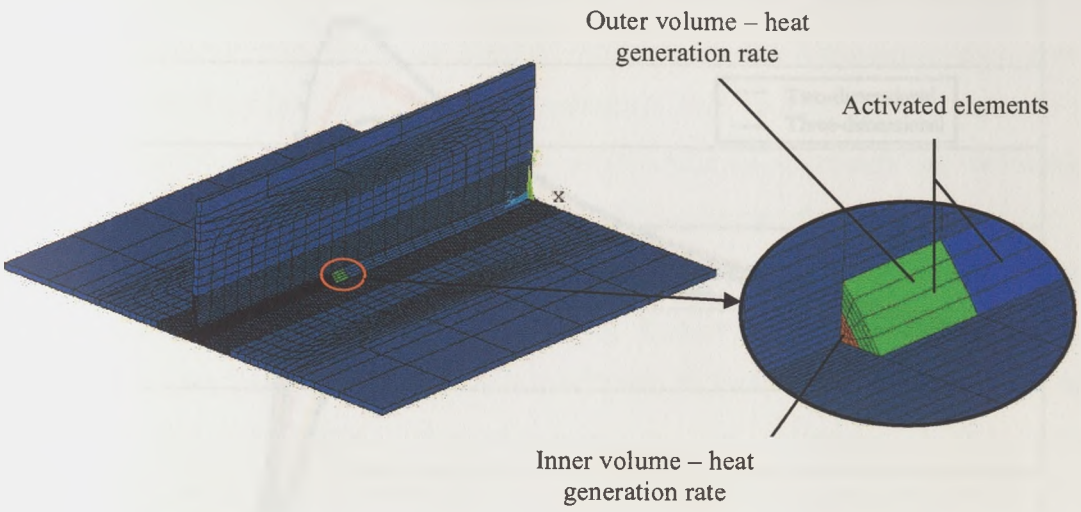

Figure 5.29: Three dimensional finite element model and heat input positions.

Using the same welding parameters, weld pool dimensions and the same proportional outer and inner volume efficiencies as in the latter two dimensional analysis, together with unmerged nodes between the stiffener and the plates, a good agreement with the experimental results was attained when the total efficiencies were reduced to 0.845 and 0.841 for the first and second weld runs respectively. This reflects the unabsorbed heat due to the undeposited weld and the heat flow ahead of and behind the arc.

Figures 5.30 and 5.31, compares the thermal histories of the two-dimensional and three-dimensional analyses at weld position z = 0.24 (time = 50s), for weld run one and two respectively. A good agreement was attained for weld run one, when the efficiency was reduced. Slight deviations can be seen for weld run two, in particular the maximum temperatures attained in the three-dimensional model reflect more the realistic experimental results. This suggests that in double-sided fillet welding the assumption of no heat flow in the longitudinal direction still holds but the undeposited weld in weld run two distorts the heat flow patterns. However, the use of a two dimensional cross sectional model is very economic and gives results which are adequate as input to the structural phase of the uncoupled distortion simulation.

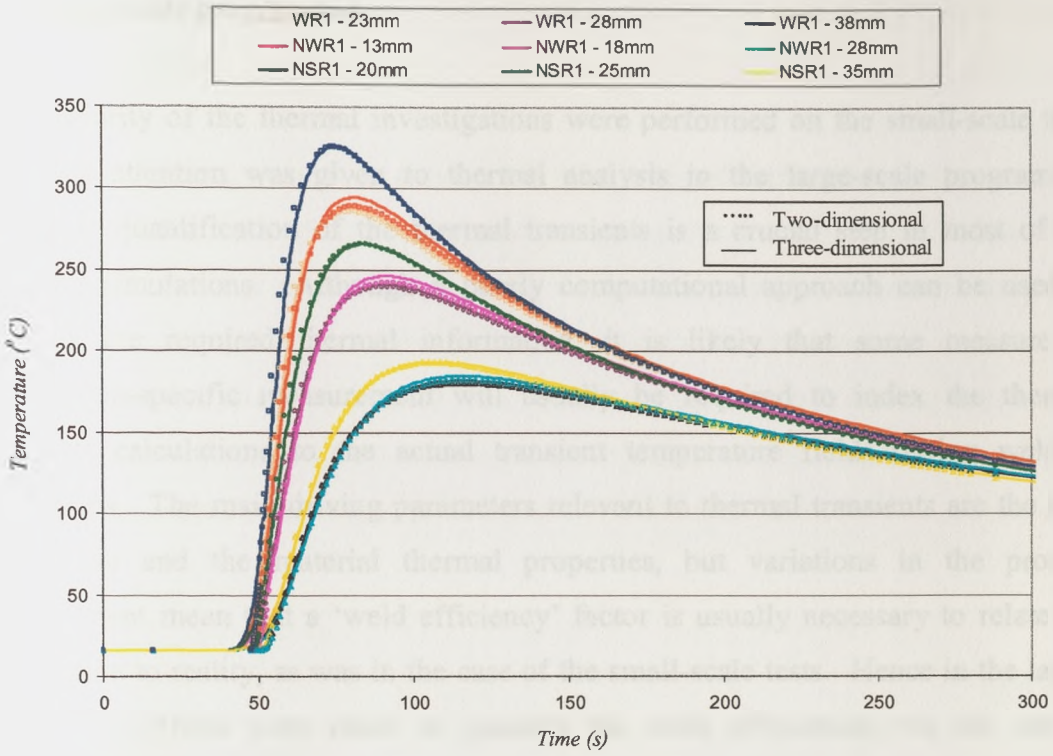

Figure 5.30: Comparison between three-dimensional and two-dimensional finite element models – run one.

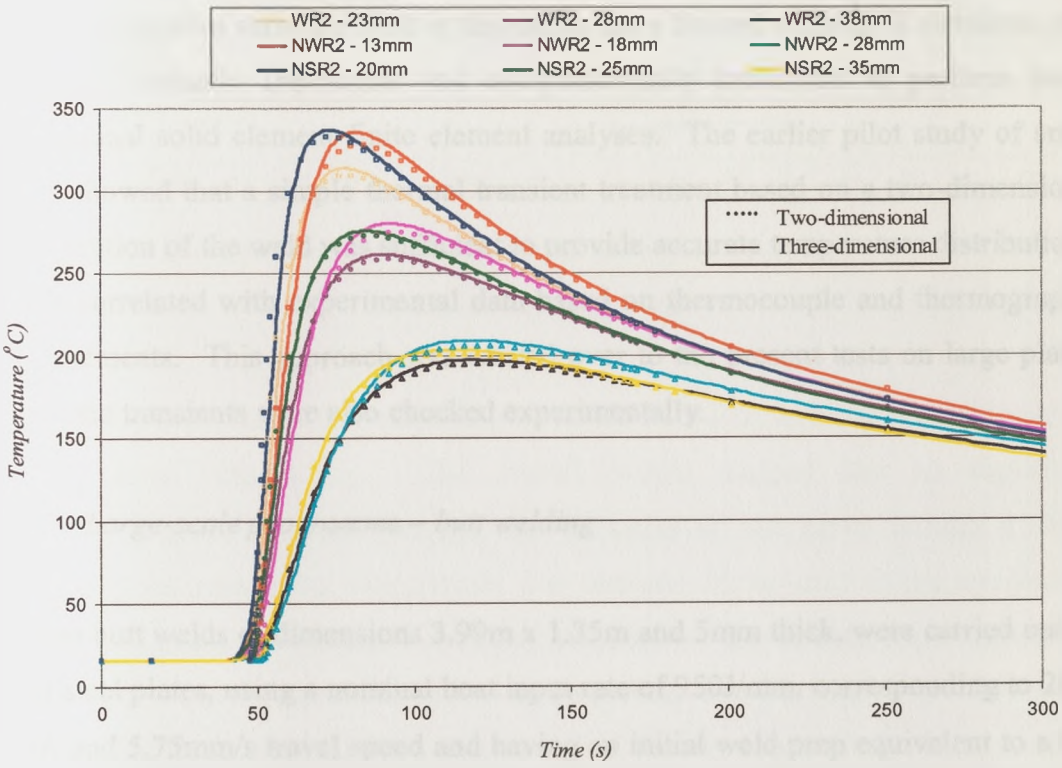

Figure 5.31: Comparison between three-dimensional and two-dimensional finite element models – run two.

5.4 Large-scale programme

The majority of the thermal investigations were performed on the small-scale tests and less attention was given to thermal analysis in the large-scale programme. However quantification of the thermal transients is a crucial step in most of the welding simulations. Although a purely computational approach can be used to provide the required thermal information, it is likely that some measure of application-specific measurement will usually be required to index the thermal transient calculations to the actual transient temperature fields during welding operations. The main driving parameters relevant to thermal transients are the heat input rate and the material thermal properties, but variations in the process environment mean that a 'weld efficiency' factor is usually necessary to relate the calculation to reality, as was in the case of the small-scale tests. Hence in the large-scale tests efforts were made to quantify the weld efficiencies via the use of thermocouple arrays, in line with finite element simulations.

The finite element software used in this thesis has a limited number of elements, thus making it virtually impossible and computationally inefficient to perform three-dimensional solid element finite element analyses. The earlier pilot study of small plates showed that a simple thermal transient treatment based on a two-dimensional cross-section of the weld was sufficient to provide accurate temperature distributions, which correlated with experimental data based on thermocouple and thermographic measurements. This approach was carried over to the present tests on large plates, where the transients were also checked experimentally.

5.4.1 Large-scale programme – butt welding

Six test butt welds of dimensions 3.99m x 1.35m and 5mm thick, were carried out on CMn steel plates, using a nominal heat input rate of 950J/mm, corresponding to 26V, 210A and 5.75mm/s travel speed and having an initial weld prep equivalent to a 60° included angle and an average 1mm weld gap. Due to alignment and machining problems, the weld gap was not constant throughout, but ranging from no weld gap

to a 2mm gap. Hence, the use of a backing strip was essential to prevent any possible burn-outs.

Previous weld tests have shown that there is an insignificant difference between the upper and lower faces of the welded plate, for plate thickness 6mm and below. The use of backing strip might have altered the thermal patterns, hence a study was performed to find the effect of the backing strip on the far-field thermal transients, in particular for temperatures below 300°. Four small scale 5mm thick test plates, were butt welded, with and without backing strip, together with an initial 1mm and zero weld gap, using the same welding parameters as the larger plates.

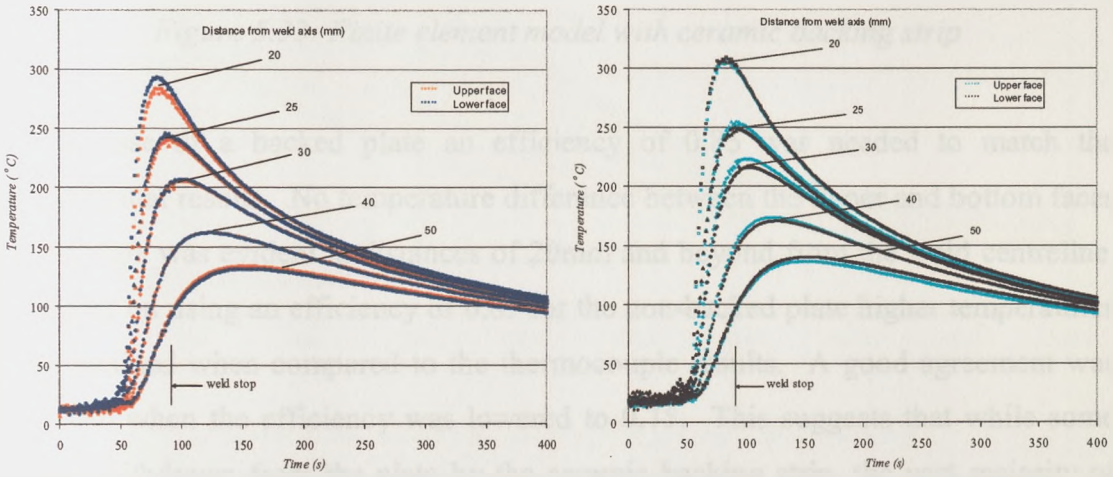

Figure 5.32: Comparison between upper and lower face thermal transients, with and without backing strip.

Figure 5.32a and b show the temperature transients for butt welding with and without backing strip, respectively. The overall results suggest that no significant temperature gradients exist through the thickness of the plate, though a slight increase in the maximum temperatures was attained, in the case of the non-backed plates. This is a result of some heat being absorbed by the backing strip. This effect was studied via two dimensional cross-sectional finite element analyses, where it was assumed that the ceramic backing strip absorbed heat by conduction, via the merging of nodes at the ceramic/plate interface as shown in Figure 5.33. Constant thermal material properties of a ceramic compound (55% SiO, 30% AO and 8% MgO)

similar to the backing strip, were applied to these elements, while the weld heat input was applied as a volumetric heat input to the weld pool region.

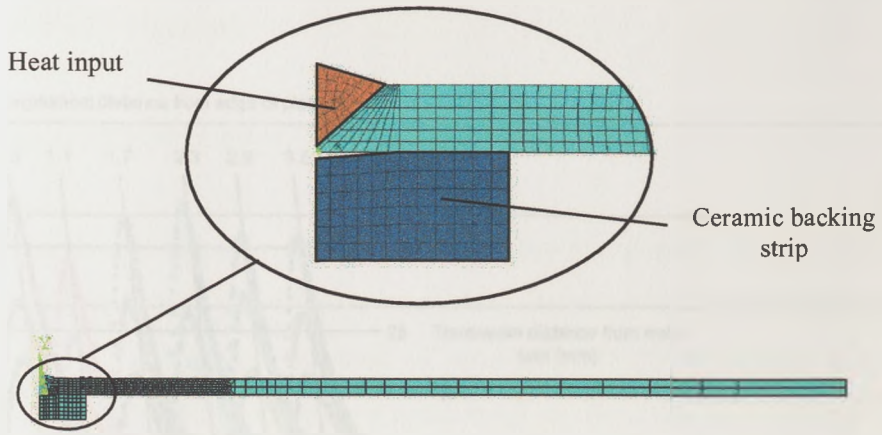

Figure 5.33: Finite element model with ceramic backing strip

In the case of a backed plate an efficiency of 0.85 was needed to match the experimental results. No temperature difference between the upper and bottom faces of the plate was evident at distances of 20mm and beyond from the weld centreline. However on using an efficiency of 0.85 for the non-backed plate higher temperatures were attained when compared to the thermocouple results. A good agreement was achieved when the efficiency was lowered to 0.75. This suggests that while some heat is withdrawn from the plate by the ceramic backing strip, the vast majority of the heat lost to the environment is reabsorbed back by the ceramic, via radiation. In essence it may be concluded that the ceramic backing strip had an insignificant effect on the thermal patterns, and the effect can be simply adjusted via an arbitrary efficiency.

In the large-scale butt-welded plates, six thermocouple arrays, consisting of five thermocouple each were used to measure the temperature transients. The thermocouples were placed on the bottom surface of the plate at distances 0.5m, 1.1m, 1.7m, 2.3m, 2.9m and 3.5m from the starting edge of the plates. The five thermocouples in each array were placed at 20mm, 25mm, 30mm, 40mm and 50mm away from the weld line.

Figure 5.34 shows the thermal transients for test specimen four, while Table 5.8 gives the average maximum temperatures at specific positions from the weld line, together with the time, such temperatures were attained, relative to the arc position.

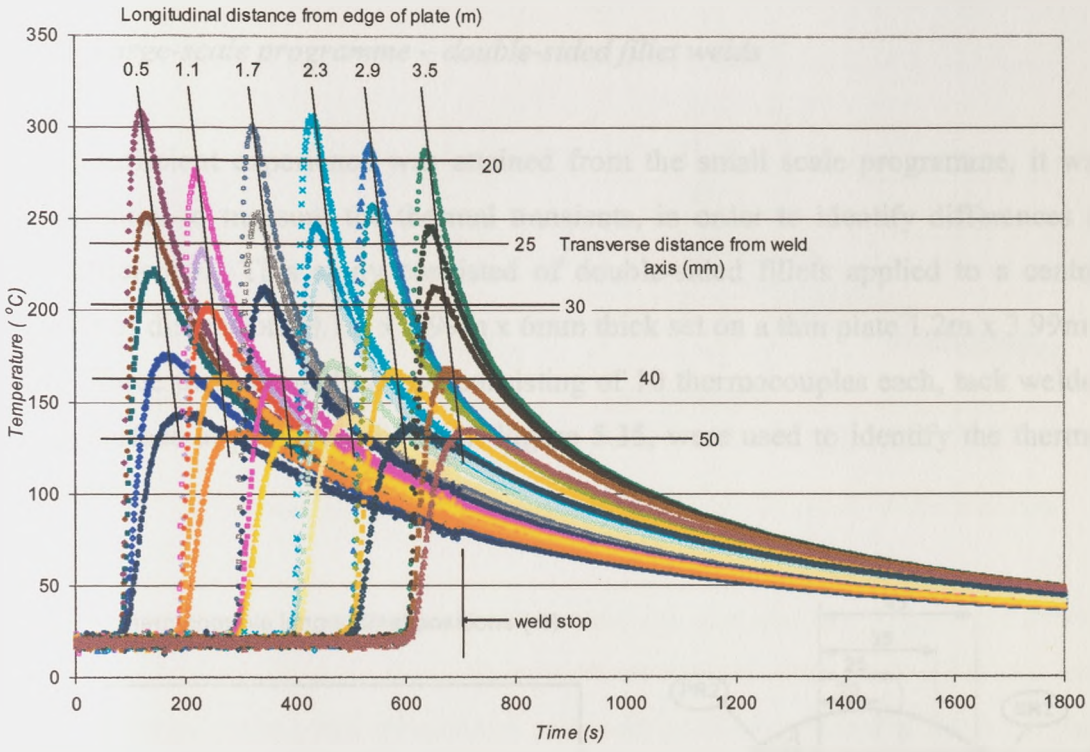

Figure 5.34: Thermal history plot for test specimen B4

Position from weld line (mm)	20	25	30	40	50
Average maximum temperature (°C)	293.8	246.5	214.1	167.6	137.3
Average relative time at maximum temperature (s)	27.88	38.57	48.81	73.91	101.07

Table 5.8: Average maximum temperatures and relative time

The inconsistent peaks are thought to be due to the inaccuracies of the thermocouple positions relative to the weld axis, in particular due to the different weld gaps present throughout the welded plates and the high thermal gradient transverse to the weld.

A two-dimensional cross-sectional finite element model was used to simulate the thermal transients. Alternative computations were carried out using two different configurations of volumetric heat input. In the first instance, the thermal energy was applied to a fully penetrated V-preparation and in the second, a 0.5mm un-penetrated

root was simulated. The temperature difference between the two models was no greater than 5°C at 20mm distance from the weld centreline. Furthermore a strong agreement was attained between the simulation and experimental results when a weld efficiency of 0.725 was used.

5.4.2 Large-scale programme – double-sided fillet welds

While, sufficient experience was attained from the small scale programme, it was still essential to measure the thermal transients, in order to identify differences in weld efficiency. This study consisted of double-sided fillets applied to a central stiffener of dimensions 0.1m x 3.99m x 6mm thick set on a thin plate 1.2m x 3.99m x 5mm. Three thermocouple arrays consisting of 10 thermocouples each, tack welded on the surface at positions shown in Figure 5.35, were used to identify the thermal transients.

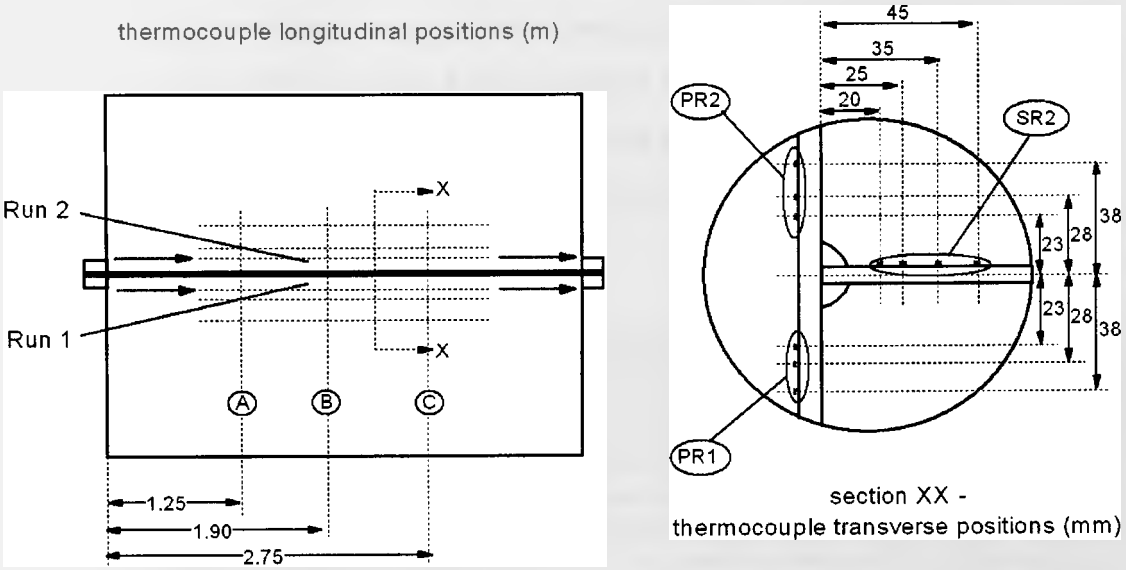

Figure 5.35: Thermocouple positions of double-sided large plate fillet welding

The nominal heat input used ranged from 1.13 to 1.17kJ/mm, corresponding to 221A, 25.9V and 5mm/s. Though there are only small fluctuations in the nominal heat input, there are greater fluctuations in the heat flow patterns, depending on the welding gun position / angle relative to the plate/ stiffener. Thus every weld run

produced different thermal patterns and hence the thermal analyses reflect the independent welding runs. Figure 5.36 shows the thermocouple results of test specimen two for the first and second weld runs respectively.

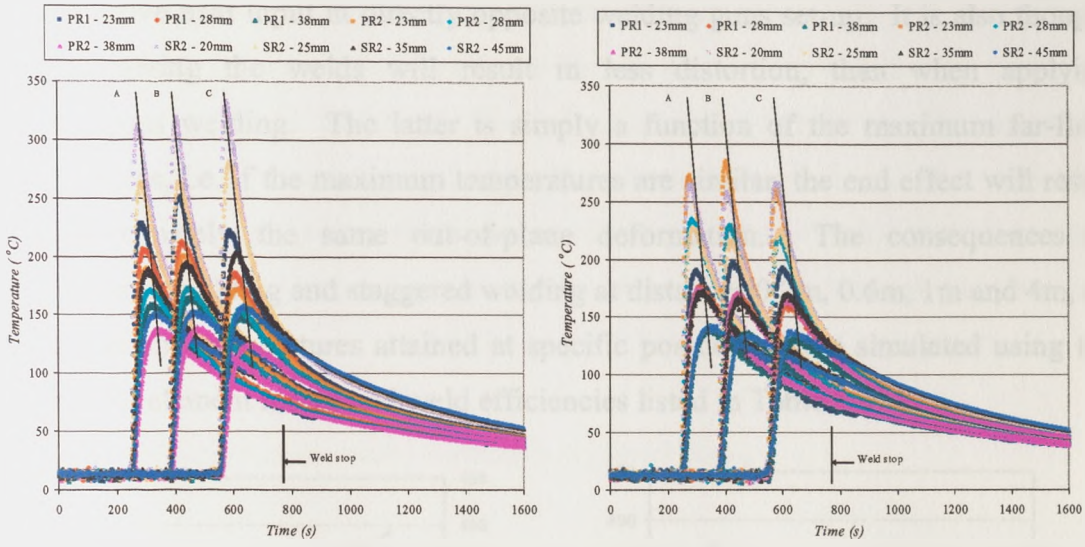

Figure 5.36: Thermocouple results test two a) Weld run one b) Weld run two

The different thermal transients evident in weld run one and two suggest a different heat generation profile, such that a finite element analysis with dual volumetric heat input, unmerged nodes, and efficiencies and weld profiles as listed in Table 5.9, was required for correct matching with the experimental results. The second run was more efficient in this case, as before.

	Test One		Test Two	
	Run 1	Run 2	Run 1	Run 2
Total efficiency	0.787	0.825	0.7875	0.850
Outer volume efficiency (OUT1/OUT2)	0.500	0.500	0.500	0.500
Inner volume efficiency (IN1/IN2)	0.287	0.325	0.2875	0.350
Weld leg length on stiffener L1 / L5 (mm)	11.0	8.5	10.0	8.5
Weld leg length on plate L2 / L6 (mm)	4.5	7.5	6.0	7.5

Table 5.9: Efficiencies and weld profiles assumed in double-sided large plate fillet welding

Furthermore the thermal transients attained during simultaneous and staggered double sided fillet welding were investigated via finite element simulations. This reflects the real shop-floor welding sequence by the ship-building company collaborating in this project, whereby double sided welding is performed in a

staggered fashion, such that the two welding guns are separated by a distance of approximately 600mm. While reducing the production time for welding stiffeners, a staggered approach was adopted due to metallurgical imperfections resulting from the excessive heat input in directly opposite welding guns set-up. It is also thought that staggering the welds will result in less distortion, than when applying simultaneous welding. The latter is simply a function of the maximum far-field temperatures, i.e. if the maximum temperatures are similar, the end effect will result in approximately the same out-of-plane deformation. The consequences of simultaneous welding and staggered welding at distances 0.2m, 0.6m, 1m and 4m, on the maximum temperatures attained at specific positions, were simulated using the same finite element model and weld efficiencies listed in Table 5.9.

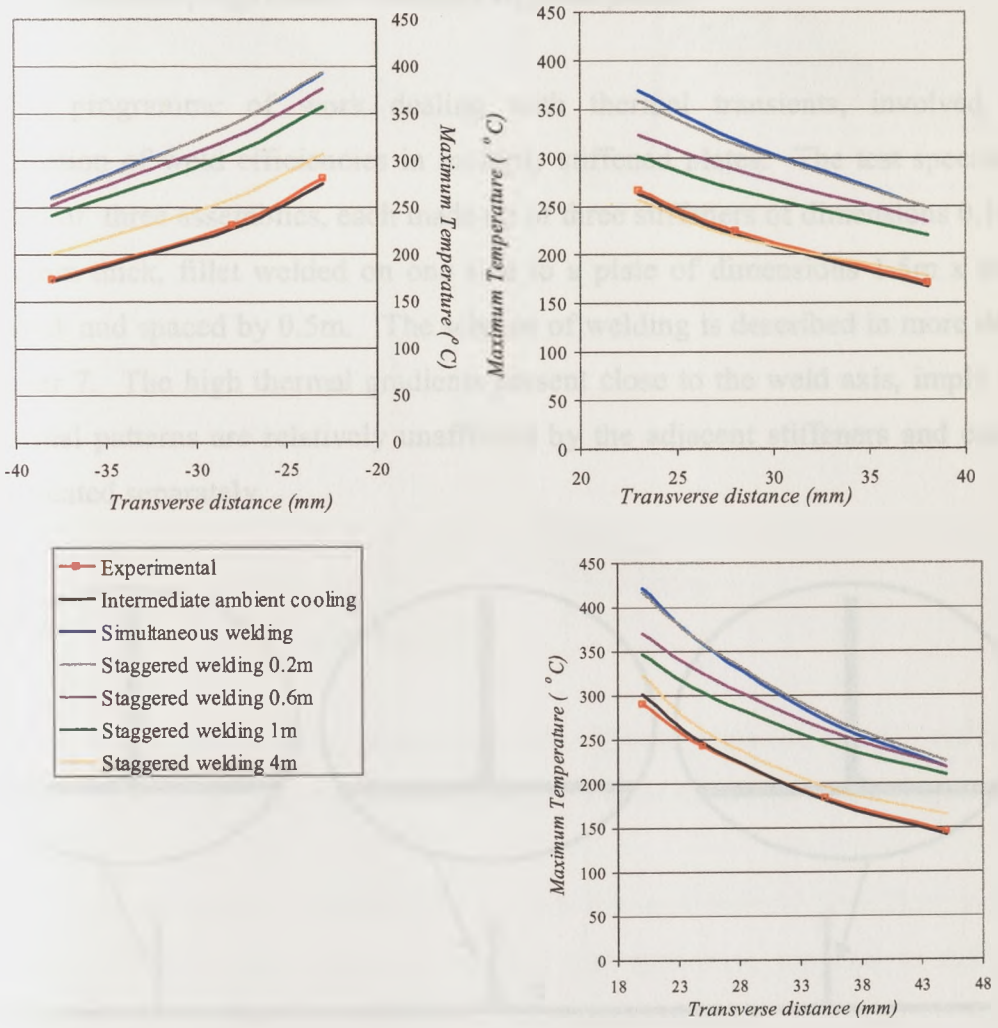

Figure 5.37: Maximum temperatures attain at a) PR2, b) PR1 and c) SR2.

Figure 5.37, shows the maximum temperatures attained at the far-field positions for the different offset distances of the two welding heads. It is evident that the highest maximum temperatures are obtained in simultaneous welding, resulting in the highest contraction forces and out-of-plane deformations. On the other hand staggering the welding heads, reduces the maximum temperatures (relative to simultaneous welding), the amount depending on the cooling time. The sequential complete welding of one run and immediate deposition of the another weld after complete welding of the first weld pass, resulted in the closest temperature transients, however not enough time was given for the heat to dissipate through the plate and lost to ambient.

5.4.3 Large-scale programme – multiply stiffened plates

The last programme of work dealing with thermal transients, involved the quantification of weld efficiencies in multiply stiffened plates. The test specimens consisted of three assemblies, each made up of three stiffeners of dimensions 0.1m x 4m x 6mm thick, fillet welded on one side to a plate of dimensions 1.5m x 4m x 5mm thick and spaced by 0.5m. The scheme of welding is described in more detail in chapter 7. The high thermal gradients present close to the weld axis, imply that the thermal patterns are relatively unaffected by the adjacent stiffeners and can be simply treated separately.

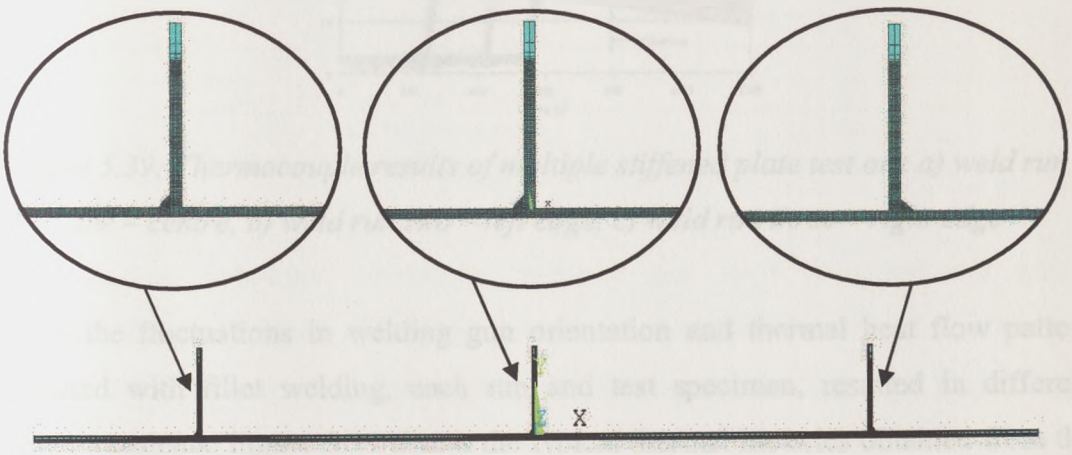

Figure 5.38: Finite element model of multiple stiffened plate.

A two-dimensional cross-sectional finite element analysis, as described in 5.3.2 was used to match the weld efficiencies to the experimental results. The finite element model is shown in Figure 5.38. The nominal heat input was similar to the double-fillet weld tests specimens and corresponded to an average heat input of 1.124kJ/mm, equivalent to 25.9V, 217A and 5mm/s travel speed.

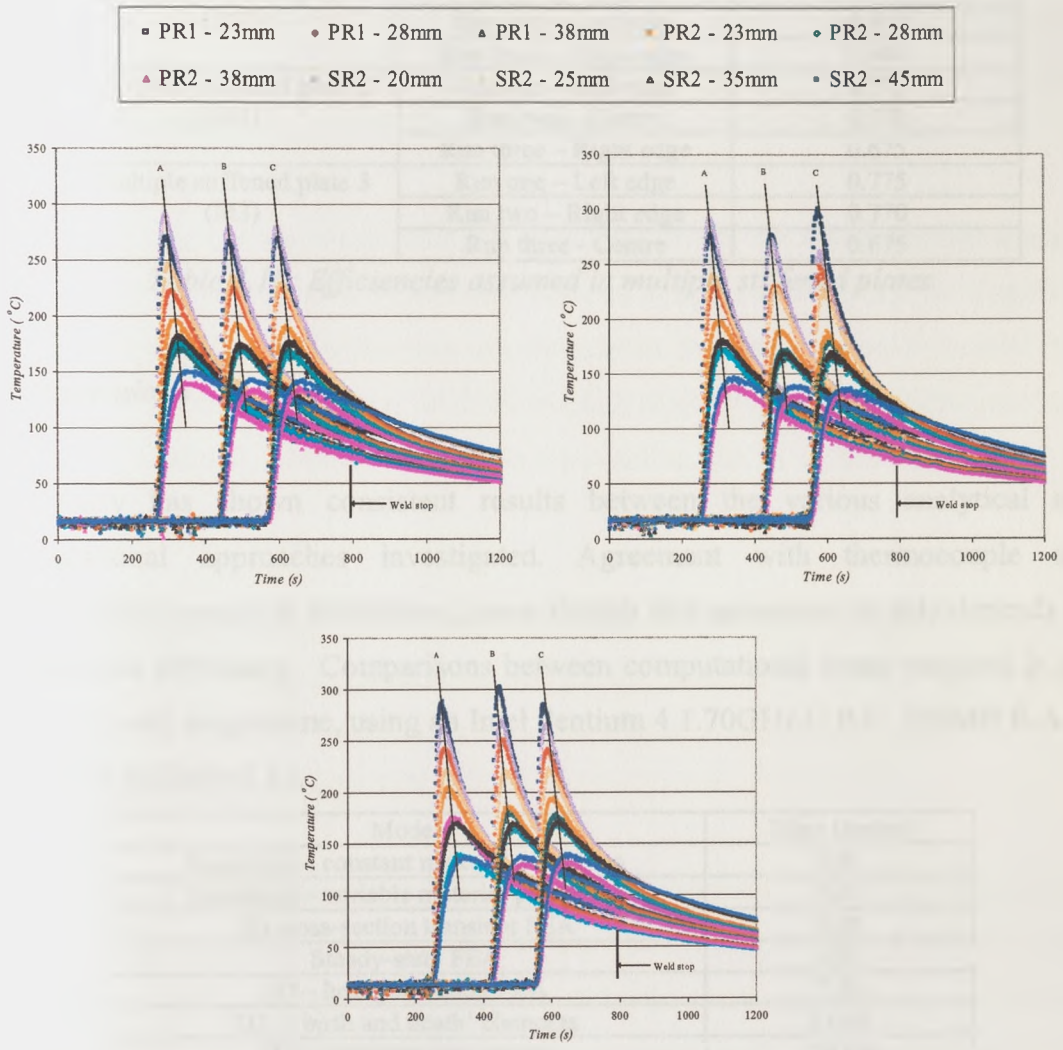

Figure 5.39: Thermocouple results of multiple stiffened plate test one a) weld run one – centre, b) weld run two – left edge, c) weld run three – right edge

Due to the fluctuations in welding gun orientation and thermal heat flow pattern associated with fillet welding, each run and test specimen, resulted in different thermal transients. Figure 5.39 shows the typical thermal histories obtained from the thermocouple results for test specimen one. Note that the positions of the thermocouples are similar to the double-sided experiments, Figure 5.35, such that

PR1 refers to the welded side of the plate, i.e. the side were the weld is deposited. The final correlation between the experimental and simulation results was obtained by the adjustment of an arbitrary weld efficiency given in Table 5.10.

Test Specimen	Weld run	Total efficiency
Multiple stiffened plate 1 (M1)	Run one - Centre	0.815
	Run two – Left edge	0.800
	Run three – Right edge	0.840
Multiple stiffened plate 2 (M2)	Run one – Left edge	0.775
	Run two – Centre	0.770
	Run three – Right edge	0.675
Multiple stiffened plate 3 (M3)	Run one – Left edge	0.775
	Run two – Right edge	0.770
	Run three - Centre	0.675

Table 5.10: Efficiencies assumed in multiple stiffened plates

5.5 Discussions

The study has shown consistent results between the various analytical and computational approaches investigated. Agreement with thermocouple and thermographic results is satisfactory, even though this agreement largely depends on the assumed efficiency. Comparisons between computational times required in the pilot butt weld programme, using an Intel Pentium 4 1.70GHz C.P.U. 256MB R.A.M are shown in Table 5.11.

Model	Time (hours)
Rosenthal – constant material properties	0.01
Rosenthal – variable material properties	0.20
2D cross-section transient FEA	0.08
Steady-state FEA	0.50
3D – heat generation FEA	7.50
3D – 'birth and death' elements	14.00
3D – Friedman heat source	24.00

Table 5.11: Simulation times for the different models

The analytical solutions, obviously, required the least computational effort. However, these solutions will only provide temperature history plots during a continuous welding cycle and do not model subsequent cooling of a finite length welding operation. Hence if a coupled or uncoupled, staggered thermo-mechanical analysis is performed, the results obtained will not be sufficient unless the plate is very long. Furthermore analytical solution are dedicated to simple geometries and

become complex when dealing with heat sinks and other thermal breaks as is in the case of fillet welding. This makes analytical solutions confined to simple geometries and inadequate to simulate fillet welding.

The steady state computational analysis was also economic but the results deviated largely from the three-dimensional analysis pattern. This effect is most probably due to the limitation of the Flotran CFD code in modelling temperature-dependent material properties.

The various approaches to modelling of heat input in the three dimensional analysis gave consistent results in the temperature regions of interest and hence the simplified method of applying heat in the form of a volumetric heat input seems to be sufficient for the weld parameters chosen. In fillet welding arbitrary positions of the heat input have to be assumed, as these depend on the welding gun orientation relative to the weld.

The two dimensional approach proves to be the least time consuming of the methods used and provides accurate thermal results (but this does not mean that this approach will be adequate for the elasto-plastic and structural simulations as pointed out by Berglund and Runnemalm [5.12]).

In essence the thermal transients obtained from the finite element analyses, depend largely on the experimental results. In the test specimens investigated, thermocouple results were sufficient for the correlation with the simulation results, but thermal imaging provides whole-field information in a practical situation and therefore constitutes an unique tool for the evaluation of inputs to a thermo-mechanical determination of distortion or residual stress, caused by a welding process in more complex geometries and boundary conditions as is in the shop-floor case.

5.6 References

[5.1] Shu Wen, data obtained in study on CMn plate steel, private communication, 2003.

[5.2] Lindgren,L.E., 'Finite Element Modeling and Simulation of Welding. Part 2: Improved Material Modeling,' *Journal of Thermal Stresses,* Vol.24, pp.195-231, 2001.

[5.3] Birk-Sorensen,M., 'Simulation of Welding Distortions in Ship Section,' *PhD Thesis, Department of Naval Architecture and Offshore Engineering, Technical University of Denmark,* 1999.

[5.4] Rosenthal,D., 'The Theory of Moving Sources of Heat and its Application to Metal Treatments,' *Transactions of the American Society of Mechanical Engineering,* Vol.68, No.8 pp 849-866, 1946.

[5.5] Rosenthal,D., 'Mathematical theory of Heat Distribution During Welding and Cutting,' *Welding Journal,* 20(5), pp. 220s-234s, 1941.

[5.6] Rykalin,N.N., 'Thermal Welding Principles.' *I.A.N., SSSR (1947).*

[5.7] Camilleri,D., Comlekci,T., Lee,C.K., Tan,H. and Gray,T.G.F., 'Investigation of Temperature Transients During Flux-Cored Ar/CO_2 Butt Welding of CMn Steel Plates,' *Proceedings of the International Conference on Metal Fabrication and Welding Technology (METFAB – 2003),* pp. 107 – 116, 2003.

[5.8] Friedman,E., 'Thermomechanical Analysis of the Welding Process Using the Finite Element Method,' *ASME Journal of Pressure Vessel Technology,* Vol. 97, No.3, pp 206-213, 1975.

[5.9] Younan,M.Y.A., Wifi,A.S., and Fanous,I.F.Z, '3D Finite Element Modelling of the Welding Process using Element Birth and Element Movement Techniques,'

ASME Pressure Vessel and Piping Conf., Vancouver, Canada, Vol.422, pp 165-172, 2002.

[5.10] Candy,J., 'Measurement and Analysis of Transient Heat Transfer and Distortion in the Welding Process', *MEng Thesis, Mechanical Engineering Department, University of Strathclyde,* 2000.

[5.11] Olden,E. and Leggatt,R., 'Modelling of Residual Stresses at Grith Welds in Pipes,' *Recent Advances in Welding Simulation, ImechE Seminar Publication 2000-13,* pp 21-32, 1999.

[5.12] Berglund,D. and Runnemalm,H., Comparison of Deformation Pattern and Residual Stresses in Finite Element Models of a TIG-welded Stainless Steel Plate, *Proc.6th International Conf. On Trends in Welding Research,* Pine Mountain, Georgia, USA, 2002.

CHAPTER SIX

CHAPTER 6

INVESTIGATION OF WELDING DISTORTIONS – PILOT PROGRAMME

6.1 Introduction

This chapter describes the experimental and computational investigation of out-of-plane welding distortion in butt welded 0.5m square, 6mm thick plates and double – sided fillet welding of a central stiffener of dimensions 0.1m x 0.5m, 6mm thick to 0.5m square, 6.5mm thick steel plates. This study was designed as a pilot programme, to test out the distortion measurement techniques and computational approaches before up-scaling to a typical industrial size of fabrication. The overall longitudinal and transverse (angular) out-of-plane deformations of the plates were measured dynamically during the welding and cooling phases of the tests. A separate scanning system was applied before and after welding to measure the deformation profiles generated by welding.

The thermal transient stage of the uncoupled welding analysis was addressed in chapter five and this study sets out to investigate use of the thermo-elastic-plastic contraction algorithms presented in chapter three. The final, structural phase of the uncoupled computational strategy is then provided by standard finite-element software. A number of different methods have been examined and these were then cross-referenced to the experimental results obtained from linear-variable-displacement transducers and a laser distance measurement system.

6.1.1 *Mechanical properties of CMn steel*

Welding involves a high temperature thermal cycle and this means that the mechanical properties required for the welding simulations are non-linear and depend on temperature transients and history. The predominant temperature dependant mechanical properties in welded steel plates are the co-efficient of expansion, driving the thermal strains, while the yield strength, elastic and plastic modulus of the material determine the strength of different zones in the welded plate at different stages in the welding cycle.

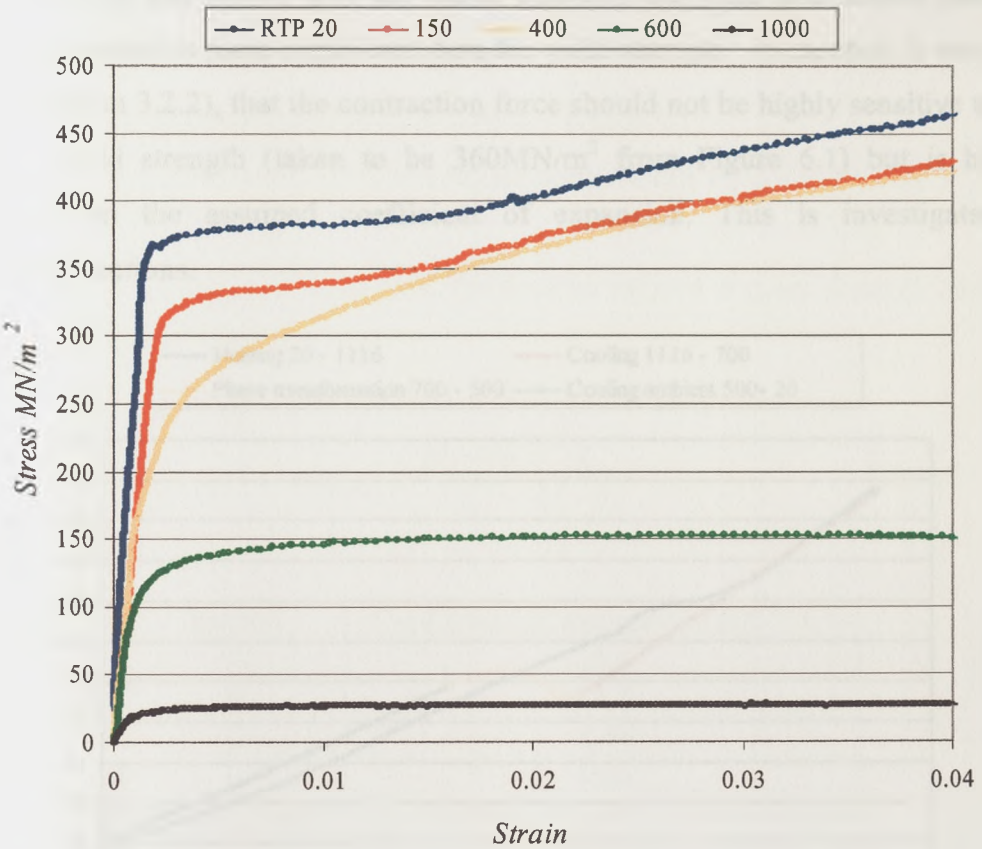

Figure 6.1: Stress vs strain curves at different temperatures

The stress-strain curves of CMn steel, given in Figure 6.1, were attained via tensile tests, performed at 5 different temperatures (Room temperature 20°C, 150°C, 400°C, 600°C and 1000°C). In the first instance the test specimens were heated to the aforementioned temperature and then subject to a tensile load. Figure 6.1 indicates that the strength of the material is highly dependant on the temperature. The

proposed simplified approach reduces the complexity of the welding simulation by prescribing constant material properties in conjunction with an elastic structural analysis. Furthermore an elastic, perfectly plastic material and a room temperature yield strength were assumed in the thermo-elasto-plastic algorithm.

The effect of non-linear material properties on the longitudinal contraction force was investigated in [6.1], with the conclusion that the strain hardening is a more significant mechanical property than yield strength. Furthermore a sensitivity analysis on the factors effecting the final out-of-plane deformation performed by Lightfoot [6.2] has shown that the ration between the yield and tensile strength (strain hardening) is more significant than the yield strength. In essence, it was also shown (section 3.2.2), that the contraction force should not be highly sensitive to the assumed yield strength (taken to be 360MN/m^2 from Figure 6.1) but is highly dependant on the assumed coefficient of expansion. This is investigated in subsequent sections.

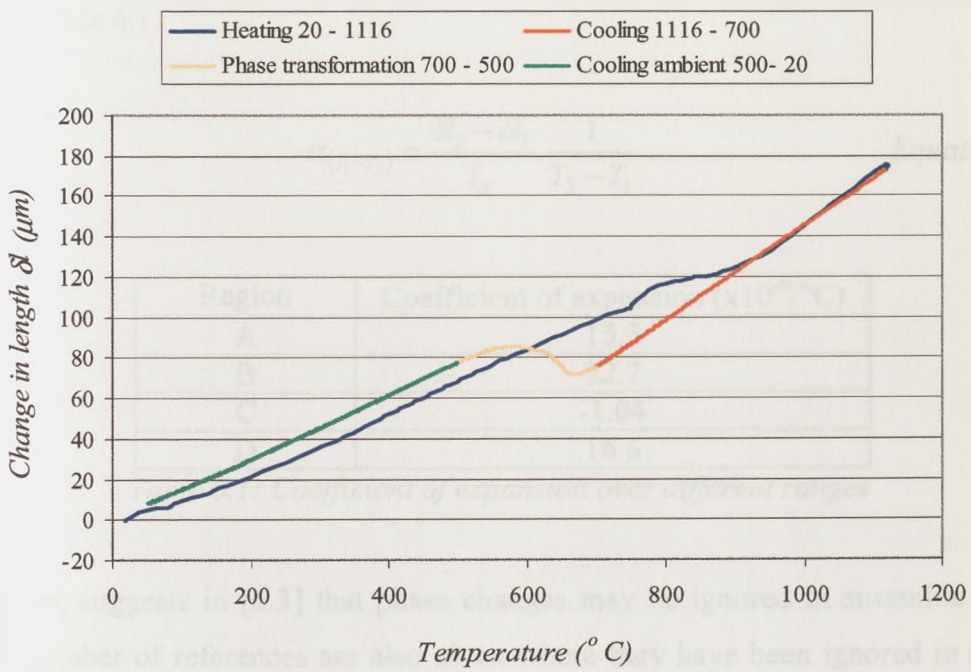

Figure 6.2: Change in length from dilatometer test

The coefficient of thermal expansion derived from the thermal dilatation of a sample is influenced by the thermo-mechanical history of the material, particularly since

phase transformations are present in CMn steel in the 725°C to 500°C range. Phase transformations are accompanied by volume changes, which lead to different thermal dilatations during heating and cooling. The coefficient of expansion for the plate materials used in the pilot programme, was found through a dilatometer tests, following a typical temperature history for points reaching a maximum temperature of 1116°C and obtained from the thermal simulations performed in chapter five.

Figure 6.2 shows the change in length of the sample with temperature of a specimen having 10mm original length. The graph may be divided in four sectors including:

- Heating (Ambient temperature 20°C to 1116°C – region A)
- Cooling (1116°C to 700°C – region B)
- Phase transformation (700°C to 500°C – region C)
- Cooling to ambient (500°C to ambient temperature 20°C – region D)

The averaged coefficient of expansion, for the four regions is given through equation 6.1, in Table 6.1.

$$\alpha_{(T_1-T_2)} = \frac{\delta l_2 - \delta l_1}{l_o} \cdot \frac{1}{T_2 - T_1} \qquad \textit{Equation 6.1}$$

Region	Coefficient of expansion ($x10^{-6}$/°C)
A	15.3
B	22.7
C	-1.04
D	16.6

Table 6.1: Coefficient of expansion over different ranges

Lindgren, suggests in [6.3] that phase changes may be ignored in austenitic steels, and a number of references are also given where they have been ignored in ferritic steels. This study ignores the effects of phase changes, and uses a constant coefficient of expansion. In the work performed by Okerblom [6.4] and Gray *et al* [6.5], [6.6] the expansivity was taken to be the coefficient of expansion at ⅓ of the melting temperature – taken to be $14x10^{-6}$. An averaged coefficient of expansion

that takes into account volume change due to phase transformations may be incorporated in the mismatched and contraction thermal strain algorithms, making the analyses significantly closer to reality. Typically for points cooling from a maximum temperature of 1000°C the averaged co-efficient of thermal expansion is 14.72×10^{-6}.

6.2 Out-of-plane distortion of butt welded steel plates

Butt welds were carried out on 10 assemblies, each comprising of two tack-welded plates and run-on/off tabs. The tabs were tack welded first, followed by a tack weld 3cm long at the mid-length of the plate. Half of the tacked assemblies, test specimens 6 – 10, were then thermally stress relieved at 600°C for two hours, followed by slow cooling. These samples were used to investigate effects in 'as-received' plates, being subject to initial residual stresses derived from their corresponding manufacturing processes and underwater laser cutting. Note that no restraint on in-plane or out-of-plane deformation was applied to the test specimens, the plates being simply supported at four points as shown in Figure 6.3.

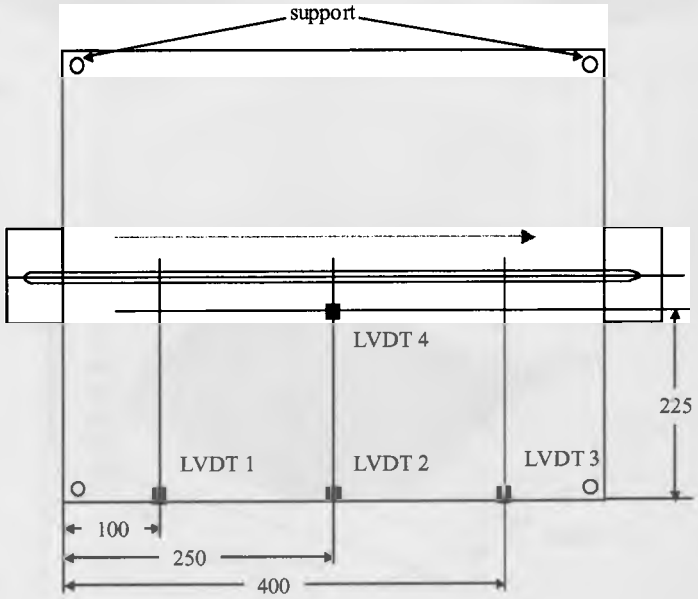

Figure 6.3: Positions of linear-variable displacement transducers and supports

Four linear variable displacement transducers (LVDT) placed at positions shown in Figure 6.3, were used to measure dynamic out-of-plane deformations, such that

LVDT 1, 2 and 3 gave the transient longitudinal curvature at the edge of the plate, while LVDT 2 and 4 recorded the transient angular distortion, during the welding and cooling stages of the plate.

6.2.1 Test observations and results

The assemblies deformed typically by transverse angular distortion accompanied by longitudinal curvature corresponding to the first buckling mode, i.e. assuming a saddle shape. Figure 6.4, shows a typical result (test specimen 1), from the static, before-and-after measurements, where the initial form of the tacked assembly happened to be relatively flat. The final deformation was calculated by subtracting the initial measurements from the final profile, as given in Figure 6.4c.

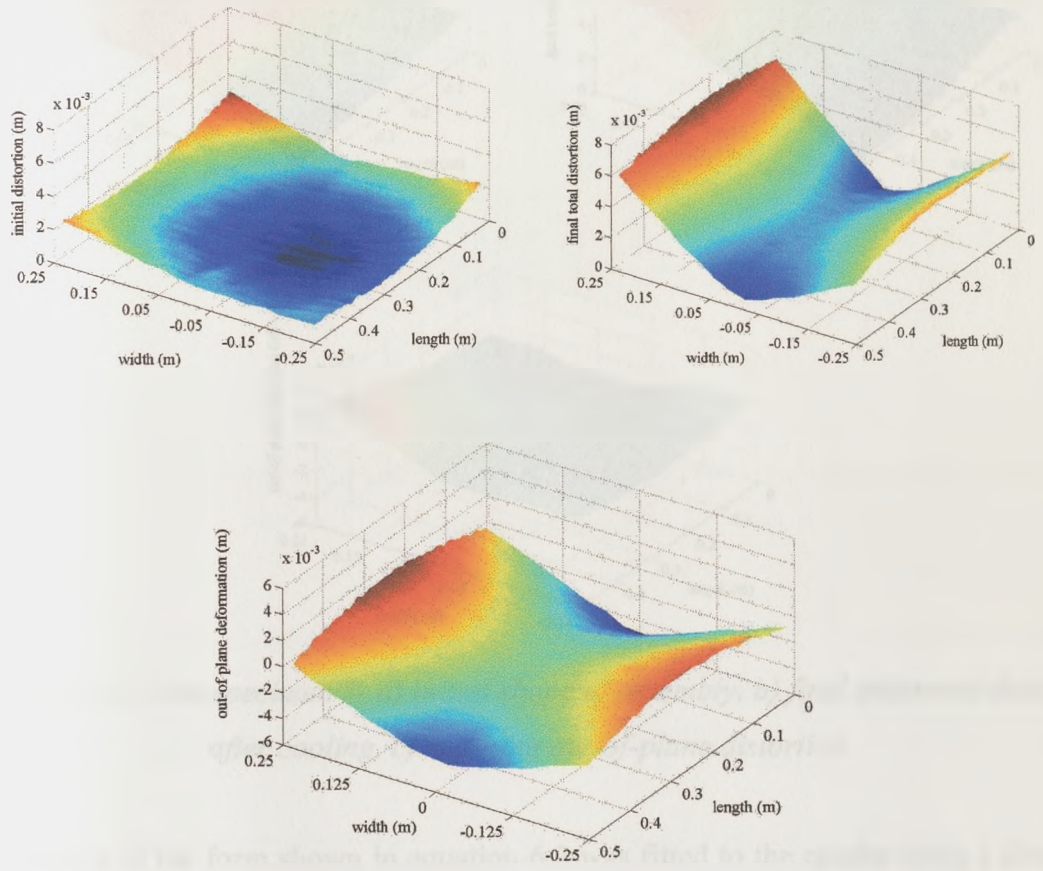

Figure 6.4: Test-specimen 1- a) initial shape of assembly, b) final deformed shape after cooling, c) resulting out-of-plane distortion

Nonetheless, small differences in the initial shape and restraint could stimulate different modes of out-of-plane longitudinal bending and this was found in three of the ten experiments, two of which had been stress relieved initially. It was observed that a small, negative, initial angular setting of the tacked plates means that the longitudinal contraction force acts above the neutral axis, thus reversing the longitudinal curvature relative to the case where the plate is initially relatively flat. Test specimens five, seven and eight exhibited such an effect. This suggests that the initial shape of the tacked assemblies has a stronger role in the final deformation than initial residual stresses. A typical result is shown in Figure 6.5.

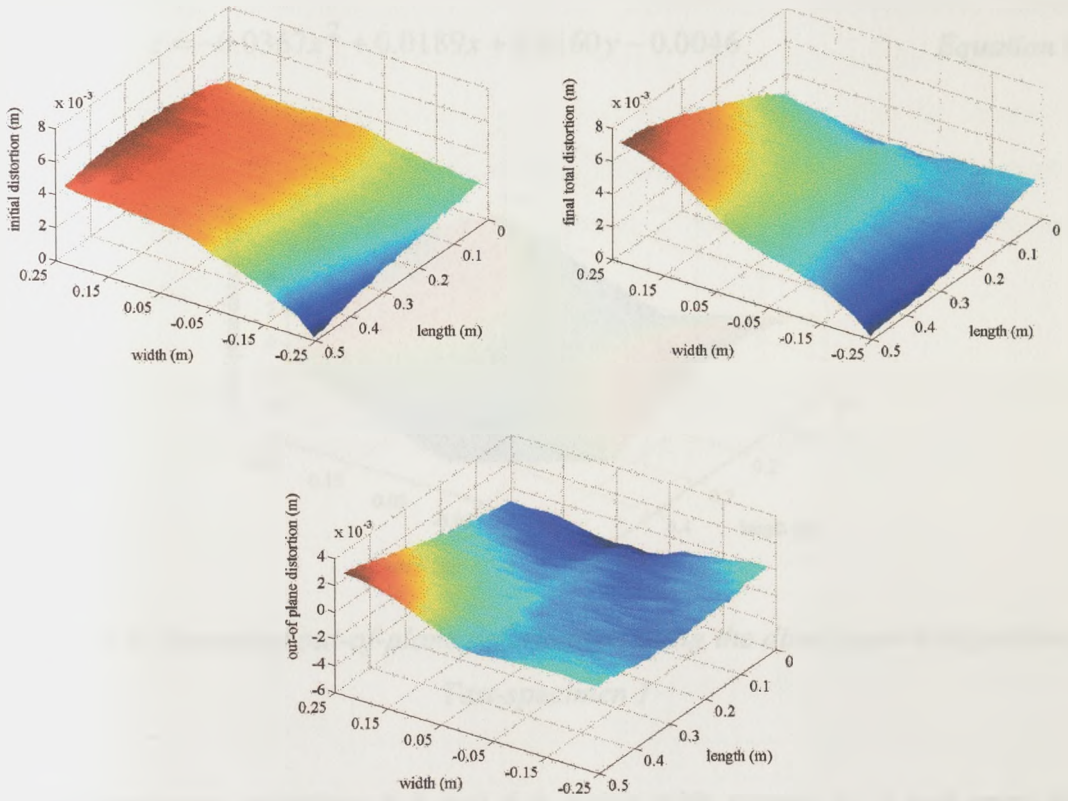

Figure 6.5: Test-specimen 7- a) initial shape of assembly, b) final deformed shape after cooling, c) resulting out-of-plane distortion

A function of the form shown in equation 6.2 was fitted to the results using a direct-search algorithm [6.7] to generate detailed, smooth, out-of-plane deformation profiles, comparable with the computational results, such that the quadratic function defines the longitudinal curvature and the linear function defines the V-shaped angular distortion – typical of the majority of the specimens.

$$z = Ax^2 + Bx + Cy + D \qquad \textit{Equation 6.2}$$

The final out-of-plane distortion of test specimen 1, which is a more typical case, follows the equations below, where equation 6.3 represents the distortion in the left-hand half of the plate (in the direction of welding) and equation 6.4 represents the distortion in the right hand half. The equivalent out-of-plane deformation is given in Figure 6.6.

$$z = -0.0365x^2 + 0.0188x + 0.0122y - 0.0044 \qquad \textit{Equation 6.3}$$

$$z = -0.0367x^2 + 0.0189x + 0.0160y - 0.0046 \qquad \textit{Equation 6.4}$$

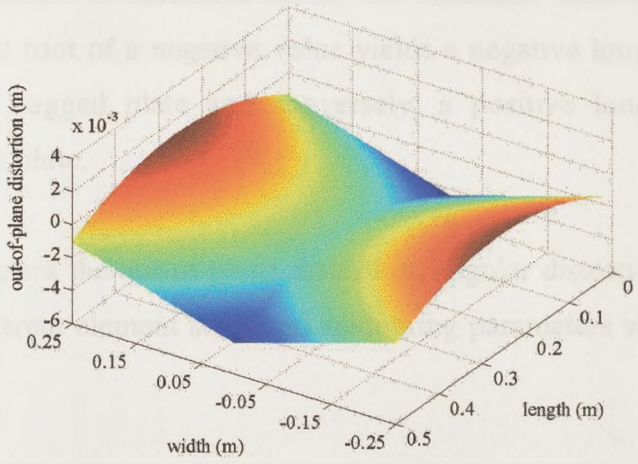

Figure 6.6: Smoothed out-of-plane deformation using the direct search algorithm - Test-specimen 1

By differentiating equations 6.3 and 6.4, twice with respect to y and once with respect to x, the longitudinal curvature and angular distortion can be characterised by two constants, given in Table 6.2.

	Left hand half	Right hand half	Average
Longitudinal curvature $\frac{\partial^2 z}{\partial x^2}$ (m^{-1})	-0.0730	-0.0734	-0.0732
Angular distortion $\tan^{-1}\left(\frac{\partial z}{\partial y}\right)$ (°)	0.699	0.917	0.808

Table 6.2: Longitudinal curvature and angular distortion of test specimen 1

The above equations are not sufficient to represent the out-of-plane deformation of the inverted, sagged (initially negative angular setting) test specimens. In these cases the smoothing algorithm presented in chapter 4, section 4.7.4, after the work of Feng et al [6.8] and Comlekci et al [6.9] is more representative. The algorithm was initially tested out to find the best element dimensions and smoothing parameter, sufficient to obtain a good representation of the final out-of-plane distortion of test specimen 1. Note that if the smoothing parameter (ζ) set to zero, this does not smooth the measurements obtained from the laser scanning system, but will average the results to the nodal positions of the elements, defining the plate. For further comparison the root-mean-squares of the out-of-plane deformation, angular distortion and longitudinal curvature were found. Note that in the case of the longitudinal curvature the direction vector was included, such that the square and subsequent square root of a negative value yields a negative longitudinal curvature, thus implying a hogged plate and conversely, a positive longitudinal curvature indicates a sagged plate.

Table 6.3 summarises the out-of-plane distortion, angular distortion and longitudinal curvature for different element sizes and smoothing parameters when applied to test specimen one.

Number (size mm) of elements	Average samples per element	Smoothing parameter	RMS out-of-plane deformation (mm)	RMS angular distortion (°)	RMS Longitudinal curvature (m^{-1})
2x2 (250x250)	196	0.0	1.9923	0.9552	(-) 0.0599
2x2 (250x250)	196	0.025	1.9212	0.8117	(-) 0.0246
4x4 (125x125)	49	0.0	1.7854	0.9398	(+) 0.0021
4x4 (125x125)	49	0.025	1.8052	0.8273	(+) 0.1566
Values from direct search algorithm			2.0002	0.8080	(-) 0.0732

Table 6.3: Numerical test for finite element smoothing of distortion

The number of samples per finite element has a significant effect on the accuracy of the smoothed results. The best representation was attained when the smoothing parameter was set to zero and a 2x2 element model was used. Furthermore the use of the smoothing algorithm gives a graphical representation of the angular distortion

and longitudinal curvature, as given in Figure 6.7. It is evident that the angular distortion is largely concentrated at the centre of the plate, suggesting that the angular distortion is a localized effect.

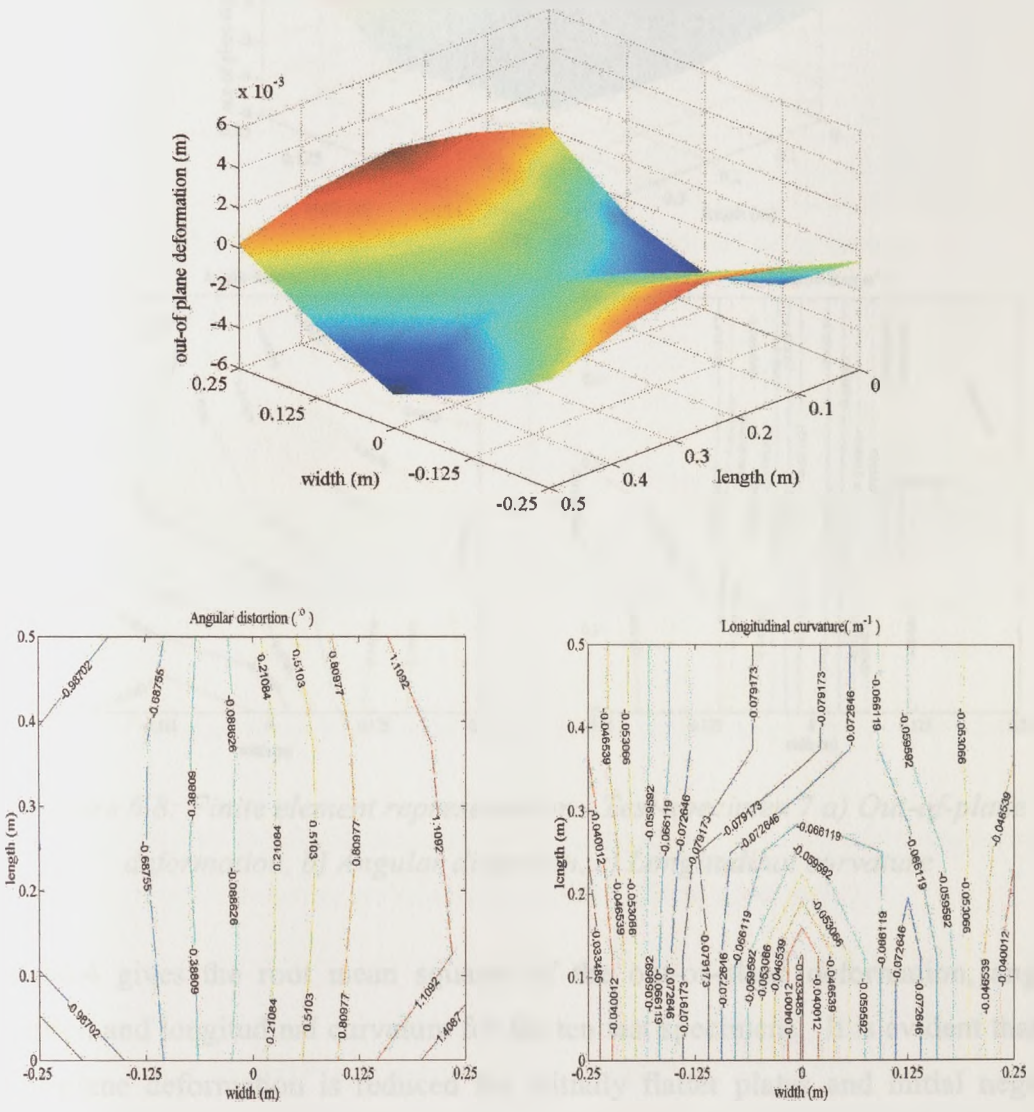

Figure 6.7: Finite element representation - Test-specimen 1 a) Out-of-plane deformation, b) Angular distortion, c) Longitudinal curvature

Distinct from the majority of the experiments, test specimens five, seven and eight resulted in a smaller angular distortion, thought to be due to the initial restraint arising from the initial negative angular setting. Figure 6.8 shows the smoothed out-of-plane deformation, angular distortion and longitudinal curvature of test specimen seven.

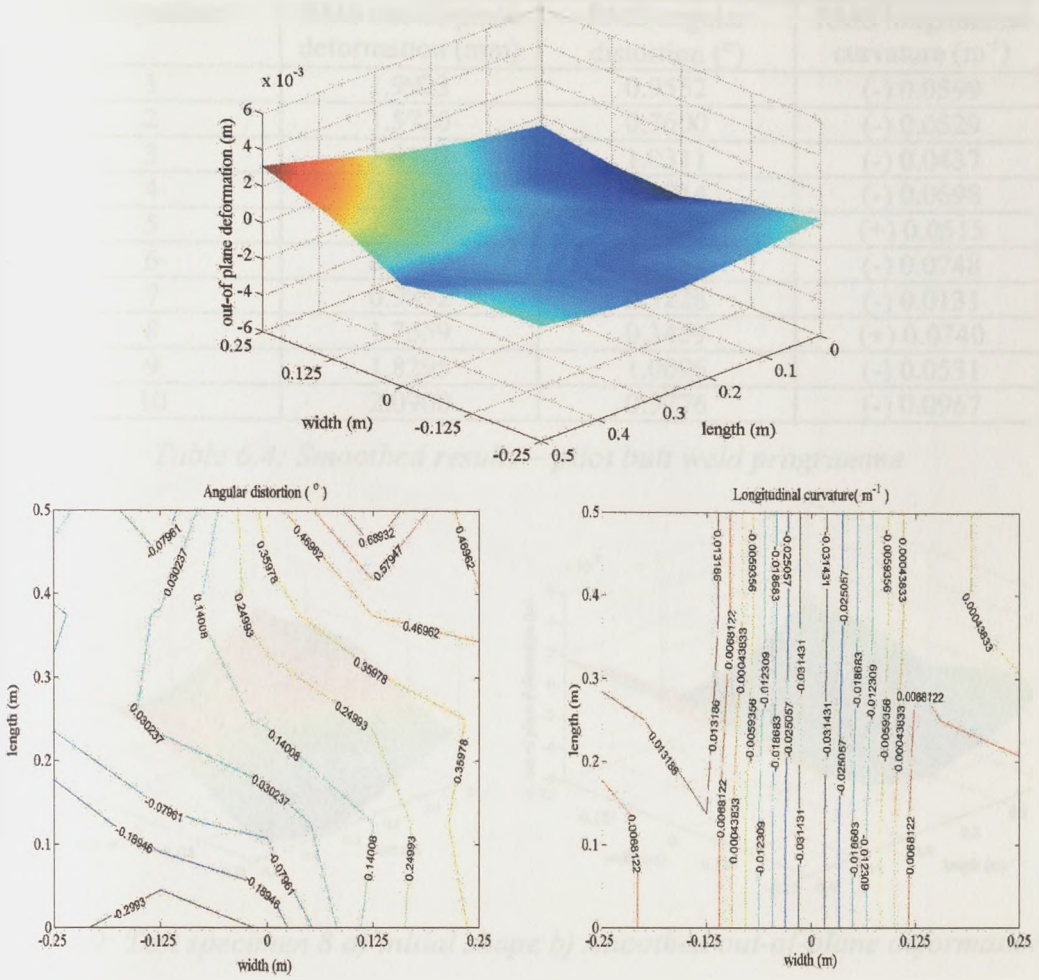

Figure 6.8: Finite element representation - Test-specimen 7 a) Out-of-plane deformation, b) Angular distortion, c) Longitudinal curvature

Table 6.4 gives the root mean squares of the out-of-plane deformation, angular distortion and longitudinal curvature for the ten test specimens. It is evident that the out-of-plane deformation is reduced for initially flatter plates and initial negative angular setting. However, in the case of test specimen 8 the initial negative angular distortion was large to an extent that the plate sagged to the same degree as in the hogged plates, as shown in Figure 6.9.

Though the stress-relieved plates exhibited a higher mean out-of-plane distortion, particularly a higher longitudinal deformation, a hypothesis test determined that the probability that the different distortion was due to stress relieve was not greater than 5 percent.

Test specimen	RMS out-of-plane deformation (mm)	RMS angular distortion (°)	RMS longitudinal curvature (m^{-1})
1	1.9923	0.9552	(-) 0.0599
2	1.5720	0.7600	(-) 0.0529
3	1.9103	1.0311	(-) 0.0437
4	2.2140	1.2014	(-) 0.0698
5	1.4200	0.2577	(+) 0.0515
6	2.1999	1.2257	(-) 0.0748
7	0.9892	0.3228	(-) 0.0131
8	1.7659	0.3459	(+) 0.0740
9	1.8295	1.0096	(-) 0.0531
10	2.0900	0.9776	(-) 0.0967

Table 6.4: Smoothed results – pilot butt weld programme

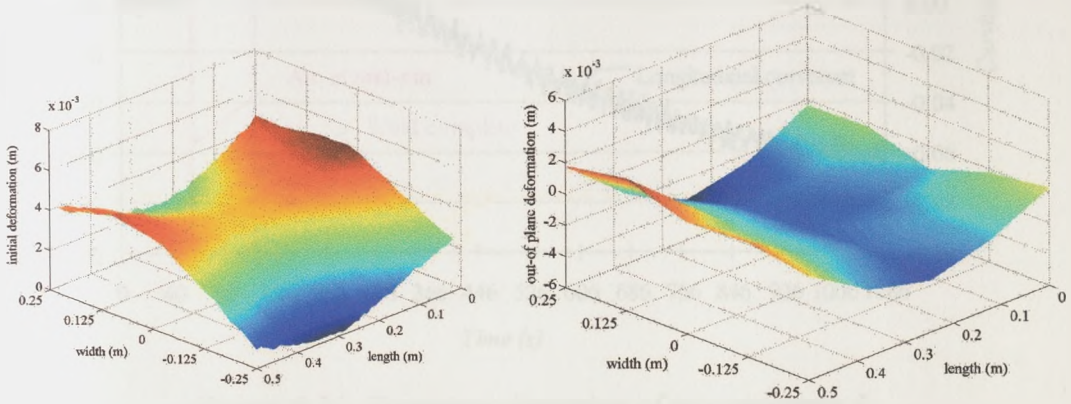

Figure 6.9: Test specimen 8 a) initial shape b) smoothed out-of-plane deformation

Figure 6.10, shows the displacements of the individual linear-variable displacement transducers, recorded during welding and cooling of test specimen 1.

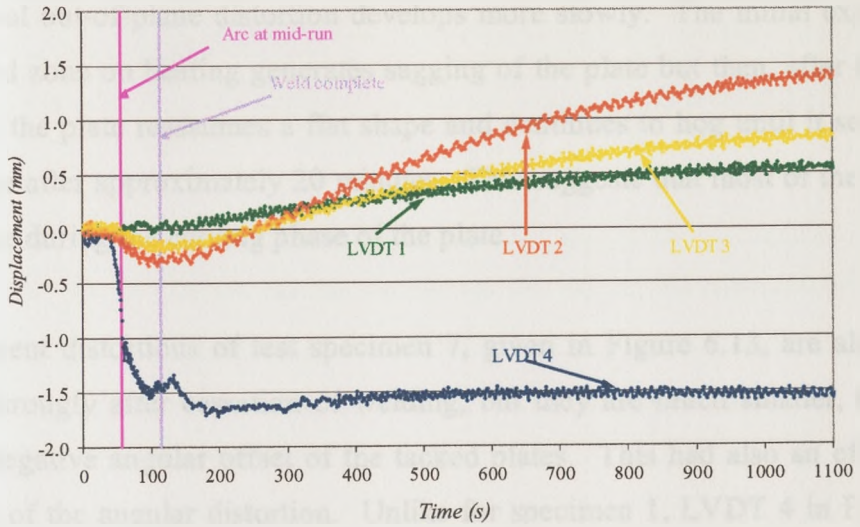

Figure 6.10: Displacements of LVDT's for test specimen 1

By fitting a quadratic function to the positions of the three outer LVDT's (1,2 and 3) and a linear function to the mid-plane LVDT's (2 and 4), the transient longitudinal curvature and angular distortion can be recorded, via the differentials of the quadratic and linear functions. The transient distortions are given in Figure 6.11.

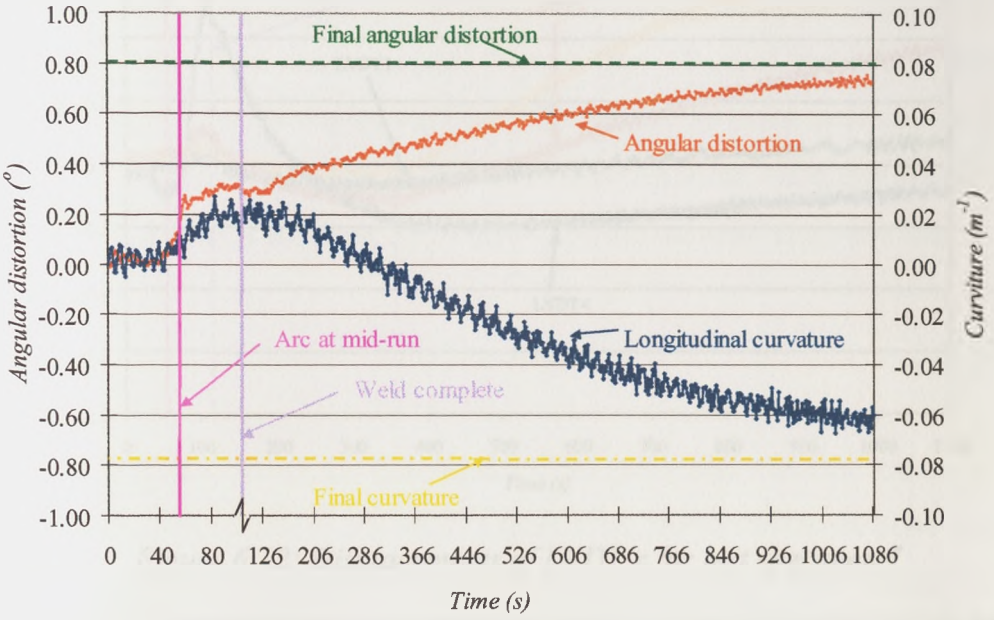

Figure 6.11: Transient distortion of test specimen 1

The immediate depression of LVDT 4 in Figure 6.10, shows that the angular distortion is also immediate and increases with arc movement. Further increase takes place on cooling, partly as a result of the anticlastic effect. On the other hand, the longitudinal out-of-plane distortion develops more slowly. The initial expansion of the yielded zone on heating generates sagging of the plate but then, after welding is complete, the plate reassumes a flat shape and continues to hog until it settles to its final shape after approximately 20 minutes. This suggests that most of the distortion takes place during the cooling phase of the plate.

The transient distortions of test specimen 7, given in Figure 6.13, are also seen to develop strongly after cessation of welding, but they are much smaller, due to the initially negative angular offset of the tacked plates. This had also an effect in the evolution of the angular distortion. Unlike for specimen 1, LVDT 4 in Figure 6.12 does not exhibit a depression as the arc passes the transducer. This further suggests

that an initially negative angular shape will restrain the plate to an extent that the angular distortion does not manifest itself to the maximum.

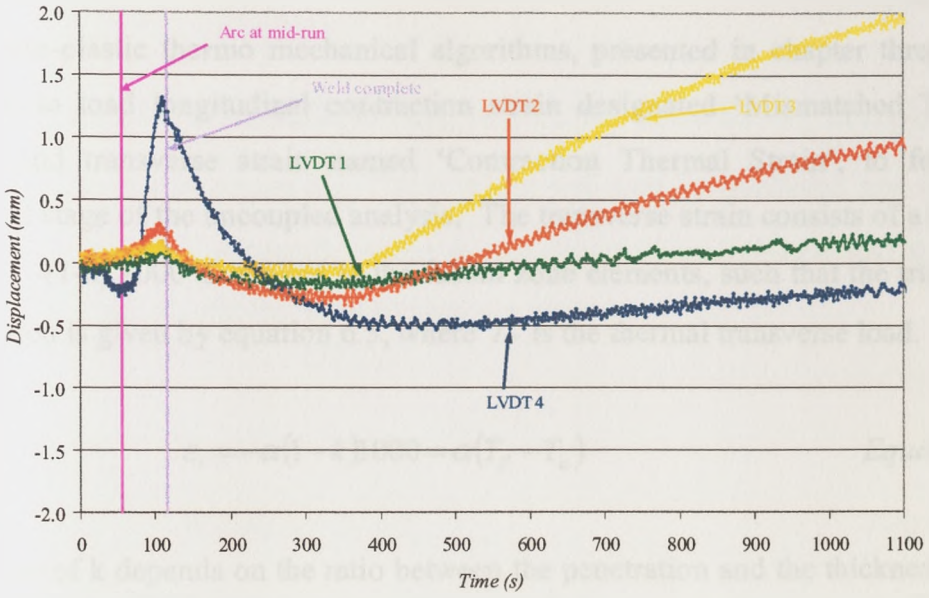

Figure 6.12: Displacements of LVDT's for test specimen 7

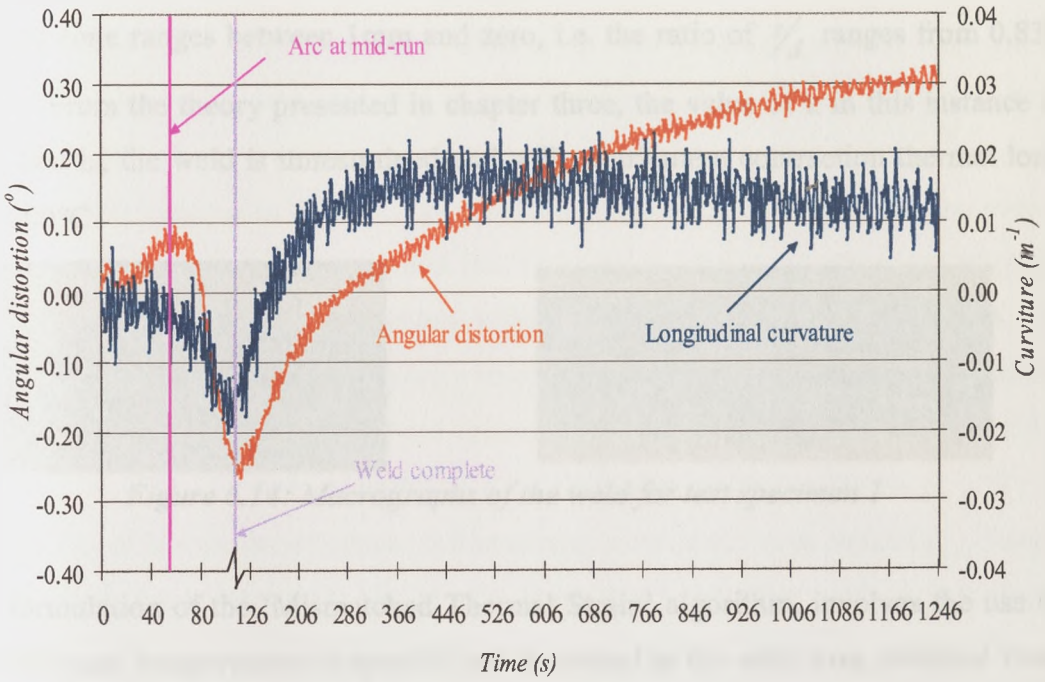

Figure 6.13: Transient distortion of test specimen 7

6.2.2 *Determination of thermal loads applied to the uncoupled structural computational analysis*

The elasto-plastic thermo mechanical algorithms, presented in chapter three, were adopted, to load longitudinal contraction strain designated 'Mismatched Thermal Strain' and transverse strain named 'Contraction Thermal Strain', to form the structural stage of the uncoupled analysis. The transverse strain consists of a thermal load of -(1-k).1000°C applied to the fusion zone elements, such that the transverse contraction is given by equation 6.5, where T_T is the thermal transverse load.

$$\varepsilon_t = -\alpha(1-k)1000 = \alpha(T_T - T_a) \qquad \textit{Equation 6.5}$$

The value of k depends on the ratio between the penetration and the thickness of the plate, as well as the shape of the weld. Figure 6.14, shows the fusion zone shape of a typical butt-welded test specimen, at two cross-sections. The thickness of the unfused zone ranges between 1mm and zero, i.e. the ratio of s/d ranges from 0.833 and 1. From the theory presented in chapter three, the value of k in this instance is zero, that is, the weld is unrestrained and will contribute a contraction thermal load of -1000°C

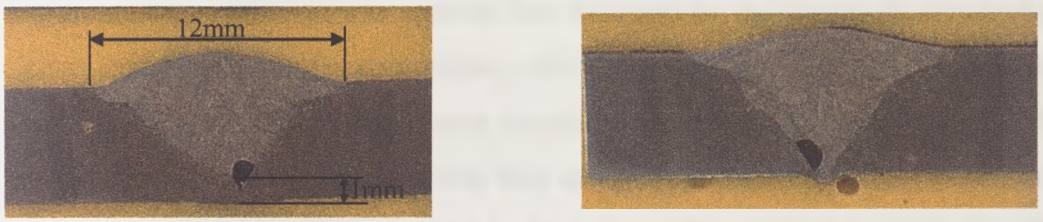

Figure 6.14: Macrographs of the weld for test specimen 1

The formulation of the 'Mismatched Thermal Strain' algorithm, involves the use of the maximum temperatures at specific points normal to the weld axis, obtained from the thermal stage described in detail in chapter five. The longitudinal contraction may be divided into three sectors, a yield level thermal contraction (A), a region of zero thermal strain (B) and an elastic residual stress region (C). Introducing the ambient temperature T_a, the overall longitudinal strain in the structural model can be

found by applying a 'load' profile corresponding to an artificial temperature drop, given by

$$\varepsilon_l = \alpha(T_l(y) - T_a) \qquad \textit{Equation 6.6}$$

The magnitude of $T_l(y)$ is sufficient to give a thermal strain of $-\varepsilon_y$ in region A and $-\lfloor\alpha(T_M - T_a) - \varepsilon_y\rfloor$ in region C. These values can then be translated into artificial temperature loadings at specific nodes in the structural model such that the nodal temperature load, T_{li}, for the three regions are given by:

Region A: $T_{li} = T_a - \varepsilon_y / \alpha$ *Equation 6.7*

Region B: $T_{li} = T_a$ *Equation 6.8*

Region C: $T_{li} = 2T_a + \frac{\varepsilon_y}{\alpha} - T_{Mi}$ *Equation 6.9*

These formulations were therefore applied to the problem alternatively via a 'sequential' load step analysis and a 'simultaneous' three-dimensional structural analysis [6.10], using a line search, Newton-Raphson, sparse direct equation solver and non-linear geometry effects. In the first 'sequential' method, the transverse contraction thermal strain was applied first followed by the longitudinal out-of-plane mismatched thermal strain contraction, whereas in the 'simultaneous' approach, the angular and longitudinal effects were considered together. In both instances elastic static analyses were performed. Note that as pointed out in the study performed by Berglund *et al* [6.11], it is essential to do a three dimensional analysis in order to capture the different out-of-plane deformations associated with welding. Hence, eight noded linear elements 'Solid 45' were used, together with a non-linear geometric analysis, taking into account large strains and rotations.

6.2.3 Sequential mismatched thermal strain structural algorithm

The immediate change in angular distortion with arc movement, as shown in Figures 6.8 and 6.9, suggests that the angular distortion should be treated first, followed by

the longitudinal contraction. Furthermore, an increase in angular distortion will increase the offset distance between the neutral axis of the plate and the centroid of the mismatched thermal strain contraction force, giving rise to more out-of-plane deformation. The two treatments were first analysed separately. Starting from an initial flat shape the contraction thermal strain and mismatched thermal strain were applied separately in two different independent elastic static load steps, i.e. the transverse strain was applied to the fusion zone shape, then removed, followed by the application of the longitudinal contraction force. Since an elastic analysis was performed, the plate assumed the initial flat shape, on removal of the contraction thermal strain. Hence the centroid of the mismatched thermal strain profile, was in line with the neutral axis of the plate. Figure 6.15, shows the out-of-plane deformation due to the angular transverse strain and longitudinal contraction force respectively, when the co-efficient of expansion was assumed to be $14x10^{-6}$, while the yield strength was taken to be $405MN/m^2$, as certified by the plate supplier.

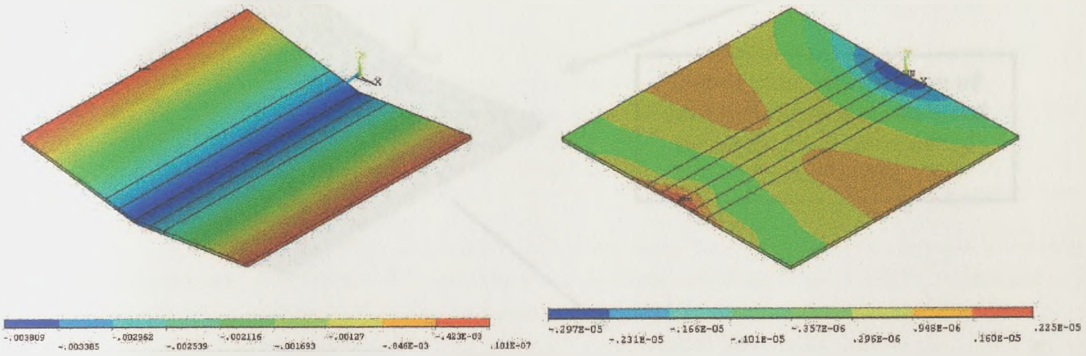

Figure 6.15: Out-of-plane deformation for separate thermal strains

The longitudinal out-of-plane deformation was small, suggesting that the distance between the neutral axis and centroid of the force is an important factor and must be modelled. This also suggests that a means of reducing the out-of-plane deformation is to make sure that the offset distance is kept as small as possible, either restraining the angular distortion or by presetting the angular distortion. The final deformation from the above strategy is found by addition of the separate thermal strain structural analyses. It is evident that the final out-of-plane deformation does not match the experimental results, lacking longitudinal out-of-plane deformation.

Since an elastic analysis is performed, a means of integrating the angular distortion effect to the mismatched thermal strain is by either applying an initial residual stress or reaction force or an initial imperfection related to the contraction thermal strain, to the second load step analysis. The application of the reaction force or initial stress proved to be intricate and inadequate, hence the out-of-plane deformation resulting from the angular distortion was applied as an initial imperfection to the perfectly initially flat plate.

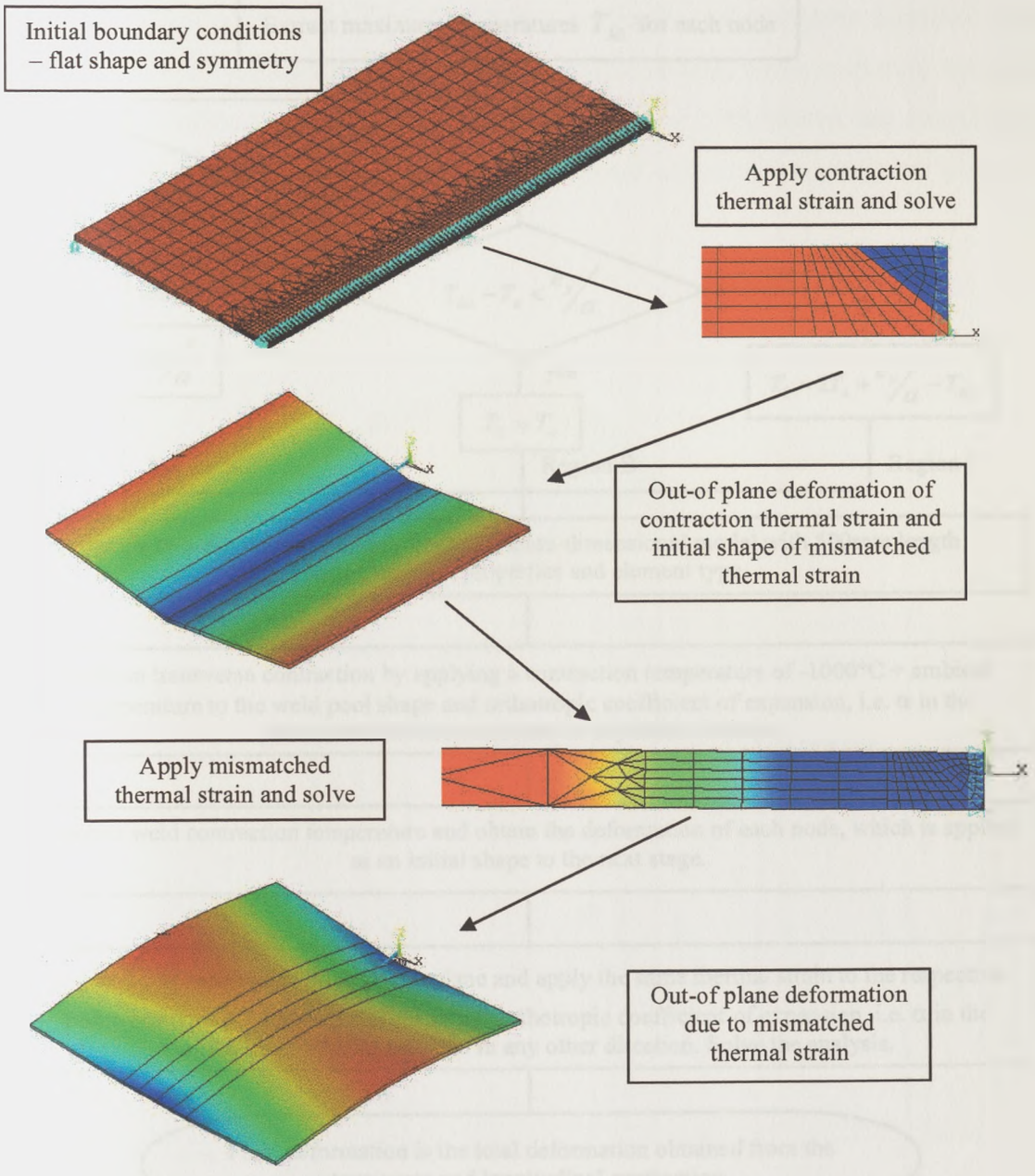

Figure 6.16: Block diagram of 'sequential' algorithm

The sequence of the sequential analysis is described in Figure 6.16, while Figure 6.17 gives a flow diagram of the sequential algorithm. The final out-of-plane deformation arises from the addition of the distortion obtained from the contraction thermal strain and mismatched thermal strain simulations.

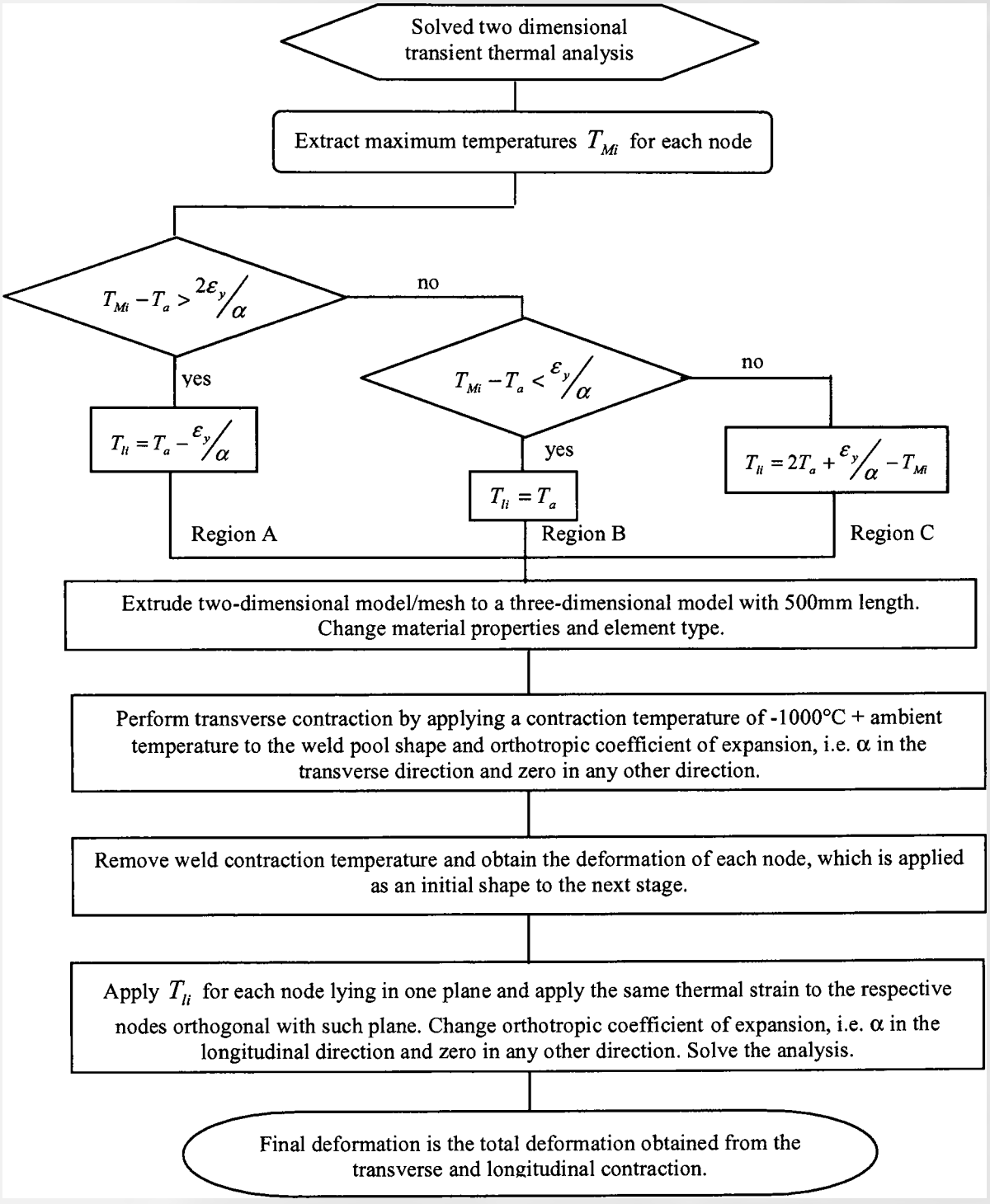

Figure 6.17: 'Sequential' algorithm

The sequential method was applied in two different ways. First, the contraction thermal strain was assumed to be acting over the weld preparation volume (SEQ 1) and secondly acting over the fusion zone (SEQ 2). The strategies reflect the cases where only the deposited weld material contributes to the transverse thermal strain and in the second instance assumes that the thermal strain developed during the heating phase across the fused zone is nullified because the liquefied material is weak, thus only imposes a contraction strain during the cooling phase. The out-plane distortion developed in the first simulation, particularly the angular distortion, was not sufficient when compared to the experimental results, while a closely matching result was obtained using the second scheme. Figure 6.18, shows the out-of-plane deformation, angular distortion and longitudinal deformation contour plots for structural analysis SEQ 2.

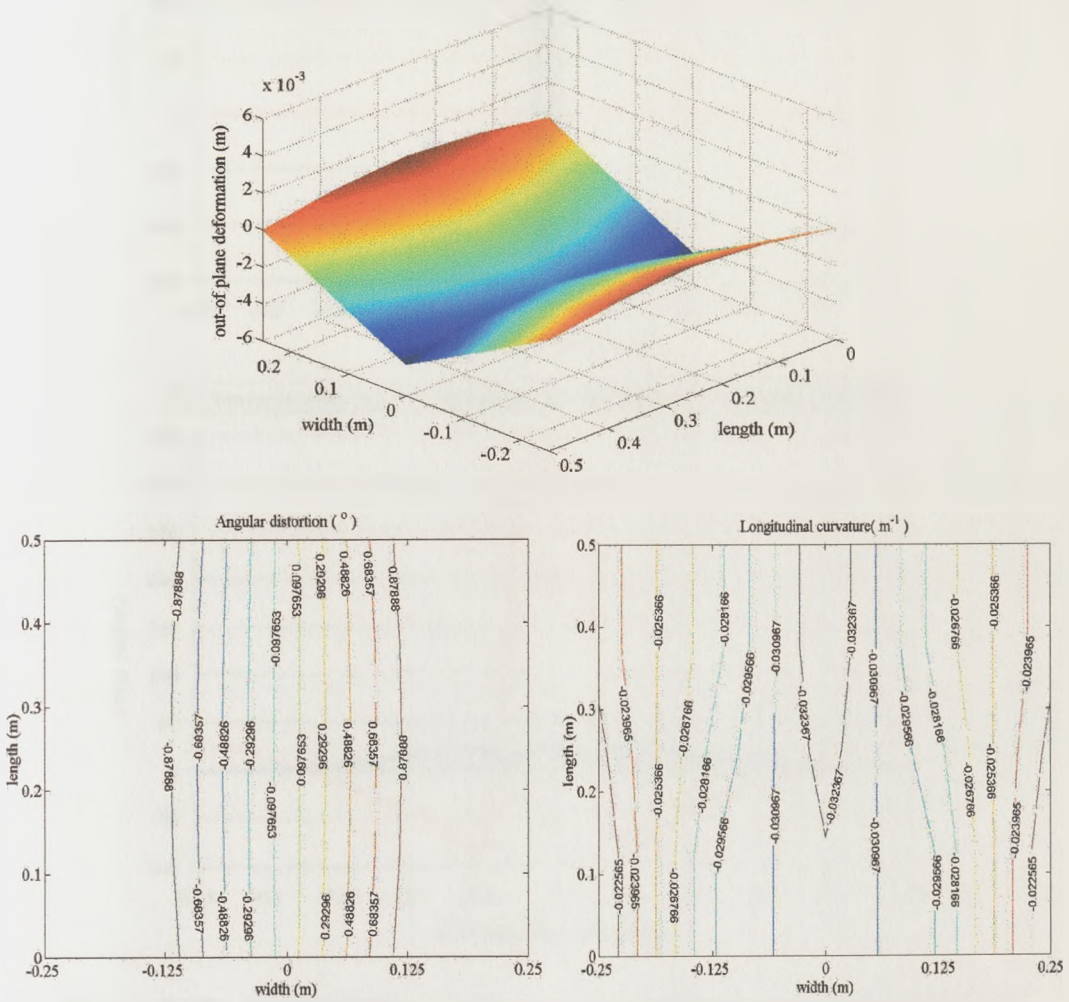

Figure 6.18: Sequential algorithm - a) Out-of-plane deformation, b) Angular distortion, c) Longitudinal curvature

Figure 6.19, shows the residual stresses evolved during the different stages of the 'sequential' algorithm. While the longitudinal residual stress follows typical welding residual stress patterns given in the literature [6.12], the transverse residual stress is overestimated and exceeds the yield strength. This is due to the high, localised thermal load imposed to the fusion zone, suggesting that while the simplified algorithms gives a relatively good estimate of the longitudinal residual stresses and out-of-plane deformation, the algorithm fails to predict the localized transverse residual stresses.

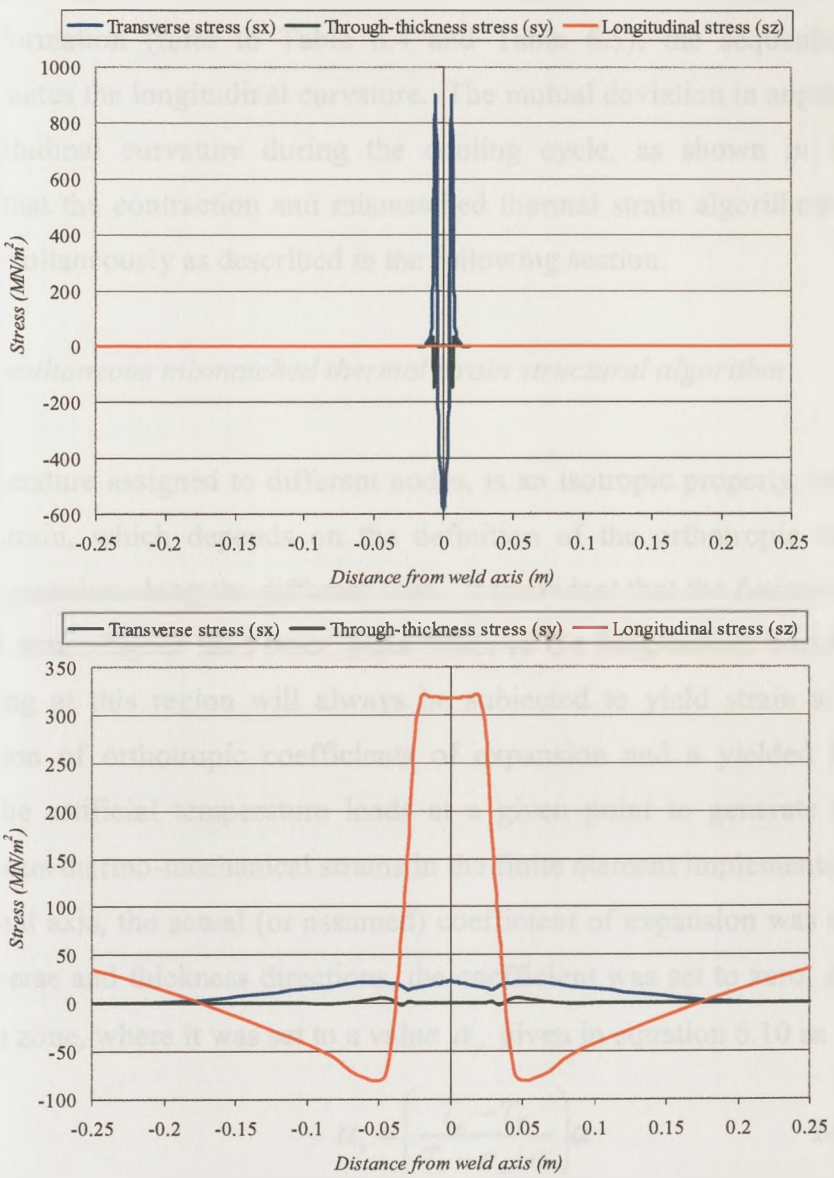

Figure 6.19: Residual stresses due to a) 'Contraction thermal strain', b) 'Mismatched thermal strain', at mid-section

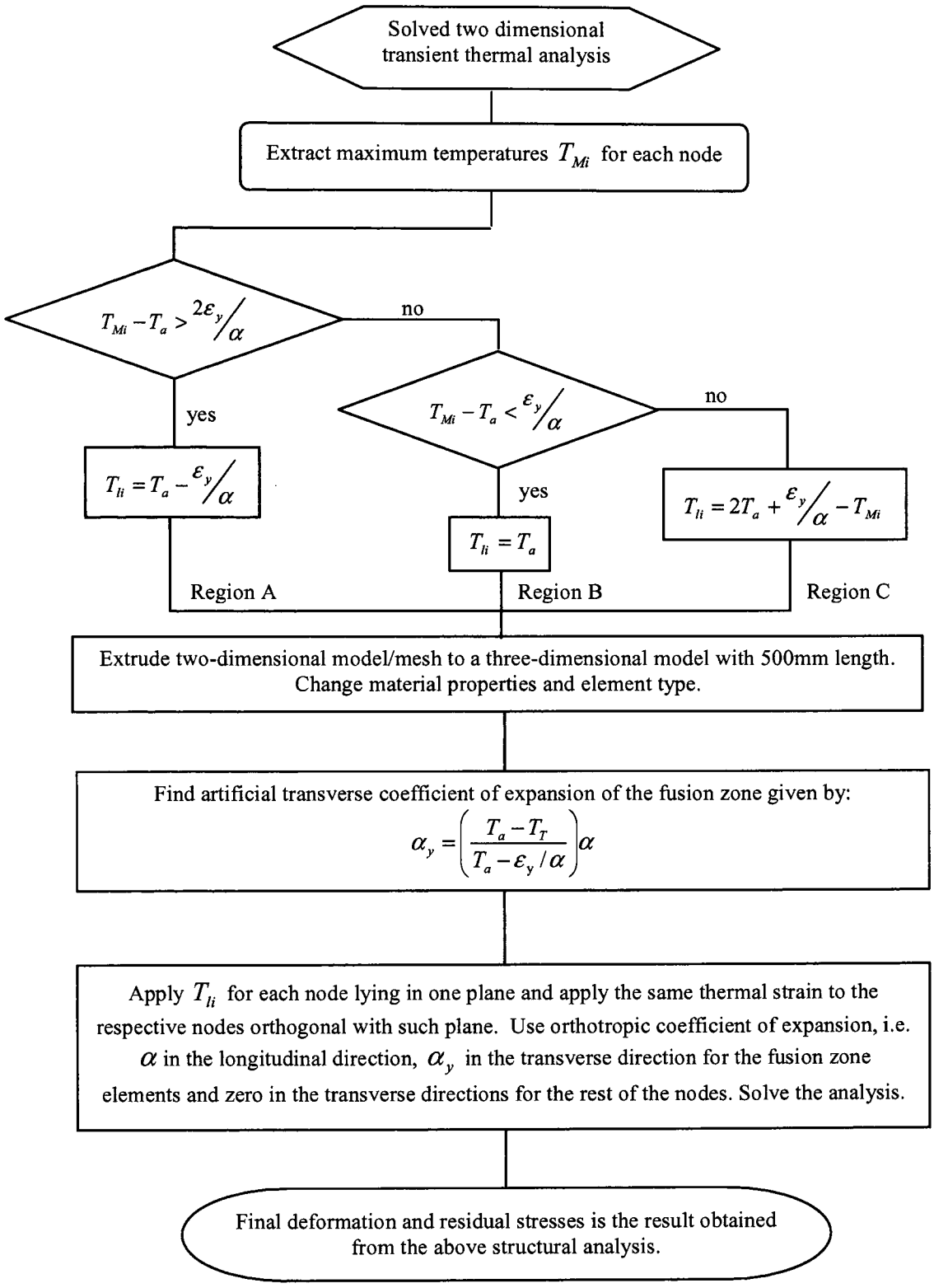

Figure 6.20: 'Simultaneous' algorithm

In the 'simultaneous' algorithm a yield strength of 405MN/m^2 and a coefficient of expansion of 14x10^{-6} were used, such that the yield zone thermal load in the mismatched thermal strain algorithm is -139.75 + ambient temperature, resulting in a transverse orthrotropic coefficient of expansion of 114.57x10^{-6} applied to the fusion zone.

Figure 6.21 shows the out-of-plane deformation, angular distortion and longitudinal deformation contour plots for simultaneous structural analysis. The respective root mean square values are given in Table 6.6.

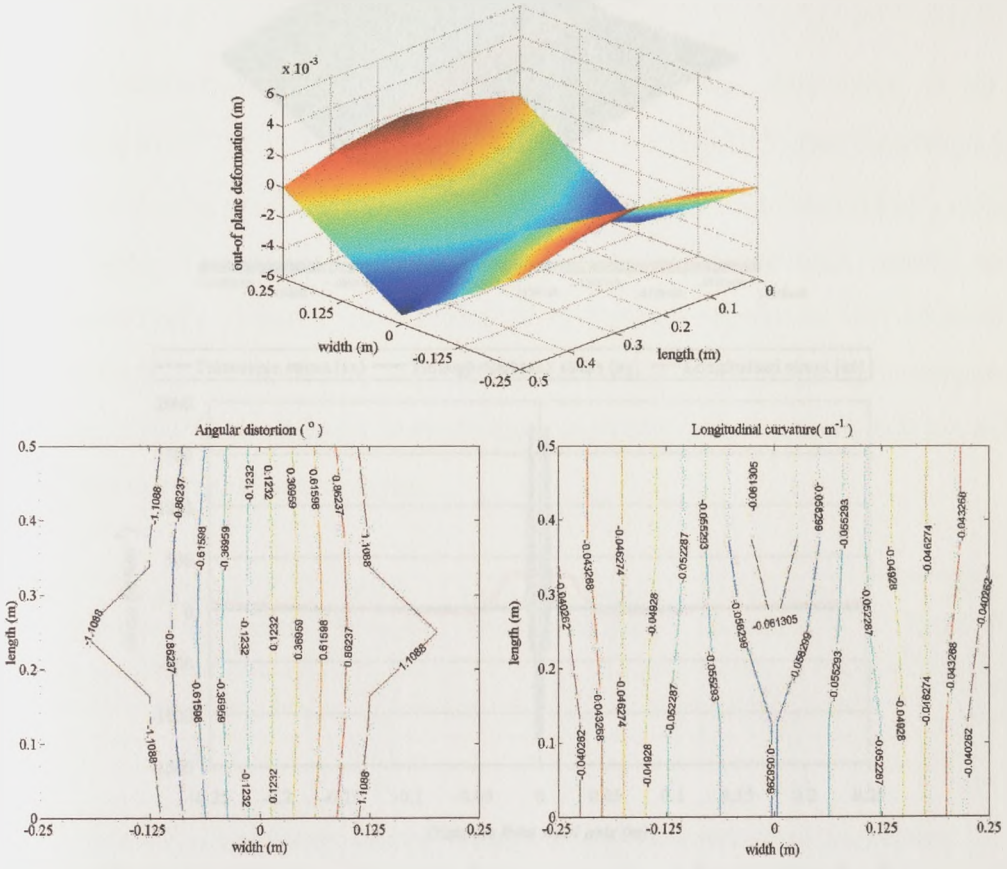

Figure 6.21: Simultaneous algorithm - a) Out-of-plane deformation, b) Angular distortion, c) Longitudinal curvature

Computational analysis	RMS out-of-plane deformation (mm)	RMS angular distortion (°)	RMS longitudinal curvature (m^{-1})
SIM	2.3917	1.0672	(-) 0.0491

Table 6.6: Root mean square values of the simultaneous structural analysis

A stronger agreement was attained between the experimental and computational longitudinal curvature, suggesting that the anticlastic effect is a significant consequence in welded plates. Furthermore, the simultaneous algorithm gives the combined transverse and longitudinal residual stresses, in a single load step analysis.

Figure 6.22a, shows the contour plot of the longitudinal residual stresses, while Figure 6.22b gives the residual stresses in the middle of the plate.

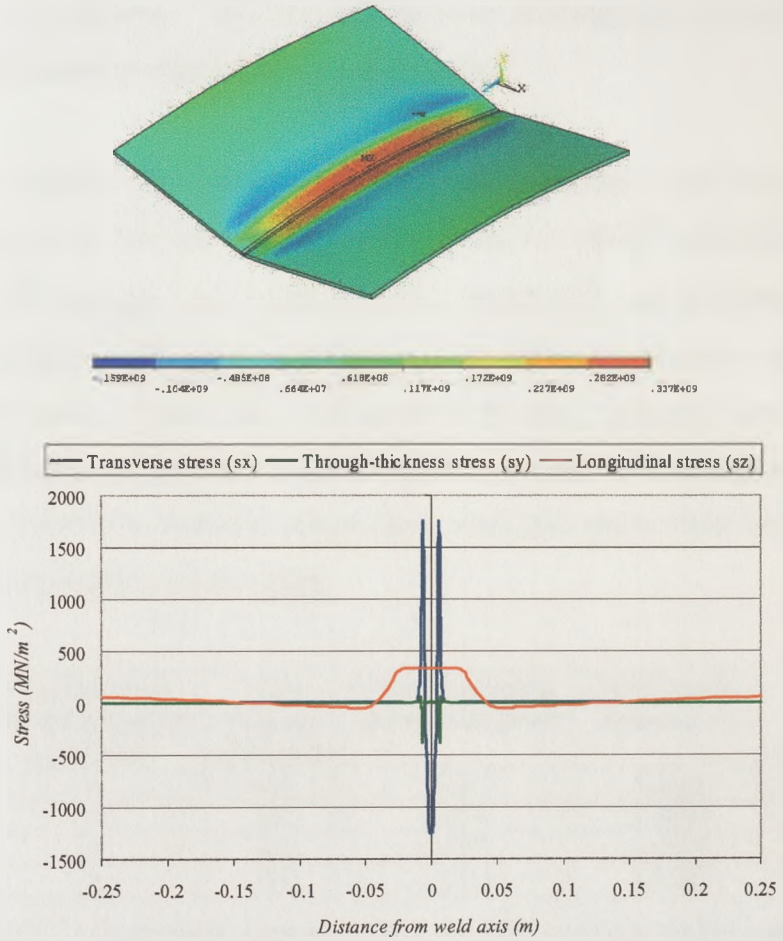

Figure 6.22: a) Longitudinal residual stress contour plot, b)Residual stresses at mid- plane

As pointed out for the sequential algorithm, the simultaneous algorithm overestimates that transverse residual stresses but gives a typical longitudinal residual stress pattern.

6.2.5 *Effect of material properties on the results of the simplified algorithm*

The effect of material properties on the simplified algorithm was investigated theoretically in chapter 3 section 3.2.2. The study concluded that if an inverse linear relationship exists between T_M and the transverse distance y, the yield strength magnitude drops out of the analytical formulation making the longitudinal contraction force independent of the yield strength. On the other hand, the longitudinal and transverse contraction forces, are highly dependant on the coefficient of expansion. The two effects were investigated via four simulations using the simultaneous algorithm, described below.

In the first instance the coefficient of thermal expansion was taken to be that corresponding to ⅓ the melting temperature value, i.e. 14×10^{-6} after Okerblom [6.4], while the yield strength was varied between $405 MN/m^2$ and $360 MN/m^2$, obtained from the supplied steel plate certification and room temperature tensile testing results, respectively. Finally the coefficient of thermal expansion was increased to 16×10^{-6}, reflecting an averaged expansivity for material undergoing a temperature history from 1200°C to ambient temperature, such that phase transformation effects are taken into account to some extent.

Model no	Co-efficient of thermal expansion ($x10^{-6}$/°C)	Yield Strength (MN/m^2)	RMS out-of-plane deformation (mm)	RMS angular distortion (°)	RMS longitudinal curvature (m^{-1})
1	14	405	2.3917	1.0672	(-) 0.0491
2	14	360	2.4297	1.0790	(-) 0.0467
3	16	405	2.7956	1.2457	(-) 0.0574
4	16	360	2.8447	1.2605	(-) 0.0538

Table 6.7: Root mean square values for different material properties

Table 6.7, shows the root mean square values of the out-of-plane deformation, angular distortion and longitudinal curvature for the four modelling approaches. It may be concluded that the yield strength had an insignificant effect on the final out-of-plane deformations, particularly since the thermal maximum isotherms, follow an approximate inverse proportional relationship with the transverse distance. The slight differences are related to meshing accuracies. On the other hand, as expected,

an increase in the out-of-plane deformations was found when using a higher coefficient of expansion. Although the final angular distortion is over estimated, the longitudinal curvature matches the experimental results, suggesting that careful choice of an average coefficient of expansion is essential.

6.3 Out-of-plane distortion due to double-sided fillet welded attachment

The tests were designed to investigate the out-of-plane deformation arising from double-sided fillet welding, with intermediate ambient cooling between the two runs. Four test plates each consisting of a central stiffener 0.5m x 0.15m x 6mm thick, welded to a 0.5m square, 6.5mm thick plate, were investigated. The main consideration was the out-of-plane deformation developed in the plates and less importance was given to the deformation arising on the stiffeners, particularly since the out-of-plane deformation of the plate is more significant, and leads to the main rectification costs in bringing subassemblies to match.

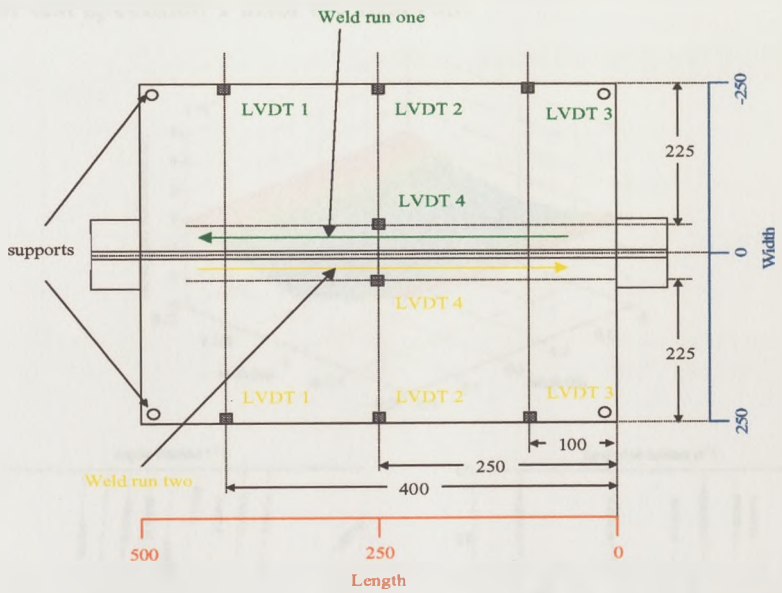

Figure 6.23: Positions of linear-variable displacement transducers and supports for double sided fillet welding pilot tests

Again linear variable displacement transducers and a laser scanning system were used to measure the transient and static deformations. Figure 6.23, shows the fixed locations of the four transducers for weld run one and two. Note that the welding

directions were opposed, and no restraint on in-plane or out-of-plane deformations was applied to the test specimens, apart from the restraint arising from the tack welds. In this instance the run on and run off tabs were tack welded first followed by a tack weld between the stiffener and plate at mid-length.

6.3.1 Test observations and results – first weld run

The increased second moment of area of the stiffener-plate assembly, made the structure stiffer such that the longitudinal contraction was not sufficient to bow the plates. While, there was considerable out-of-plane deformation due to angular movement, but the specimens remained relatively flat in the longitudinal axis. The final out-of-plane deformation was not affected by the initial profile of the assembly. This gives further proof that angular distortion is a localized effect. Figure 6.24 shows the smoothed out-of-plane deformation, angular and longitudinal contour plot of the plate for test specimen 1 after the first run.

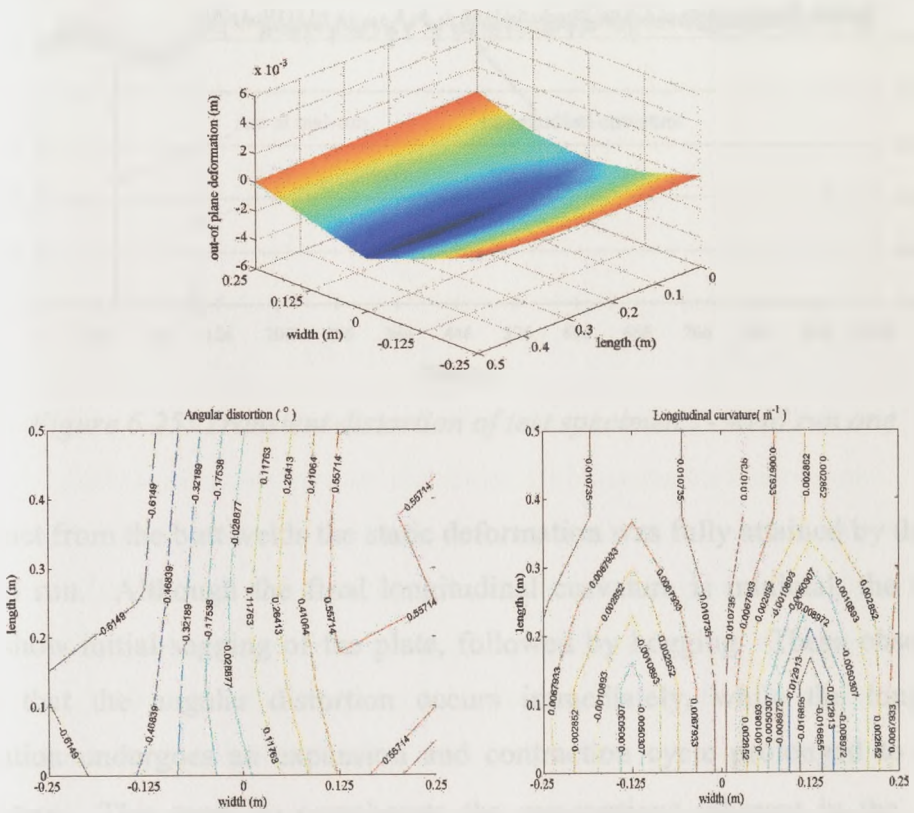

Figure 6.24: Smoothed deformation – Test specimen 1 a) Out-of-plane deformation, b) Angular distortion, c) Longitudinal curvature

Test specimen	RMS out-of-plane deformation (mm)	RMS angular distortion (°)	RMS longitudinal curvature (m^{-1})
1	1.2633	0.5204	(+) 0.0057
2	1.1007	0.4948	(-) 0.0058
3	1.0129	0.4487	(+) 0.0060
4	1.2391	0.5330	(+)0.0092

Table 6.8: Smoothed results – pilot double-sided fillet welding tests – run one

The four test observations show an increase in angular distortion as the weld progresses, such that the final static angular distortion at the end of the weld (length 0.5m) was higher than at the starting edge (length 0m). This observation, could also be seen in the transient deformation results obtained from the linear variable displacement transducers, as shown in Figure 6.25.

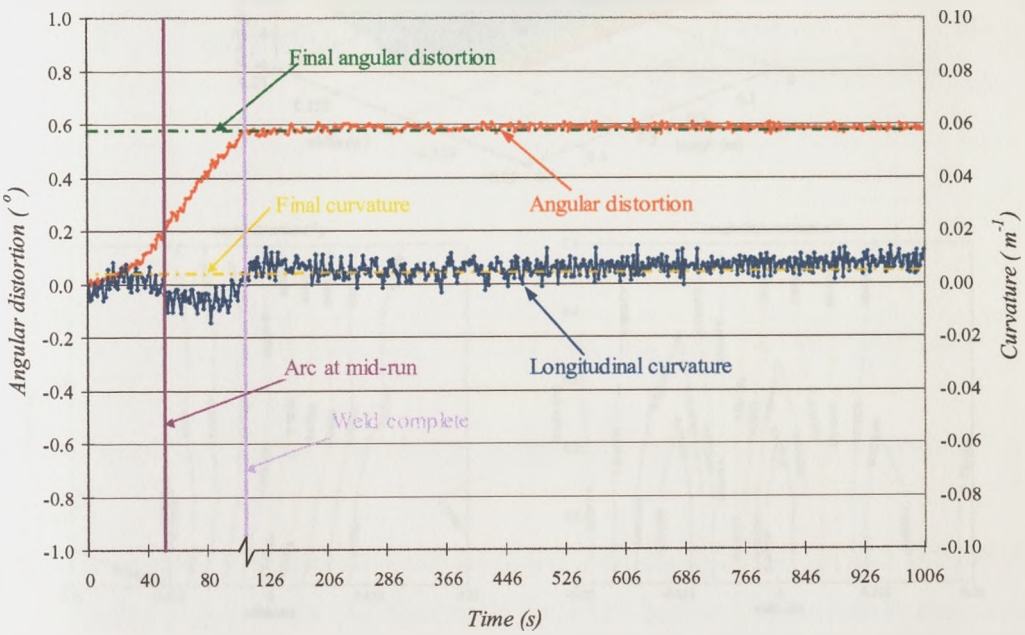

Figure 6.25: Transient distortion of test specimen 1- weld run one

As distinct from the butt welds the static deformation was fully attained by the end of the weld run. Although the final longitudinal curvature is minimal, the transient results show initial sagging of the plate, followed by hogging. These observations suggest that the angular distortion occurs immediately, while the longitudinal deformation undergoes an expansion and contraction cycle prolonged to ambient temperature. This tends to corroborate the assumptions inherent in the -1000°C contraction thermal strain and mismatched thermal stain algorithms.

6.3.2 *Test observations and results – second weld run*

This section presents the results for out-of-plane deformation caused by the second weld pass in double-sided fillet welding with intermediate ambient cooling. Figure 6.26 shows the static, smoothed, out-of-plane deformation, and the angular and longitudinal contour plots for a typical welded assembly, due to the second weld pass only.

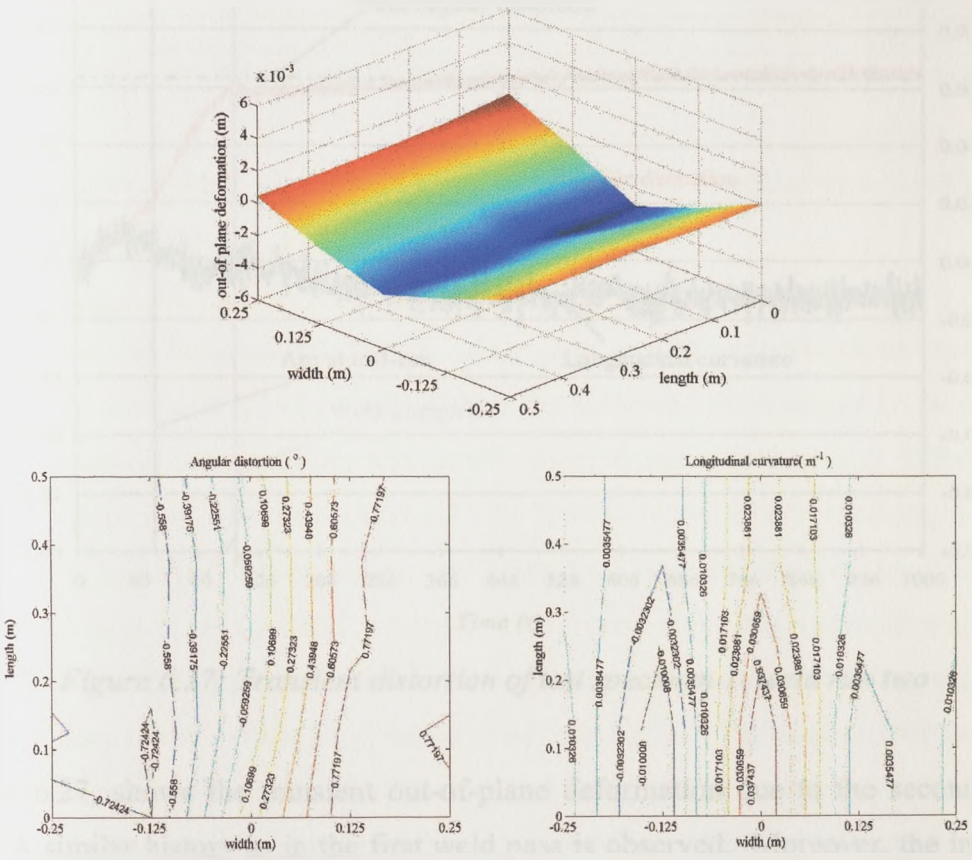

Figure 6.26: Smoothed deformation – Test specimen 1 run two a) Out-of-plane deformation, b) Angular distortion, c) Longitudinal curvature

The plates deformed in a similar manner to the first weld pass. This again suggests that the longitudinal contraction was small and did not exceed the buckling load of the assembly. The root mean square value of the out-of-plane deformation for the four specimens is given in Table 6.9.

Test specimen	RMS out-of-plane deformation (mm)	RMS angular distortion (°)	RMS longitudinal curvature (m^{-1})
1	1.4283	0.6420	(+) 0.0172
2	1.2689	0.5724	(+) 0.0053
3	1.5756	0.7296	(+) 0.0176
4	1.1678	0.5920	(+) 0.0095

Table 6.9: Smoothed results – pilot double-sided fillet welding tests – run two

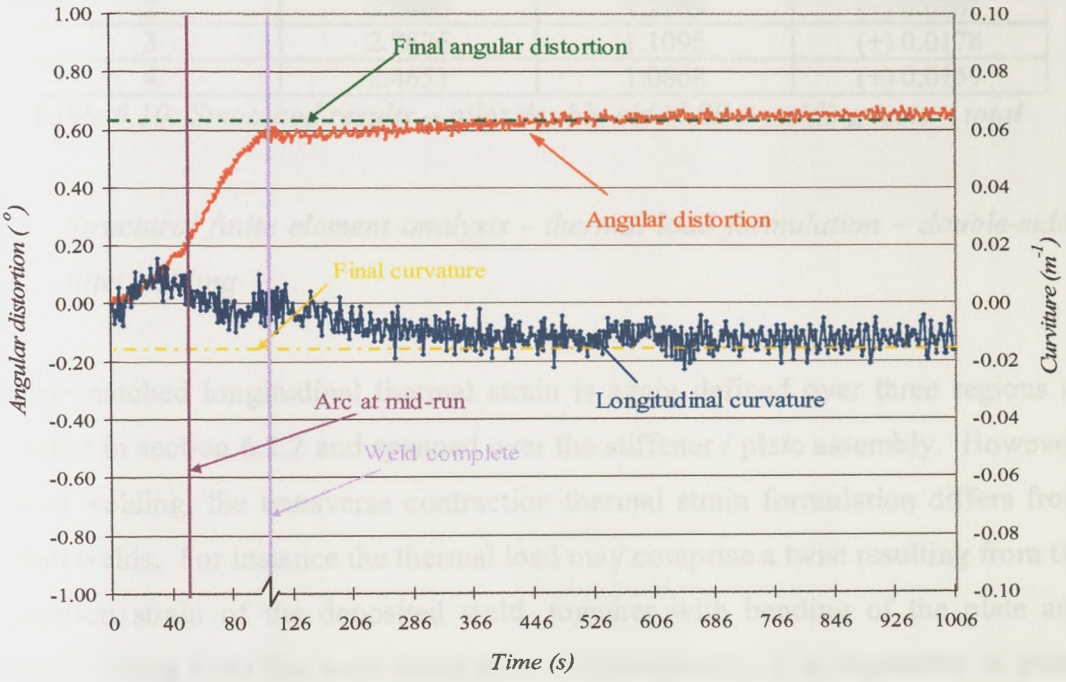

Figure 6.27: Transient distortion of test specimen 1- weld run two

Figure 6.27, shows the transient out-of-plane deformation due to the second weld pass. A similar history as in the first weld pass is observed. Moreover, the increase in longitudinal curvature due to the second weld pass is minor. This implies that, in double-sided fillet welding with intermediate ambient cooling the total contraction force arises from the overlapping contraction forces of the two independent welds, resulting in a minor increase of the longitudinal contraction reflecting the offset distance between the two weld passes. On the other hand the angular distortion was doubled, suggesting that in double sided fillet welding and for this plate sizes the transverse thermal contraction may be considered to be independent of the previously laid welds.

Table 6.10 gives the final total out-of-plane deformations due to double-sided fillet welding, obtained by adding the respective out-of-plane deformation due to the first and second weld passes.

Test specimen	RMS out-of-plane deformation (mm)	RMS angular distortion (°)	RMS longitudinal curvature (m^{-1})
1	2.8796	1.0483	(+) 0.0213
2	2.8406	1.2109	(+) 0.0205
3	2.7876	1.1095	(+) 0.0178
4	2.4651	1.0868	(+) 0.0159

Table 6.10: Smoothed results – pilot double-sided fillet welding tests – total

6.3.3 Structural finite element analysis - thermal load formulation – double-sided fillet welding

The mismatched longitudinal thermal strain is again defined over three regions as discussed in section 6.2.2 and spanned over the stiffener / plate assembly. However, in fillet welding, the transverse contraction thermal strain formulation differs from the butt welds. For instance the thermal load may comprise a twist resulting from the contraction strain of the deposited weld, together with bending of the plate and stiffener arising from the weld penetration. Consequently, it is imperative to know the fusion zone dimensions, either via macrographs of the welds or via thermal finite element simulations defining the fusion zone boundaries. The accuracy of the latter depends on the way the heat input is modelled, in particular carrying out a precisely positioned and shaped weld which coincides with an idealised heat input model, making it a rather inadequate option.

The fusion zone in fillet welds may be divided in three sectors (Figure 6.28):

1. Cross-sectional area of deposited weld material (Section 1 - A_{wd})
2. Penetrated cross-sectional area in the plate (Section 2 - A_{wp})
3. Penetrated cross-sectional area in the stiffener (Section 3 - A_{ws})

Okerblom [6.4] suggests (for steel) that the contraction thermal strain arising from the deposited weld is $\varepsilon_t = -\alpha 1000$, while the bending arising from the penetrated

weld material may be analysed like a butt weld, such that the thermal contraction strain is given by $\varepsilon_t = -\alpha(1-k)1000$ where k depends on the penetration to thickness ratios L_4/d_s and L_3/d_p of the respective stiffener and plate assembly, as discussed in chapter 3 section 3.3.1. Note that in this instance the penetrated area may be assumed to be a parabolic fused zone. Assuming that the contraction thermal strain is applied to sector 1 the final thermal load is given by equation 6.11.

$$T_T = T_a - 1000\left(1+\frac{A_{wp}}{A_{wd}}(1-k_p)+\frac{A_{ws}}{A_{wd}}(1-k_s)\right) \qquad \textit{Equation 6.11}$$

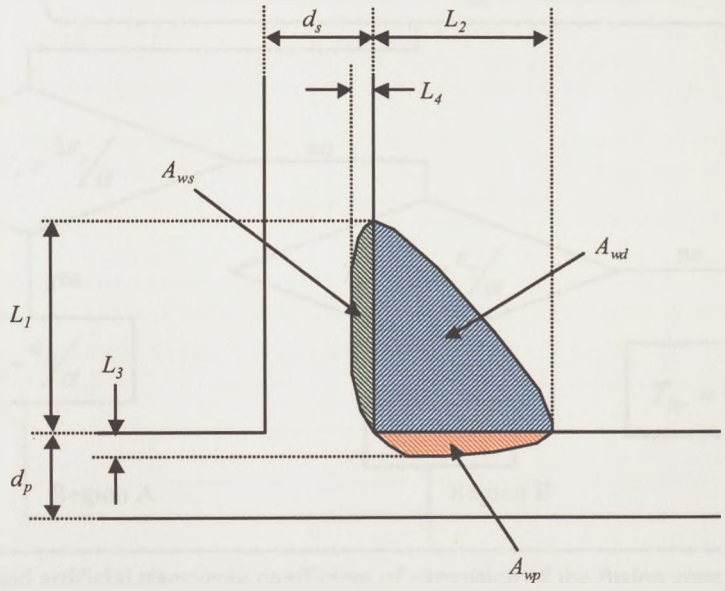

Figure 6.28: Cross – section of fillet welding

In the mismatched thermal strain algorithm, the overall maximum temperatures attained in the region for the whole welding cycle (weld pass one – cooling to ambient – weld pass two – cooling to ambient), are used to find the total thermal longitudinal contraction load to be applied to specific points transverse to the weld. In so doing the contraction forces of the first and second pass are superimposed and may be analysed in a single load step analysis.

If the concern is to analyse the first weld pass then the maximum temperatures attained during the first weld cycle are used. For instance if in the thermal transient

analysis the time taken for the plate to cool to ambient temperature is t_a, the maximum temperatures attained during the time ranging from 0 to t_a are used. However the elements constituting the deposited material due to the second weld run must be deactivated.

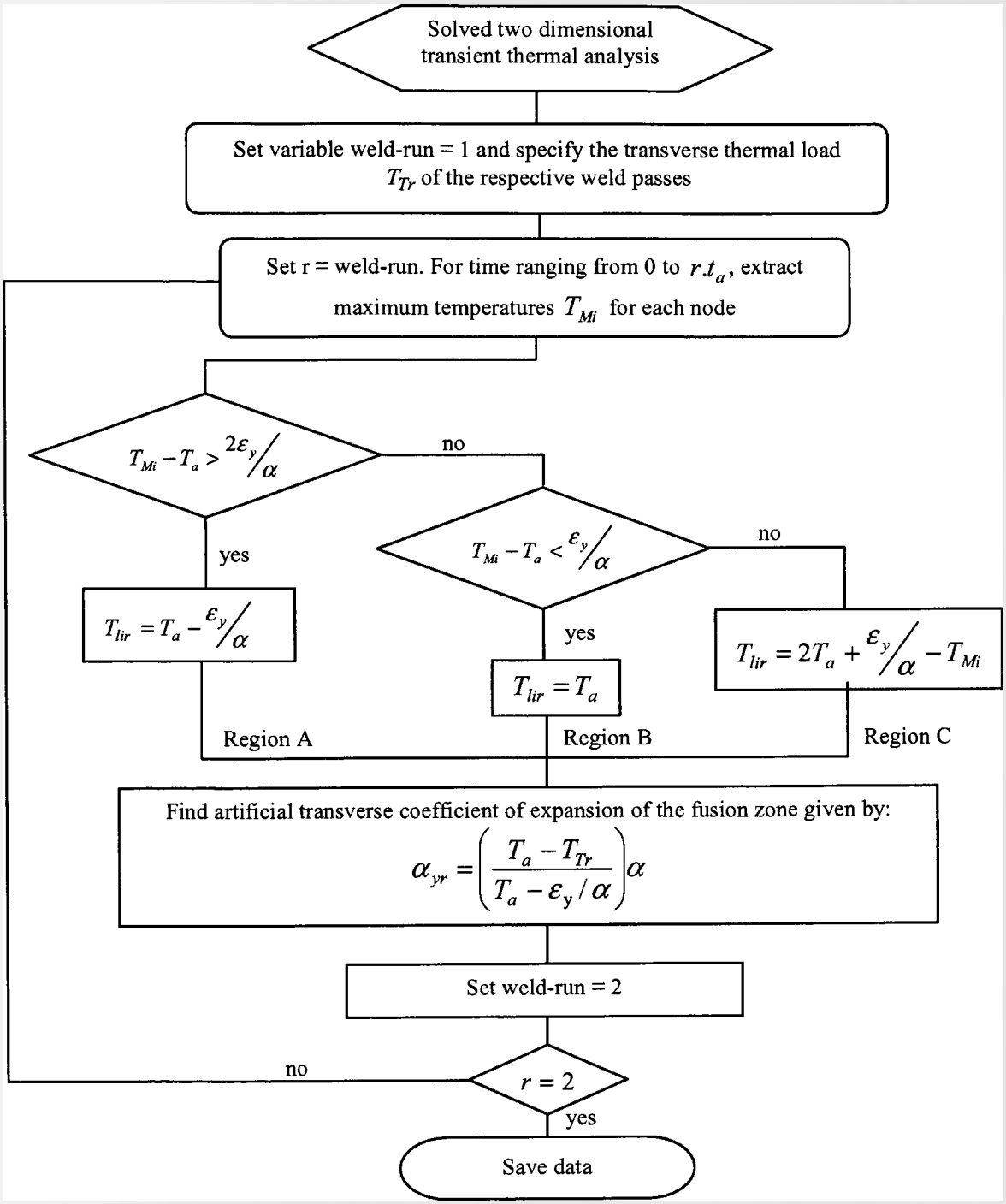

Figure 6.29: Retrieval of thermal loads in double-sided fillet welding

The above formulations were used in a simultaneous manner for the application of the thermal loads due to the first and second weld runs, via an orthotropic coefficient of thermal expansions as described in Figure 6.29 and Figure 6.30.

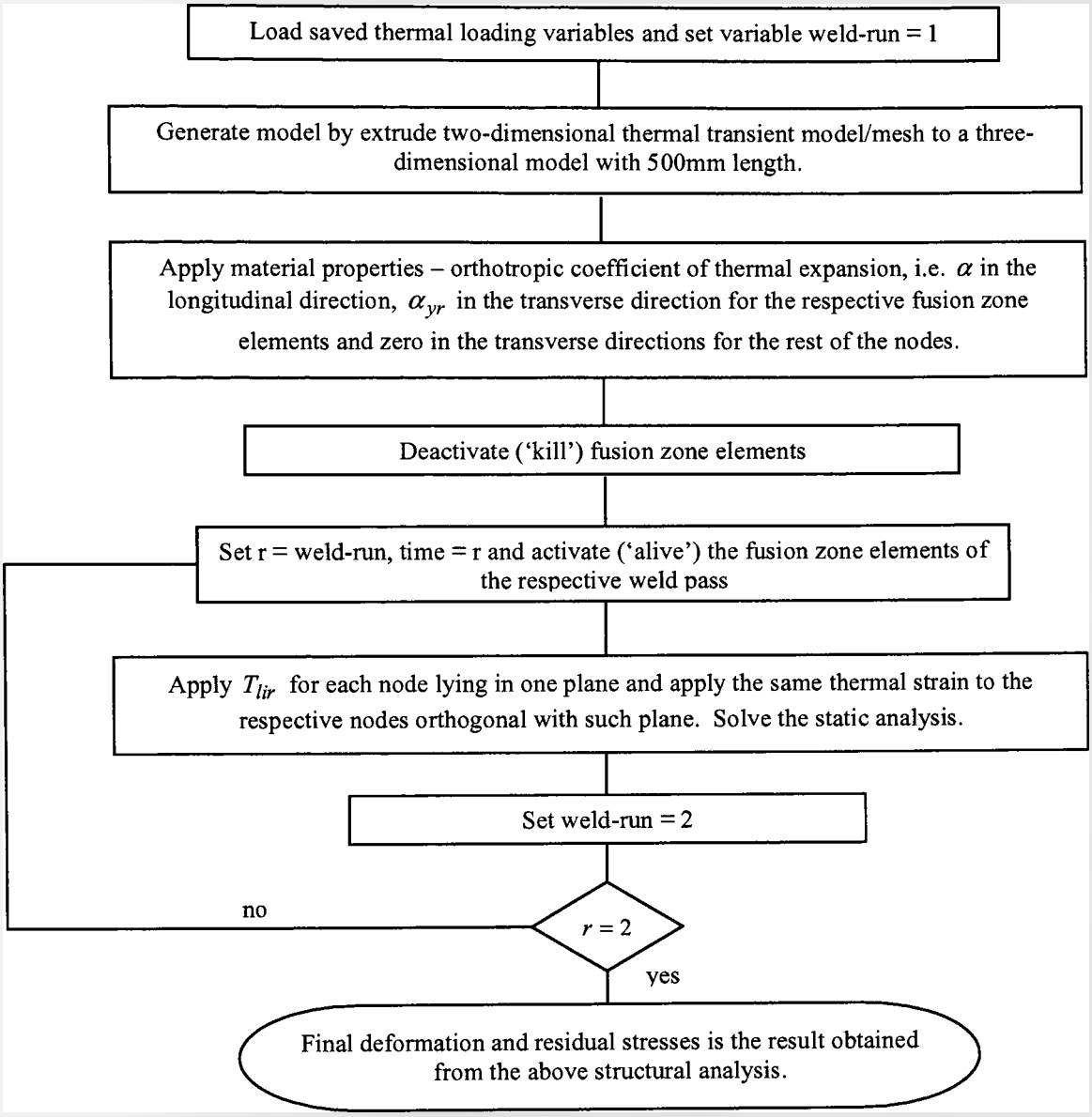

Figure 6.30: Structural analysis in double-sided fillet welding

The algorithms presented in the above were used for the prediction of the out-of-plane deformation. In the first instance the thermal load constituting the transverse thermal contraction was established. Figure 6.31, shows the macrographs of a double-sided fillet weld for test specimen 1. Although the four specimen welds resulted in different weld pool dimensions, the overall area contributing to the

transverse contraction was similar. This is also suggested by the approximately equal angular distortion attained in the four test specimens.

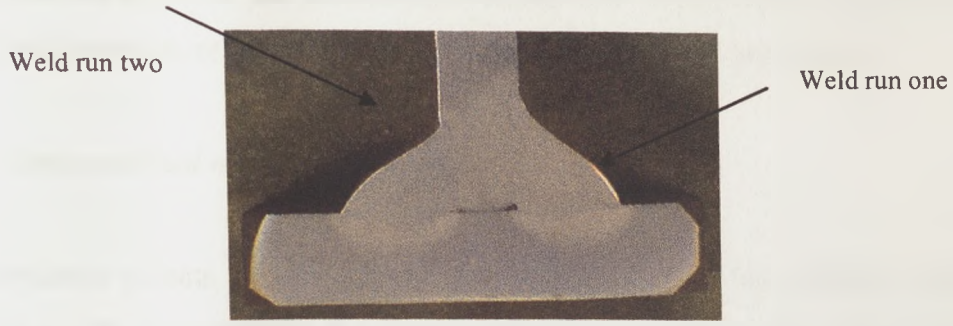

Figure 6.31: Fusion zone shape of test specimen 1

Using the fusion zone dimensions, a coefficient of expansion of 16×10^{-6}, a yield strength of $405 MN/m^2$, and equation 6.11, the thermal contraction loads T_T for the first and second weld run, are -1103.11°C and -1064.29°C respectively.

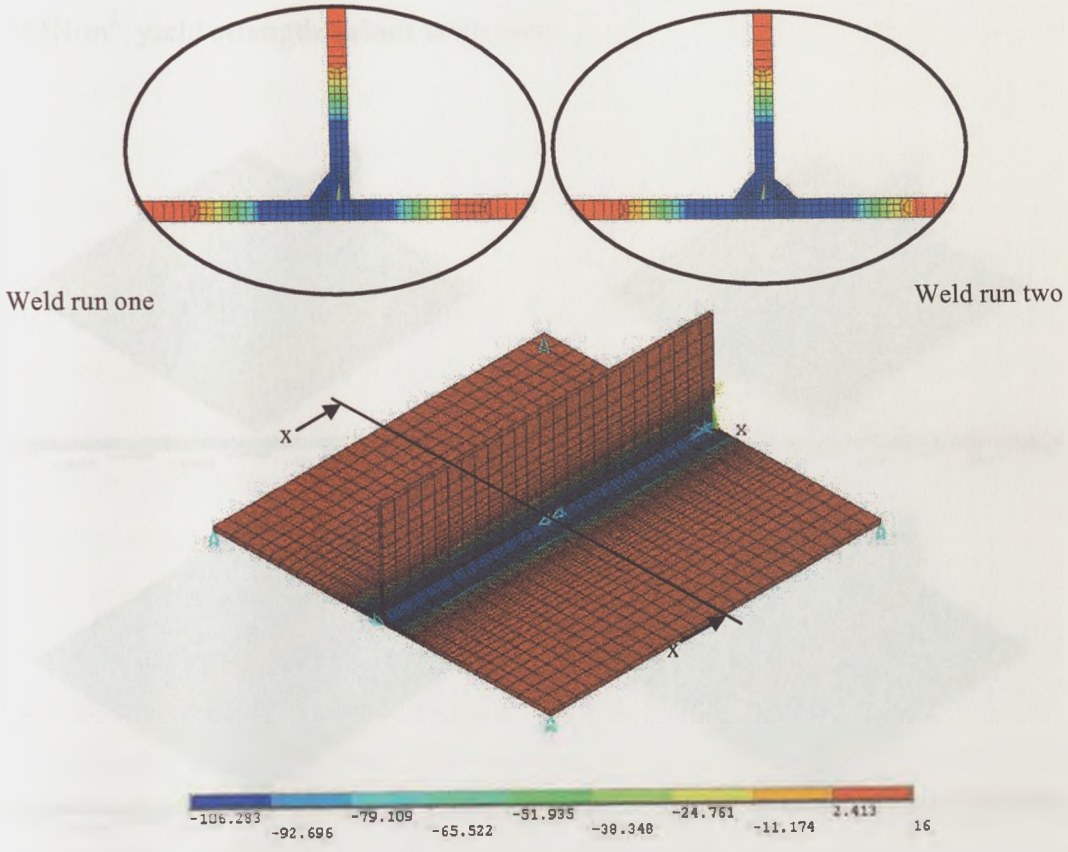

Figure 6.32: Thermal longitudinal load

Figure 6.32 shows the boundary conditions applied to the finite element model, together with the thermal longitudinal loads for the first and second pass. It is evident that the effect of the second pass on the final longitudinal contraction is to give a slight increase, resulting from the offset distance of the two welds.

6.3.4 Computational methods and results

The alternative effects of merged and unmerged nodes at the stiffener and plate boundary on the out-of-plane deformation was investigated. As distinct from the thermal transient analysis, the differences between these two approaches were insignificant. Secondly the effects of yield strength and coefficient of thermal expansion on the out-of-plane deformation were explored. Figure 6.33 shows the final out-of-plane deformations after weld run one and two, together with the corresponding longitudinal stress values, when $16x10^{-6}$ coefficient of expansion and $405MN/m^2$ yield strength values were used.

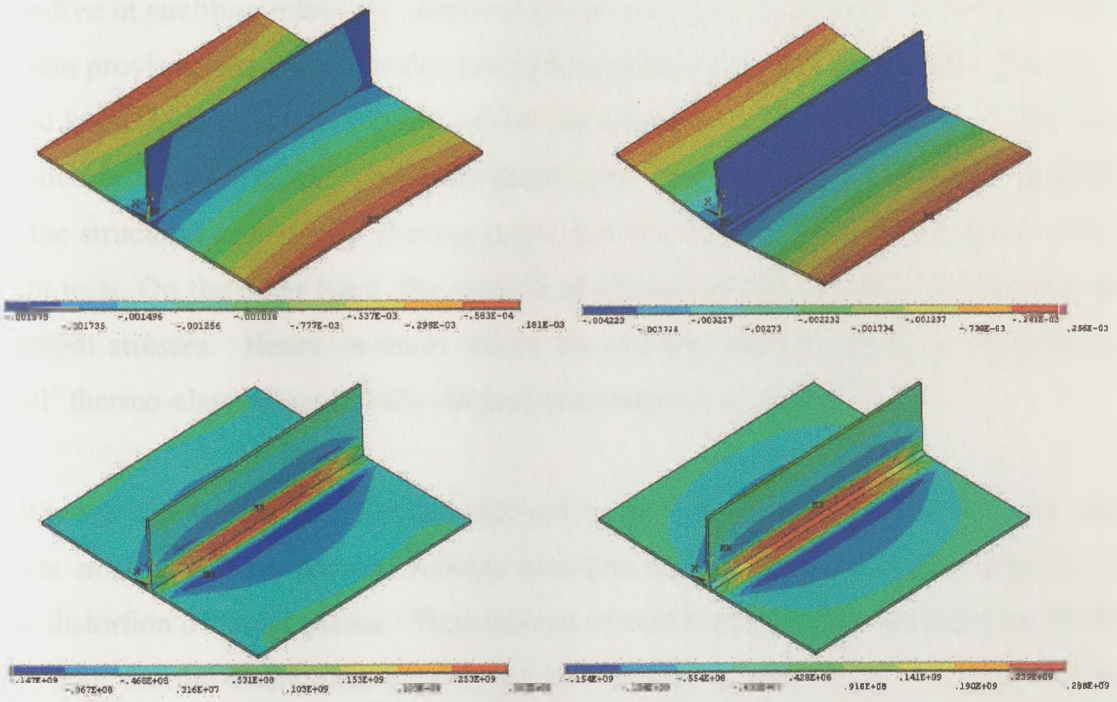

Figure 6.33: Out-of-plane deformation and longitudinal stress in double – sided fillet welding a) weld run one b)weld run two

Table 6.11 gives the root mean square of the total out-of-plane deformation for the respective material models. A stronger agreement with the experimental results was obtained when the expansivity was assumed to be $16x10^{-6}$ (refer to previous tables). Similar to the butt weld computational results, the yield strength showed no significant effect on the final deformation.

Model no	Co-efficient of thermal expansion ($x10^{-6}$/°C)	Yield Strength (MN/m^2)	RMS out-of-plane deformation (mm)	RMS angular distortion (°)	RMS longitudinal curvature (m^{-1})
1	14	405	1.9233	0.7624	(-) 0.0063
2	14	360	1.9434	0.7683	(-) 0.0060
3	16	405	2.2266	0.8810	(-) 0.0068
4	16	360	2.2522	0.8863	(-) 0.0063

Table 6.11: Smoothed computational results

6.4 Discussions

Comparison between the experimental deformation profiles and the computational prediction of out-of-plane distortion shows that the algorithms referred to earlier are effective in enabling relatively simple prediction of the out-of-plane distortions, with certain provisos – in particular that the initial profile of the plates is flat and there is a good knowledge of the coefficient of thermal expansion. The method should also be applicable to plates that are non-flat initially, provided that the initial shape is applied to the structural model as a starting point, but this has not been investigated in the pilot tests. On the other hand, the simplified algorithms fail to predict the transverse residual stresses. Hence in cases where the residual stresses are to be studied the 'full' thermo-elasto-plastic finite element simulation is necessary.

Although the sequential algorithm proved to be less accurate, the differences are quite small and the sequential scheme broadens applicability in terms of simulating the distortion of larger plates. Thus instead of performing a three dimensional, solid element, thermo-elastic-plastic, thermal and structural analysis, a two dimensional analysis can be performed for the thermal stage and for the angular distortion. This is then fed to a two-dimensional in-plane shell model to calculate the full out-of-

plane distortion. Such an approach reduces the number of elements required and the computational feasibility for complex models.

6.5 References

[6.1] Mollicone,P., Camilleri,D. and Gray,T.G.F, 'Simple Thermo-elastic-plastic Models for Welding Distortion Simulation,' *Science Technology of Welding and Joining,* (to be submitted).

[6.2] Lightfoot,M., 'Prediction of Distortion Control and Techniques to Avoid Rework,' *A Report on the General Causes of Fabricated Steel Plate Distortion, School of Marine Science and Technology, University of Newcastle Upon Tyne,* 2003.

[6.3] Lindgren,L.E., 'Finite Element Modeling and Simulation of Welding. Part 2: Improved Material Modeling,' *Journal of Thermal Stresses,* Vol.24, pp.195-231, 2001.

[6.4] Okerblom,N.O., 'The calculations of deformations of welded metal structures,' *Her Majesty's Stationery Office, London*, 1958.

[6.5] Wickramasingh and Gray, 'A Simple Treatment of Welding Distortion,' *Welding Research International,* vol. 8, 1987.

[6.6] Cadden,S. and Gray,T.G.F., 'Validation of a simple treatment of welding contraction,' *Euromech 221 Conference, Lulea,* 1987.

[6.7] Hooke,R. and Jeeves,T.A., 'Direct search of numerical and statistical problems,' *Journal of the ACM,* Vol.8, pp 212-229, 1961.

[6.8] Feng,Z. and Rowlands, R.E., 'Continuous Full-Field Representation and Differentiation of Three Dimensional Experimental Vector Data,' *Computers and Structures,* Vol.26, No.6, pp. 979-990, 1987.

[6.9] Comlekci,T., 'Development of Hybrid Experimental-Numerical Methods for Thermoelastic Stress Analysis,' *PhD Thesis, Mechanical Engineering Department, University of Strathclyde,* 1996.

[6.10] Camilleri,D., Comlekci,T., and Gray,T.G.F., 'Out-of-plane Distortion of CMn Steel Plates During Flux-Cored Ar/CO_2 Automatic Butt Welding,' *Proceedings of the International Conference on Metal Fabrication and Welding Technology (METFAB – 2003),* pp. 117 – 127, 2003.

[6.11] Berglund,D. and Runnemalm,H., ' Comparison of Deformation Pattern and Residual Stresses in Finite Element Models of TIG-welded Stainless Steel Plate,' *Proc.6th International Conf. On Trends in Welding Research,* Pine Mountain, Georgia, USA, 2002.

[6.12] Lindgren,L.E., 'Finite Element Modeling and Simulation of Welding. Part 1: Increased Complexity,' *Journal of Thermal Stresses,* Vol.24, pp.141-192, 2001.

CHAPTER SEVEN

CHAPTER 7

INVESTIGATION OF WELDING DISTORTION – INDUSTRIAL-SCALE PROGRAMME

7.1 Introduction

The overall project aims to improve the applicability of computational distortion prediction by providing simple and adaptable methodologies, which can be readily validated through experience of application in industrial-scale welded components. A key factor that underlies this aim is an uncoupled computational strategy. This technique has already been demonstrated for smaller plates, as described in chapter six and substantial agreement with the experimental results was obtained. However the scale of these test pieces was not entirely realistic in relation to common industrial practice. Typical industrial scale assemblies in the present study explore further complexities not present in the smaller models, such as buckling phenomena, the effects of gravity and support positions and variations in pre-welding assembly practices. The study also encompasses other difficulties related to mesh density and other finite element modeling problems, which make the full thermo-elasto-plastic finite element analyses complex and inefficient to use in the context of industrial scale welded structures.

The first step in the uncoupled approach to welding distortion is to establish the transient thermal distributions. This may be achieved in a variety of ways, and some of these have been analysed in chapter five. In the second computational stage of the uncoupled approach, differential strains induced by the transient thermal gradients are translated into contraction stresses, which produce mechanical distortion. The thermo-elasto-plastic simplified models, developed from the early insights of

Okerblom [7.1] and presented in chapter three, were used in the present treatment, with certain extensions, relating to buckling, restraints and gravity effects which will occur in thin, large scale welded structures. This chapter addresses various simplifications and modelling approaches essential in the prediction of the out-of-plane deformation in typical industrial scale welded structures and investigate ways to minimize the final out-of-plane deformation, via an optimisation of the welding sequences in multiply stiffened plates. Three forms of welded structures and procedures are considered:

1. Butt-welding of 3.99m x 1.35m x 5mm thick, CMn steel plates.
2. Attachment of a single stiffener to a large plate, through double-sided fillet welding of a CMn steel 100 x 6mm stiffener, attached at the centre, to a 4m x 1.2m x 5mm thick base plate of the same material.
3. The attachment of multiple stiffeners to a large plate, through single fillet welds applied on one side only of each stiffener. The welded attachments consist of three CMn steel stiffeners of dimensions 100 x 6 mm, attached at 0.5m pitch to 4m x 1.5 m x 6 mm thick base plates of the same material.

The theoretical models and results generated in the above schemes have been supported at all stages by welding tests of a realistic nature to maintain confidence in the validity and applicability of the treatments. This approach has been demonstrated in chapter six, where experimental and computational results were given for the welding distortion of a pilot test series of small steel plates.

7.2 Out-of-plane distortion of large-scale butt welded steel plates

Six test butt welds were carried out using a purpose-built rig (see Figure 7.1) described in chapter four, to carry out the following functions:

- Complete a single-pass, full-penetration, automatic MIG weld with Ar/CO_2 shielding and flux-cored wire on 3.99m x 1.35m x 5mm thick plates, while continuously monitoring voltage, current and travel speed.

- Measure temperatures continuously during welding and cooling, using thermocouples in fixed locations on the plate and a thermographic camera for whole-field recording.
- Measure overall, out-of-plane, transient deformations, during welding and cooling, using Linear Variable Displacement Transducers (LVDT) in a fixed array (see Figure 7.2).
- Measure out-of-plane deformations over the whole plate, before and after welding and cooling, using a laser scanning system.

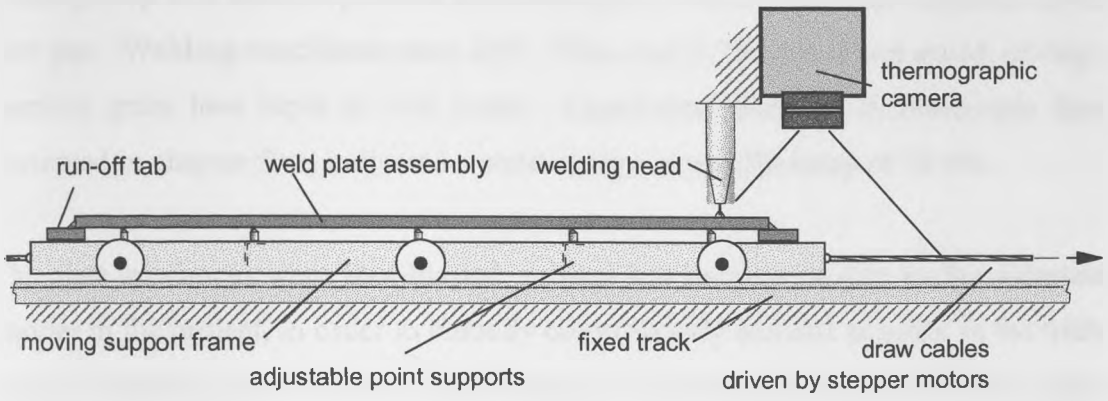

Figure 7.1: Schematic of welding rig

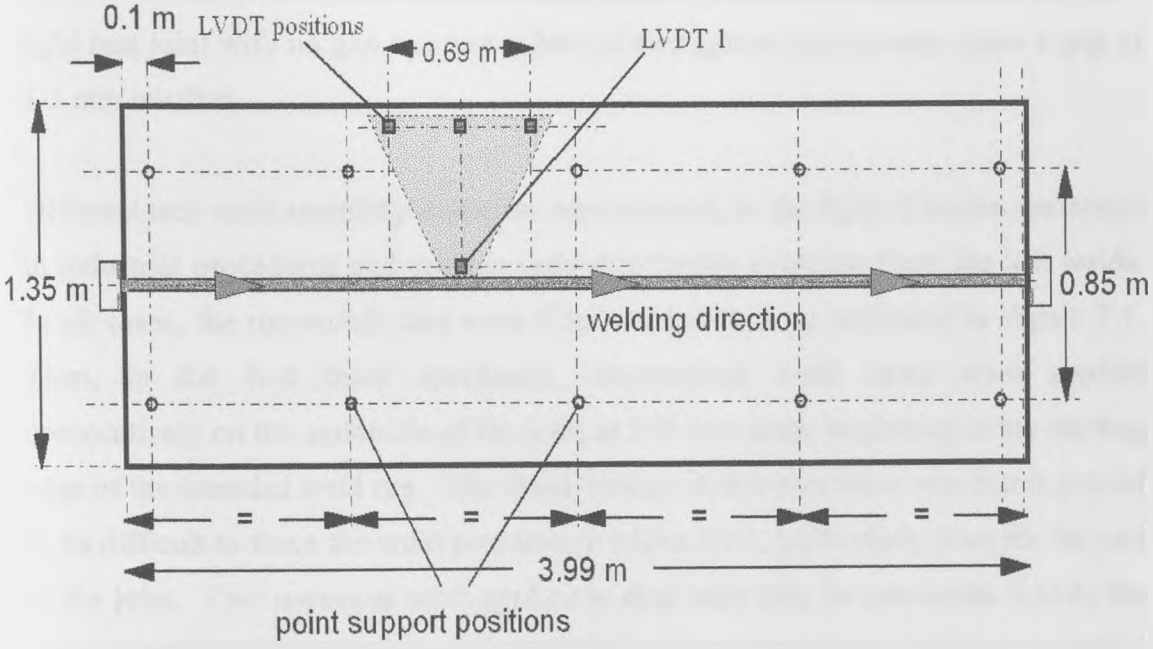

Figure 7.2: Layout of supports and LVDTs

The CMn steel plates (LLYODS 2000 DH36) were supported on an array of height-adjustable point supports, fixed to a moving frame in the layout shown in Figure 7.1 and Figure 7.2. This frame was traversed at the required welding speed under the welding head and thermographic camera, which were mounted in a fixed position. The relative deformation data acquired by the LVDTs was processed to measure the angular distortions and longitudinal profiles over the plate area spanned by the array.

The MIG weld was applied to a 60° included angle V-preparation. A ceramic backing strip was used to prevent burn-through, as there was some variation in the root gap. Welding conditions were 26V, 210A and 5.75mm/s travel speed, giving a nominal gross heat input of 950 J/mm. Correlation with the thermocouple data, presented in chapter five, indicated a weld energy input efficiency of 72.5%.

The plate specimens were shot-blasted, primed and laser-cut to size by the industrial partner in the project, in order to embody commercially realistic practice in the trials. Typical variations in fit-up and weld tacking procedure were also tolerated, to give some indication of sensitivity to such variations. The plates, when offered up for assembly and tacking, proved not to be ideally flat and it was not always possible to align both sides of the joint to a common plane. Likewise, the initial aim to have a tight butt joint with no gap was not achieved throughout and in some cases a gap of 1-2 mm resulted.

Different tack weld assembly strategies were applied, in the light of known variations in industrial procedures and continuously developing evidence from the test welds. In all cases, the run-on/off tabs were fillet-welded first, as indicated in Figure 7.1. Then, in the first three specimens, longitudinal weld tacks were applied consecutively on the underside of the joint at 250 mm pitch, beginning at the starting edge of the intended weld run. The disadvantage of this procedure was that it proved to be difficult to force the weld preparation edges level, particularly towards the end of the joint. Two measures were applied to deal with this. In specimens 3 to 6, the tack spacing was increased to 307 mm pitch (this also reflected advice on typical practice from the industrial partner). Also for specimens 4-6, a symmetrical tacking

strategy was adopted, starting at the centre of the weld run and working outwards, towards both ends. Eventually, in the two final tests, small mismatches in plate height were simply tolerated, in order to further reduce any 'locked in' bending moments due to forced levelling and tacking procedures, as applied in specimens one to four.

7.2.1 Test observations and results – Butt welds

Each tack-welded assembly was scanned prior to welding and then after complete cooling to ambient temperature, each scan comprising 394 longitudinal x 22 transverse points. The data points where then smoothed using the algorithm presented in chapter four after the work of Feng *et al* [7.2] and Comlekci [7.3]. In this instance the smoothing parameter (ζ) was set to zero, and 16 x 9, nine-noded 0.249m x 0.27m Langragian plane elements were used for the representation of the butt welded plates.

The initial out-of-plane deformation patterns of the assembled plates mounted on the rig could fairly be described as unstable, as relatively small out-of-plane forces on the surface of the assembled plates could flip the initial shape from one configuration to another. This is relevant to the outcomes of each test, as will be noted later. In particular a larger initial angular out-of-plane setting was noticed in specimens 4 to 6 as opposed to specimens 1 to 3. This is attributed to the fact that symmetric tacking (specimens 4 – 6) required less force to bring the specimens into alignment, consequently the plates were subject to less inherent residual stresses such that gravitational effects are more predominant. In the event, the net (final minus initial) root mean square out-of-plane deformation of each of the six specimens was similar. However the deformation profiles varied substantially for each specimen in the series. Test specimens two and four were particularly eccentric, as the final half-meter of these plate assemblies flipped from positive to negative angular deformation, leaving a severe transverse fold at the transition point (see Figure 7.3). (Note in this figure that the zero co-ordinate on the 'length' axis corresponds to the start-of-weld position).

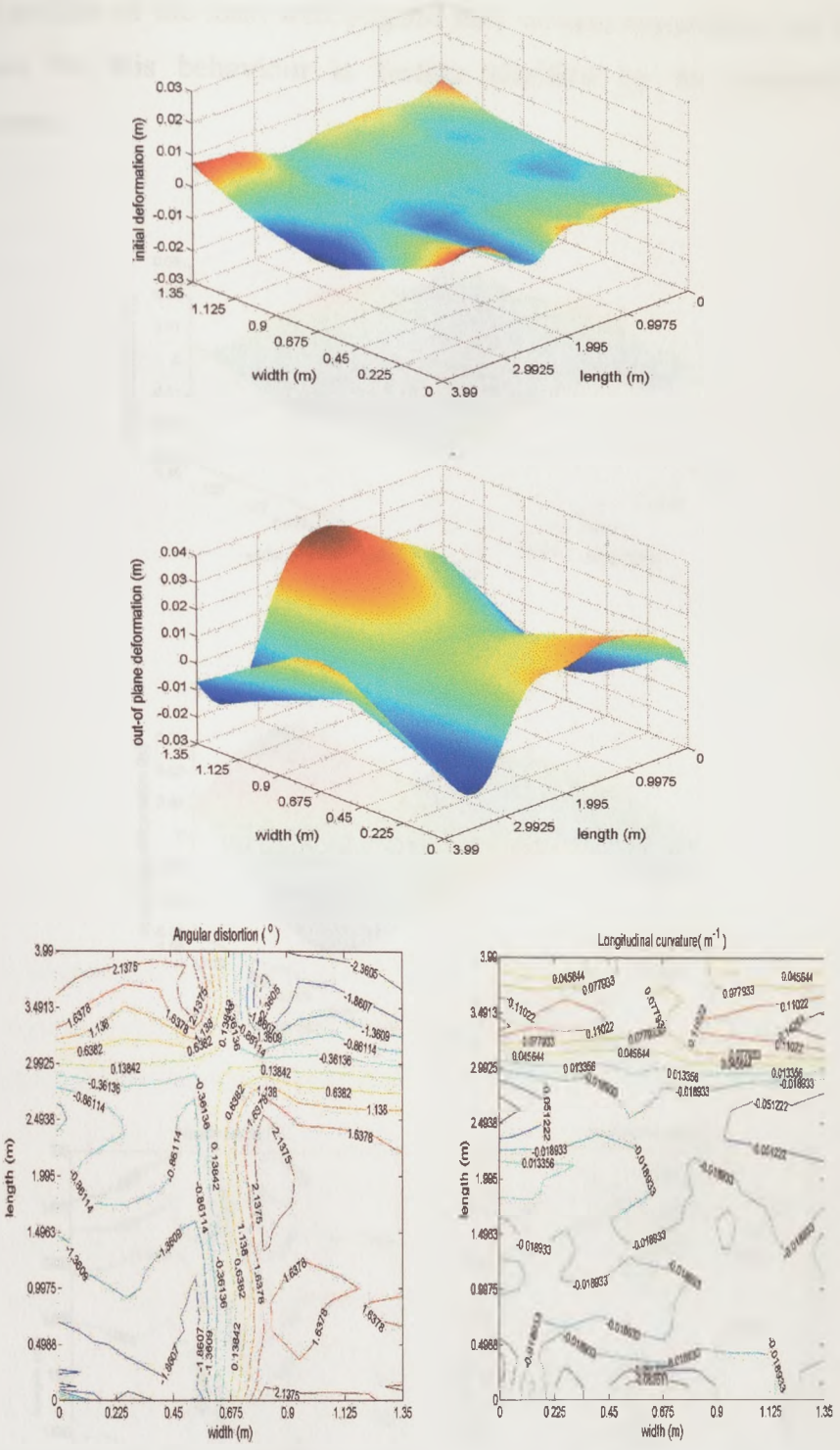

Figure 7.3: a) Initial profile b) net out-of-plane deformation c) angular distortion contour plot d) longitudinal curvature contour plot of specimen two

Aside from these two cases, the deformation patterns were characterised largely as magnifications of the initial deformations. In particular specimens 5 and 6 followed

the initial profiles of the least well aligned tack welded assemblies (see Figure 7.4). The reason for this behaviour is further clarified by the transient distortion measurements.

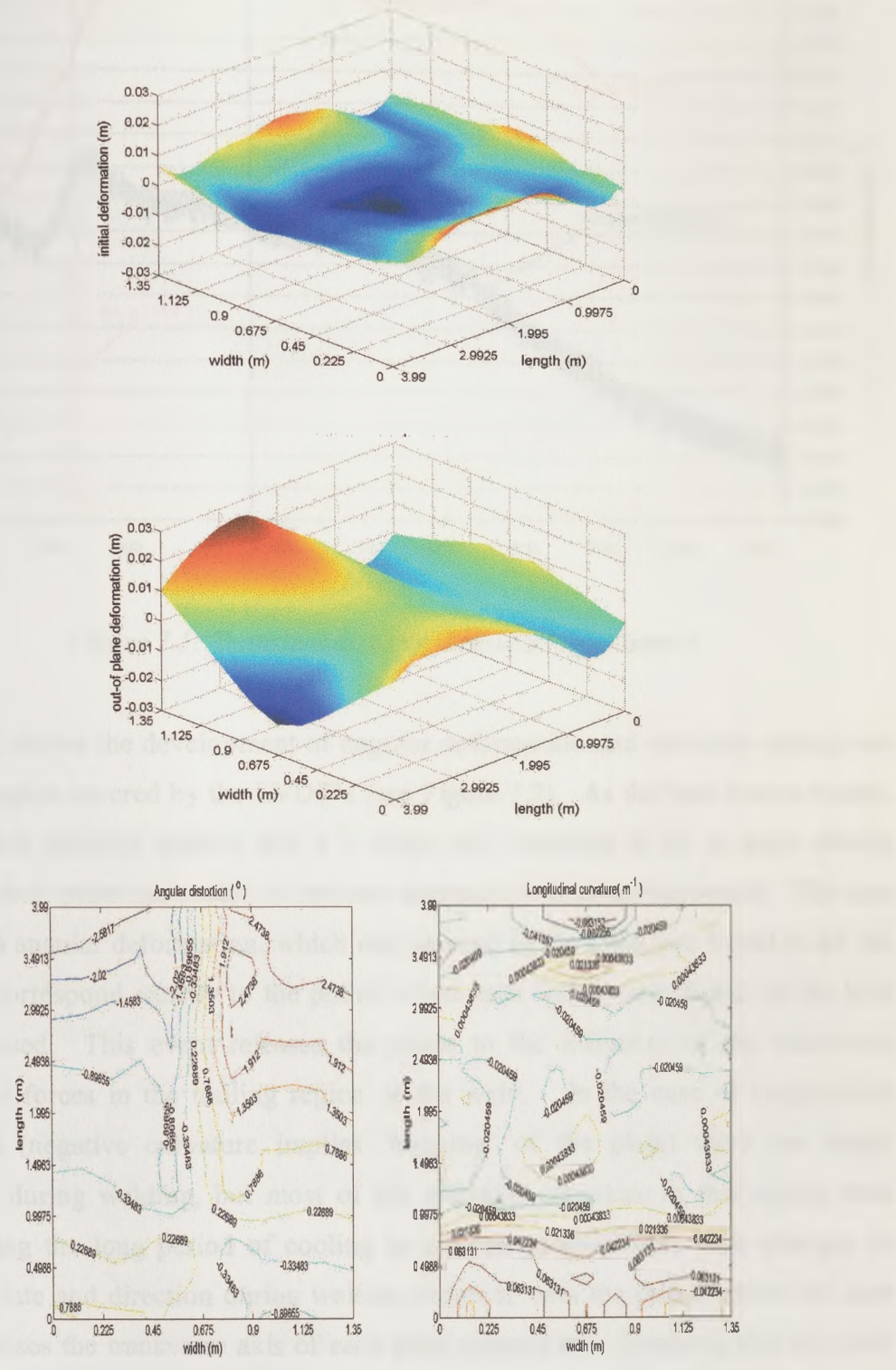

Figure 7.4: a) Initial profile b) net out-of-plane deformation c) angular distortion contour plot d) longitudinal curvature contour plot of specimen six

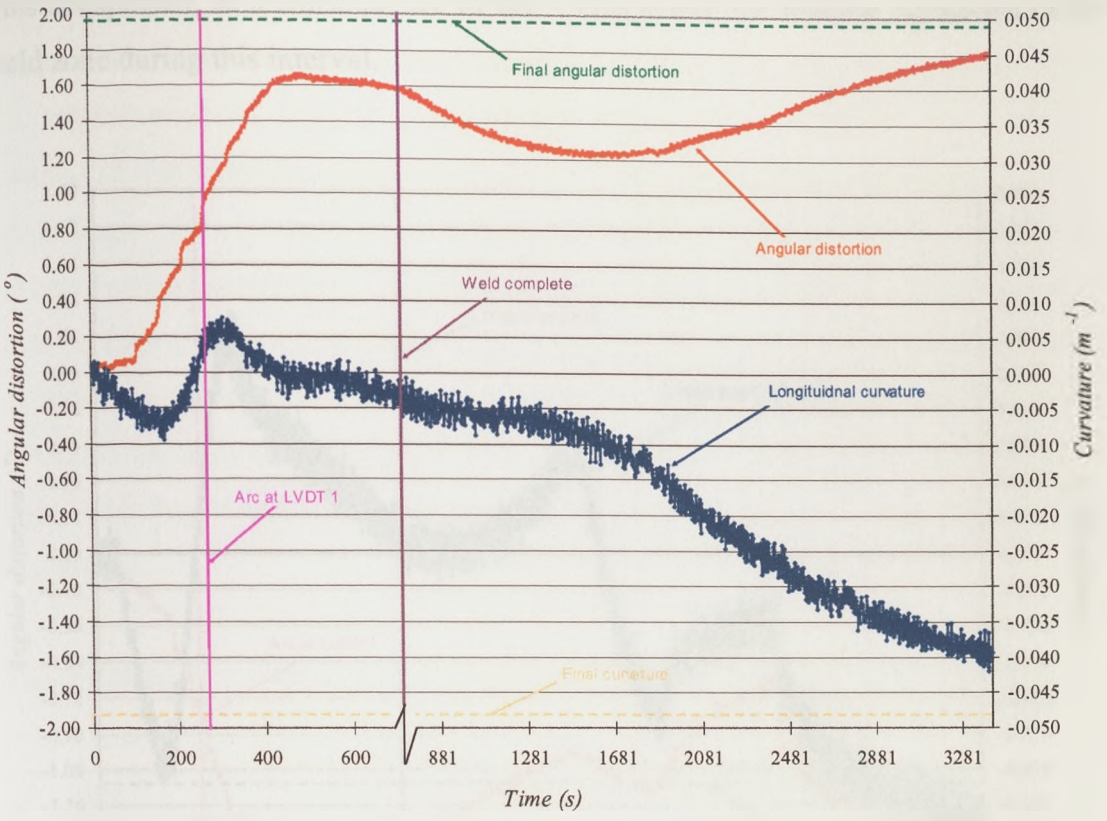

Figure 7.5: Transient distortion results – specimen 5

Figure 7.5, shows the development of angular deformation and curvature during test 5, in the region covered by the LVDT's (see Figure 7.2). As the heat source passes, the assembly deforms quickly into a V-shape and continues to do so more slowly until the whole plate has cooled to ambient temperature over a long period. The step changes in angular deformation, which can be seen in the trace, are found in all the tests and correspond exactly to the points where tack welds were fused, as the heat source passed. This event releases the plates to the influence of the transverse contraction forces in the trailing region of the weld. In the case of longitudinal curvatures (negative curvature implies 'hogging' of the plate) there are minor variations during welding, but most of the eventual curvature in this region took place during the long period of cooling to ambient temperature. The changes in curvature rate and direction during welding coincide with the points where the heat source crosses the transverse axis of each plate support pair, implying that the plate was lifting off various supports, as indeed was observed. Also note that sagging curvature is promoted when the heat source passes through the monitored region.

This is expected, as a consequence of the V-shape and the relative expansion of the weld zone during this interval.

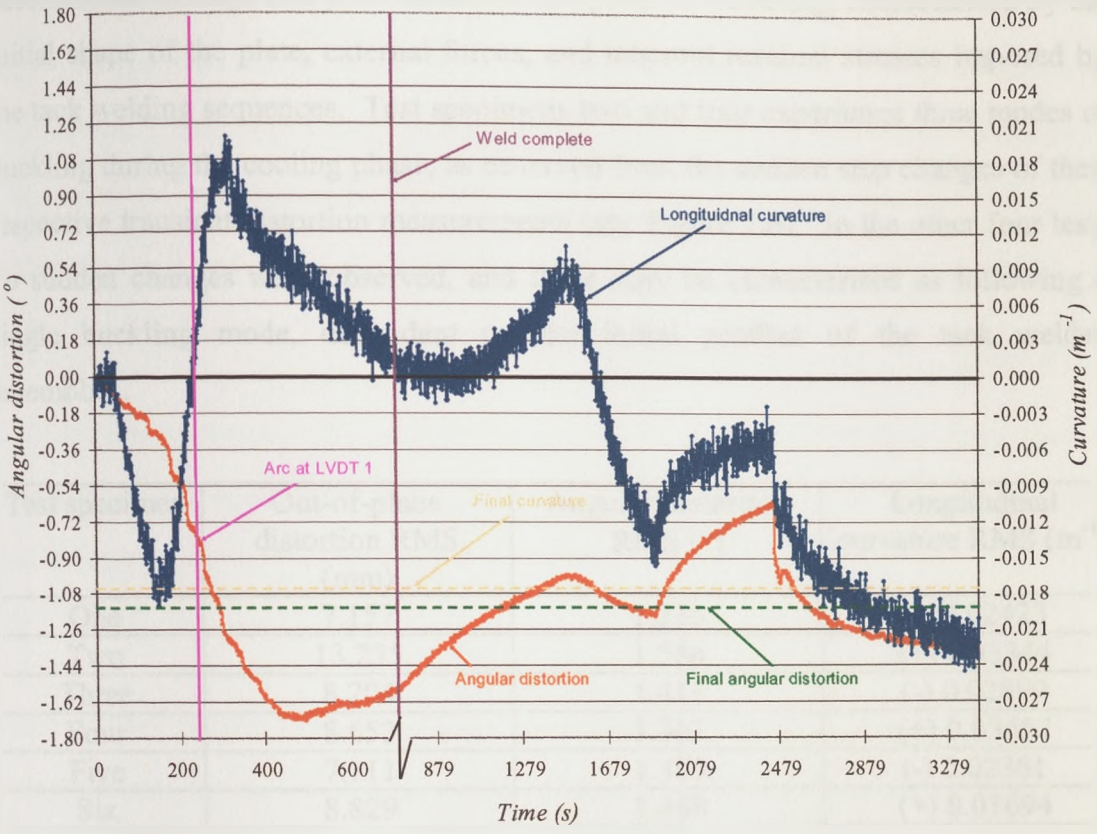

Figure 7.6: Transient distortion results – specimen 2

The pattern of dynamic deformation behaviour in test 2, which was unstable, is shown in Figure 7.6. The curvature changes are much more exaggerated, but also relate to the support positions. In this case, the implication is that changes of curvature after weld completion have been enough to raise the plate off the final pair of supports and the cantilevered weight of overhanging plate has triggered an unstable reversal of angular deformation and curvature at the 2479 s marker.

As distinct from the pilot tests, no single definite shape can be associated with the six experiments. A comparison between the six tests is given in Table 7.1 in terms of the root mean square (RMS) of the out-of-plane deformation, angular distortion and longitudinal curvature. While the angular distortion is approximately equal for all

specimens, the flatness (curvature) of the plates varied between a net hogged to a net sagged plate (where a negative and a positive RMS longitudinal curvature implies a net sagged and net hogged plate respectively). This suggests that the final deformations in large thin plate structures are prone to buckling, characterised by the initial shape of the plate, external forces, and inherent residual stresses imposed by the tack welding sequences. Test specimens two and four experience three modes of buckling during the cooling phase, as observed from the sudden step changes of their respective transient distortion measurements (see Figure 7.6). In the other four tests no sudden changes were observed, and these may be characterised as following a single buckling mode, dependant on the initial profiles of the tack welded assemblies.

Test specimen	Out-of-plane distortion RMS (mm)	Angular distortion RMS (°)	Longitudinal curvature RMS (m^{-1})
One	7.157	1.235	(-) 0.02423
Two	13.235	1.586	(+) 0.03344
Three	8.204	1.415	(-) 0.02899
Four	8.653	1.361	(+) 0.03657
Five	7.111	1.383	(-) 0.02381
Six	8.829	1.448	(+) 0.01694

Table 7.1: Root mean square of the deformations

7.2.2 Thermo-mechanical algorithms and computational features

The elasto-plastic thermo mechanical algorithms, presented in chapter three, were again adopted to load a longitudinal strain 'Mismatched Thermal Strain' and transverse strain 'Contraction Thermal Strain' on elastic finite element models of the large plate assemblies. This section describes further simplifications and other computational features, essential for the simulation of large thin plate models. In particular the mesh strategy adopted was different from the small-scale tests presented in chapter six. It is not efficient to simply extrude the two dimensional thermal models to generate the three dimensional large plate models. Transition regions (see Figure 7.9) from the fine mesh at the weld axis to the outer boundaries of the plate are essential to reduce the number of elements, thus substantially

reducing the computational time. However this implies that a direct node (2d thermal) to node (3d structural) thermal loading (as performed in the small scale test) is not viable. By assuming the maximum temperatures at distances transverse to the weld, to be inversely proportional to their respective distances y, the thermal load $T_l(y)$ maybe defined in terms of the transverse distance y. The longitudinal contraction is thus defined by three regions, relative to the transverse distance y. The innermost region is of yield level thermal ($T_{li} = -\varepsilon_y + T_a$) strain, bounded by the distances $y = 0$ and $y = y_1$ such that the maximum temperature at y_1 is given by:

$$T_M(y_1) = \frac{2\varepsilon_y}{\alpha} + T_a \qquad \textit{Equation 7.1}$$

The outermost region within elastic limit hence a net zero thermal strain (points undergoing an elastic cycle, $T_{li} = T_a$), are points residing at $y = y_2$ and beyond, such that the maximum temperature at y is given by:

$$T_M(y_2) = \frac{\varepsilon_y}{\alpha} + T_a \qquad \textit{Equation 7.2}$$

In the elastic/ plastic zone, an average proportional constant (A_t), derived from the computational thermal analysis, was used such that the artificial temperature load was in the form of

$$T_{li}(y_i) = 2T_a + \frac{\varepsilon_y}{\alpha} - \frac{A_t}{y} \qquad \textit{Equation 7.3}$$

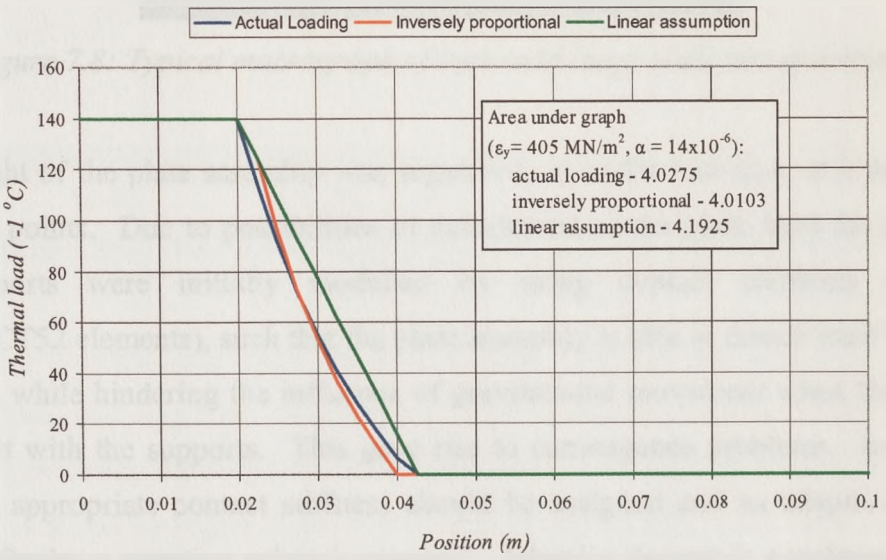

Figure 7.7: Artificial temperature load profiles

Figure 7.7, shows the different artificial load temperature profiles, when inversely and linear proportional alternative assumptions are used. Comparison with the actual temperature profile (as obtained by a direct node to node thermal load) shows an insignificant difference in the contraction force when an inversely proportional simplification is used.

In the case of the transverse contractions, the penetration of the fusion zone profiles in the test welds (see Figure 7.8) exceeded the values where the correction parameter k would have been applicable refer to chapter 3 section 3.3.1. Hence, the fusion zone was simply defined by the points corresponding to the 'start of cooling' temperature of 1000° C. Again, orthotropic coefficients of expansion were used to enable the artificial temperature loads at a given point to generate the required simulated thermo-mechanical strains in the finite element implementation. In the longitudinal axis, the actual coefficient of expansion was used, but in the transverse and thickness directions, the coefficient was set to zero, apart from in the fusion zone, where it was set to a value α_y (refer to equation 6.10).

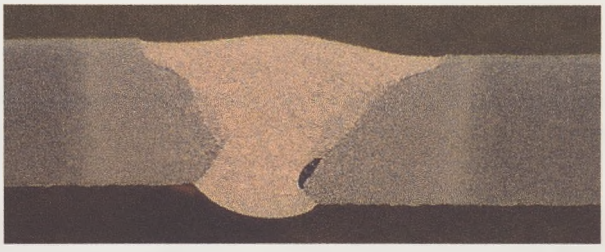

Figure 7.8: Typical macrograph of butt-weld large scale test specimens

The weight of the plate assembly was supported, as in the real case, at a number of specified points. Due to possibilities of detachment of the plate from the supports, the supports were initially modelled by using contact elements (ANSYS CONTACT52 elements), such that the plate assembly is able to detach itself from the supports, while hindering the influence of gravitational movement when the plate is in contact with the supports. This gave rise to convergence problems. In the first instance, appropriate contact stiffness should be assigned and an adaptive descent Newton-Raphson equation solver is required. Adaptive descent is a technique which

switches to a 'stiffer' matrix if convergence difficulties are encountered and switches back to full tangent as the solution converges, in order to find the appropriate contact stiffness. This gave rise to a number of convergence problems, particularly since a stiff matrix is not wanted when large displacements are involved. Disabling the adaptive descent option and using a line search, Newton-Raphson, sparse direct equation solver, reduced convergence problems. Alternatively ANSYS LINK 10 elements were used to model the supports. These elements were set to exhibit stiffness under compressive loads but have zero stiffness in tension. The finite element model, including boundary conditions and thermal loads is given in Figure 7.9.

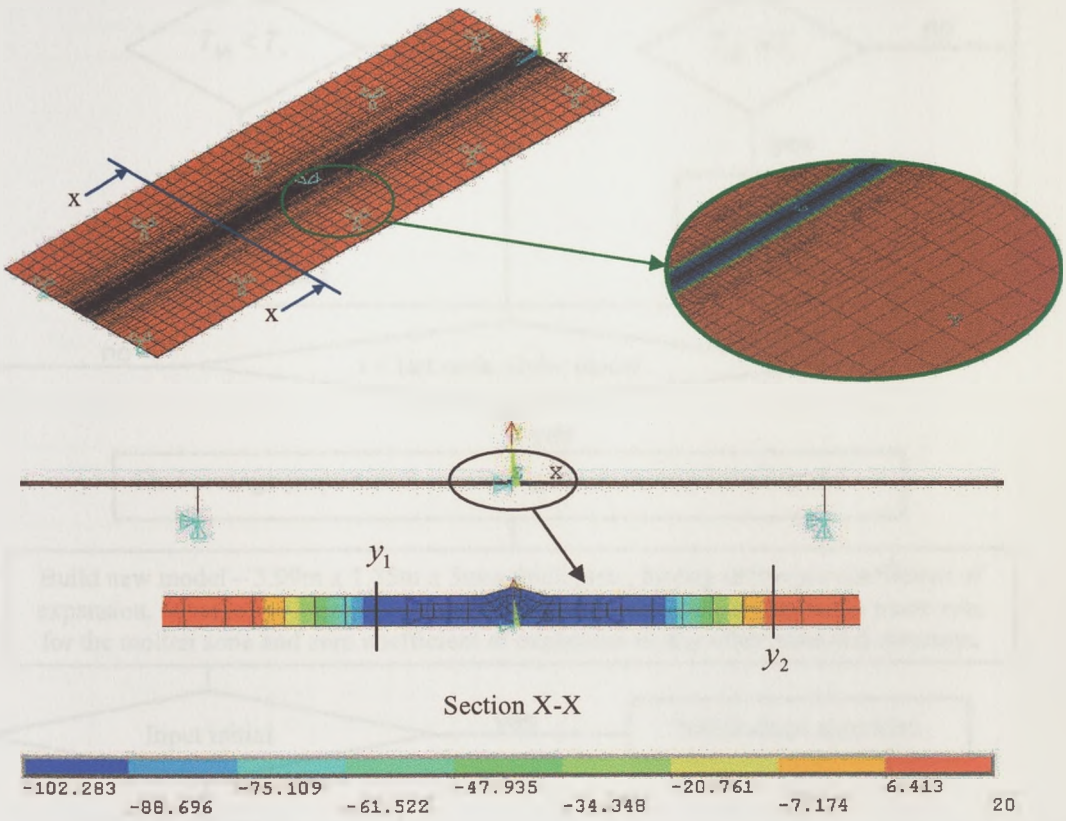

Figure 7.9: Finite element modelling of large-scale butt weld specimens

The above formulations were applied to the problem via two approaches – simultaneous and sequential algorithms. The flow chart for the 'simultaneous' algorithm, whereby the transverse and longitudinal temperature loads were applied together, is given in Figure 7.10. This strategy has already been demonstrated in

chapter six, however in this case the thermal loading assumes an inversely proportional assumption, for mesh conservation.

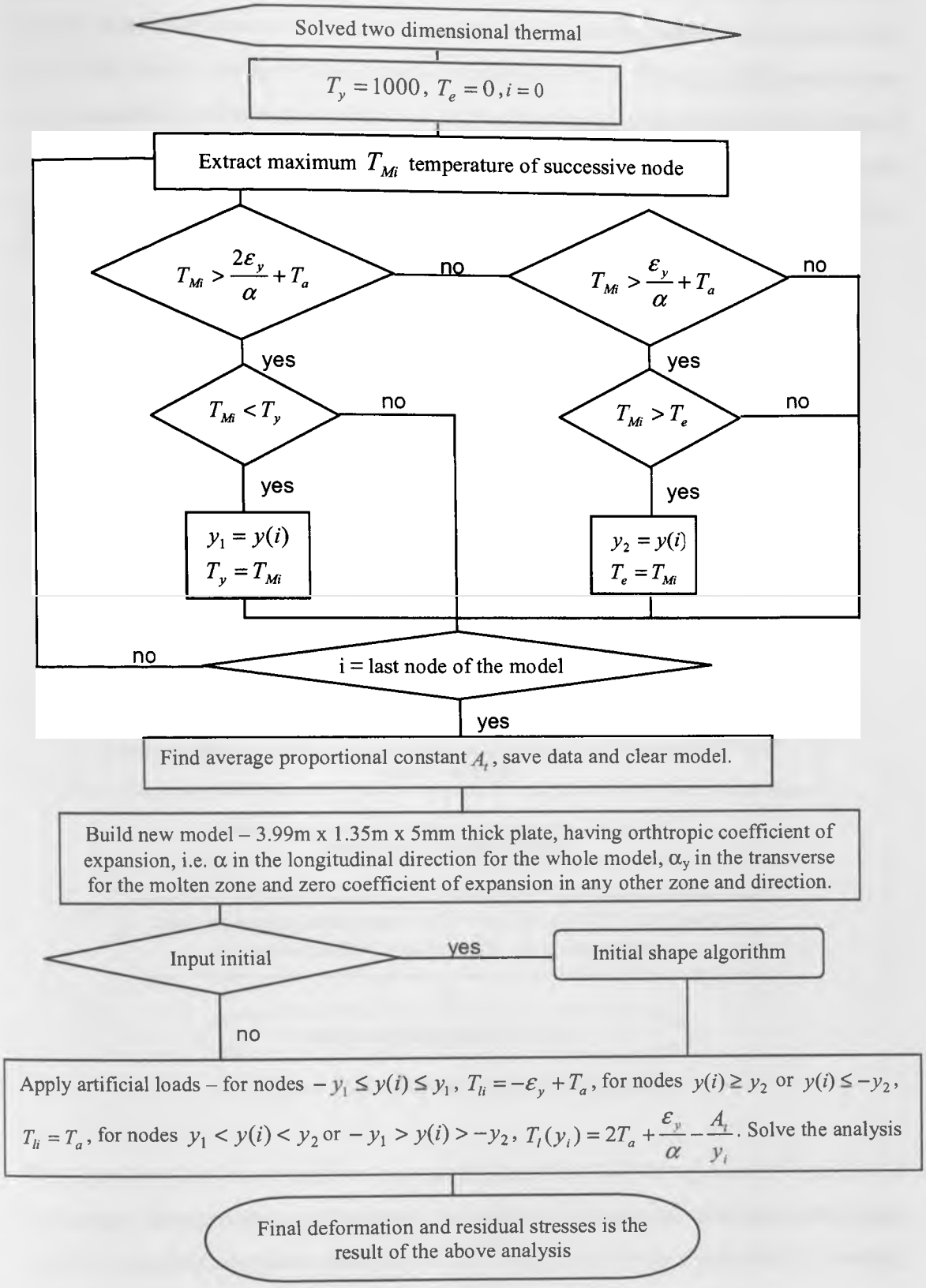

Figure 7.10: Thermo-elastic simultaneous algorithm

The flow chart also shows that the computation can be carried out alternatively in terms of a plate assembly which is initially perfectly flat, or one where the initial out-of-plane shape has been measured and is used as the starting point for the simulation. The 'initial shape' sub-algorithm is shown in Figure 7.11. This algorithm makes use of the smoothed initial shape of the respective butt weld experiments, consisting of equal 0.249m x 0.27m nine-node elements, together with shape functions, to evaluate the initial deformations of the different nodal points constituting the finite element model of each test specimen.

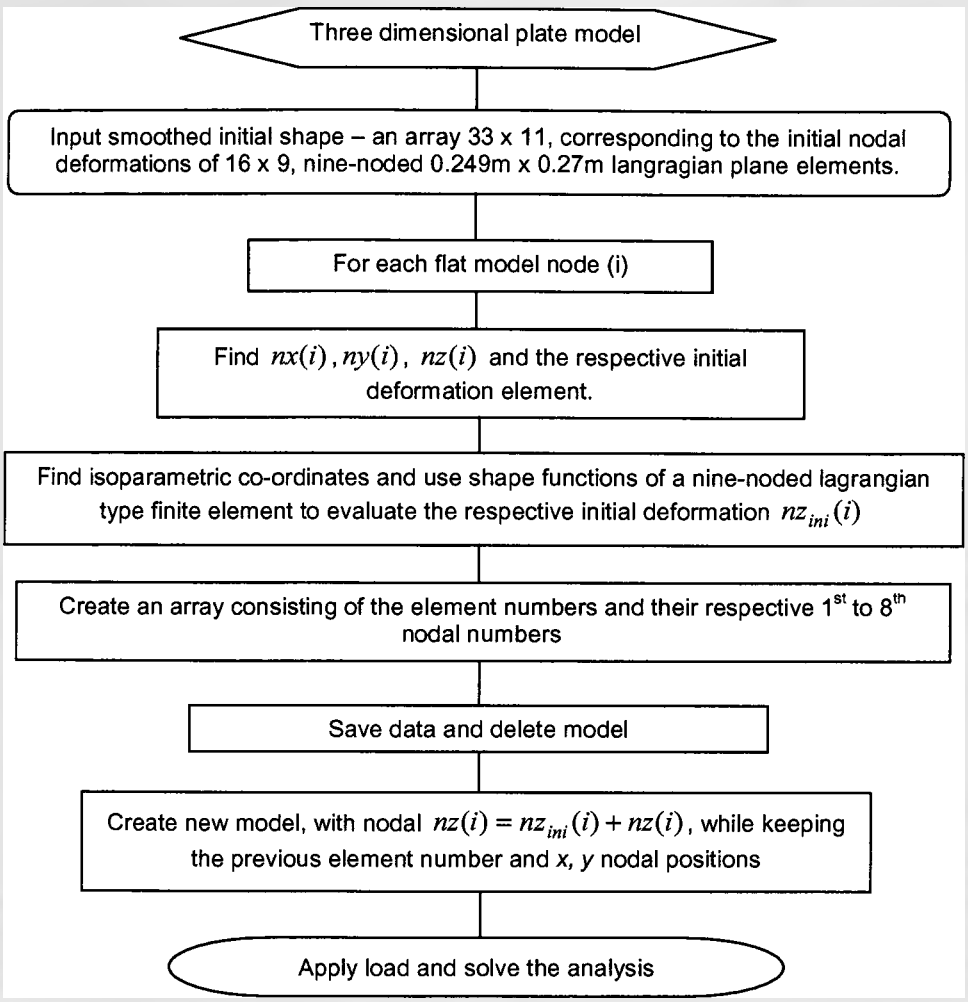

Figure 7.11: Initial shape sub-algorithm

The algorithm for the alternative 'sequential' implementation is given in Figure 7.12. In this case the transverse deformations are applied first and the resulting plate shape, which is distorted angularly along the whole length of the plate, provides the starting point for simulation of the longitudinal deformation process.

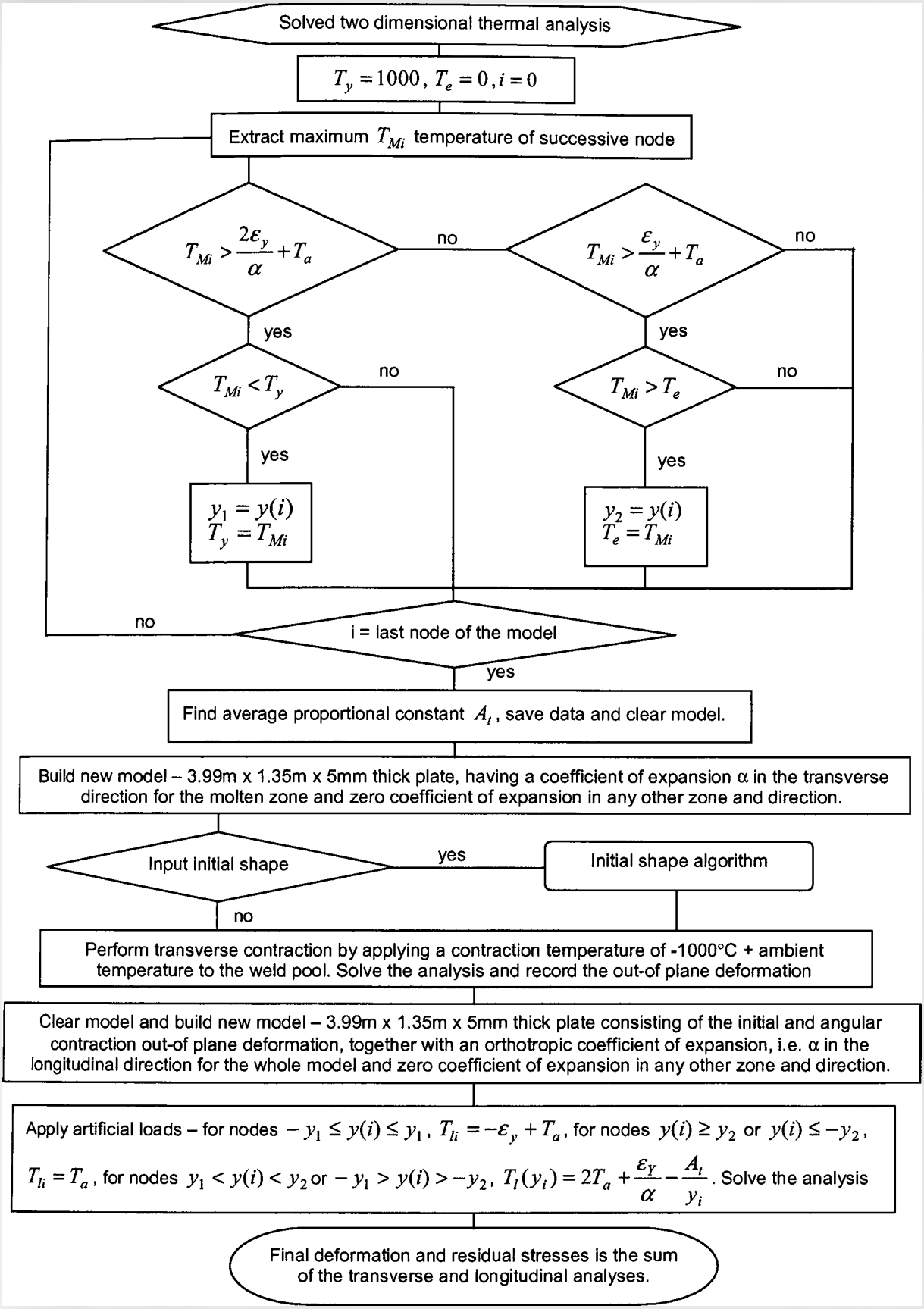

Figure 7.12: Thermo-elastic sequential algorithm

Other computational features essential in the analysis of large thin plate structures include gravitational loading, incorporated in the analysis via the ANSYS command ACEL together with large displacement strain analyses activated via the ANSYS command NLGEOM, ON.

7.2.3 Computational results

The structural finite element results may be grouped into three. In the first instance (referred to as 'flat plate simultaneous' analysis 'FPSIM'), the initial profile of the plate was assumed to be flat while the second group (IPSIM) comprised analyses where the initial out-of-plane deformation of the respective six butt weld tests was incorporated in the start of the analyses. In both of the above mentioned approaches, the longitudinal and transverse contraction where applied in a simultaneous fashion as described in Figure 7.10. Finally, a group of analyses (IPSEQ) in which the thermal loads were applied in a sequential fashion as described in Figure 7.12, and having the initial out-of-plane deformation fed into the analyses, were also performed. Various effects related to the choice of Poisson's ratio (set to 0 or 0.3), coefficient of expansion (set to $14\text{x}10^{-6}$ or $16\text{x}10^{-6}$), fusion zone shape relating to a fully penetrated and unpenetrated weld having a root of 0.5mm, and load stepping strategies were investigated to optimise the computational process.

Although assuming an initial flat profile in the 'FPSIM' analyses, the self weight of the plate generated an initial small out-of-plane deformation dependant on the support positions. These ripples are then magnified by the longitudinal tension in the welding simulation and this is accompanied by a root mean square angular distortion of 1.05°. The changes in the final out-of-plane deformation of 'FPSIM' computational results resulting from the aforementioned parameters are not significant with respect to the final out-of-plane deformation profile, particularly since only one definite shape is evident in all the configurations (See Figure 7.13). No change was observed when the artificial thermal loads were applied in a one load step analysis and a ten load step analysis, when LINK 10 elements were used to model the supports, particularly since an elastic analysis was performed. Note that

when contact elements were used changes in the final profile of the plate were noticed, but this is thought to be due to the non-consistent stiffness matrix of the contact elements assigned during the simulation by ANSYS solver, resulting in over penetration of specific supports during the different stages of the analysis.

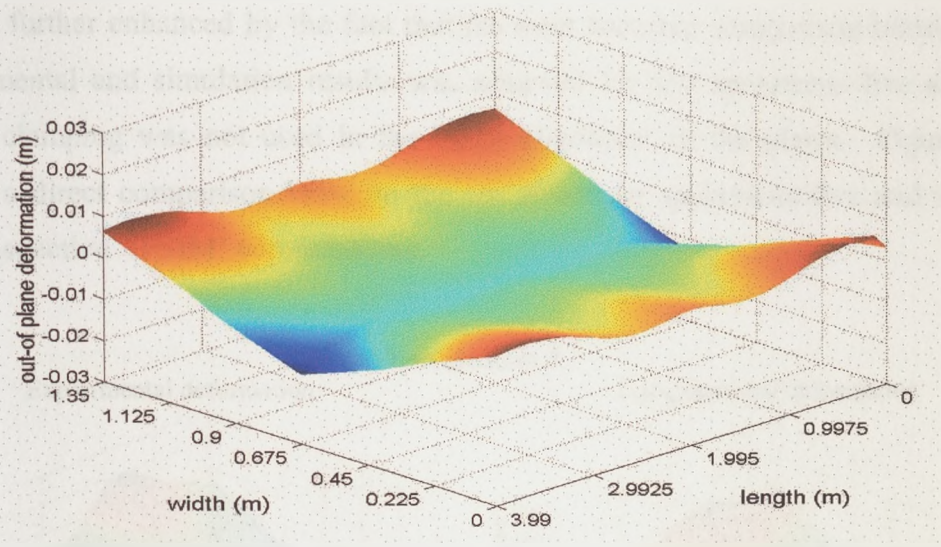

Figure 7.13: Computed out-of-plane deformation of an initially flat plate

The root mean square of the out-of-plane deformation of a typical 'FPSIM' computational analysis, when assuming a zero Poisson ratio, $14x10^{-6}$ coefficient of expansion and a fully penetrated fusion zone as shown in Figure 7.8, was 4.049mm. This is accompanied by a longitudinal curvature of (-) 0.01452 m^{-1}, suggesting that the initial profile of the different test welds plays an important aspect for the correlation of the simulation and the test weld results.

When applying the initial profile to the start of the simulation (IPSIM), the final out-of-plane deformation varied substantially for each specimen. The deformation pattern of the simulation results were characterised as magnifications of the initial deformation. Aside from test specimens two and four a strong correlation between the simulation and experimental results exists. The reason for the unmatching results in test specimens two and four, lies in the fact that large displacement structural analysis was performed, such that the final assumed 'buckled' shape mainly depends on the initial restraints at the beginning of the simulations, i.e. the initial out-of-plane

profile, support positions and self-weight. Any other buckling modes for the same longitudinal contraction force are not possible, unless a buckling analysis is performed. Other factors affecting the final deformation include locked in forces, such as bending moments and residual stresses, due to the initial alignment and tack welding procedures and these have not been modelled due to the lack of information. This is further enhanced by the fact that the most accurate comparison between the experimental and simulation results was achieved for test specimens five and six, where clamping was not used in the initial alignment of the plates. Figure 7.14 shows a direct comparison between the test result for specimens five and six and their respective 'IPSIM' computations.

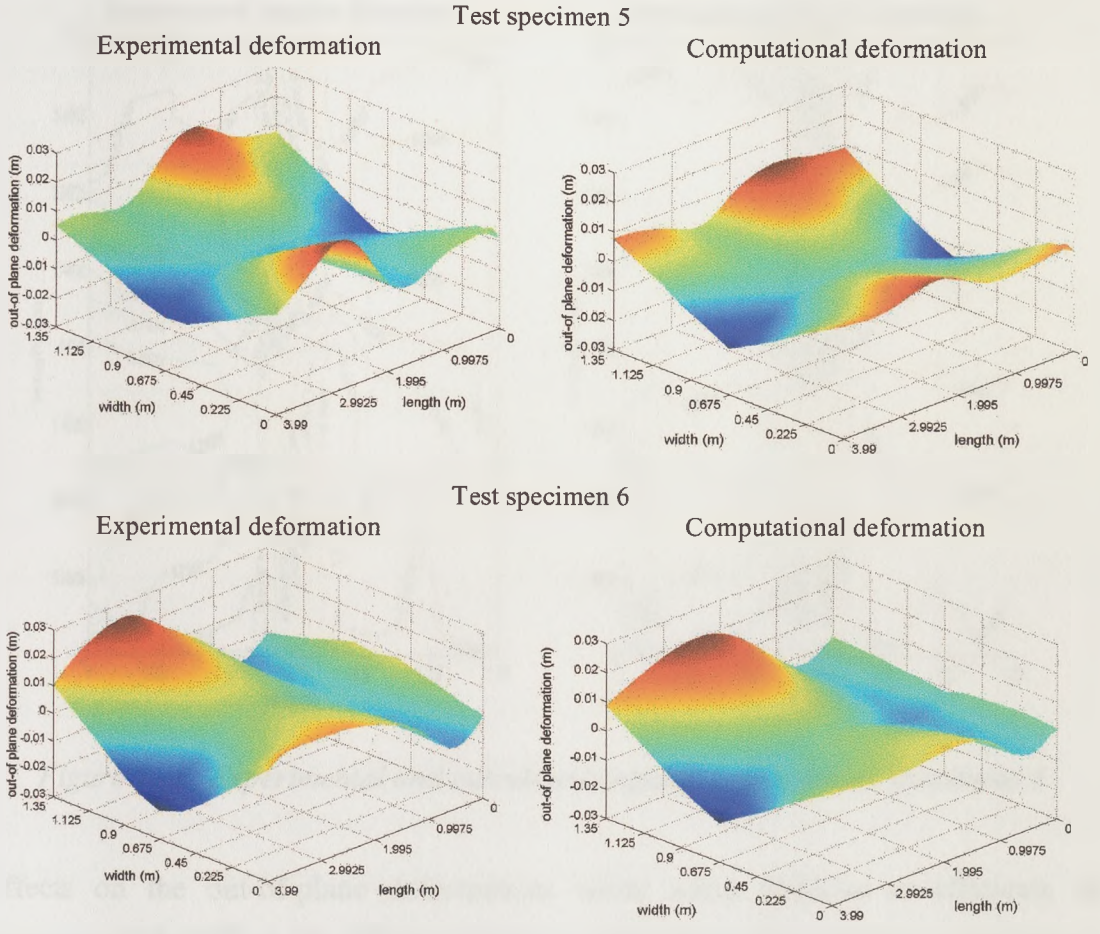

Figure 7.14: Experimental and calculated deformations test specimens 5 and 6

The capability of the computational method to model angular deformation is particularly important, as the resulting angular distortion drives the longitudinal

behaviour. The effect of the fusion zone shapes, assumed in the computational analysis, had a significant role on the final out-of-plane deformation. Closely matching results were attained when a non-fully penetrated weld was modelled throughout the whole length of the plate. This is somewhat subjective, as the weld pool shape in the test welds was not constant, due to variations in weld gaps. Nonetheless a non-fully penetrated weld zone was more evident in the test welds. Figure 7.15 shows overall contour maps of angular deformation in specimen 5 and again indicates good comparison. It is also noteworthy that in both the experimental and simulation cases, the angular deformation is highly concentrated in the fusion zone, as assumed in the simple Okerblom model for transverse deformation.

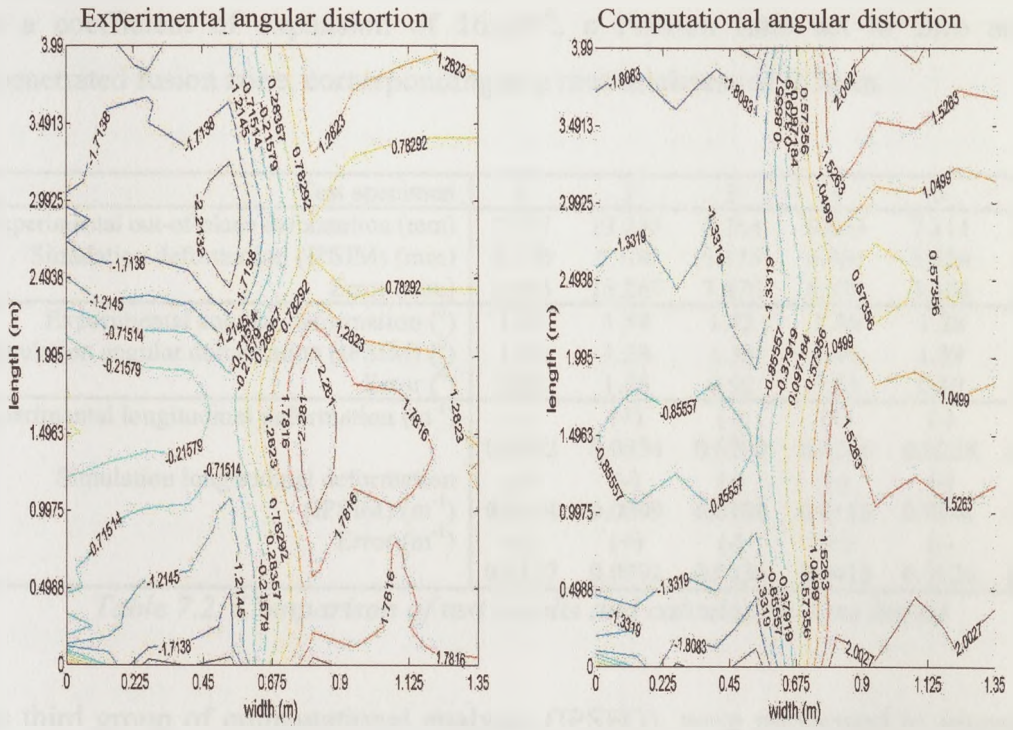

Figure 7.15: Experimental and calculated angular deformations specimens 5

Effects on the out-of-plane deformation, when using different co-efficients of expansion ($14x10^{-6}$ or $16x10^{-6}$) and Poisson ratios (0 or 0.3), were also tested out. The Poisson ratio had the least significant effect on the final deformation, but was more significant with respect to the residual stress across and in the vicinity of the fusion zone. In essence, the closest matching results, when compared with the experimental results, were attained when the Poisson ratio was set to zero. An

increase in coefficient of expansion gave an expected increase in the final out-of-plane deformation and a stronger correlation with the experimental results. Even with an expansivity of $16x10^{-6}$, the computational results still underestimated the deformation of the test welds.

Overall comparison of calculated and test results is difficult to characterise in the light of these variations, but Table 7.2 provides a measure of comparison in terms of root mean square values. The values in the 'error' rows represent the root mean squares of the differences between experimental and calculated values at discrete points on the measurement and the remaining data represent the root mean square values of all deformations. Note that the simulation results presented in Table 7.2 use a coefficient of expansion of $16x10^{-6}$, a Poisson ratio set to zero and an unpenetrated fusion zone, corresponding to a root thickness of 0.5mm.

Test specimen	1	2	3	4	5	6
Experimental out-of-plane deformation (mm)	7.157	13.235	8.264	8.653	7.111	8.829
Simulation deformation (IPSIM) (mm)	5.176	5.108	5.135	6.001	5.554	6.554
Error (mm)	5.843	13.267	7.875	8.574	3.906	3.235
Experimental angular deformation (^{0})	1.23	1.59	1.42	1.36	1.38	1.45
Simulation angular deformation (IPSIM) (^{0})	1.30	1.28	1.33	1.46	1.39	1.18
Error (^{0})	0.82	1.56	0.92	1.83	0.49	0.57
Experimental longitudinal deformation (m^{-1})	(-) 0.0242	(+) 0.0334	(-) 0.0290	(+) 0.0366	(-) 0.0238	(+) 0.0169
Simulation longitudinal deformation (IPSIM) (m^{-1})	(-) 0.0104	(-) 0.0099	(-) 0.0106	(-) 0.0116	(-) 0.0101	(+) 0.0093
Error (m^{-1})	(-) 0.0157	(+) 0.0392	(-) 0.0236	(+) 0.0415	(-) 0.0126	(+) 0.0110

Table 7.2: Comparison of test results and calculation (rms basis)

The third group of computational analyses (IPSEQ), were performed to investigate the development of the longitudinal deformation with respect to the angular. The separation of the two thermal strains resulted in an insignificant change in the final out-of-plane deformation and thus the simplified algorithms may be simulated together or independently. It is worth noting that the sequential method can be used to identify other aspects relating to the transverse contraction thermal strain via an independent two dimensional analysis, however due to the increase in complexity and computer efficiency in the total analysis, it is recommended to perform the computational analyses using the simultaneous algorithm.

7.3 Out-of-plane distortion in large thin plates due to double-sided fillet welded attachment

Fillet welding is the most common and convenient method used to attach plain, bulb or angle stiffeners to plates in structural fabrication. The choice between single and double sided fillet welding attachment presents a conflict in respect of achieving important structural and fabrication targets, such as to produce light, efficiently stiffened structures and a production aim to achieve a minimally distorted structure. The strategies which should be used to reduce out-of-plane distortion are well-known, in particular minimisation of thermal input energy per length of weld and per stiffened plate is essential, but these techniques are often to the detriment of achieving maximum bending stiffness of the welded structure and production time. Single fillet welds will reduce the heat input, but double fillets are usually preferred from the point of view of fatigue and corrosion resistance. This section sets out to investigate alternative fabrication sequences for the reduction of the out-of-plane deformation via simultaneous or staggered double-sided fillet welding, while minimizing production time. That is, the investigation of double-sided fillet welding using two welding heads placed oppositely (simultaneous welding) and offset at specific distances (staggered welding).

In the first instance the simplified algorithms are cross-referenced with typical industrial size welded attachments. Three separate plate/ stiffener assemblies, consisting of the attachment of a single stiffener to a large plate, through fillet welds applied at each side of the stiffener, were welded. The CMn steel stiffeners of dimensions 100 x 6 mm were attached to 4m x 1.5m x 5mm thick base plates of the same material. In the experimental work, the two welds were applied consecutively and the fabrication was permitted to cool back completely to ambient temperature after the first weld. Various theoretical finite element strategies were investigated, in the context of optimizing the longitudinal and transverse thermal simplified models in large plate, double-sided fillet welded structures. Again, out-of-plane transient deformations during the welding and cooling stages, were measured using LVDT placed at a fixed array as shown in Figure 7.16. Furthermore, the out-of-plane

deformation over the whole stiffened plate assembly was measured during each stage of stiffener fillet weld completion, before and after welding and cooling. This comprised 394 longitudinal x 22 transverse points, which were then smoothed out to form the plate profile made up of 16 x 6, nine-noded 0.249m x 0.2m Langragian plane elements. Note that the displacements in the stiffener were not recorded and only the out-of-plane deformations of the base plate are presented and examined.

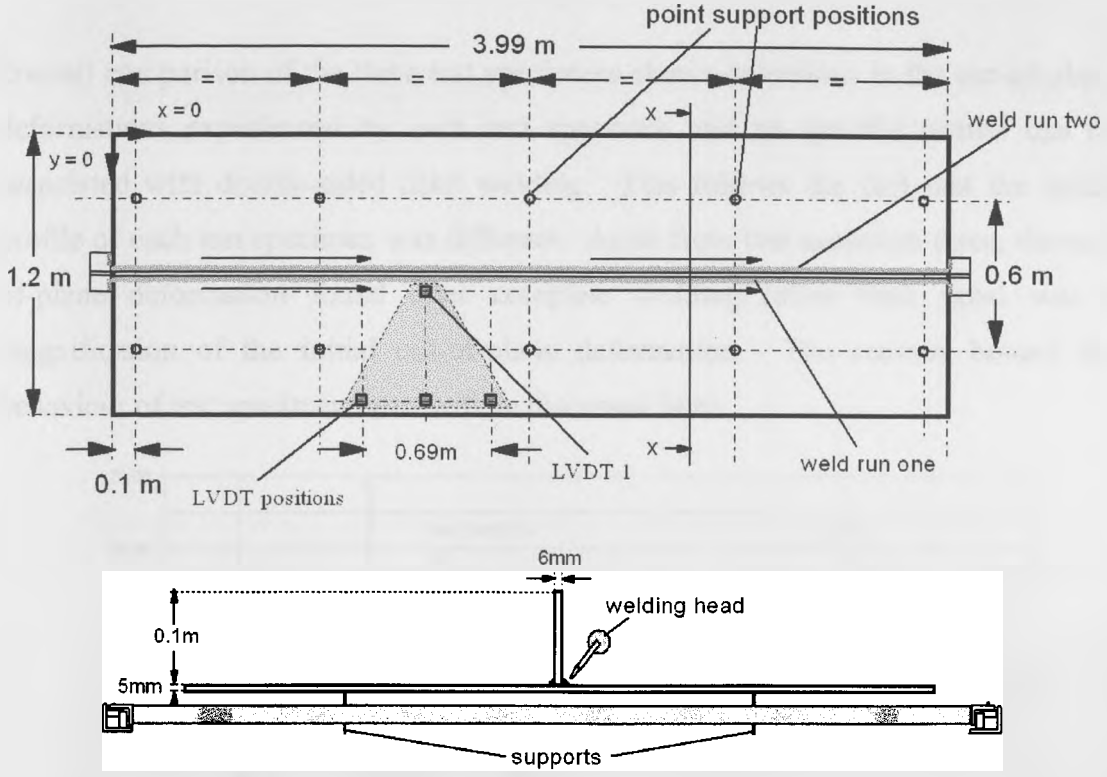

Figure 7.16: Layout and set-up in fillet welded attachments

The plates were firstly shot-blasted, primed and laser-cut to size by the industrial partner in the project. The stiffener was then tack welded to the base plate at 307mm intervals, starting from the centre of the plate and then working symmetrically outwards towards the edges. Note that clamping was required to align the plate to the stiffener, in particular toward the ends of the plate. The presence of the tack welds creates a stiff attachment between the stiffener and the plate, and hence it was assumed in the simulation that the assembly behaved as an integral structure throughout the sequence of welding.

The welds were applied consecutively (after complete cooling to ambient temperature) on both sides of the stiffener to give 45° fillet welds of 8mm nominal leg length, although these conditions were not always achieved precisely particularly in test specimen three. Welding conditions were 221A, 25.9V and 5mm/s travel speed, giving a nominal gross heat input of 1.14kJ/mm.

7.3.1 Test observations and results – double-sided fillet welds

Overall comparison of the three test specimens shows deviations in the out-of-plane deformations experienced by each test specimen and no specific profile can be associated with double-sided fillet welding. This follows the fact that the initial profile of each test specimen was different. Aside from test specimen three, the out-of-plane deformation found after complete welding (after both runs) was a magnification of the initial out-of-plane deformation. The reasons behind the behaviour of test specimen three will be discussed later.

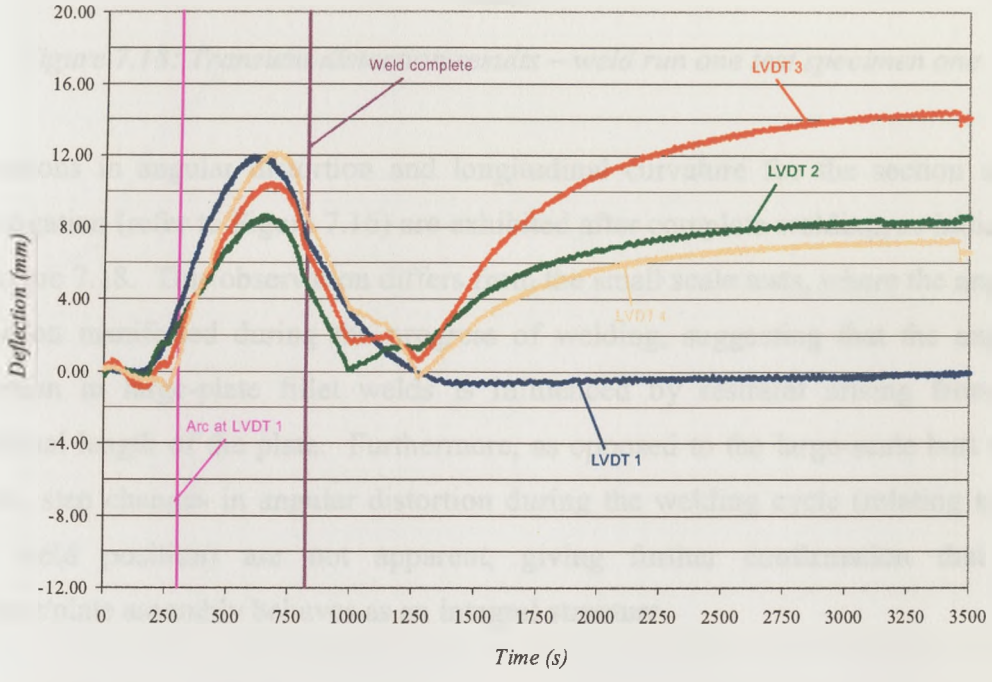

Figure 7.17: LVDT transient displacement – weld run one test specimen one

The initial expansion during first weld run, hogged the plates to an extent that the weight of the plate was distributed on the outer supports only along the lengths, as

indicated by the offsetting displacements of the four LVDT between the 200 – 1000 seconds marks, as shown in the transient LVDT displacement results for test specimen one (Figure 7.17).

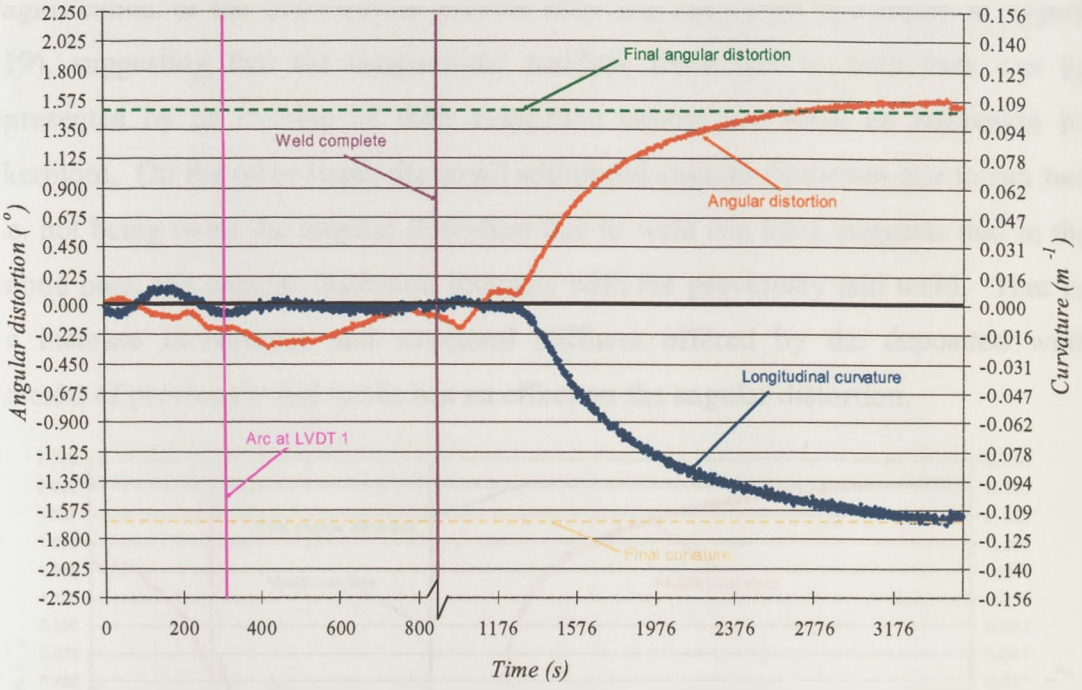

Figure 7.18: Transient distortion results – weld run one test specimen one

Deviations in angular distortion and longitudinal curvature for the section under investigation (refer to Figure 7.16) are exhibited after complete welding, as indicated by Figure 7.18. This observation differs from the small scale tests, where the angular distortion manifested during the progress of welding, suggesting that the angular distortion in large-plate fillet welds is influenced by restraint arising from the additional length of the plate. Furthermore, as opposed to the large-scale butt weld results, step changes in angular distortion during the welding cycle (relating to the tack weld position) are not apparent, giving further confirmation that the stiffener/plate assembly behaves as an integral structure.

The transient deformations evolved in the second weld run are of particular interest. In this case, the initial expansions of the plate due to welding re-flattens the plate such that the perturbations exhibited in the first weld run are cancelled and the plate regains approximately its initial shape. This suggests that the initial residual stresses

due to weld run one are approximately nullified during the heating process. Once more, the angular and longitudinal deformations occur after complete welding, during the cooling stages. The final out-of-plane deformation converges to a small magnification in the deformation present after the first weld run (refer to Figure 7.19), suggesting that the longitudinal residual stress due to both runs can be represented by an overlap of their respective contraction force as indication by Okerblom. On the other hand, the small additional angular distortion due to run two (i.e. not being twice the angular distortion due to weld run one), suggests that in the second pass, the angular distortion interacts with the previously laid weld. That is, the increase in restraint and structural stiffness offered by the deposited weld material of previously laid welds has an effect on the angular distortion.

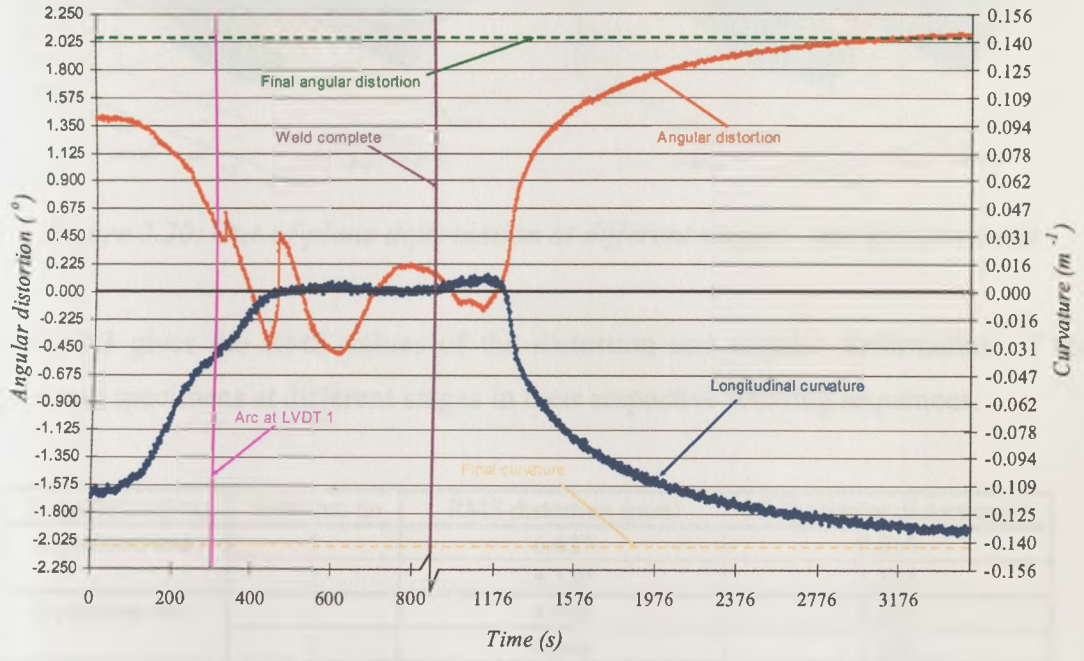

Figure 7.19: Transient distortion results – weld run two test specimen one

The above observations are also confirmed in the static distortion measurements. Figure 7.20 shows the out-of-plane deformation at the different stages in the welding procedure for test specimen one. The induced contraction forces due to the second weld pass, result in a slight increase in longitudinal out-of-plane deformation, coupled with a more significant increase in angular distortion. This effect is indicated in Figure 7.20c and was obtained by subtracting the total deformation (Figure 7.20d) from the distortion due to the first weld pass (Figure 7.20b).

a) Initial out-of-plane deformation

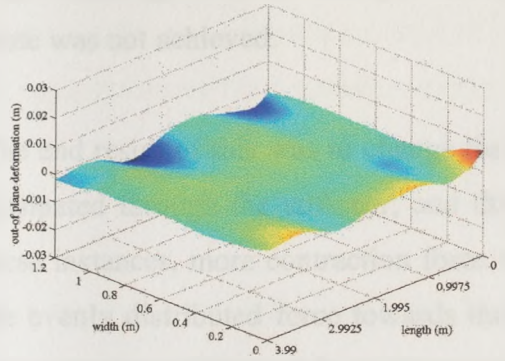

c) Out-of-plane deformation due to second weld pass

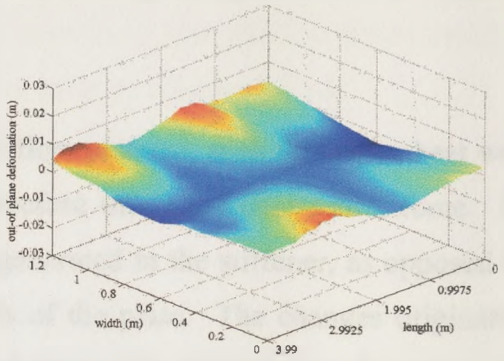

b) Out-of-plane deformation due to first weld pass

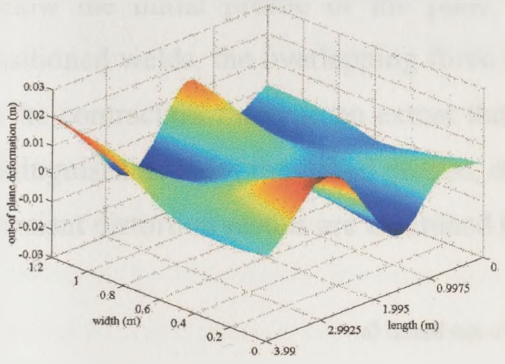

d) Total out-of-plane deformation

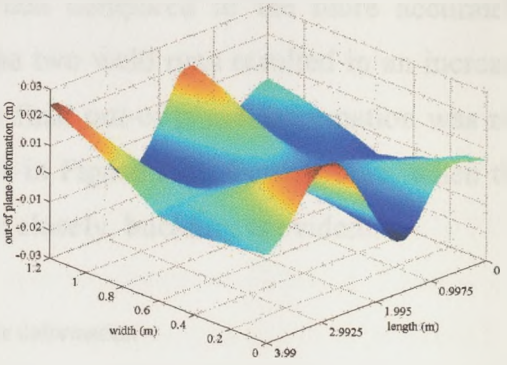

Figure 7.20: Out-of-plane deformation at different stages – test specimen one

Table 7.3 gives the RMS values of the distortion and angular deformation of the three test specimens at different stages in their respective welding sequences.

Test specimen no	Weld run no	RMS distortion (mm)	RMS angular distortion (°)
Specimen one	1	6.627	0.916
	2	8.120	1.314
Specimen two	1	4.998	0.897
	2	6.566	1.303
Specimen three	1	9.568	1.439
	2	14.606	2.153

Table 7.3: Out-of-plane deformation of double-sided fillet welds (rms basis)

Position control of the welding head relative to the stiffener/plate assembly was not proficiently achieved, particularly in cases where large plate displacements were present during the final welding stages, hence resulting in fluctuation of welding head angle. Test specimen three was drastically affected, such that a consistently sound weld was not achieved for the first weld pass. At mid-section of the plate,

required changes in the welding head angle were too high and penetration in the base plate was not achieved.

The end result of this was to change the heat flow patterns, such that more heat was dissipated through the stiffener, and this therefore offset the contraction force. In these instances, more contraction force was generated in the stiffener, as opposed to the evenly distributed force towards the ends of the plate. The changes originated other spurious effects such as moments, and hence the deformation did not quite follow the initial profile of the plate. When compared to the more accurately positioned welds, the overlapping force of the two weld runs resulted in an increase in the contraction force, to an extent that the final out-of plane deformation was not distinguishable from the initial profile, shown in Figure 7.21. Furthermore, when the transient distortion results are examined more closely, buckling is evident.

a) Initial out-of-plane deformation

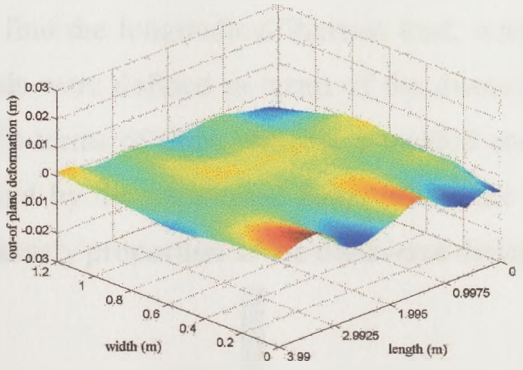

b) Out-of-plane deformation due to first weld run

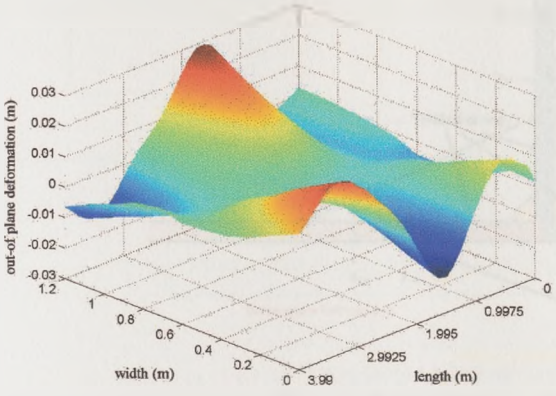

c) Total out-of-plane deformation

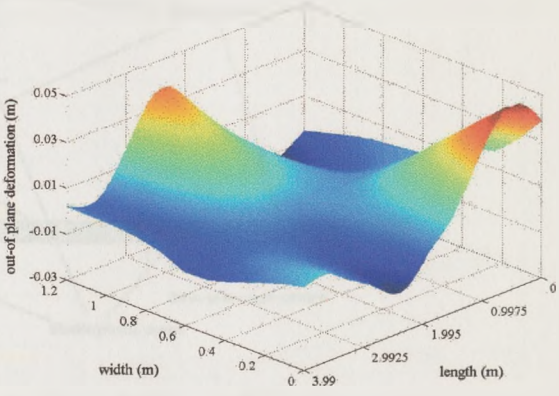

Figure 7.21: Out-of-plane deformation at different stages – test specimen three

Due to lack of information, relating to the thermal transients developed in test specimen three and the unpentrated weld, test specimens one and two only were used to cross-reference the simulation results described in the section below.

7.3.2 Simplified computational models for double-sided fillet welding

The thermal transients caused by double-sided fillet welding have already been discussed in detail in chapter five. In the case of double-sided fillet welds it was observed that the thermal condition patterns of the joint assembly in the second fillet weld will differ from the first fillet, with respect to thermal heat transfer.

The second step is to establish the thermal loads applied to the structural analysis for the evaluation of the out-of-plane deformation. Various strategies have been delineated in this thesis to give longitudinal Mismatched Thermal Strains and transverse Contraction Thermal Strain. The same approach as in the large-scale butt welds was adopted to find the longitudinal thermal load, with certain modifications. Again the thermal loads were defined in terms of the distance and thus the thermal load was represented in terms of three regions; a yielded zone, an elastic zone and finally a region bounded by the mentioned zones where the maximum temperature was assumed to be inversely proportion to the transverse distance.

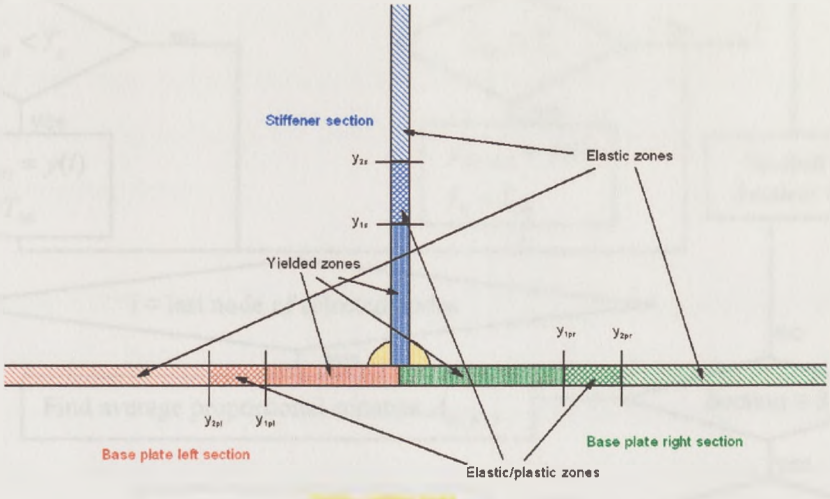

Figure 7.22: Thermal loads in fillet welding

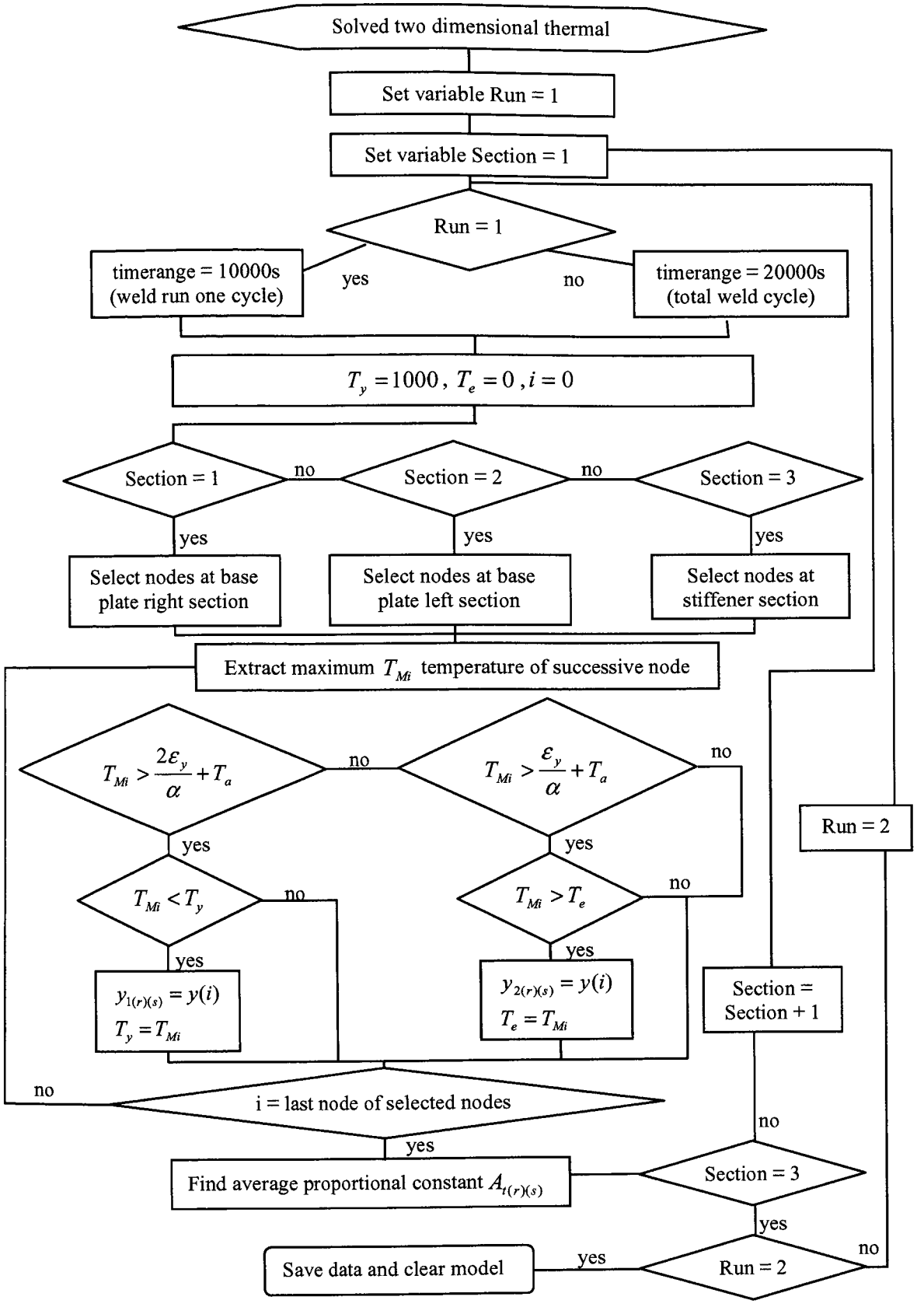

Figure 7.23: Algorithm to find the mismatched thermal strain in fillet welding

Note that in the case of fillet welding the stiffener will also exhibit these thermal loads. Furthermore, unlike the butt welds where symmetry prevails, different sections of the stiffener/plate assembly will follow different thermal histories and hence the extraction of the three bounded regions will have to been done independently by considering three different sections as described in Figure 7.23 and illustrated in Figure 7.22.

The quantification of the longitudinal thermal strain is quite straight forward, for the first fillet weld. However in the case where the two fillet welds residing in close proximity are applied sequentially, there are additional factors, which introduce non-additive or non-linear behaviour:

1. The first run will develop out-of-plane distortion, which will influence deformation behaviour during the following fillet weld;
2. The plate assembly will contain significant longitudinal residual stress field generated by the first weld.

The first of these factors is addressed automatically by sequencing the individual weld simulation in the same order as the actual fabrication sequence, but the residual stress factor requires more detailed discussion. In double-sided fillet welding, the two welds are slightly displaced such that the individual thermal strain fields will overlap. In sequentially deposited welds (with intermediate ambient cooling) the second weld will only contribute a slight increase in the thermal strain relating to the extra contraction force found by overlapping the individual contraction forces as described in chapter three.

The transverse Contraction Thermal Strain algorithm in sequentially applied fillet welds has already been addressed in the pilot-programme. In this instance the transverse strain was established in relation to the deposited weld material and area of penetration in the base plate and stiffener assembly, following equation 7.1

$$T_T = T_a - 1000\left(1 + \frac{A_{wp}}{A_{wd}}(1-k_p) + \frac{A_{ws}}{A_{wd}}(1-k_s)\right) \qquad \textit{Equation 7.1}$$

There are several implications in this approach. Firstly, the transverse thermal strains in the cross-section outside the fusion zone are assumed to be elastic and it is assumed that there is no restraint on the angular deformation of the base plate, other than that provided by the unwelded area below the fusion zone. The two-dimensional treatment also relies on the finding that the thermal gradient is small along the length of the weld and steep in the transverse direction. When applied to the pilot-programme these assumptions were consistent with the experimental results, for both weld runs. However in large plate analysis, the welding time plays a significant role in angular distortion, that is while sections have already undergone a heating stage and following a cooling phase other sections are still at ambient temperature. This gave rise to an extra restraint, particularly when applying the second weld. Here further structural rigidity is attained due to the previously laid weld. Thus, for the second weld run, the transverse thermal contraction was considered to be a triangular fused butt weld, having a depth of penetration equal to the perpendicular bisector of the weld length, restrained by a thickness as shown in Figure 7.24. In the computational model, the area prescribed by A_{wd} was modelled. Hence the final transverse thermal strain in the second weld is given by equation 7.2, k_f being dependant on the penetration s_f and thickness d_f and the theory presented in chapter three. The alternative models for angular deformation process were explored in the computational analysis presented in the following section.

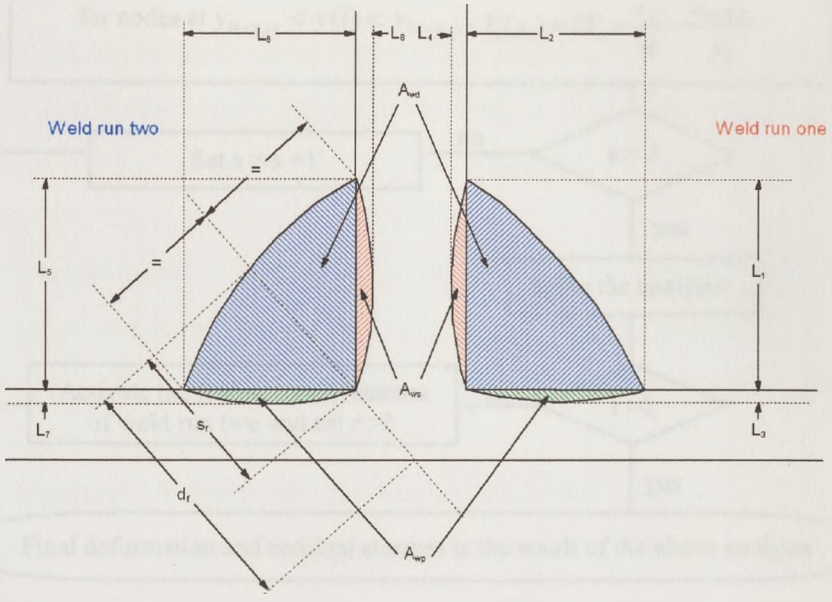

Figure 7.24: Cross-section of double-sided fillet weld

$$T_T = T_a - 1000\left(1 + \frac{A_{wp}}{A_{wd}} + \frac{A_{ws}}{A_{wd}}\right)(1 - k_f) \qquad \textit{Equation 7.2}$$

A number of possible computational methods are possible to apply the mentioned thermal loads. Orthotropic coefficients of expansion were used to enable the artificial temperature loads at a given weld pass to generate the required simulated thermo-mechanical strains in a simultaneous fashion. Other computational features incorporated in the computational models include gravitational, support position and non linear geometry effects applied via the use of ANSYS LINK 10 elements, and ACEL together with NLGEOM, ON, ANSYS commands.

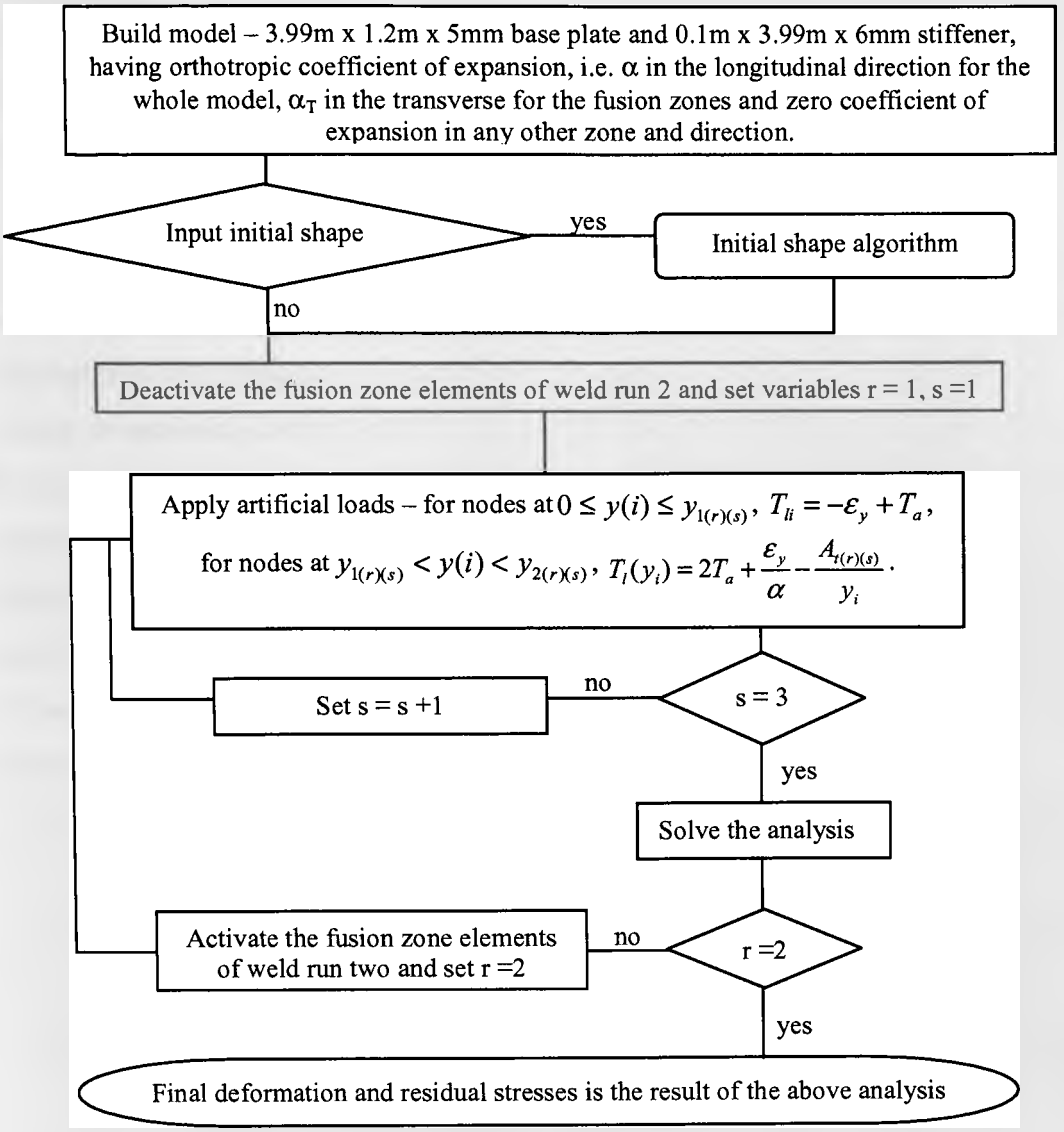

Figure 7.25: Structural finite element algorithm for double-sided fillet welding

The final out-of-plane deformation at different stages of the welding procedure can be simulated in different ways. In the first instance, the two fillet welding operations were simulated in sequence, with the out-of-plane displacements from the first run and the initial perturbations being used as the starting point for the second. Note that in such cases the mismatched thermal strain for the second weld will only include the extra contraction thermal strain due to the displaced welds, achieved by overlapping the individual contraction forces. Starting from the initial deformation of the respective test plate, a more computationally efficient approach is to apply the resulting contraction force due to the first weld run and that of both weld runs in a two load step analysis (refer to Figure 7.25). In both the above strategies element 'birth and death' was used to deactivate the contraction forces resulting from the deposited weld material of the second run, during the computational analysis of the first weld pass. Little difference between the above mentioned strategies was apparent.

Substantial economy in computational time may be achieved by applying the total contraction force in a single load step, provided that the correct maximum temperatures and locations are used for the whole welding cycle (weld run one – cooling to ambient – weld run two – cooling to ambient). However, the disadvantage of this procedure is that the out-of-plane deformation at different stages of the welding cycle could not be quantified and hence was not used in the initial cross-reference of the simulation and experimental results, but was employed in the analyses of simultaneous and staggered welding i.e. the deposition of two welds at the same time or out of phase at specific distances. In addition, the following assumptions were taken, for the latter analyses:

1. The heat input of the two welds assumed the same thermal efficiency of their respective welds in the intermediate ambient cooling analyses;
2. The simulations assumed the initial out-of-plane deformation of test specimen one and two respectively;
3. The transverse thermal contraction, in staggered welding, of the leading and lagging weld followed equation 7.1 and equation 7.2 respectively. In

simultaneous welding, both welds assumed restraining condition and thus utilizing equation 7.2;

4. The fusion zone elements of both welds are presented throughout the whole welding cycle (i.e. the simulations do not make use of element birth and death).

The above assumptions are questionable and should be verified experimentally, nonetheless the computational analyses offer a benchmark between the various sequences used for double-sided fillet welding.

7.3.3 Computational results and comparisons

The deformations, due to sequential application of fillet welds on an ideal, 'as-delivered', perfectly flat plate were first computed, to act as a baseline result. Of course the initial shape of the ideal plate as presented to the welding operation would not be flat, as gravity loading relative to the support positions generates small deflections. The simulated deformations after the first and second fillet welds are shown in Figure 7.26 and the root mean square average values, together with their respective error when compared to the experimental results are shown in Table 7.4. Note that the transverse contraction due to the second weld run was assumed to be unrestrained by the deposited weld material due to the first run and thus in both welds the transverse contractions followed equation 7.1.

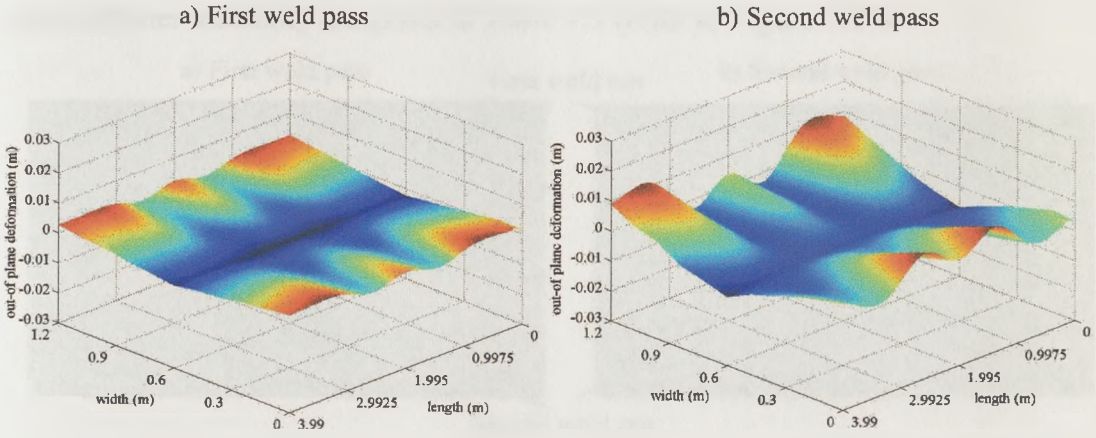

Figure 7.26: Out-of-plane deformation for an initially flat plate

Weld run no.	RMS distortion (mm)	RMS distortion error – test specimen one (mm)	RMS distortion error – test specimen two (mm)	RMS angular distortion (°)	RMS angular distortion error – test specimen one (°)	RMS angular distortion error – test specimen two (°)
1	1.546	6.504	4.827	0.453	0.838	0.761
2	4.584	8.011	6.548	1.210	1.114	1.021

Table 7.4: Out-of-plane deformation of an initially flat plate (rms basis)

Two main effects are evident from these results. The out-of-plane deflection pattern in the longitudinal case is essentially a magnification of the initial gravity-induced pattern and the average angular and absolute out-of-plane distortions generated by the second run were almost twice those for the first run. Of course, as found in the earlier work on butt-welded plates, greater angular distortion will generate greater longitudinal out-of-plane deformation for the same force. Hence, this result does not necessarily contradict the earlier predictions in section 7.3.2 that the final contraction force generated after the second run will only be a little greater than that after the first run. On the other hand the unrestrained transverse contraction of the second pass fusion zone has generated a larger angular deformation (more than twice). This does not reflect the experimental results, suggesting that in the second weld pass the angular deformation is restrained.

Further simulations were carried out, using as starting points the initial measured plate/stiffener shapes. Macrographs of the two full-sized test pieces that have been analysed and simulated are shown in Figure 7.27 and the associated weld dimensions averaged over three macrographs taken from three different section of the welded plate/stiffener assembly are given in Table 7.5 (refer to Figure 7.24).

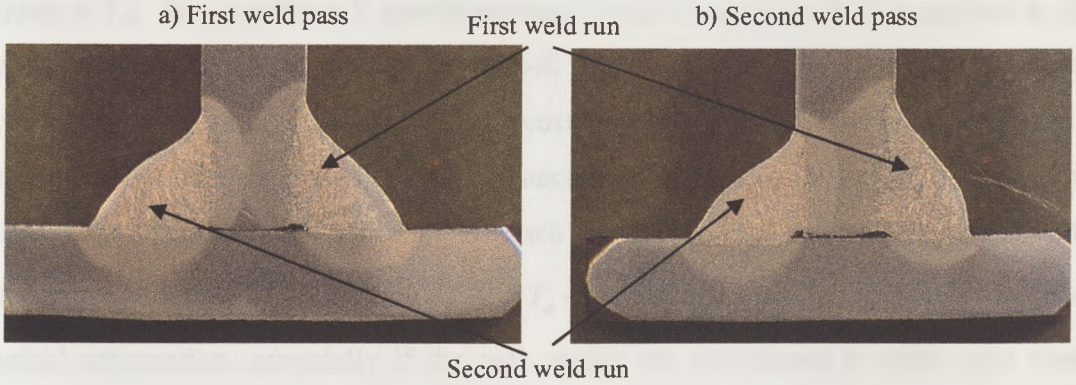

Figure 7.27: Macrographs of test specimens one and two

Test specimen no	One		Two	
Weld run no	1	2	1	2
L_1 / L_5 (mm)	7.600	7.165	8.696	7.102
L_2 / L_6 (mm)	5.732	6.748	4.815	6.120
L_3 / L_7 (mm)	0.339	0.515	0.354	0.483
L_4 / L_8 (mm)	1.014	0.918	0.998	0.966
A_{wd} (mm^2)	25.272	27.568	26.138	25.077
A_{wp} (mm^2)	1.297	2.318	1.137	1.971
A_{ws} (mm^2)	5.160	4.384	5.787	4.576
$T_T - T_a$ condition 1 (°C)	-1049.1	-1043.1	-1050.7	-1047.6
$T_T - T_a$ condition 2 (°C)	-644.0	-732.1	-507.6	-687.5
$T_T - T_a$ condition 3 (°C)	-1049.1	-732.1	-1050.7	-687.5
$T_T - T_a$ condition 4 (°C)	-119.6	-119.6	-119.6	-119.6

Table 7.5: Fusion zone dimension and transverse thermal load

In the case of the test specimen two, the welding process conditions applied in the first run favoured the stiffener and this feature was reflected in the thermal analysis simulation and in the weld shape assumed for the structural simulation. Alternative models for the angular deformation process were explored via the quantification of the magnitude of k in the transverse thermal contraction, thus reflecting different restraint conditions. The greatest deformation results from an assumption that the angular change is due entirely to contraction of the fillet weld fusion zone from the arbitrary 1000°C starting temperature and the contraction arising from the penetrated weld material in the plate and stiffener (refer to equation 7.1). This was applied to both welds and is referred to as 'condition 1'. A modification of this would be to consider that this contraction is resisted by bending of the base plate - for both welds ('condition 2'), such that the fusion zone will be partially restrained and following equation 7.2. In 'condition 3' partial restraint (refer to equation 7.2) is applied to the second weld only, while the first weld will contribute the maximum thermal strain (equation 7.1), based on the grounds that completion of the first weld has generated a strong stiffener/base plate structural connection. Maximum restraint is applied to the angular distortion in 'condition 4' such that both welds will exert a transverse thermal contraction of yield nature ($T_T = T_a - \varepsilon_y / \alpha$). Condition 3 is probably the most logical assumption, especially if the tack welds are considered to offer only weak resistance to bending, where as 'condition 4' reflects the case where an in-plane

restraint is applied to the structure. As can be seen from Table 7.6, 'condition 3' results in the least errors. Though the differences are not great between conditions 1 to 3, the higher deviations resulting from condition 4 suggest that the transverse thermal strain is not of yield nature but higher.

		Condition no:	RMS distortion (mm)	RMS distortion error (mm)	RMS angular distortion (°)	RMS angular distortion error (°)
Test specimen one	First weld pass	1	3.145	5.216	0.645	0.663
		2	2.906	5.247	0.520	0.659
		3	3.145	5.216	0.645	0.663
		4	2.897	5.201	0.443	0.716
	Second weld pass	1	5.082	5.585	1.283	0.727
		2	4.280	5.651	0.949	0.679
		3	4.642	5.586	1.106	0.677
		4	3.592	6.243	0.562	0.976
Test specimen two	First weld pass	1	3.816	2.784	0.624	0.476
		2	3.717	3.019	0.523	0.563
		3	3.816	2.784	0.624	0.476
		4	3.791	3.247	0.506	0.652
	Second weld pass	1	4.198	3.547	0.826	0.613
		2	4.843	3.438	0.854	0.606
		3	5.060	3.177	1.015	0.511
		4	4.744	4.317	0.642	0.957

Table 7.6: Out-of-plane deformation of initially deformed plates (rms basis)

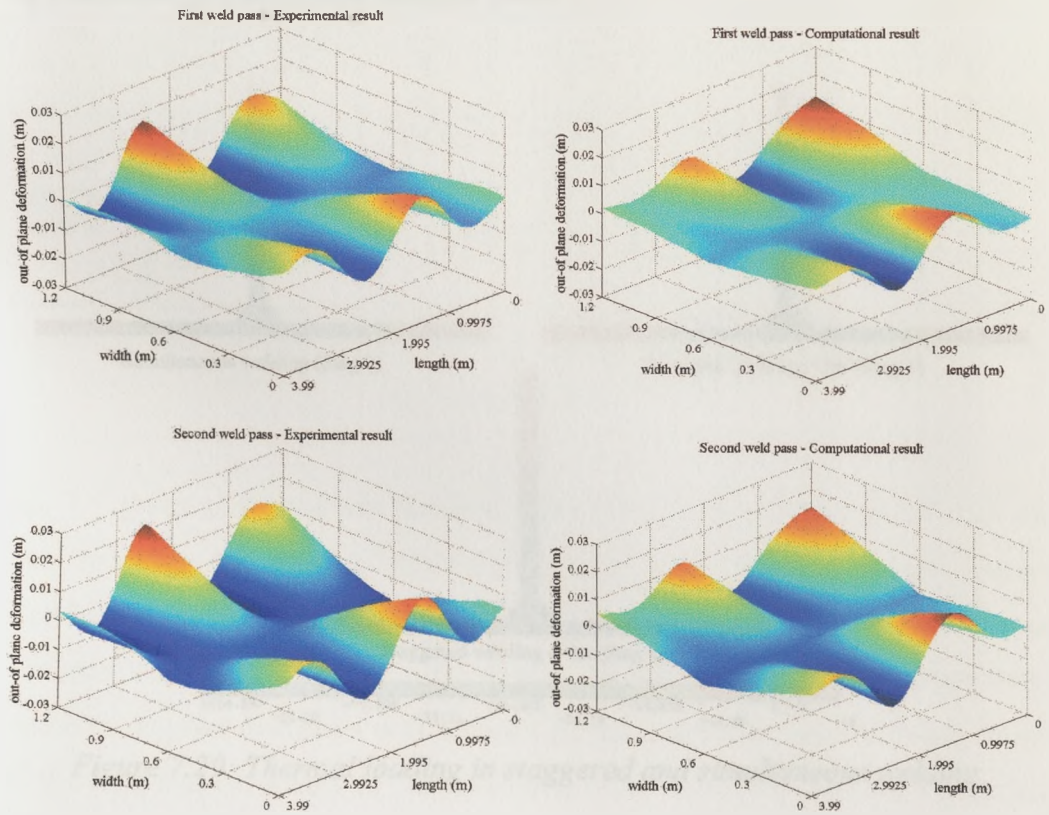

Figure 7.28: Experimental and calculated results –test specimen two

Figure 7.28 shows a direct comparison between the test result for specimen two and the corresponding simulation result when using condition 3. In general, the simulations underestimate the magnitudes of the out-of-plane plate deflections, although the angular deformations are more nearly correct. One implication is the value of 16×10^{-6} assumed for the average expansivity of the steel used in the above simulations is incorrect. An increase in longitudinal contraction force is thus essential for the correlation with the experimental results such that any extra effects such as strain hardening and average expansivity of the weld are included in the simulations. In fact further simulations suggest that an expansivity value of 20×10^{-6} gives a close match to the final experimental deformations, giving an increase in contraction force of 25%.

Simultaneous and staggered welding in double-sided fillet welding was investigated via five computational analyses such that the distance between the welding heads was set to 0m, 0.2m, 0.6m, 1m and 4m (referred to as Stag 0, Stag 0.2, Stag 0.6, Stag 1, and Stag 4, respectively). In essence the thermal transients described in section 5.4.2 were used to evaluate the thermal loads.

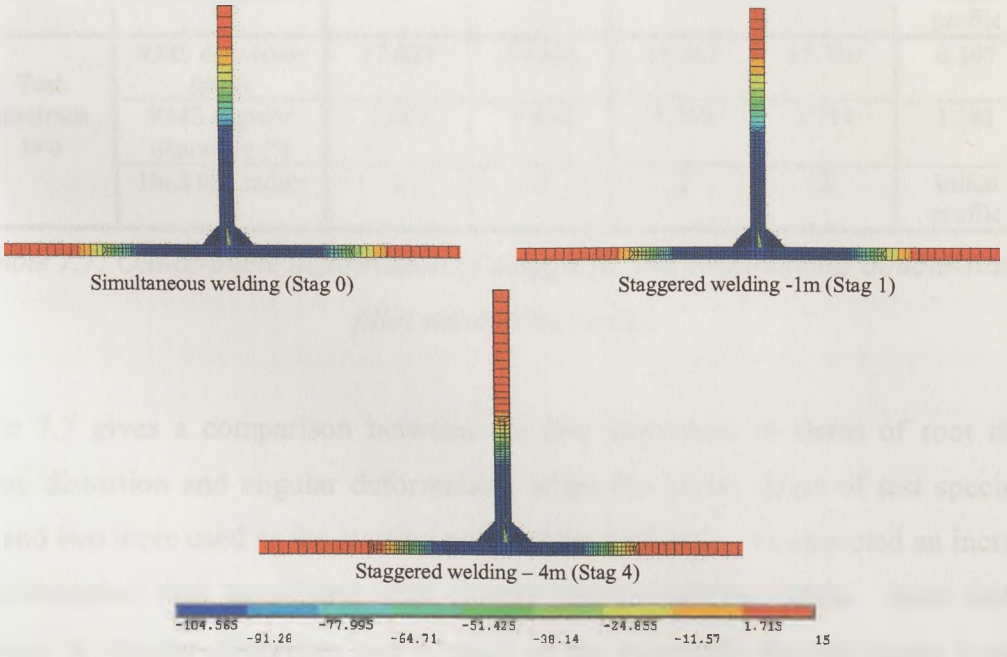

Figure 7.29: Thermal loading in staggered and simultaneous welding

Figure 7.29 shows a comparison between the thermal loads applied to simultaneous and staggered welding. It is apparent that the thermal loading is drastically reduced in the 4m welding case when compared to the other sequences, but is still slightly higher than the intermediate cooling welding pattern. In the first instance the thermal strains were applied in a one load step analysis, however, apart from the 4m welding case, the simulations did not converge. Convergence problems were encountered in the other sequences due to instability of the plate. In particular, the contraction force was high enough to exceed the buckling load of the stiffener/plate assembly. The analyses fluctuated from one mode to another even though the PSTRES, SSTIF and PRED ANSYS commands (commands that account for buckling) were switched on. Convergence was enhanced when the thermal strains were incremented over three load steps and using full Newton-Raphson, Sparse direct, non-linear geometry, prestress effects, and line search method equation solver.

	Computational analysis	Stag 0m	Stag 0.2m	Stag 0.6m	Stag 1m	Stag 4m
Test specimen one	RMS distortion (mm)	18.179	16.958	16.211	16.620	5.633
	RMS angular distortion (°)	1.913	1.781	1.711	1.766	1.295
	Buckling mode	1	2	2	1	Initial profile
Test specimen two	RMS distortion (mm)	17.003	16.936	16.367	15.780	6.107
	RMS angular distortion (°)	1.813	1.816	1.798	1.714	1.161
	Buckling mode	2	2	2	2	Initial profile

Table 7.7: Out-of-plane deformation of staggered and simultaneous double-sided fillet welds (rms basis)

Table 7.7 gives a comparison between the five sequences in terms of root mean square distortion and angular deformation, when the initial shape of test specimen one and two were used as the starting point of the analyses. As expected an increase in deformation was associated with closely spaced welding heads. Note that an increase in angular distortion was a result of the transverse thermal strain coupled with the torsional deformation. Nonetheless, when compared with the intermediate ambient cooling welding cases and considering the reduction in manufacturing time,

Stag 4 models produced an insignificant increase in deformation over the two discrete weld run procedure. Furthermore the final profile of Stag 4 was again a magnification of the initial shape of the plate.

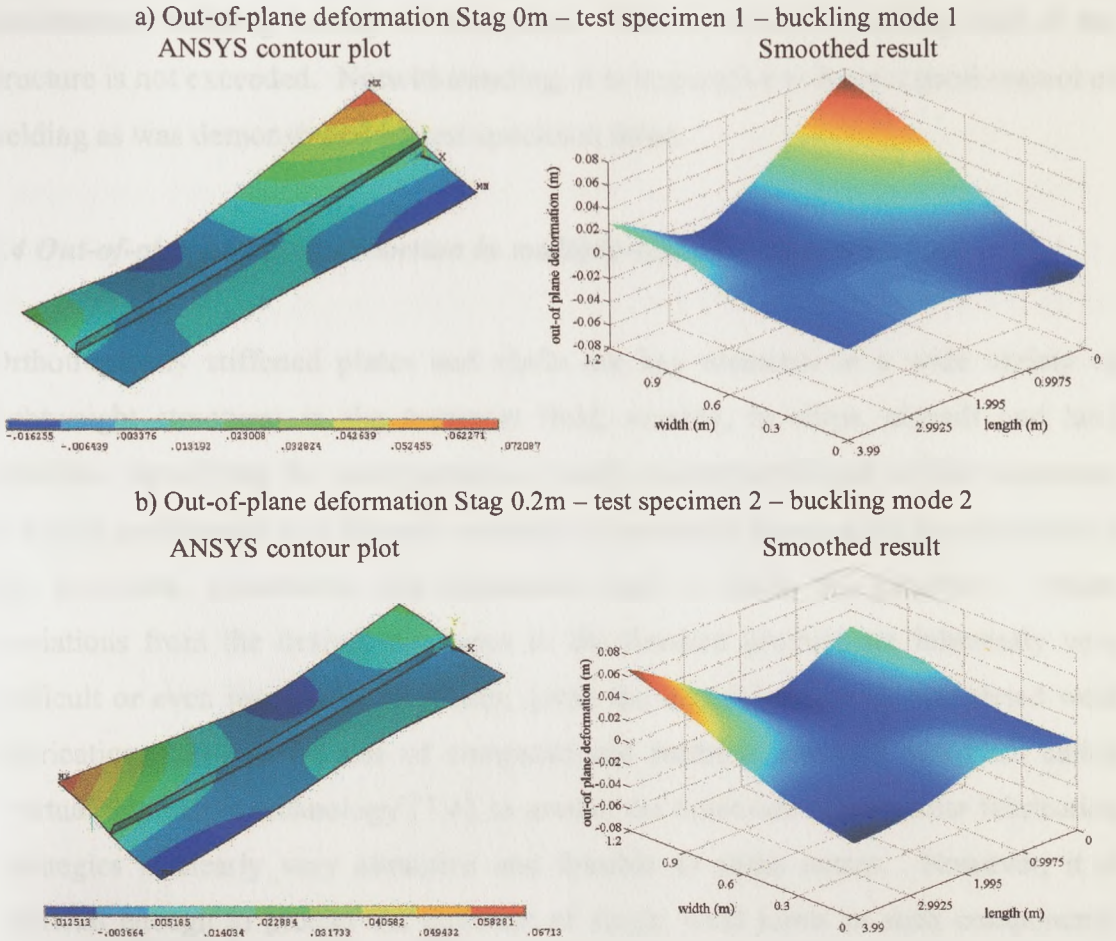

Figure 7.30: Deformation profiles in staggered and simultaneous welding

This was not the case in the other sequences, where the final deformation was not associated to the initial shape. A similar profile was achieved for test specimen one and two in Stag 0.2 and Stag 0.6 welding cases, suggesting that the final deformation is independent of the initial profile when a critical buckling load is exceeded but are subject to the buckling mode assumed by the analyses. In fact two modes of deformation prevailed, and are shown in Figure 7.30. The final profiles are somewhat similar to the out-of-plane deformation exhibited in test specimen three, suggesting that in this experiment the contraction forces were displaced such that the end effect resulted in a force exceeding the critical buckling load. The highest root

mean square values were attained when the plates deformed to the final profile shown in Figure 7.30a, as in the case of Stag 0m and Stag 1m in test specimen one. A direct comparison between the different sequences cannot be made unless all plates follow the same buckling mode, however it is apparent that staggered or simultaneous welding is only advantageous when the critical buckling load of the structure is not exceeded. Notwithstanding, it is imperative to have a good control of welding as was demonstrated by test specimen three.

7.4 Out-of-plane welding distortion in multiply-stiffened plate structures

Orthotropically stiffened plates and shells are key elements in a wide variety of lightweight structures in the transport field, notably, in ships, aircraft and land vehicles. Specifying the configuration of such multiply-stiffened welded structures is highly problematic and depends currently on practical, incremental development of the processes, procedures and sequences used to build the structure. Shape deviations from the desired outcomes in the finished product are inherently very difficult or even impossible to rectify, given the integral nature of completed weld fabrications. Hence the use of computational methods or, what has been called 'virtual fabrication technology'[7.4], to predict the outcomes of particular fabrication strategies is clearly very attractive and feasible to some extent. However, it is difficult enough to predict the outcome of single weld joints in such components, given the wide variety of possible inputs, in terms of process variables, deviations from initial flatness, boundary constraints and many other parameters. The problem is substantially compounded when one considers the further variables introduced by sequential, non-linear addition of several stiffeners and welds, together with the residual stress fields and developing deviations from flatness associated with these additional joints.

These considerations have led the author to develop simplified models and algorithms to predict the forces and deformations associated with the application of individual weld runs, so that the overall effects of applying the welds according to particular sequences can be explored. The overall aim is to provide design support

tools that can be used to investigate alternative fabrication routes and methods and therefore to guide design and manufacturing decisions.

The theoretical models and results generated in the project have been supported at all stages by welding tests of a realistic nature to maintain confidence in the validity and applicability of the treatments. This approach has been demonstrated in other sections of this thesis. This section deals with the attachment of multiple stiffeners to a large plate, through single fillet welds applied on one side only of each stiffener. Three CMn steel stiffeners of dimensions 100 x 6 mm were attached at 0.5 m pitch to 4m x 1.5 m x 6 mm thick base plates of the same material. The particular aim of this work was to investigate the extent to which the use of different stiffener attachment sequences and consequent effects on distortion could be simulated using the simplified models.

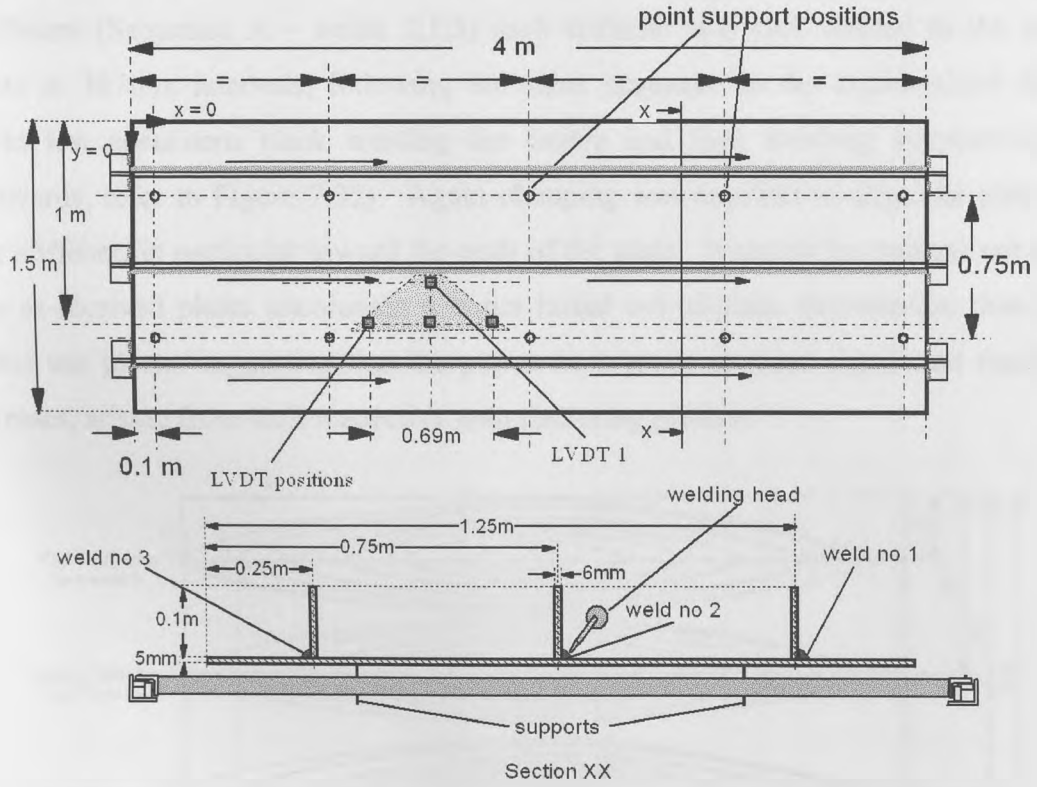

Figure 7.31: Stiffened plate test assembly

The stiffened plate assembly configuration is shown in Figure 7.31. Three separate assemblies where welded, using different weld completion sequences, as follows:

- Sequence A – Centre first then outside welds (welds 2, 1, 3) – test specimen one;
- Sequence B – Sequential welding (welds 1, 2, 3) – test specimen two;
- Sequence C – Outside first then centre weld (welds 1, 3, 2) – test specimen three.

Previous work, presented in section 7.3, has shown that, where two fillets are placed separately on a stiffener with intermediate ambient cooling, the effect is simply to increase the distortion slightly, relative to the single fillet case. Hence, in the present case, single weld fillets were applied to simplify analysis of the results.

The plates were primarily shot-blasted, primed and laser-cut to size by the industrial partner in the project. Starting from the central stiffener and followed by the outside stiffeners (Sequence A – welds 2,1,3) each stiffener was tack welded to the base plate at 307mm intervals, following the same sequence as the double-sided fillet weld test specimens (tack welding the centre and then working symmetrically outwards, refer to Figure 7.32). Again clamping was required to align the plate to the stiffener, in particular toward the ends of the plate. It should be pointed out that the as-received plates encompass a larger initial out-of-plane deformation then the other test plates, suggesting that the plates were prone to more significant residual stresses, arising from their respective manufacturing process.

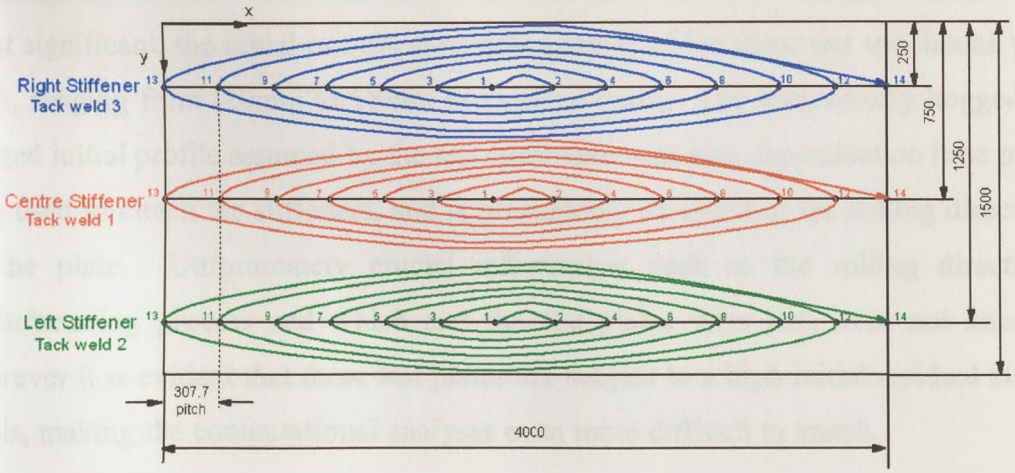

Figure 7.32: Tack-welding procedure in multiply stiffened test plates

The welds were applied consecutively (after complete cooling to ambient temperature) following the three sequences described above to give 45° fillet welds. Welding conditions were 217A, 25.9V and 5mm/s travel speed, giving a nominal gross heat input of 1.124kJ/mm, however these conditions were not always achieved precisely and each test weld constituted different weld lengths and welding conditions. Hence the thermal and structural analyses were specific and differed from each weld test, to reflect the different fusion zones and their respective thermal strains.

The computational analyses were supplement by out-of-plane transient deformations measured during the welding and cooling stages, via LVDT, placed at a fixed array as shown in Figure 7.31. Furthermore, the out-of-plane deformation over the whole stiffened plate assembly was measured during each stage of stiffener fillet weld completion, before and after welding and cooling. This comprised of 394 longitudinal x 18 transverse points, which were then smoothed out to form a the plate profile made up of 16 x 3, nine-noded 0.25m x 0.5m Langragian plane elements. Note that the displacements in the stiffener were not recorded and only the out-of-plane deformations of the base plate are presented and examined.

7.4.1 Test observations and results – multiply stiffened plates

Although the supports were placed in a manner such that gravitational effects were least significant, the initial out-of-plane deformation of the three test specimens was high, ranging from -20mm to 18mm in extreme cases. The transversely hogged or sagged initial profile assumed by the test specimens was also dependant on base plate side used to attach the stiffeners, and is presumably an effect of the rolling direction of the plate. Unfortunately crucial information such as the rolling direction, manufacturing process and which end the test plates were cut, were not known. However it is evident that these test plates are subject to a high initial residual stress fields, making the computational analyses even more difficult to match.

Transient LVDT displacement results have again shown a deformation cycle, i.e. that the plate initially hogged and then rested on most of the supports, followed by a final cooling deformation. The extent by which the plate hogged was dependant on the weld position, such that when welding the central stiffener, the plate detached itself from the central supports and rested on the four outer supports. On the other hand when welding the outer stiffener, the plates detached from the closely placed supports only. This is a consequence of the initial expansion of the heated region close to the weld, coupled by the restraint offered by the other stiffeners, residing at ambient temperature.

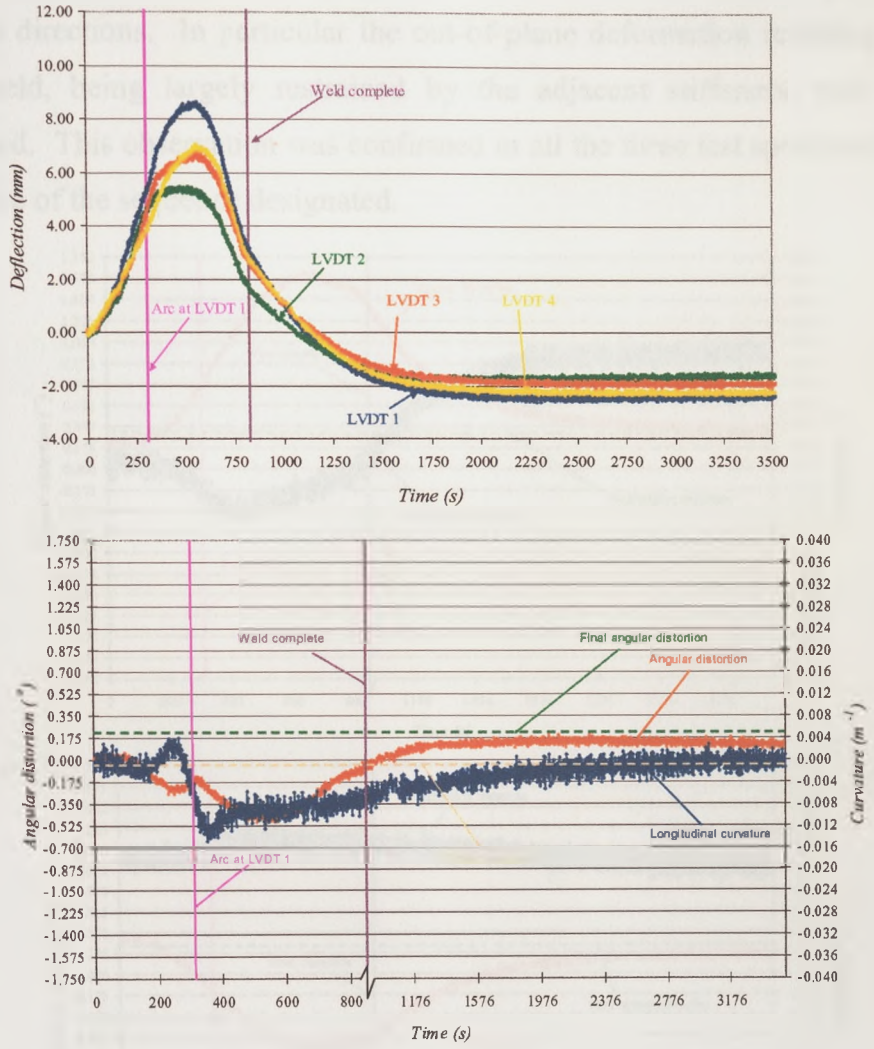

Figure 7.33: Transient deformation –test specimen one – weld no 1

Figure 7.33 and Figure 7.34 show the transient deformation results of test specimen one at different stages of welding sequence A. The results are not quite

representative of the whole stiffener plate assembly, but are specifically designed to investigate the angular distortion and longitudinal curvature arising in the region of the central stiffener (refer to Figure 7.31). Following the first weld (centre weld), the ambient cooled deformation was small and is presumably due to the restraint offered by the adjacent stiffeners. An increase in out-of-plane deformation for the region under investigation was observed during weld run two (weld no 1), but a near constant distortion was attained during the last weld. This suggests that the stiffener positions and their respective second moments of area play an important role in the final deformation, with respect to imposed restraints in both longitudinal and transverse directions. In particular the out-of-plane deformation resulting from the central weld, being largely restrained by the adjacent stiffeners, was the least pronounced. This observation was confirmed in all the three test specimens and was irrespective of the sequence designated.

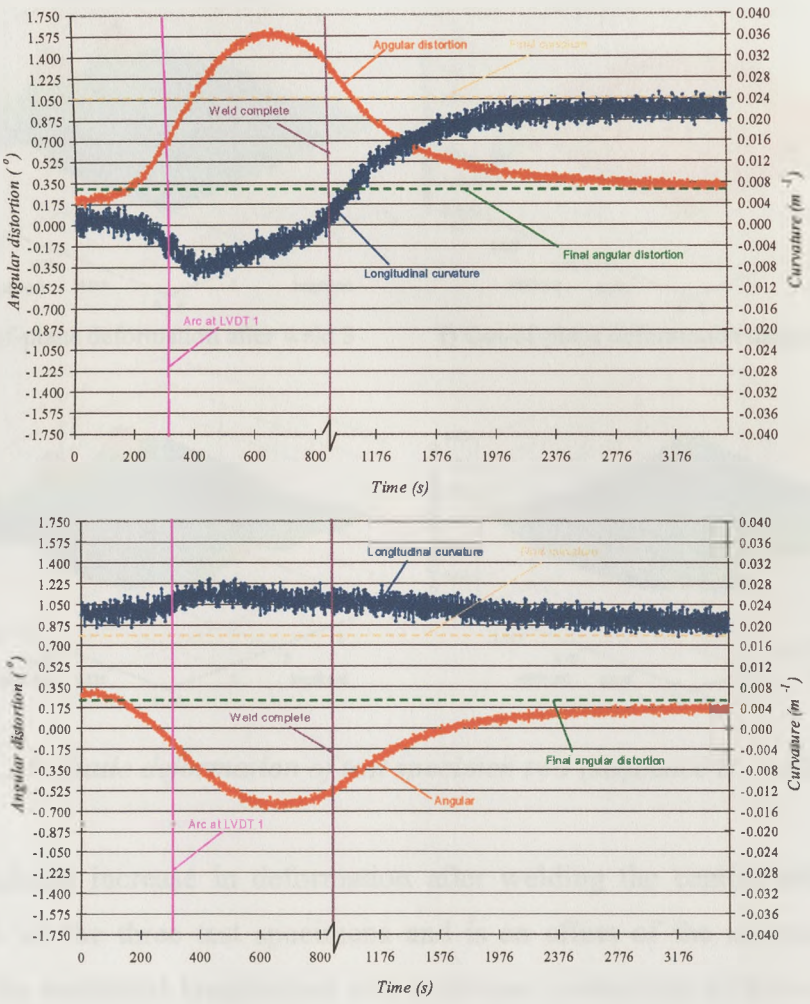

Figure 7.34: Transient deformation –test specimen one a) weld no 2 b) weld no 3

Static distortion results showed a significant increase in out-of-plane deformation after welding the outer stiffeners, while the deformation was not particularly changed when welding the central stiffener. Figure 7.35 shows the out-of-plane deformation of test specimen two, at different stages in the welding sequence.

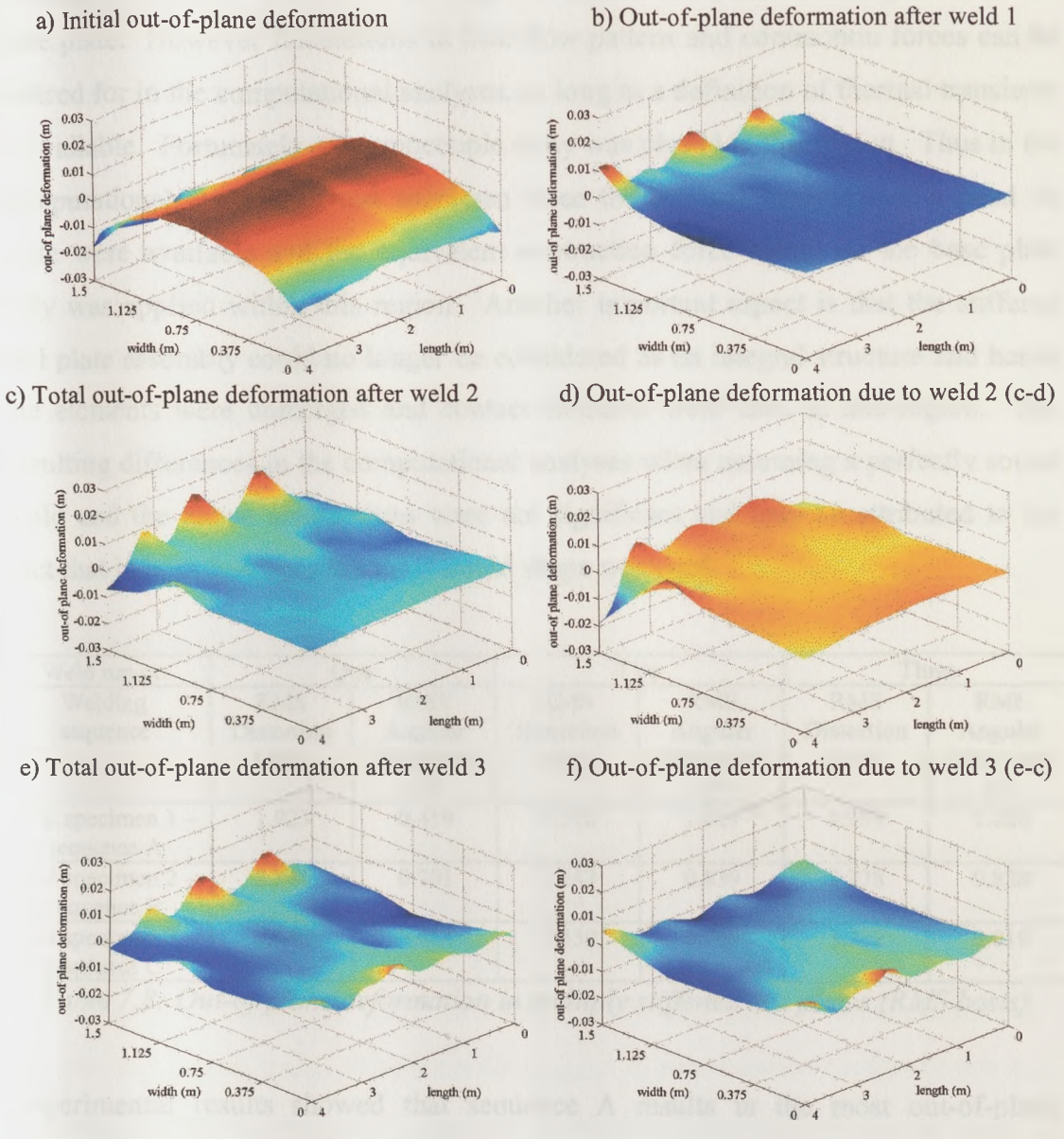

Figure 7.35: Static deformation of test specimen two (sequence B - weld 1, 2, 3)

The insignificant increase in deformation after welding the central stiffeners was observed in all the three test specimens and is an effect of the unrestrained plate edges and the restrained longitudinal and transverse contraction of the central weld. However, the residual stress levels during the welding of the central stiffener in test

specimen three (contraction at the outer stiffeners and tension at the central stiffener) were large enough to detach tack weld 6 (refer to Figure 7.32) from the plate as welding progressed, such that the gap between the stiffener and the plate increased to 10mm. In essence complete sound fillet welding was not achieved at distances ranging from 2.5m – 2.9m from the edge of the plate and a bead was deposited on the base plate. However fluctuations in heat flow pattern and contraction forces can be catered for in the computational analyses, as long as a definition of thermal transients is available. Fortunately a thermocouple array was placed in this region. Thus in the computational analysis of test specimen three the thermal transients of a bead on plate were available and the equivalent contraction force acting on the base plate only was applied within this region. Another important aspect is that the stiffener and plate assembly could no longer be considered as an integral structure and hence the elements were unmerged and contact elements were used at this region. The resulting differences in the computational analyses when assuming a perfectly sound weld and the above assumptions were not significant and may be attributed to the fact that in both instances the same initial shape was used.

Weld run no	One		Two		Three	
Welding sequence	RMS Distortion (mm)	RMS Angular Distortion (°)	RMS Distortion (mm)	RMS Angular Distortion (°)	RMS Distortion (mm)	RMS Angular Distortion (°)
Test specimen 1 – sequence A	1.923	0.419	4.116	1.017	4.139	1.028
Test specimen 2 – sequence B	2.541	0.701	3.143	0.839	3.278	0.820
Test specimen 3 – sequence C	2.540	0.684	2.459	0.769	3.292	0.819

Table 7.8: Out-of-plane deformation in multiply stiffened test plates (RMS basis)

Experimental results showed that sequence A results in the most out-of-plane deformation (refer to Table 7.8). Given the wide variety of possible inputs, in terms of process variables and deviations from initial flatness, this conclusion is debatable. The three test specimens were subject to different initial profiles, not to mention the different initial residual stresses present in the as-received plates. While keeping the variables similar for the different sequences, the finite element analyses presented in the next section are used to elucidate the best welding sequence in terms of welding

distortions. However, the primary aim is to investigate and calibrate the simplified thermo-elasto-plastic algorithms for the case of multiply stiffened plates.

7.4.2 Computational analyses and results

As distinct from double-sided fillet welding on a single stiffener, in multiply stiffened plates, the welds are usually placed sufficiently apart such that the elastic longitudinal contraction force fields do not overlap. In the multiple case, the contraction force of the later welds will be influenced by the stress fields present at the region of welding. The theory has already been demonstrated in chapter 3, and concluded that if the longitudinal residual stress field in the region where the second weld is placed is tensile, this will reduce the contraction force relative to the contraction force developed in a stress free region. On the other hand if the residual stress is compressive, this will increase the contraction force. The new contraction force may be found by using equation 7.3 below, where F_2 is the new longitudinal force and ε_i is the initial strain in the region of the second weld (negative if it is compressive strain).

$$\frac{F_2}{F_1} = \frac{\ln\left(\dfrac{2\varepsilon_y}{\varepsilon_y + \varepsilon_i}\right)}{\ln 2} \qquad \textit{Equation 7.3}$$

Primarily the contraction forces of the respective welds (central and outer stiffeners) when applied to a stress free region are first extracted from the thermal analyses. This was done by dividing each stiffener/plate assembly into three sectors as described in section 7.3.2 (refer to Figure 7.23), and hence obtain the bounded regions $y_{1(r)(s)}$ and $y_{2(r)(s)}$ together with $A_{t(r)(s)}$. In this instance r refers to the weld number. Note that the local co-ordinate positions are altered such that the origin is moved to the intersection of the stiffener/plate assembly under investigation. Subsequently the mismatched thermal loads of each weld are found in terms of nodal positions and node numbers. The above information together with fusion zone dimensions and their respective transverse contraction forces are then fed in computational analysis as described in Figure 7.37 and Figure 7.36.

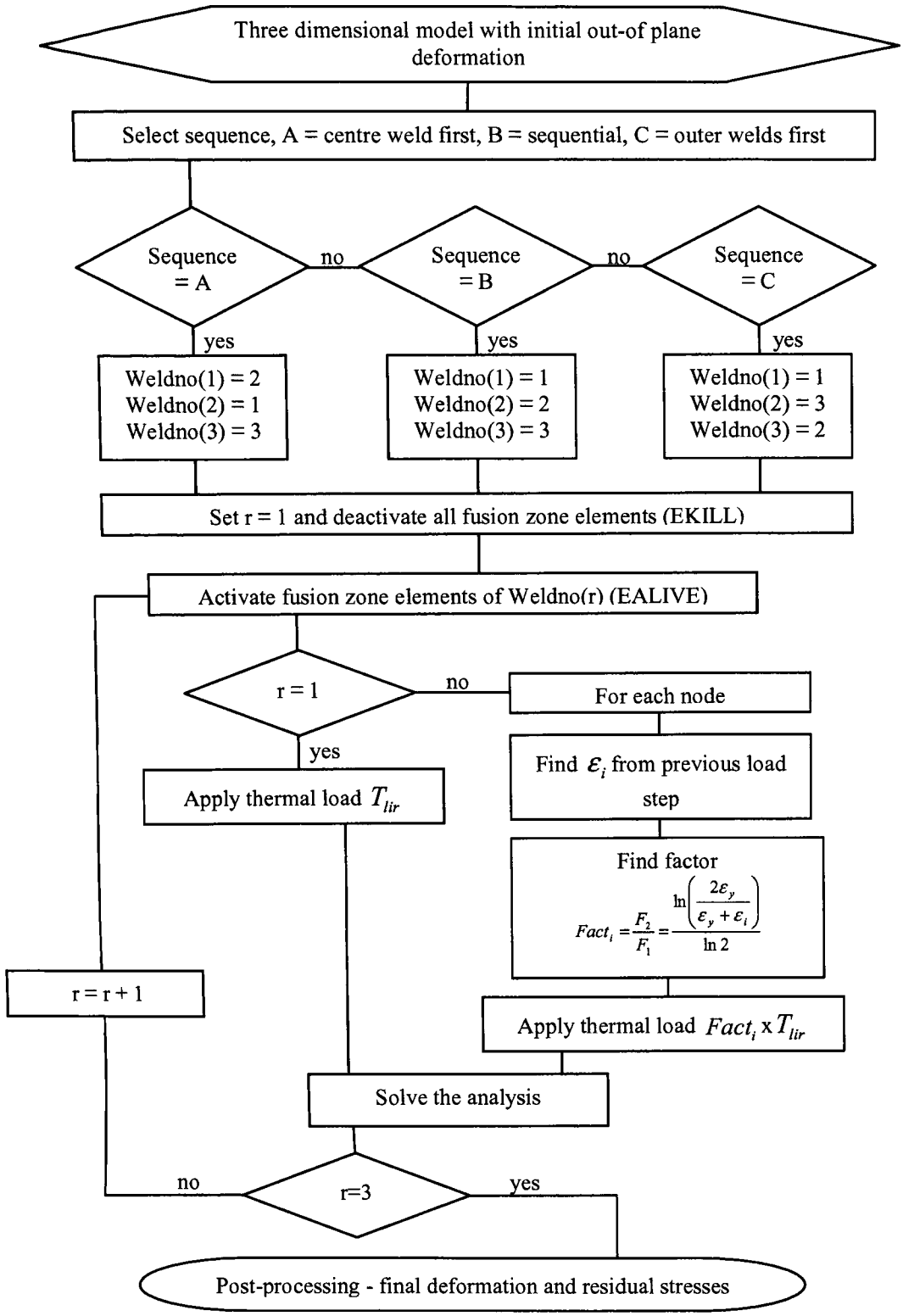

Figure 7.36: Structural finite element algorithm for multiply stiffened plates

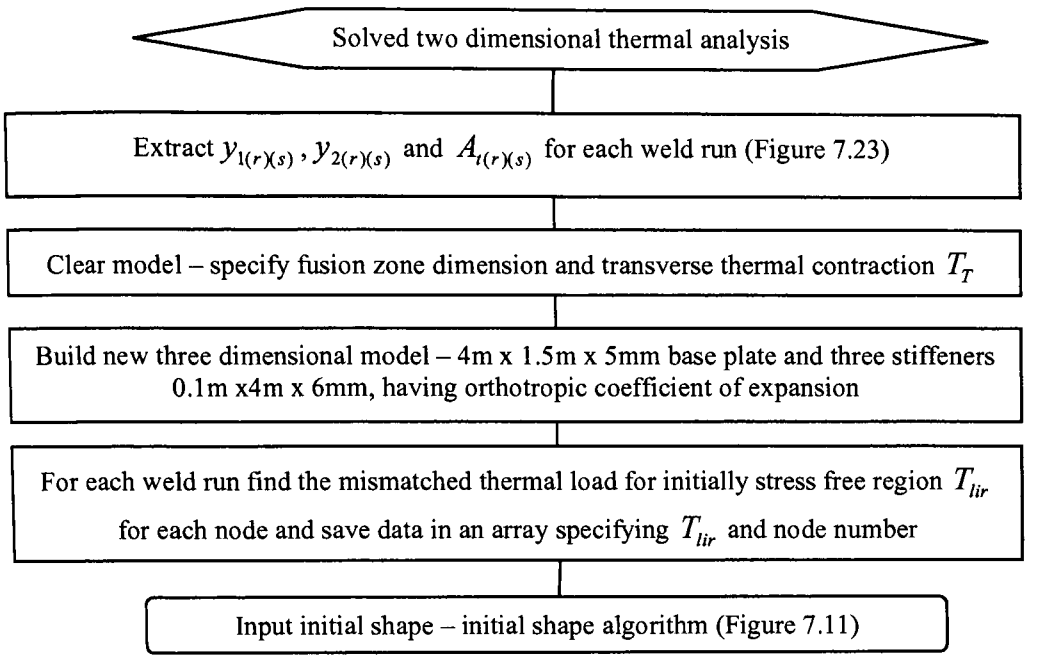

Figure 7.37: Algorithm to input initial shape and find the mismatched thermal loads

The above algorithms were applied to the three test specimens to validate the thermo-elasto-plastic algorithms. Different conditions of transverse thermal strains were investigated. Condition one assumed that the angular distortion was unrestrained and arising entirely from the fusion zone elements. In condition two, the fusion zone was assumed to be partially restrained and hence following the same principle devised for the second fillet weld in double-sided welds. Finally condition three partially restrains the angular distortion for the outer stiffeners but fully restrains the fusion zone at the central stiffener, thus the angular distortion for the outer welds followed equation 7.2 and for the central stiffener T_T was set to $T_a - {}^{\varepsilon_y}/_{\alpha}$ (yield strain). In multiply stiffened plates, the extra restraint arises from the adjacent stiffeners rather than from the previously laid welds, as assumed in double-sided fillet welds. The highest restraint is found at the central stiffener, being bounded by two stiffeners at adjacent sides. On the other hand the outer stiffeners are exposed to a free edge and therefore will assume partial restraint. Condition 3 maybe the most realistic, particularly since a distinct angular distortion is observed at the outer stiffeners of the test specimens, as opposed to the insignificant angular deformation arising at the central stiffener. In essence, Michaleris and DeBicarri [7.6], Hinrinchsen [7.7], Conrardy and Dull [7.8] found out that in multiply stiffeners the angular distortion is

small when compared to the buckling distortion and did not consider the transverse shrinkage effect in there analyses. The weld dimensions, averaged over three macrographs taken from three different section of the welded plate/stiffener assembly, together with the associated transverse thermal loads are given in Table 7.9.

Test specimen no	One			Two			Three		
Weld no	2	1	3	1	2	3	1	3	2
L_1 (mm)	7.039	6.829	5.945	6.778	6.459	5.850	6.101	7.191	6.691
L_2 (mm)	6.144	6.578	7.324	5.510	6.369	7.395	6.194	5.899	5.890
L_3 (mm)	0.569	0.567	0.907	0.521	0.502	0.887	0.635	0.659	0.525
L_4 (mm)	1.071	0.817	0.478	1.156	0.839	0.678	0.931	1.066	1.270
A_{wd} (mm^2)	25.04	25.07	23.59	22.48	22.91	23.13	23.13	25.18	22.18
A_{wp} (mm^2)	2.330	2.485	4.429	1.915	2.131	4.374	2.624	2.591	2.060
A_{ws} (mm^2)	5.024	3.717	1.893	5.225	3.611	2.642	3.786	5.109	5.666
$T_T - T_a$ condition 1 (°C)	-1057	-1042	-1052	-1065	-1042	-1057	-1050	-1059	-1075
$T_T - T_a$ condition 2 (°C)	-699.4	-719.3	-767	-649.6	-704.6	-774.2	-699.7	-676.8	-697.9
$T_T - T_a$ condition 3 (°C)	-119.6	-719.3	-767	-649.6	-119.6	-774.2	-699.7	-676.8	-119.6

Table 7.9: Fusion zone dimension and transverse thermal load for multiply stiffened test plates

A stronger agreement with the experimental results was attained when using 'condition 3'. However, the magnitude of the out-of-plane deformation obtained from the computational results underestimate the experimental results and hence the assumed average coefficient of expansion was increased from 16 x10^{-6} to 20x10^{-6}. In fact, dilatometer tests of this set of plates have shown a higher averaged coefficient of expansion (16.8x10^{-6}), in particular an elevated expansivity was observed in the region between 500°C and 200°C. Note that although the test plates conform to Lloyds 2000 Grade DH36, they were obtained from a different source. Figure 7.38 shows a direct comparison between the experimental and finite element simulations results when applying 'condition 3' and using 20x10^{-6} coefficient of thermal expansion. Although the increased expansivity matched more closely the experimental results in terms of root mean square errors, the three test specimens were subject to a higher longitudinal out-of-plane deformation. This is presumably

an effect of the high initial residual stresses present in the as-received plates, which was not quantified and could not be used in the finite element simulations. Nonetheless, equivalent numbers of crests are present in both the experimental and simulation results.

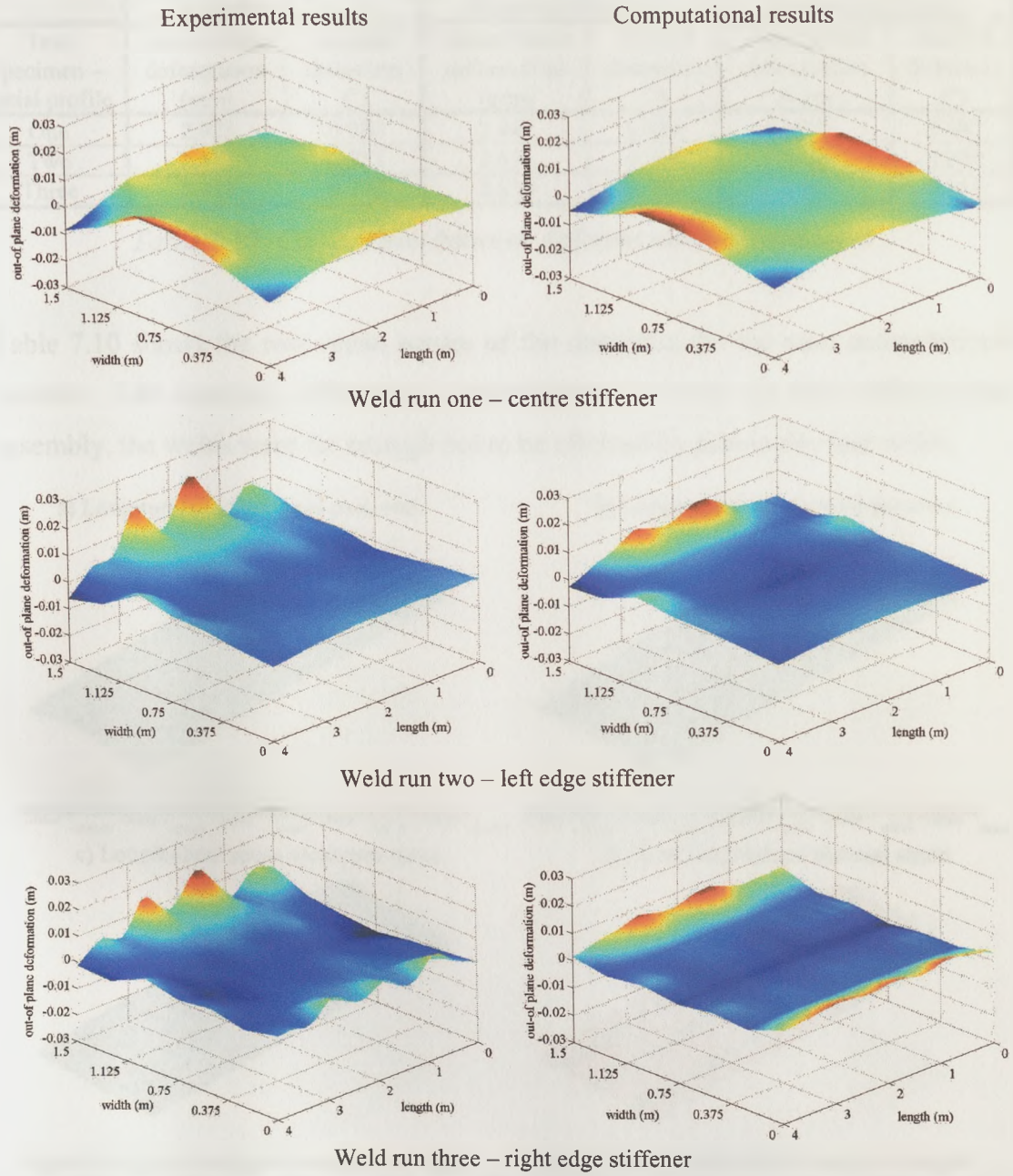

Figure 7.38: Comparison between experimental and simulation results – test specimen one – sequence A

The effect of welding sequence on the final out-of-plane deformation was investigated via nine computational models. Starting from the initial deformation of each individual test plate, the three welding sequences mentioned in section 7.4.1 were explored, whereby the angular transverse contraction followed 'condition 3' and an averaged $20x10^{-6}$ co-efficient of expansion was used.

	Sequence A (2,1,3)		Sequence B (1,2,3)		Sequence C (1,3,2)	
Test specimen – initial profile	Out-of-plane deformation (mm)	Angular distortion (°)	Out-of-plane deformation (mm)	Angular distortion (°)	Out-of-plane deformation (mm)	Angular distortion (°)
One	2.923	0.980	2.941	0.986	2.957	0.987
Two	2.577	0.873	2.571	0.866	2.569	0.870
Three	2.418	0.778	2.523	0.799	2.685	0.815

Table 7.10: Comparison between different welding sequences

Table 7.10 shows the root mean square of the distortion for the nine computational models. The resulting difference is insignificant, however for this stiffener/plate assembly, the welds were far enough not to be effected by previously laid welds.

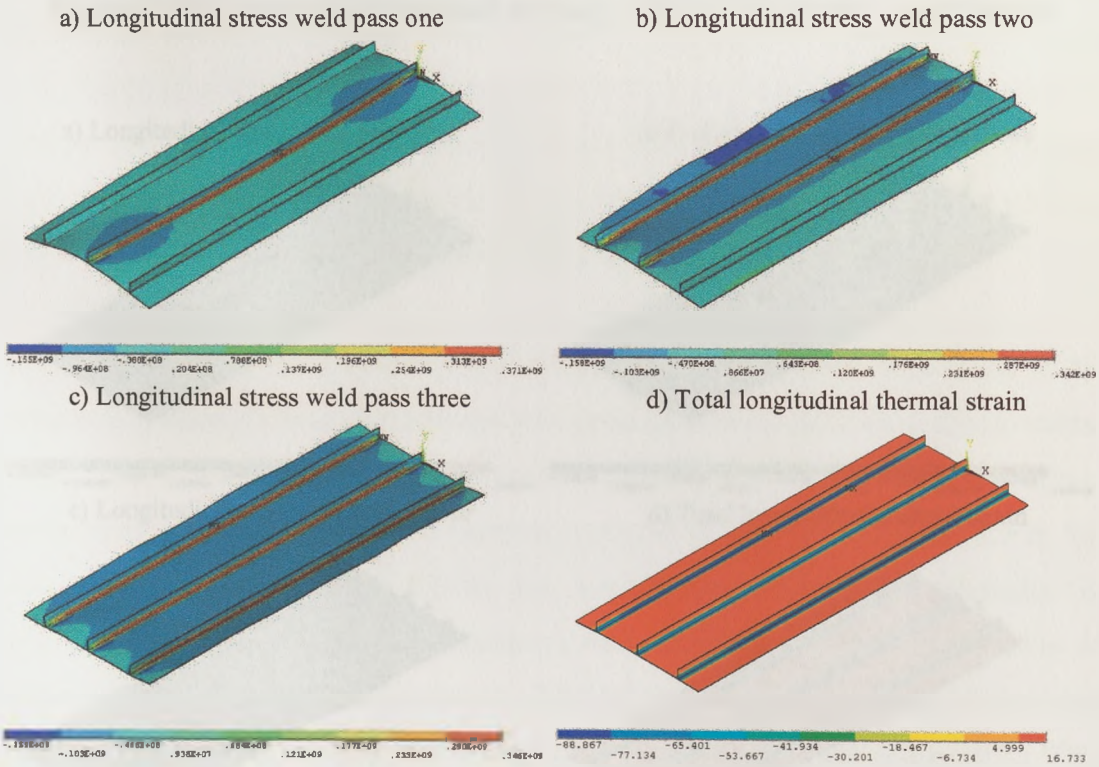

Figure 7.39: Longitudinal residual stresses – test specimen one – sequence A

Figure 7.39 to Figure 7.41 show the longitudinal residual stresses during different stages in the welding cycle for test specimen one.

a) Longitudinal stress weld pass one

b) Longitudinal stress weld pass two

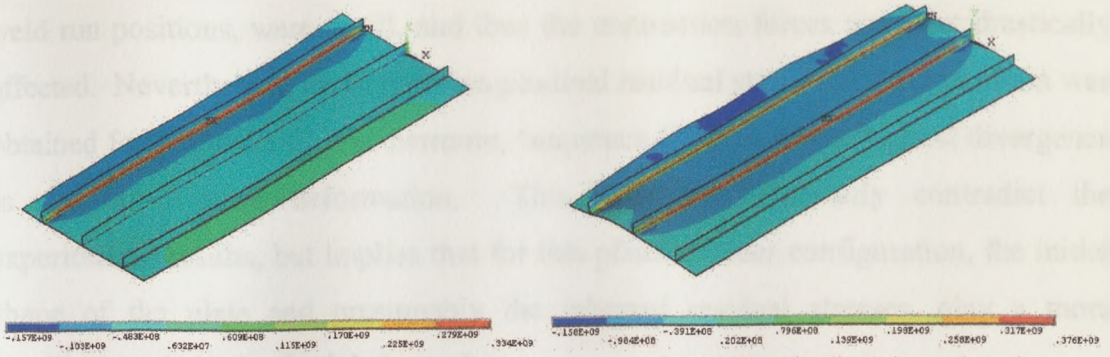

c) Longitudinal stress weld pass three

d) Total longitudinal thermal strain

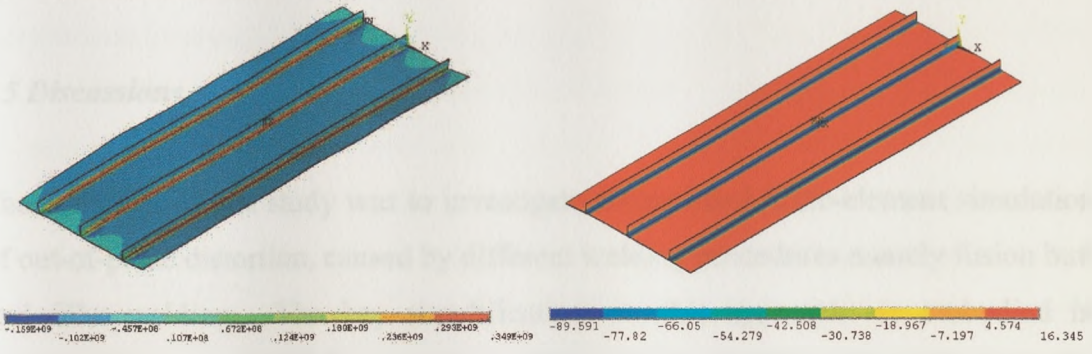

Figure 7.40: Longitudinal residual stresses – test specimen one – sequence B

a) Longitudinal stress weld pass one

b) Longitudinal stress weld pass two

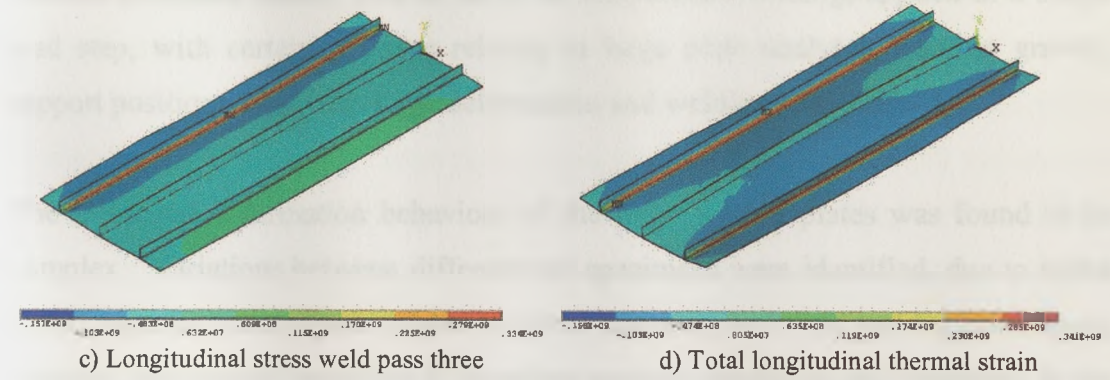

c) Longitudinal stress weld pass three

d) Total longitudinal thermal strain

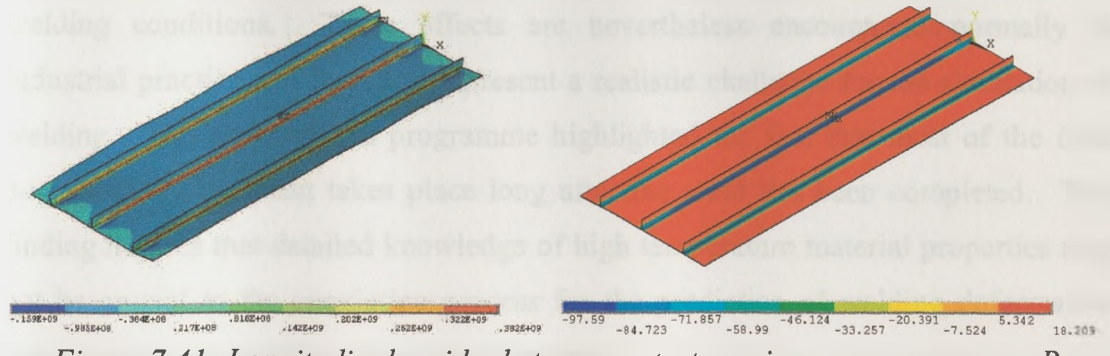

Figure 7.41: Longitudinal residual stresses – test specimen one – sequence B

The compressive residual stresses due to previously laid welds and at subsequent weld run positions, were small, and thus the contraction forces were not drastically affected. Nevertheless, the highest longitudinal residual stress and thermal strain was obtained for sequence C. Furthermore, 'sequence C' showed the highest divergence in the out-of-plane deformation. This does not necessarly contradict the experimental results, but implies that for this plate/stiffener configuration, the initial shape of the plate and presumably the inherent residual stresses, play a more significant role in the final deformation.

7.5 Discussions

The main aim of this study was to investigate a simplified finite-element simulation of out-of-plane distortion, caused by different welding procedures namely fusion butt and fillet welding. The key simplifications in this approach are embodied in analytical treatments of the angular and longitudinal deformations through the 'contraction thermal strain' and 'mismatched thermal strain' algorithms respectively. From the computational viewpoint, the problem has been reduced to an elastic finite-element structural model, with an artificial temperature loading, applied in a single load step, with certain provisos relating to large plate analyses, such as gravity, support positions, buckling, large deformation and welding sequences.

The measured deformation behaviour of the large welded plates was found to be complex. Variations between different test specimens were identified, due to initial shape imperfections, effects related to initial assembly and weld tacking procedures, transient mechanical variations in boundary support conditions and variations in the welding conditions. These effects are nevertheless encountered normally in industrial practice and therefore represent a realistic challenge for the simulation of welding. The experimental programme highlighted the fact that most of the final out-of-plane movement takes place long after the weld has been completed. This finding implies that detailed knowledge of high temperature material properties may not be crucial to the simulation process for the prediction of welding deformation (but accurate expansivity values are important).

Various computational strategies have been investigated, namely the application of the thermal loads in a sequential or simultaneous formulations, the influence of the initial out-of-plane deformation on the final deformation outcome, and the effect of welding configurations on the transverse and longitudinal thermal strains. The sequential and simultaneous approaches interacting with the angular and longitudinal deformations gave slightly different results, the latter probably being the more realistic.

Comparison between the results of the simulations and the out-of-plane deformations measured was good, bearing in mind the substantial variations found in practice. Overall shape comparisons were good, except for certain test plates, where other factors intervened, such as buckling and offsetting of the longitudinal contractions, prevailed. The magnitudes of angular deformations and overall out-of-plane deformations were predicted well enough to be useful as a guide to what would happen in a practical case. However a good definition of the coefficient of thermal expansion is required

As, distinct from the pilot programme, it is demonstrated that the initial profile plays an important role in the final deformation and must be included in the finite element model. This may take different forms i.e. the direct input of the initial displacements or the quantification of the initial as-received residual stresses, included the inherent welding residual stresses during the tack welding procedures. The latter is difficult to enumerate unless the inherent residual stresses are measured and mapped onto the finite element model at fine discrete points. Nonetheless the finite element analysis can be used to estimate the initial profile by performing buckling analyses of the different geometries or computing the initial residual stresses due to the tack welds via the simplified computational algorithm presented in this thesis.

The different welding configurations gave rise to different evolutions in both longitudinal and transverse contractions. The evolution of the thermal strains is fairly straightforward in unrestrained butt-welding of two plates and replicates the behaviour of the small-scale test plates. However the transverse thermal strains of

large plate fillet welding may be influenced by restraints arising from the geometry, particularly due to the high thermal gradient between the ends of the plate and the stiffness of the stiffener/plate configuration or previously laid welds. As distinct from the small-scale test plates, in double-sided fillet welding the second weld pass was restrainted by the deposited material of the previous weld pass. Hence, Okerblom's theory was adopted and modified to give a partially restrained transverse thermal contraction, dependant on the thickness of the base plate and fusion zone dimensions. In multiply stiffened plates the angular transverse contraction was found to be less significant. In these cases the angular distortion cannot be analysed as a plane section but the whole three dimensional model should be taken into account. In essence it was found that the highest restraint arises in bounded stiffeners (such as in the central stiffener of the test specimen). In these cases the maximum transverse contraction is of yield strain nature. On the other hand the outer stiffeners are exposed to a free edge and hence may be assumed to be partially restrainted. The following assumptions have been demonstrated and good agreement was achieved when compared with the experimental results.

The longitudinal thermal strain, (mismatched thermal strain) was found to be dependant on previously laid welds and in particular the distance between welds. In double-sided fillet welding, the final longitudinal thermal strains of two consecutive welds with intermediate ambient cooling gave a slight increase in contraction force produced by a single weld and are related to the offsetting distance between the two welds. However, this is highly dependant on the welding sequence adopted. In fact, in simultaneously laid double-sided fillet welding, the final longitudinal contraction was approximately twice that of one fillet weld.

The application of double-sided fillet welds using simultaneous and staggered welding was also examined, with respect to mitigation of out-of-plane deformation while reducing the manufacturing time to the maximum. Not surprisingly, closely spaced welding resulting in higher deformations, however drastic increases in deformation were observed when the critical buckling load of the stiffener/plate configuration was exceeded. It is also evident that when buckling occurs, the final

deformation is largely independent of the initial deformation and assumes a profile dependant on the buckling mode assumed by the computational model. It is also recommended to stagger the two welds such that the final longitudinal thermal strain does not exceed the critical buckling load. In so doing, the final deformation is not significantly increased while the manufacturing time is considerably reduced, when compared to double-sided fillet welding with intermediate cooling.

The effect of welding sequences was also investigated in multiply stiffened plates. While the experimental results have shown that sequence A (welding the central stiffener and then the outer stiffeners) results in the highest out-of-plane deformation the computational analyses have shown that this is an effect of the initial shape and presumably the inherent residual stresses. If one considers the effect of welding residual stresses on the welding sequence, the computational models have shown that welding the central stiffeners first and the subsequent outer stiffeners results in least distortion. This effect would have been more pronounced in closely spaced welds and hence the stiffener/plate configuration, in particular the distance between the stiffeners, plays an important role in the final out-of-plane deformation.

7.6 References

[7.1] Okerblom,N.O., 'The calculations of deformations of welded metal structures,' *Her Majesty's Stationery Office, London*, 1958.

[7.2] Feng,Z. and Rowlands, R.E., 'Continuous Full-Field Representation and Differentiation of Three Dimensional Experimental Vector Data,' *Computers and Structures,* Vol.26, No.6, pp. 979-990, 1987.

[7.3] Comlekci,T., 'Development of Hybrid Experimental-Numerical Methods for Thermoelastic Stress Analysis,' *PhD Thesis, Mechanical Engineering Department, University of Strathclyde,* 1996.

[7.4] Yang,Y.P., Brust,F.W. and Cao,Z., 'Virtual Fabrication Technology Weld Modeling Tool and its Applications in Distortion Predictions,' *ASME, Pressure Vessels and Piping Division PVP,* Vol.464, pp 29-33, 2003.

[7.5] Michaleris,P. and DeBiccarri,A. 'Prediction of Welding Distortion,' *Welding Research Supplement,* Vol.76, No.4 pp 172s-181s, 1997.

[7.6] Michaleris,P. and DeBicarri,A., 'A Predictive Technique for Buckling Analysis of Thin Section Panels Due to Welding,' *Journal of Ship Production,* Vol.12, No.4, pp. 269-275, 1996.

[7.7] Hinrinchsen,B., 'Prediction of Welding Induced Distortion in Thin-walled Ship Panels,' *Ship Technology Research,* Vol.46, pp. 153-163, 1999.

[7.8] Conrardy,C. and Dull,R., 'Control of Distortion in Thin Ship Panels,' *Journal of Ship Production,* Vol.13, No.2, pp 83-92, 1997.

CHAPTER EIGHT

CHAPTER 8

CONCLUSIONS AND RECOMMENDATIONS

8.1 Conclusions

Many industries concerned with the fabrication of thin plate structures experience difficulties and high rectification costs related to cutting and welding thermal distortion. It is attractive to quantify the thermal deformations by mathematical or finite element models. In so doing, design engineers would be able to explore alternative parameters and joining sequences during the design stages, such that the required tolerances of the sections can be achieved by a minimum rework.

Various welding finite element models exist but the complexity involved makes such analyses unsuitable at the design stages of welded structures. A number of simplified approaches have been established by various researchers and are reviewed in chapter two. The main aim of these analyses is to reduce the computational time. Typically this is done via a two-dimensional non-linear transient finite element analysis that establishes the welding residual stresses which are later applied to the full three-dimensional model, thus making the analyses dependant on knowledge of the non-linear material properties. At the other end of the spectrum, efforts have been made to perform simple elastic finite element analyses using some crude assumptions, such that a cooling contraction and shrinkage volume is chosen to suit and match the expected level of deformation. These assumptions are based on experimental results and the methods are not easily transferable to other materials.

In the present study a finite-element computational procedure for simulating the process of industrial scale welding has been demonstrated using simple and adaptable methodologies. The method is generic with respect to material properties, welding processes and thickness and efforts have been made to produce a computationally economic and robust welding distortion simulation. A key factor that underlies this study is an *uncoupled* computational strategy, whereby the thermal transient, thermo-elastic-plastic and structural stages of the thermo-mechanical welding process, are treated separately. The integration of the thermal transient to the thermo-elastic-plastic welding residual stress evolution was achieved via two algorithms named *'Mismatched Thermal Strain'* and *'Contraction Thermal Strain'* thus applying two contraction mechanisms in the longitudinal and transverse directions respectively. Effects of previously laid welds and restraints arising from the structure are also incorporated in the algorithms. The theoretical models and results generated in the project have been supported at all stages by welding tests of a realistic nature to maintain confidence in the validity and applicability of the treatments.

The main conclusions that can be drawn, based on the investigations carried out in this study, are gathered in this chapter and include:

1. General conclusions:

- A number of simplifications of the phenomena leading to welding deformations are possible, but if the main concern is the prediction of the residual stresses then a more detailed non-linear analysis is required. The simplified thermo-elasto-plastic algorithms presented in this thesis use constant material properties that mainly reflect the room temperature material properties. However averaged coefficients of thermal expansion that take some account of metallurgical phase transformation were also incorporated in the analyses and found to be essential in the prediction of the out-of-plane deformation.

- From the computational viewpoint, the problem has been reduced to an elastic finite-element structural model, with an artificial temperature loading applied in a single load step per weld pass. This was relatively simple to implement and solved quickly. Typically the simulations required 2 to 8 hours, depending on the number of weld passes, when performed on a dual processor workstation with 2.2GHz CPU and 1GB RAM.

- Comparison between the results of the simulations and the out-of-plane deformations measured was good, bearing in mind the substantial variations found in practice. Overall shape comparisons were good, except for specific specimens where special factors intervened. The magnitudes of angular deformation and overall out-of-plane deformations were predicted well enough to be useful as a guide to what would happen in a practical case.

- The success of the simulation process clearly depends on the quality of input data and it was found, not surprisingly, that it was crucial to input information on the initial shape of the test specimens for accurate prediction. It was also clear that the deformations due to self-weight were important, both in the initial state and transiently during the welding and cooling process.

- Simulations have shown that the simplified computational thermo-elasto-plastic algorithm is insensitive to the yield strength of the welded structure, particularly if an inverse relationship exists between the transverse distance and the maximum temperature of specific nodal points. For the test specimens performed in this study, this relationship was close to an inverse proportional relationship and hence the insensitivity of the algorithm to yield strength was shown. This outcome should not be specific to mild steel but might depend on process conditions relative to thermal properties.

2. *Experimental observations:*

- The experimental work using the two welding rigs was found to be very informative in the analysis of welding distortions. Thermal imaging, coupled with thermocouple results were essential for the correlation of the computational transient models with the real behaviour. The use of linear variable displacement transducers also gave insight into the evolution of welding distortions. In essence the experimental results have shown two important results, firstly that the vast majority of welding distortions occur during the cooling stages and secondly that a high thermal gradient exists in the transverse direction as opposed to the low longitudinal thermal gradient behind the heat source.

- It was initially thought that transverse out-of-plane (angular) distortions were associated with temperature gradients between the top and bottom surfaces of the plate in the regions experiencing temperatures of 600°C and below, where the parent material achieves significant mechanical strength. Thermocouple and computational results have shown that such thermal strains do not exist to an extent likely to cause such out-of-plane distortion and it may be deduced that this phenomenon is more related to the shape of the weld zone or better the weld pool.

- Thermal imaging provides whole-field information in a practical situation and therefore constitutes a unique tool for the evaluation of inputs to a thermo-mechanical determination of distortion or residual stress caused by a welding process.

- As the thermal image provides direct evidence of transient temperatures, this approach avoids the need for complex theoretical determinations in the input stage of a thermo-mechanical computation.

- Suitable techniques and algorithms for spatial and temperature calibration of the images, necessary for accurate prediction of outcomes, have been developed and are presented in chapter four. In particular efforts were made to reduce errors related to lens aberrations.

3. *Thermal simulations:*

- The study in chapter five has shown consistency between the various analytical and computational thermal approaches and these agree satisfactorily with the experimental results. However, the thermal transients generated by analytical and computational models depend on an empirical heat input efficiency. Different welding configurations gave rise to different welding efficiencies making the analyses dependent on the experimental thermocouple / thermal imaging information.

- The various strategies adopted in modelling the heat input gave adequate simulation of the thermal transients in the far field temperature region but were not sufficient to simulate the thermal evolution of the fusion zone elements.

- Only small discrepancies were observed between the different thermal models. In particular the use the element 'birth and death' technique was not justifiable considering that the end thermal transients could be correlated with realistic results via a thermal efficiency factor.

- The analytical thermal solutions, require the least computational time, but are specific to certain geometries and are not readily available to investigate the evolution of thermal transients in complex welded structures, particularly when different boundary conditions, such as heat sinks are associated with the setup.

- The analytical solutions developed by Rosenthal have been modified to incorporate non-linear material properties via an iterative solution of the enthalpy and the integral of the conductivity (named heat absorption). Matching results to the experimental values were attained when using non-linear material properties.

- The two dimensional cross-sectional approach proves to be the least time consuming of the methods used for thermal modelling and provides accurate thermal results. For mild steel it is suggested that a two dimensional cross-sectional computational model is adequate to simulate the thermal transients.

- In fillet welding the thermal gap between the stiffener and the plate constitutes an important parameter in the thermal transients and must be modelled in the computational analysis via non-merged nodes. Furthermore the thermal conduction pattern of the joint assembly in the second fillet will differ from the first fillet with respect to time lags in the transient temperatures. Nonetheless the fluctuations in the maximum temperatures attained at far-field positions were not significant, when considering and ignoring the above boundary conditions.

- The heat distribution in fillet welded attachments fluctuates according to the angular position of the welding head. It is imperative to distribute the heat evenly in the stiffener and plate assembly such that the final longitudinal contraction force acts on the neutral axis of the assembly, thus making the consistency of fillet welding dependent on the alignment of the welding setup.

- The use of a backing strip had an insignificant effect on the thermal patterns at the far-field temperature, and a thermal gradient through the thickness of the plate was not apparent. In essence the changes between a backed and a non-backed computational model can be simply adjusted via an empirical efficiency.

4. *Out-of-plane deformation – pilot programme (small plates):*

- The pilot programme test gave an initial calibration of the simplified computational algorithm while ignoring any other effects associated with large plate analysis. In particular, the differences in out-of-plane deformation between the as-received plates and stress-relieved plates seemed not to be significant and this may be due to the smaller size of the plates. The results of butt and double-sided fillet welding are given in chapter 6.

- The vast majority of the butt-welded plates assumed a saddle or hogged shape after complete welding and cooling to ambient temperature but a quarter of the plate specimens sagged. This was due to the initial negative angular presetting of these tack welded plates and was not associated with the initial inherent residual stresses due to the tack welds or manufacturing processes. This confirms that the initial shape of the plate plays a critical role in the final out-of-plane distortion

- The alternative sequential and simultaneous application of the transverse and longitudinal thermal strains in the computational models gave rise to small differences in the final deformation. While the simultaneous algorithm reduces the computation to a one load step analysis, the sequential algorithm broadens the applicability in terms of simulating the deformation via various mesh strategies. Thus, instead of performing a three dimensional solid element, thermo-elastic plastic, thermal and structural analysis, a two dimensional analysis can be performed for the thermal stage and for the angular distortion. This is then fed to a two-dimensional in-plane shell model to calculate the full out-of-plane distortion. Such an approach reduces the number of elements required and the computational feasibility for complex models.

- The co-efficient of thermal expansion assumed in the computational analysis will determine the longitudinal contraction force. A linear relationship exists

between the expansivity and the longitudinal contraction force but does not necessarily mean that the expansivity will linearly increase the total out-of-plane deformation, the latter being also depending on the angular distortion.

- The out-of-plane longitudinal curvature is driven primarily by the offset distance between the centroid of the longitudinal force and the neutral axis of the plate, implying that an increase in angular distortion will result in an increase in longitudinal curvature. In the case of fillet welding, the heat distribution and hence the welding head position will have an influence on such distance. It is suggested to place the welding head at 45° to the assembly, thus evenly distributing the heat over the stiffener and plate.

- Double-sided fillet welding tests of the smaller plates ($0.5m^2$) showed only slight deviations in the out-of-plane longitudinal deformation, and this is an effect of the second moment of inertia arising from the tall stiffener. The majority of the deformation was in the transverse direction (angular distortion) and in this sample the test plates were small enough for the transverse contraction due to the second weld pass to be affected by previously laid welds.

5. *Out-of-plane deformation – large-scale programme (industrial scale plates):*

- Finite-element computational procedures for simulating the process of industrial scale butt and double-sided fillet and multiply stiffened plates have been demonstrated in chapter 7. Effects due to non-linear structural behaviour, support detachment, residual stresses due to previously laid welds and restraints arising from the structure, have been included in the thermo-elasto-plastic algorithm and structural models.

- In contrast to the small-scale tests, other structural factors influence the out-of-plane deformation in industrial scale welded structures. These include tack welding sequences, inherent residual stresses due to alignment tack

welds, gravitational effects, support positions and restraints arising from the size of the plate.

- Stronger correlation with the experimental results was achieved when the plates were symmetrically tack welded. This is an effect of the inherent residual stresses induced in the plates due to plate edge alignment problems. In sequential tack welding, the plates were subject to higher bending moments, particularly towards the ends of the plate. Such stresses were not modelled in the computational analyses and are difficult to quantify. Hence it is suggested to adopt a tack welding procedure that imposes the least residual stresses, that is, tack weld the plates symmetrically.

- Transient distortion results have shown that, when the second weld pass in double-sided fillet welding is completed after full intermediate cooling there is only a slight increase in longitudinal contraction force, relating to the offsetting distance between the two welds. The angular distortion is restrained by the extra stiffness offered by the previously laid weld.

- It is clear that simultaneous or closely staggered double-sided fillet welding, result in drastic out-of-plane deformations, while the least deformation is achieved if intermediate ambient cooling is employed. The optimum manufacturing time versus deformation was found to be in cases where the total longitudinal contraction force did not exceed the critical buckling load of the structure.

- In simultaneous and closely staggered double-sided welds the longitudinal force was large enough to buckle the plate, the resulting profile for the test specimens under investigation was independent of the initial out-of-plane deformation of the test specimens.

- Experimental and computational analyses of multiply stiffened plates have shown that the angular distortion in bounded stiffeners (as in the central

stiffener being bounded by the two adjacent stiffeners) is highly restrained and gives rise to a transverse contraction of yield strain, whereas the outer stiffeners are partly restrained.

- Computational analyses have shown that welding 'sequence A' (centre first then outer stiffeners) results in the least out-of-plane deformation, and this is an effect of the compressive residual stresses at regions of newly welded positions. In fact the highest residual stresses were noticed at the central stiffener when welding using 'sequence C' (outer first then centre).

- The experimental results from the three multiply stiffened test specimens have shown that welding 'sequence A' results in the highest out-of-plane deformation, however this was due to initial shape and presumably due to the inherent residual stresses of their respective manufacturing and tack welding procedures.

- The variations in the out-of-plane deformation and welding residual stresses between the different welding sequences in multiply stiffened plates were not major, however the residual stresses due to previously laid welds is more significant in closely spaced welds, that is the effect will be more detrimental for smaller pitches of stiffener assemblies.

8.2 Recommendations for future work

A simplified thermo-elasto-plastic algorithm has been successfully demonstrated for the prediction of the out-of-plane deformation in industrial scale welded structure. Effects of previously laid welds and restraints in angular distortion arising from the structure have been taken into account. The simplified algorithm outlined in this study, reduces the complexity of welding simulations to a simple one load step elastic analysis. While it is not necessary to include many non-linear aspects, the success of the simplified algorithm depends on knowledge of the welding efficiency,

fusion zone dimensions, initial out-of-plane deformations and coefficient of thermal expansion. Some further investigations are required in the following themes:

1. Welding efficiency and fusion zone dimensions:

Firstly, the welding efficiency changes between different processes and welding configurations, and a precise library of the thermal efficiencies is not available, presumably due to the number of variables associated with welding. This makes the thermal transient simulations dependant on good experimental data. While thermal imaging can be used as an input to the thermo-elasto-plastic analyses, it may be better to concentrate efforts in performing more localized computational models of the weld, including gas flows, deposition of weld material, electromagnetic-thermal-flow and other non-linear analyses. In addition to defining the weld thermal efficiencies, the computational models will also characterize the fusion zone dimensions driving the angular distortion.

2. Initial out-of-plane deformation – initial inherent residual stresses:

The study has shown that the initial shape of the plate plays an important role in the final out-of-plane deformation. In this study the initial out-of-plane deformation was measured using a laser scanning system but this is impractical in industrial context. Initial perturbations arise from inherent residual stresses due to their respective manufacturing process (such as normalizing, hot-rolling etc etc) and tack welding procedures. The former is difficult to enumerate unless the residual stresses are measured and mapped onto the finite element model at discrete points. Various strategies are possible to measure such residual stresses however, due to size of plate, the most viable systems are magnetic sensors. Though confined to ferrous materials, the apparatus is non-destructive and provides direct measurement of the principal stresses. The use of a magnetic anisotropic sensor has been investigated in a number of undergraduate projects during the term of this project and gave promising results. On the other hand the formation of the welding residual stresses due to the tack welds can be easily modelled using the simplified thermo-elasto-plastic algorithm

described in this thesis. Another approach would be to perform buckling analyses of the plate under investigation and assume an initial out-of-plane deformation representing the overall shape of the buckled plate.

3. Co-efficient of thermal expansion:

The predicted out-of-plane deformation is largely influenced by the assumed coefficient of thermal expansion. Dilatometer tests have shown that the coefficients of expansion over the temperature ranges of 1110 – 700, 700 – 500 and 500 to ambient temperature are in the region of 22.7×10^{-6}, -1.04×10^{-6} and 16.6×10^{-6} respectively (the negative expansivity reflects phase changes). These values are specific and fluctuate between different steel grades, in particular the carbon content will have an influence on the continuous cooling transformation diagram and hence the expansivity. It is proposed to investigate the evolution of welding distortions when considering different grades of steel while obtaining a good library of expansivities.

4. Aluminium welded structures:

The simplified therm-elasto-plastic algorithm was tested out and calibrated for mild steel. The assumption that the heat flow for fast welding speeds is mainly transverse to the weld might not hold for other materials. Typically, aluminium has a high thermal diffusivity when compared to mild steel. Also the assumed cut off temperature (determining the thermal transverse strain) differs for different materials. It is recommended to test out the algorithm on different materials, before adapting the thermo-elasto-plastic algorithm to advanced materials.

5. Integration of the simplified finite element model to artificial neural network:

The main aim of this project was to develop support tools for the design and manufacturing of thin plate welded structures. These tools were examined and calibrated but have not been used particularly to investigate means of mitigating

distortions (except for double-sided fillets). The simplicity of the algorithm can be easily adapted to different welding structures and configurations to investigate the welding sequence that gives rise to the least deformation. In essence every welded geometry results in different deformations and thus a knowledge base system may be developed using the proposed finite element algorithm to form a library of out-of-plane deformations with respect to stiffener/plate ratios, number of stiffeners, number of weld passes, welding sequence and pitch between stiffeners, giving an immediate predicted out-of-plane deformation. Artificial neural networks have already been demonstrated in the work performed elsewhere but this approach requires a knowledge base from the experimental results. It is proposed to integrate the two systems and build an artificial neural network – finite element knowledge base system.